Cyprus University of Technology

Department of Mechanical Engineering and Materials Science and Engineering

Doctoral Dissertation

MICROSCALE BLOOD FLOWS AND RHEOLOGY – SURFACE TENSION DRIVEN FLOW APPLICATIONS FOR POINT OF CARE DIAGNOSTICS

Student Name Surname

Dimitris Pasias

Limassol, April 2022

CYPRUS UNIVERSITY OF TECHNOLOGY

Department of Mechanical Engineering and Materials Science and Engineering

Doctoral Dissertation

MICROSCALE BLOOD FLOWS AND RHEOLOGY – SURFACE TENSION DRIVEN FLOW APPLICATIONS FOR POINT OF CARE DIAGNOSTICS

Dimitris Pasias

Limassol, May 2022

Approval Form

Doctoral Dissertation

MICROSCALE BLOOD FLOWS AND RHEOLOGY

–

SURFACE TENSION DRIVEN FLOW APPLICATIONS FOR POINT OF CARE DIAGNOSTICS

Presented by

Dimitris Pasias

Supervisor: Efstathios Kaliviotis, Associate Professor, Cyprus University of Technology.

Signature _____

Member of the committee: Nadia Antonova, Professor, Bulgarian Academy of Sciences.

Signature _____

Member of the committee (Chair): Yannis Dimakopoulos, Associate Professor, University of Patras.

Signature _____

Cyprus University of Technology

Limassol, May 2022

Copyrights

The approval of the dissertation by the Department of Mechanical Engineering and Materials Science and Engineering does not imply necessarily the approval by the Department of the views of the writer.

Acknowledgments

First and foremost, I am extremely grateful to my supervisor, Dr. Efstathios Kaliviotis for his invaluable advice, continuous support, and patience during my PhD study. His knowledge and plentiful experience have encouraged me in all the time of my academic research and daily life. I would also like to thank Dr. Loukas Koutsokeras, Dr. Georgios Constantinides, Dr. Panayiotis Keivanidis, Dr.Andreas Passos, Dr. Stavroula Balabani, Dr. Harisson Seidner and the NanoLysis LTD for helping with part of the TiO_2 coating process, and for their technical support on my study. I would also like to thank Dr. Stephanos Pavlides and the personnel of his haematology laboratory for their help in blood collection. In addition, I would like to thank and all the members in the Biorheology Laboratory for their support.

Abstract

Surface tension driven blood flow in microfluidic applications for blood diagnostics, is a simple and cost-effective approach, however, the flow and rheological characteristics of blood in such setups is not well understood. The aim of this work is to characterize the blood flow in such applications and to investigate the influence of erythrocyte deformability, aggregation and haematocrit, which dominate the non-Newtonian nature of blood. For this purpose, normal and super-hydrophilic microchannels were produced to accommodate the flow, and whole human blood, as well as erythrocyte suspensions were produced to provide various states of erythrocyte deformability, aggregation and sample haematocrit. The samples were imaged under flow, and their local and bulk velocity characteristics were assessed using micro-Particle Image Velocimetry setups and tracking techniques. Standard methods were utilised to assess the viscosity, aggregation and deformability of the samples, whereas image processing methods were developed to characterize the microstructure of the samples in the microchannel. Fluid mechanics and rheology theory was utilised to model the velocity and viscosity of the fluids. The results, show a clear influence of the viscosity, however, a complex non-monotonic influence of the aggregation, on the velocity in the microchannel affected by moderate to intense shearing conditions in the channel.

Η ροή αίματος, η οποία ωθείται από επιφανειακή τάση σε μικρορροϊκές εφαρμογές για διαγνωστικούς σκοπούς, είναι μια απλή και οικονομική προσέγγιση. Ωστόσο, η ροή και η ρεολογία του αίματος σε τέτοιες καταστάσεις δεν έχουν κατανοηθεί εις βάθος. Στόχος αυτής της εργασίας είναι ο χαρακτηρισμός της ροής του αίματος σε μικρορροϊκές εφαρμογές παθητικής ροής, και η διερεύνηση της επίδρασης της παραμόρφωσης, συσσωμάτωσης και συγκέντρωσης (αιματοκρίτη) των ερυθροκυττάρων, παράγοντες οι οποίοι επηρεάζουν σημαντικά τη μη-Νευτώνεια φύση του αίματος. Για το σκοπό αυτό, κατασκευάστηκαν ουδέτεροι και υπερ-υδρόφιλοι μικροαγωγοί, χρησιμοποιήθηκαν δείγματα πλήρους ανθρώπινου αίματος, καθώς και διαλύματα ερυθροκυττάρων, για την δημιουργία διαφόρων καταστάσεων παραμόρφωσης, συσσωμάτωσης ερυθροκυττάρων και αιματοκρίτη. Τα δείγματα απεικονίστηκαν υπό ροή και τα χαρακτηριστικά της τοπικής και μέσης ταχύτητας εκτιμήθηκαν χρησιμοποιώντας τεχνικές απεικονιστικής ταχυμετρίας και παρακολούθησης σωματιδίων. Χρησιμοποιήθηκαν τυπικές μέθοδοι για την μέτρηση του ιξώδους, της συσσωμάτωσης και της παραμόρφωσης των δειγμάτων αίματος, ενώ αναπτύχθηκαν εξειδικευμένοι αλγόριθμοι επεξεργασίας εικόνας για τον χαρακτηρισμό της μικροδομής των δειγμάτων στους μικροαγωγούς. Ρευστομηχανική και θεωρία Ρεολογίας χρησιμοποιήθηκαν για τη μοντελοποίηση της ταχύτητας και του ιξώδους των ρευστών. Τα αποτελέσματα δείχνουν μια σαφή επίδραση του ιξώδους, ωστόσο, μια πολύπλοκη μη μονοτονική επίδραση της συσσωμάτωσης στην ταχύτητα αίματος, η οποία επηρεάζεται από τις συνθήκες διάτμησης στους αγωγούς.

Keywords: Blood rheological properties, surface tension, microchannel flow

Table of Contents

Contents

List of Tables

List of Figures

List of Abbreviations

Abbreviation / Symbol	Explanation	Units	Abbreviation / Symbol	Explanation	Units
AR	Aspect ratio (W/h)	-	u	x – direction velocity component	$\mu m\ s^{-1}$
AI	Aggregation index	-	UV	Ultraviolet	-
DEX	Dextran	-	V_{RI}	Velocity ratio	-
EI	Elongation index	-	V_p	Linear velocity (plate flow)	$\mu m\ s^{-1}$
Hct	Hematochrit	-	V_{ch}	Velocity in the core of the channel	$\mu m\ s^{-1}$
M	M index	-	$\bar{V}_{ch}$	Mean value of V_{ch}	$\mu m\ s^{-1}$
NAB	Non-aggregative blood	-	$\bar{\bar{V}}_{ch}$	Mean value of $\bar{V}_{ch}$	$\mu m\ s^{-1}$
O_2	Oxygen	-	V_m	Meniscus velocity	$\mu m\ s^{-1}$
PBS	Phosphate buffered saline	-	$\bar{V}_m$	Mean value of V_m	$\mu m\ s^{-1}$
PIV	Particle image velocimetry	-	$\bar{\bar{V}}_m$	Mean value of $\bar{V}_m$	$\mu m\ s^{-1}$
RBC	Red blood cell		V_{max}	Maximum of V_{ch}	$\mu m\ s^{-1}$
RBCA	Red blood cell aggregation	-	w	z – direction velocity component	$\mu m\ s^{-1}$
ROI	Region of interest	-	W	Width of the channel	µm
SD	Standard deviation	-	x*	Normalized x-dir. (x*=x/W)	-
$SS_{1/2}$	Half shear stress	-	y*	Normalized y-dir. (y*=y/W)	-
STD	Surface tension driven (flow)	-	z*	Normalized x-dir. (z*=z/W)	-
$t_{1/2}$	Half time	-	$\lvert\dot{\gamma}\rvert$	Shear rate magnitude	s^{-1}
TiO_2	Titanium dioxide	-	$\dot{\gamma}_{i-p}$	In plane shear rate component	s^{-1}
t	time	s	$\dot{\gamma}_{o-p}$	Out of plane shear rate component	s^{-1}
WB	Whole blood	-	$\Delta P_{Y\text{-}L}$	Young-Laplace pressure difference	Pa
h	Half height of channel	µm	θ_s	Static contact angle	Deg.
h_p	Gap between the plates	µm	µ	Dynamic viscosity	mPa
I	Intensity	-	$\bar{\mu}$	Mean dynamic viscosity	mPa
k	Power law consistency index	$Pa\ s^n$	$\bar{\bar{\mu}}$	Mean of $\bar{\mu}$	mPa
L_m	Meniscus Position	mm	$\bar{\mu}_{rel}$	Relative viscosity	-
n	Power law index	-	$\bar{\mu}^*_{rel}$	Normalised relative viscosity	-
P	Pressure	Pa	σ	Surface tension	Nm^{-1}
r	Radius	µm	$\dot{\epsilon}$	Extensional strain rate	s^{-1}

CHAPTER 1. Introduction

This Thesis elaborates on certain aspects of blood flow and rheological characteristics, which are relevant in microfluidics for blood diagnostics. For this purpose, various fluid mechanics and rheological methods, techniques and theory were utilised, and certain approaches were adopted for the treatment of the fluid of interest, blood, so that specific pathological conditions were emulated.

This introductory Chapter of the Thesis broadly covers the literature review of four main aspects of interest in the work. The first regards essential background information on the structure and the molecular constituents of blood, RBC aggregation and deformability and blood rheology (Sections 1.1 to 1.5). The second aspect includes an elaboration on microfluidic applications for blood, including pressure-driven and surface tension-driven microfluidics, and the known effects of the hemorheological parameters on the flow (Sections 1.6 and 1.7). In this part experimental, computational and analytical studies are revisited. Following, issues related to the performance of surface tension-driven microfluidics are reviewed (Section 1.8 and 1.9), and lastly the chapter closes with the rationale and the aim of this work.

It is noted, that the literature is further reviewed in the Methodology section (Chapter 3) and in each of the Chapters 4, 5, 6 and 7, in which results from the work performed in this Thesis are presented. This was deemed appropriate as each of the chapters have specific and more specialised issues to be covered.

1.1 A note on the importance of blood flow studies for microfluidic applications

Microscale blood flow and rheological characteristics are fundamentally important, as they affect the circulation in the microvascular system. Of equivalent significance is the issue of the influence of blood mechanical properties on the efficiency of microfluidic devices, used in Lab on Chip or Point of care diagnostic tools, since these systems assist in the medical treatment and disease monitoring. The area of microfluidics has been widely developed and received a considerable interest over the last decades [1]. Microfluidic devices are appropriate for small sample manipulation and are suitable for miniaturizing laboratory techniques. Such devices have many benefits and hence their contribution and popularity in diagnostic and health care applications is increasing [2]: they are cost effective, can be used on site and can be disposable making them very practical for research and industrial use [3]. Furthermore, they have good potential to enhance improvements in areas such as drug discovery, biosensing and chemical

synthesis, where handling small volumes is critical [4]. Research on blood flow in microfluidic applications is extensively reviewed in following sections of this chapter.

1.2 Blood composition and physiological properties

Blood is a fluid mixture consisting of plasma (55% by volume), cells and other macromolecules. The plasma consists mainly of water (~92%), organic and inorganic salts, and proteins such as fibrinogen which is responsible for haemostasis and aggregation [5].

The proportion of red blood cells (RBCs) in blood is 40-45%, and accounts for approximately the 99% of the cellular population. Their main role is the transport of oxygen by the haemoglobin contained within them. RBCs are a biconcave disc-shaped cells with a thick rim and a thin sunken centre surrounded by an elastic membrane (Figure 1.1).

Figure 1.1 Schematic of Red blood cell shape [6]**.**

A typical red blood cell has a disk diameter of approximately 6.2–8.2 μm and a thickness at the thickest point of 2–2.5 μm and a minimum thickness in the centre of 0.8–1 μm. RBC membrane removes waste products and is critical to the deformability of RBCs in order to pass through very narrow vessels.

Platelets and white blood cells (WBCs) account for approximately 1% of the cell volume. Platelets are responsible for coagulation and haemostasis, and the role of the WBCs is to defend the immune system [7]. Blood is a non-Newtonian fluid which shows a decrease in viscosity with increasing shear rate ($\dot{\gamma}$) [8]. An important factor that affects the blood flow in capillaries is the deformability of the RBC membrane, which helps their transportation in vessel diameters less than the cell diameter (5 and 8 microns respectively).

When RBCs enter a capillary, the membrane deforms contributing positively to the pressure drop across individual capillaries. Decreased RBC deformability is observed in pathological conditions such as sickle cell disease [9].

1.3 RBC aggregation

Under low-shear conditions, the presence of specific plasma proteins (mainly fibrinogen) results in the generation of an attractive force between RBCs, causing them to aggregate, forming rouleaux structures (linear coin like stacks shown in Figure 1.2) [10].

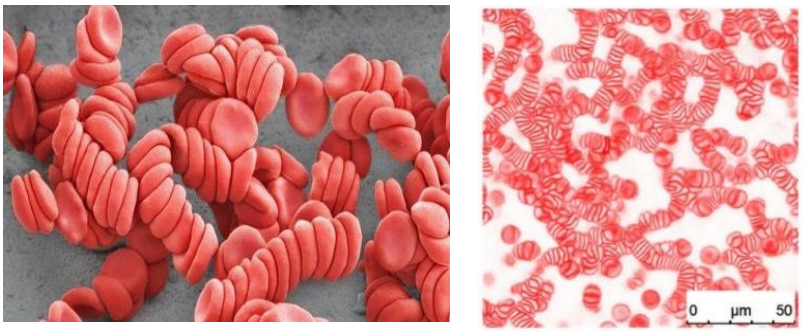

(a) (b)

Figure 1.2. Schematic of RBCs forming rouleaux structures [11]**. (a): RBCs forming rouleaux structures. (b): Confocal microscopic image of RBCs 10% Hct suspended in 60mg/ml dextran solution (dextran induces RBCs aggregation, hence RBCs form rouleaux structures).**

Red blood aggregation is the phenomenon that majorly causes the shear thinning behaviour of blood. That is at low shear rates RBC aggregation is enhanced resulting to a higher blood viscosity, whereas at higher shear rates disaggregation occurs due to higher shear forces resulting to a decreased blood viscosity. Studies on normal RBC aggregation kinetics in shear flow [12] have shown that for healthy human RBCs the disaggregation process starts form shear rates as low as $\dot{\gamma}$=2.5 s^{-1}, whereas other studies [13] have shown that a critical disaggregation shear rate lies between $\dot{\gamma}$ ~ 70 s^{-1} and 150 s^{-1}. Intense RBC aggregation occurs in many pathological conditions hence understanding it in more detail is important [14].

1.4 RBC deformability

Erythrocyte deformability is the ability of RBCs to change shape under a given level of applied stress, without haemolyzing (rupturing). RBCs can undergo large mechanical deformation due to external forces without rupture, and hence to restore their original shapes when released [15]. The deformability of RBCs is extremely important for the main function of RBCs which is to transport oxygen through blood circulation. The deformability of the RBC allows it go through the smallest capillaries of the human body, with dimensions comparable to or smaller than their size (Figure 1.3), hence successfully delivering oxygen to the tissues of the body. RBCs deformability is mainly determined by the RBC membrane mechanical properties (shape recovery after deformation, dynamic rigidity of cells in the microcirculation). Furthermore, pathological conditions such as sickle cell anaemia, malaria, or diabetes are associated with decrease in RBCs deformability [16].

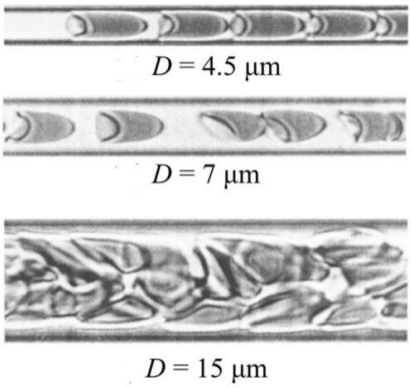

Figure 1.3. A suspension of human red blood cells moving through glass tubes with dimensions smaller and comparable to their size: approximate diameters 4.5, 7 and 15μm [17]**.**

1.5 Blood rheology

Blood rheology is the scientific field elaborating on the biophysical properties of the formed elements of blood and the flow properties of blood. Blood viscosity is a very important hemorheological parameter, which depends on plasma viscosity, haematocrit, and the ability of red blood cell to deform and aggregate under specific hemodynamic conditions. Flow properties of whole blood depend on two special mechanical properties of the RBCs, namely on red blood cell deformability (RBCD) and aggregation (RBCA) that determine the non-Newtonian (shear-thinning) behaviour of whole blood (Figure 1.4).

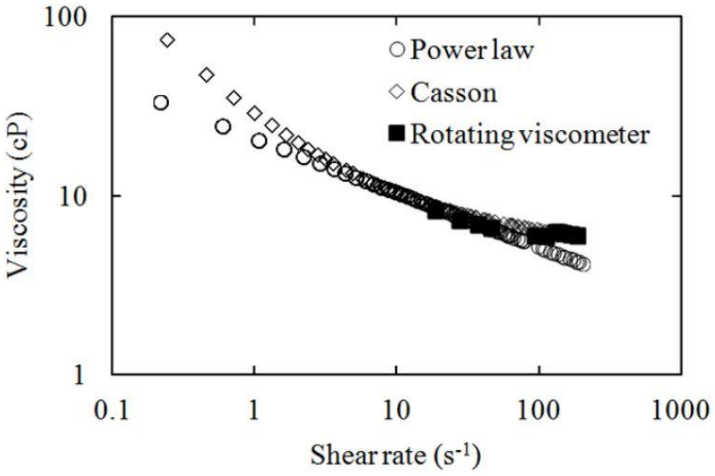

Figure 1.4. Viscosity vs shear rate of blood using a Power law model (circles), the Casson model (rombi) and experimental results from a rotating viscometer (black squares) [18]**.**

At high shear rates, strong shear forces occur, causing RBCs to exhibit an elongated shape change, which leads to an efficient orientation of them to laminar flow streamlines, resulting to a decrease in their distortion and reducing internal resistance of fluid to flow (Figure 1.5c), hence a reduction in viscosity occurs. Therefore, high shear rate viscosity is mainly determined by the ability of RBC to deform under. RBC deformability is determined by the geometric properties, cytoplasmic composition and viscosity, and membrane properties of RBC. However, at low shear rates (and hence low shear forces) RBCs return to their original biconcave discoid shape and their orientation to flow streamlines become less effective (Figure 1.5b) [19].

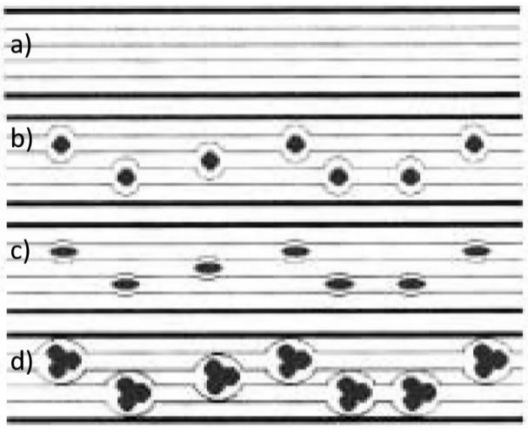

Figure 1.5. Effect of RBCs and aggregates suspended in plasma on the flow streamlines [19]**. (a): Flow streamlines of plasma in the absence of RBCs. (b): Distortion of streamlines in the presence of non-deforming RBCs. (c): Decreased distortion of streamlines because of the deformability of RBCs. (d): Increased distortion due to RBC aggregation.**

Furthermore, under low shearing conditions, RBCs tend to form aggregates, which distort the flow streamlines (Figure 1.5d) and hence increase the resistance to flow and consequently the viscosity of the fluid. RBC aggregation is a physiological process dominating under low shear or stasis conditions, and it is characterized by the formation of regular structures where RBCs form face-to-face contacts resulting in rouleaux structures. RBC rouleaux formation depends on the presence of fibrous macromolecules with molecular weights above a certain size [5].

Fibrinogen is the physiological aggregating macromolecule for RBC. RBC aggregation is determined by both plasma composition and cellular properties. However, RBCs aggregation is a reversible process since RBCs disaggregate at shear rates higher than the critical disaggregation shear rate [19].

Blood viscosity is also dependent on the haematocrit value, where the higher haematocrit results to increased viscosity [20]. The power law model, Casson model and Carreau-Yasuda model are commonly used non-Newtonian models for modelling blood viscosity, which exhibits shear thinning behaviour (Figure 1.4) [21]. The power law is a non-Newtonian fluid model that does not consider the yield stress and is expressed in the following equation:

$$\mu = k\dot{\gamma}^{n-1} \quad 1.1$$

where μ is viscosity, k is the flow consistence index and n is the power law index. The power law index n specifies the extent of the non-Newtonian behaviour. The consistency index k and the Power law index n are dependent on the constituents of blood such as hematocrit, fibrinogen, etc [21].

The Casson model contrary to power law model take also into account the yield stress needed for blood to start flowing, given by the following equation:

$$\mu = \frac{\tau_o}{\dot{\gamma}} + \frac{\sqrt{n\tau_o}}{\sqrt{\dot{\gamma}}} + n \quad 1.2$$

Where τ_o is the yield stress and n is the Casson rheological constant. The values of τ_o and n depends on haematocrit [21] . Moreover, the viscosity as a function of shear-rate is given by the Carreau-Yasuda model as follows:

$$\mu = \mu_\infty + (\mu_o - \mu_\infty)(1 + (\lambda\dot{\gamma})^2)^{\frac{n-1}{2}} \quad 1.3$$

Where μ_∞ is the viscosity at infinite shear-rate, μ_o is the viscosity at zero shear-rate, λ the relaxation time and n the power law index [21].

In addition, Kaliviotis et al [22], developed a time-dependent blood viscosity model based on an energy-rate model, which describes the total work needed to overcome the various forces developed between aggregated cells, including the adhesive, elastic and dissipative forces. The total rate of work per unit volume done on a fluid in Couette flow which is expected to be proportional to the shear stress and the shear rate was described as: $W_e = \tau_e\dot{\gamma}$. Hence by assuming that at low shear rates the kinetic energy (K_e) is negligible, the right-hand side of the above equation for W_e becomes: $W_e = (\tau V_{eN} + \tau V_{DR} + \tau_A + n_p\dot{\gamma})\dot{\gamma}$, where, τV_{eN}, τV_{DR} and τ_A represent the stress contributions due to the viscoelasticity of the aggregates and network, and $n_p\dot{\gamma}$ is the plasma viscous stress [22]. The aforementioned study [22] suggested that at

normal concentrations of RBCs the network dynamics play a predominant role in the development of blood mechanical properties.

Additional advanced blood viscosity modelling studies can be found in the literature, in which thixotropic and elastic phenomena in the behaviour of blood and plasma are included [23–25]. These approaches are also based on the dynamic effects of aggregative forces between the RBCs, which consequently are apparent in the viscosity of the fluid.

1.6 Microfluidic pressure driven set ups for whole blood studies

As mentioned a large amount of significant information about blood flow properties can be extracted from microfluidic studies. The majority of the studies for blood flows in microfluidics have been performed using pressure-driven experimental set-ups. Lima et al., [26,27] examined the effect of the haematocrit (Hct) on instantaneous velocity profiles by performing in vitro confocal micro-PIV blood flow measurements using non-aggregating samples in a square microchannel. The velocity profiles were found parabolic, however considerable velocity fluctuations were observed at increased haematocrits (Figure 1.6).

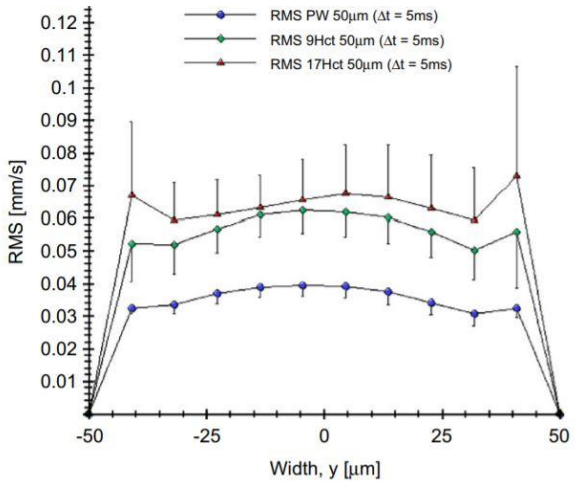

Figure 1.6. Comparison of the RMS values for pure water (PW) and in vitro blood with haematocrits of 9% (9 Hct) and 17% (17 Hct) [27]**.**

The increased velocity variation at higher Hct suggested that the presence of RBCs within the plasma strongly influences the measurements of the instantaneous velocity fields. Although the reasons of these fluctuations are not completely clear, the authors suggested that interactions between neighbouring RBCs, the high shear rate generated in the vicinity of the walls, and temporal fluctuations in the Hct may have significant impact in the disturbance effects

encountered in the blood velocity profiles [28]. The velocity profiles of the non-aggregating case in that study agreed with the velocity profiles of the analytical solution. In another study using confocal micro- particle tracking velocimetry (μ-PTV) radial displacement of labelled RBCs flowing through a 100 μm capillary was measured for a known time interval. The experiments were performed at Reynolds number ≈ 0.003 and shear rates from ≈ 3 to 25 s^{-1}. Then using the measured radial displacement, the corresponding dispersion coefficient was calculated for several Hcts (3% - 35%). It was noticed that RBCs at dense concentrations (24-35% Hct) exhibit higher erratic radial displacement compared with dilute suspensions of RBCs [29]. Furthermore, it was demonstrated that radial dispersion tends to increase with the Hct, but tends to level off at Hcts of about 25%. Near the walls, the radial displacement was found minimal, mainly because of the rolling of RBCs along the wall. They suggested that the development of the plasma layer, and the consequent decrease in the local cell density surrounding the RBCs, may enhance the radial dispersion of RBCs [29].

Sherwood et al [30,31] used RBC suspensions in dextran 2000 solutions (5g/l) to induce aggregation, and in phosphate buffer saline (PBS) for the non-aggregative cases, for flows in a rectangular microchannel with T-type bifurcations (Figure 1.7a).

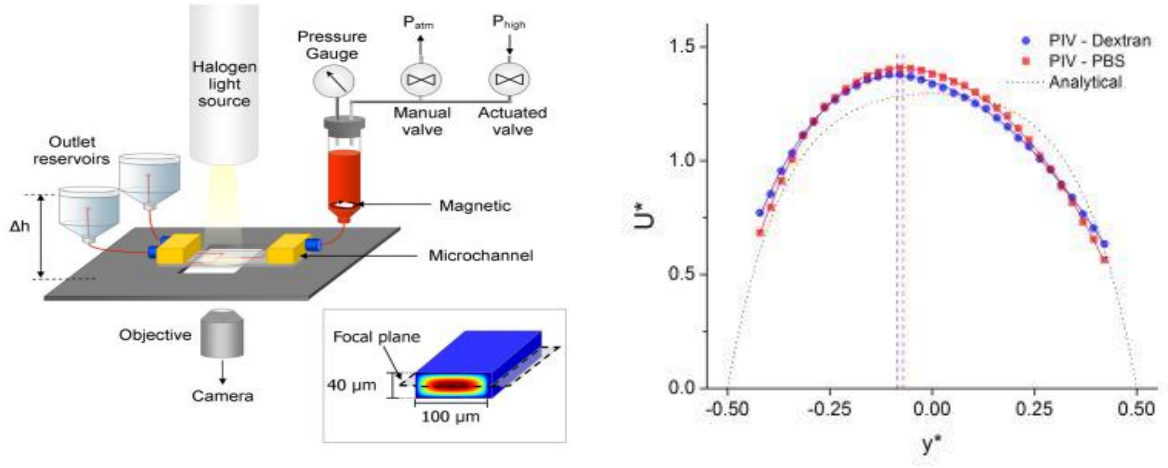

(a) (b)

Figure 1.7. (a): Experimental setup. (b): Sample averaged velocity profiles for Dextran and PBS cases at Q* ¼ 0.56. Solid lines represent fourth order polynomial fit. Dotted black line shows the analytical solution. Dashed vertical lines show location of maximum velocity [27]**.**

The effect of the flow ratio between the parent and daughter branches ($Q^* = Q_{Daughter} / Q_{Parent}$) was examined and observed that in branches of Q* up to approximately 0.5, the aggregating samples had lower hct and lower flux compared to the non-aggregating case, due to enhanced

plasma skimming. The results of their studies have shown that aggregation increases the bluntness of the velocity profile and that the velocity profiles were all skewed towards the inner wall of the daughter branches (Figure 1.7b).

In order to examine the viscosity behavior in the channel an empirical haematocrit-dependent viscosity model [32]: $\mu_{rel} = 1 + B\,[(1 - Hct)^c - 1]$ was used, where B and C are constants whose values were tabulated for various Hct ranges and tube diameters. The viscosity profiles found to be skewed in the opposite direction to the velocity profiles as expected. In addition, the maximum relative viscosity in the Dextran case found to be lower than the NAB which agrees with the Pries viscosity model, since the Hct values in the Dextran case were lower.

The haematocrit in the smaller vessels decreases due to the Fahraeus effect: migration of RBCs (i.e. radial transport to the centre of the flow) is observed, which results to non-uniform RBC concentration (haematocrit) profiles in the vessel (Figure 1.8a). This results to the velocity of the RBCs being greater than the plasma velocity, and to a decrease in the local Hct in the vessel. The reduction in the viscosity in the branches of reduced haematocrit observed in Sherwood et al., [31], reflects the Farhaeus-LIinqvist effect (Figure 1.8b) which may be enhanced due to the RBC aggregation phenomenon [33,34].

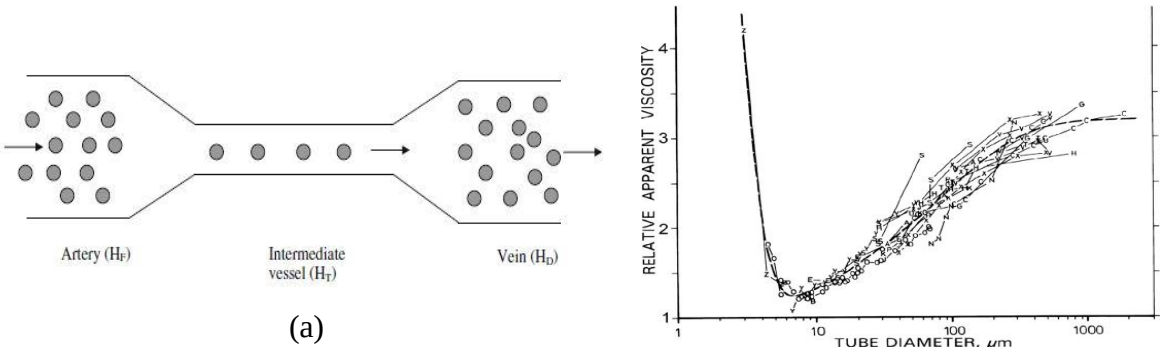

(a) (b)

Figure 1.8. (a): Schematic representing Fahraeus effect [35]. (b): Schematic representing the Farhaeus-Linqvist effect [36].

1.6.1 Effect of RBC aggregation in pressure driven Microscale flows

The effect of RBC aggregation on microscale flows has been examined in a number of other studies in the literature [30,31,37–40]. For the T-type microchannel blood flow RBC aggregation was found to influence nearly all the flow and structural characteristics: the mean width and distribution of the CDL increased proportionally with the flow ratio in the daughter

branches, and was found to be significantly greater compared to the absence of aggregation. The roughness of CDL at the interface between the RBC core and the plasma region was also found to be increased for the aggregating case [30]. In another work [38] the partitioning of red blood cell aggregates in bifurcating microscale flows was examined. The schematic in Figure 1.9 illustrates the definition of the main quantities of interest in the above-mentioned work; the area of a detected structure in an image (A, in μm^2), the normalized area of a detected structure (A^*), the mean normalised area size in one image ($\bar{A}^*$), and the mean normalised area size from all images ($\hat{A}^*$). The normalising parameter is the characteristic area of one RBC (Ac, in μm^2). The size of aggregated structures present in the flow (i.e. the detected areas) was estimated using an edge-detection image processing technique [38].

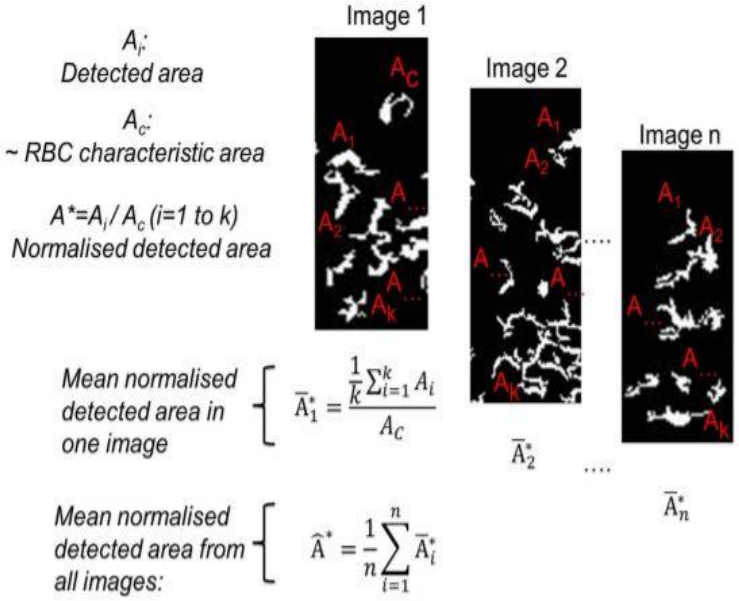

Figure 1.9. Schematic explanation of the key parameters quantified in the Kaliviotis et al [38]**, A, A_c, A^*, $\bar{A}^*$ and $\hat{A}^*$. Images shown are magnified sections from representative processed images.**

In the T-junction micro channel larger aggregates tend to concentrate towards the flow centreline in the parent branch for aggregative samples (D2000) resulting to distinct aggregate size-depleted regions near the wall. At branches of very low shear rates, however, small aggregates are found in contrast to the shear rate/aggregation relationship (Figure 1.10b and Figure 1.10d). This phenomenon resulted due to the non-uniform distributions of aggregates in the parent branch, which in combination with the existence of a near wall region depleted of aggregates of certain sizes, affect the partitioning of aggregates for any given flow ratio, and hence the aggregate size distribution in the daughter branches [38].

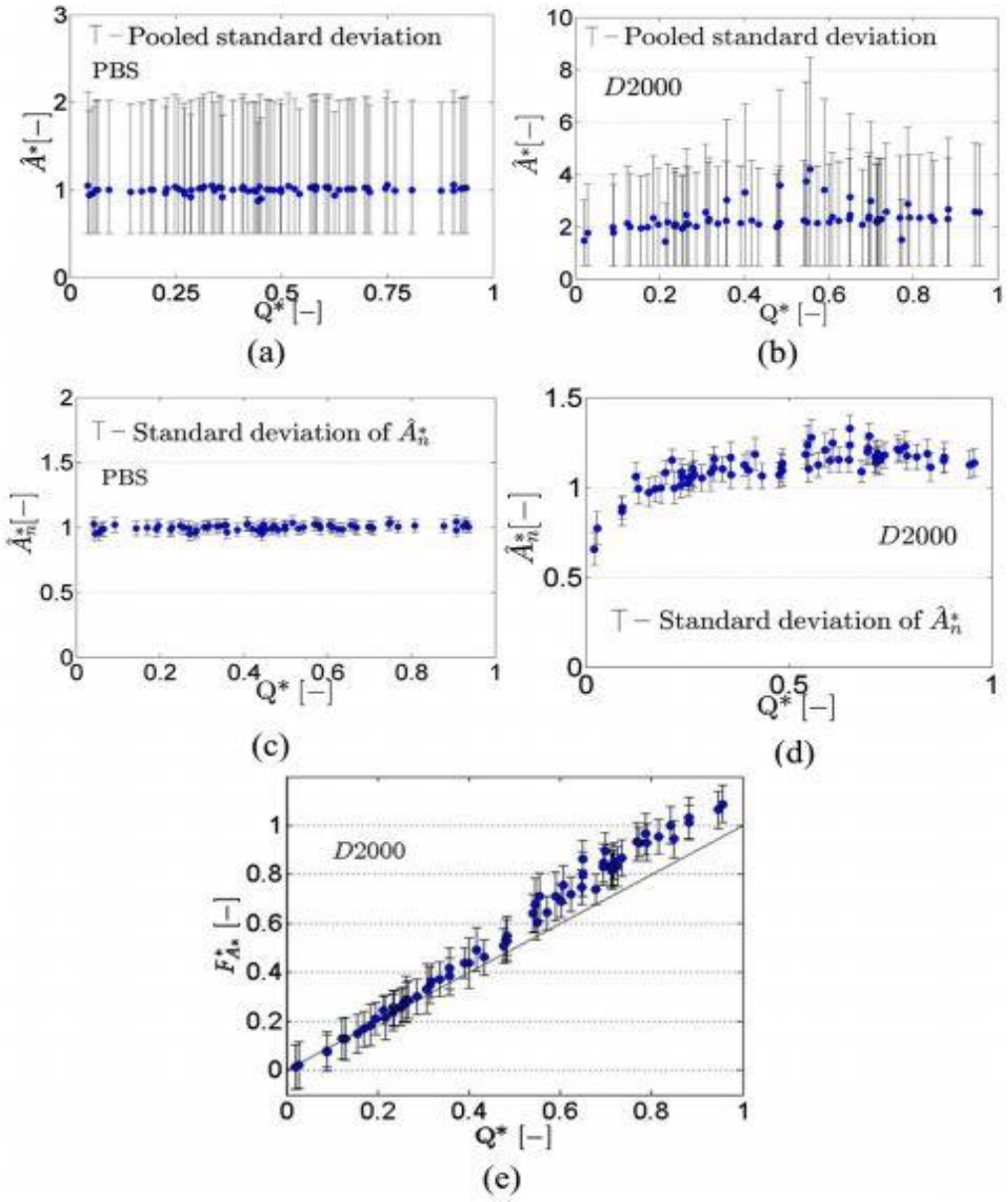

Figure 1.10. Effect of flow rate on RBCs aggregate size in a T branched channel [38]**. (a): $\widehat{A}^*$ based on 400 images against Q* for the PBS case. (b): $\widehat{A}^*$ with pooled standard deviation for the D2000 case. (c): Ensemble averaged values ($\widehat{A}_n^{\,*}$), (PBS). (d): $\widehat{A}_n^{\,*}$ values of aggregate size A* plotted against Q* (D2000 cases); the data is normalised by the $\overline{A}^*$ values in the parent branch. Data below Q*=0.5 correspond to the right daughter branch and above Q*=0.5 to the left daughter branch. (e): Size-flow parameter $F_{A^*}=Q^*A^*$ against Q^* as an index of the flow preference of different aggregate size.**

In Figure 1.10e a size-flow parameter, $F^*_{A^*} = Q^*A^*$ where ($Q^* = Q / Q_{max}$), is plotted against Q*, expressing more clearly the preference of the larger aggregates for higher flow ratio branches. For values approximately above Q*= 0.3 the size-flow parameter $F^*_{A^*}$ deviates from

the $F^*_{A^*} = Q^*$ line, indicating an increase of aggregate size relative to the mean aggregate size in the parent branch. However, for non-aggregative samples (PBS) no dependency of aggregates and shear rate was detected (Figure 1.10a and Figure 1.10c) [38].

In another work [41]* RBC aggregate flux in a bifurcating microchannel was examined. Aggregating blood was perfused in a T branch microchannel in an inverted microscope setup, where the distribution of flow between the two daughter branches (flow split) was controlled by means of hydrostatic pressure difference by independently adjusting the height of the outlet reservoirs using micrometer stages (Figure 1.11).

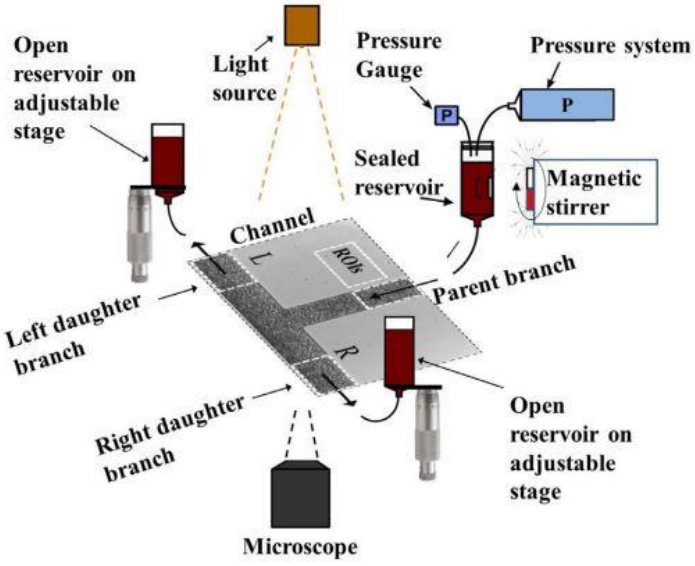

Figure 1.11. A schematic of the flow system: a pressure system was used to drive the flow entering the parent branch (P). The outlet left (L) and right (R) daughter branches led to the open reservoirs. The height of the reservoirs was adjusted to provide the desired pressure drop, and control the flow ratio. A magnetic stirrer was used in the inlet reservoir to avoid sedimentation and aggregation of cells in the samples. Regions of interest are shown as white, dashed rectangles [41]**.**

The flux (F_A^*) for each flow split was defined and calculated as the number of aggregates of certain size, per cross sectional area, per second as $F_A^* = UN_A^*V^{-1}$,

* Note that the Author of the present Thesis, Dimitris Pasias, has substantially contributed in this work by performing the analysis of the aggregate flux in the microchannel bifurcations. This work is was part of a major theme in the in the PhD program, namely the flow and microstructural characterization of blood in microchannels.

where N_A^* are the numbers of aggregate of size A*, U the mean velocity of particles with size A^* (within a range of 10% of a specific value), and V the volume of the flow configuration in the ROI.

Furthermore, the normalised flux quantity F^* (i.e. $F^* = F_{Daughter} / F_{Parent}$) was calculated for each A^* and plotted against the normalised flow ratio Q^* (i.e. $Q^* = Q_{Daughter} / Q_{Parent}$) (Figure 1.12), in order to examine how aggregates are transported in the daughter branches relative to the parent branch.

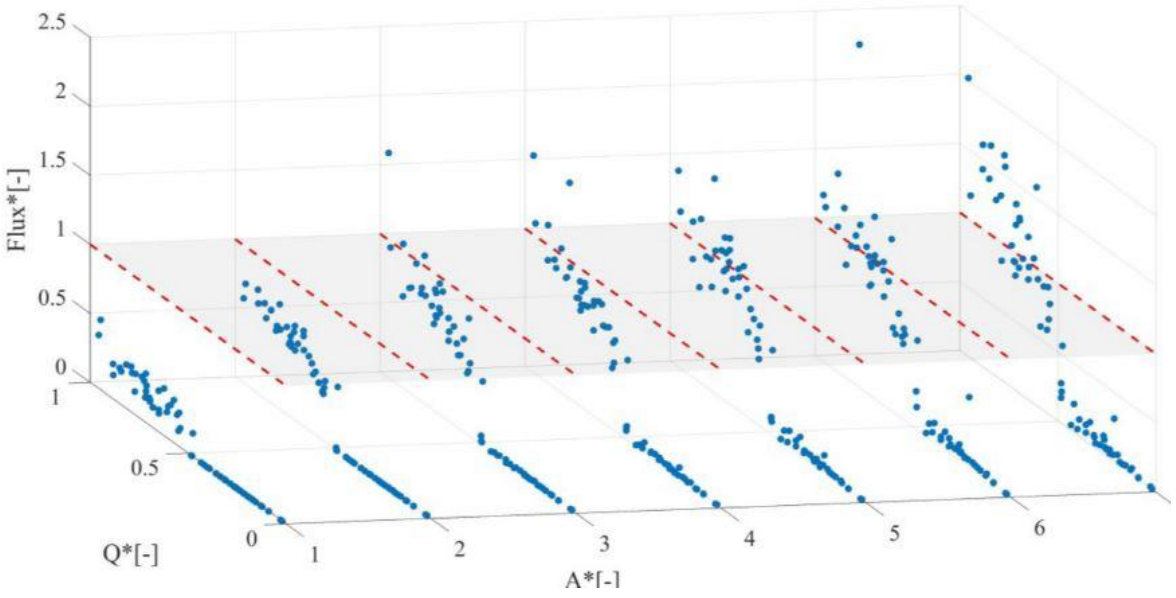

Figure 1.12. Normalised flux F^* (denoted here as Flux*) of aggregate sizes (A^*) ranging from 1 to 7 at 34 split flow cases (i.e. 68 flow ratios $Q^* = 0.0205–0.9562$). The shaded plane and the red lines indicate $F^* = 1$, i.e. the conditions for which the flux of the daughter branch is equal to the flux of the parent branch [42].

It was shown that the flux of aggregates decreases with increasing aggregate size in both the parent and the daughter branches in absolute terms. However, for large aggregates and for high flow ratios it is noticed that the flux is increased in the daughter branches relatively to the parent branch (Figure 1.12) [42].

Tomaiuolo et al [43] showed that RBC clustering, which was not caused by RBC aggregation forces, takes place in confined flows, and that the therapeutic efficacy of microparticles used in drug delivery could be affected by the particle / RBC interaction in the vasculature [44].

The effect of RBC aggregation on microscale blood flows has also been examined in a straight microchannel by Mehri et al [45,46] illustrating the relationship between aggregate size, shear

rate and viscosity and in an artificial microvascular network (Figure 1.13) [47] showing no effect of RBC aggregation on perfusion but a haematocrit increase in the capillary scale branches of the network.

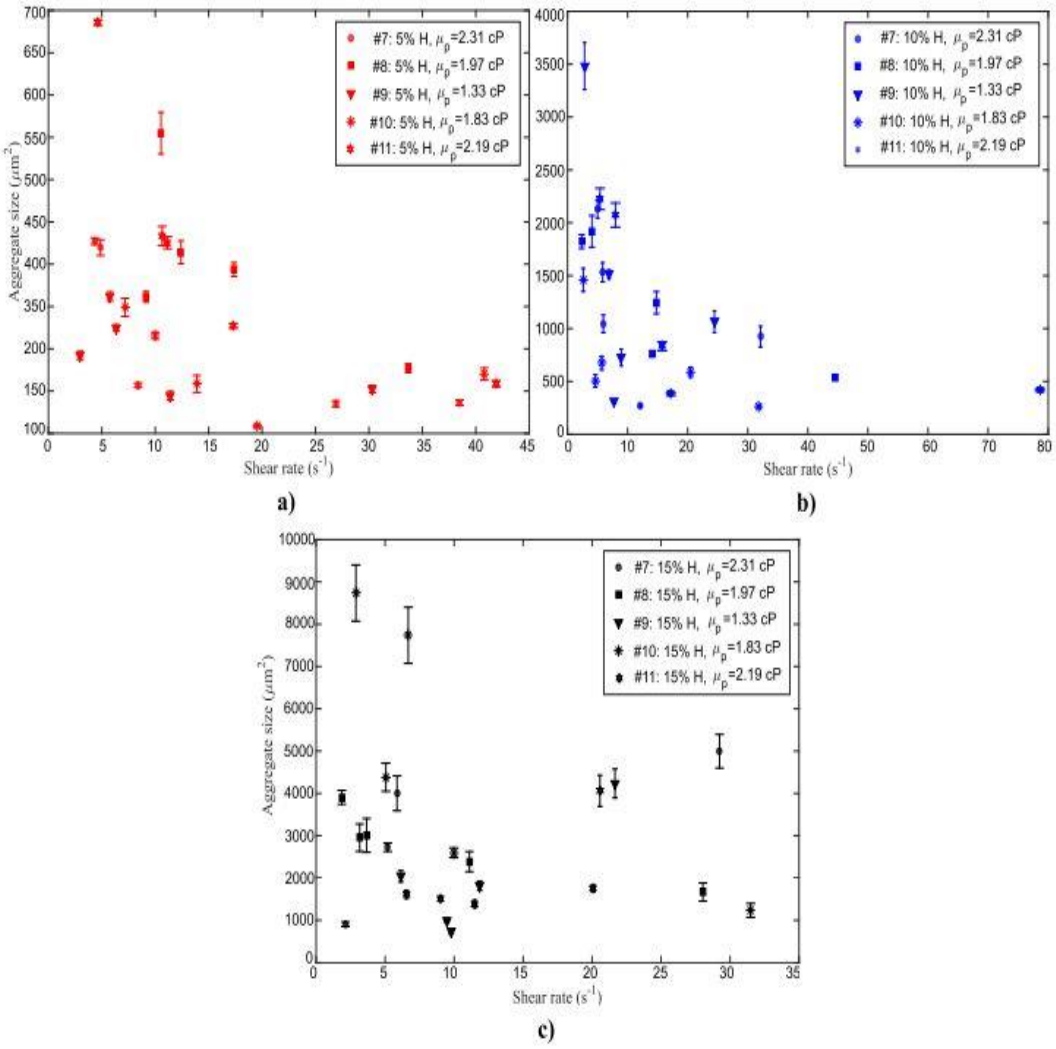

Figure 1.13. Average RBC aggregate sizes for five different human blood samples suspended at H of (a): 5% (b): 10% and (c): 15% respectively as a function of shear rate at 37˚C. Error bars for each sample are provided for the standard error of several (2–5) tests performed consecutively. The plasma viscosity μ_p is provided for each sample [46]**.**

1.6.2 Effect of RBC deformability in pressure driven Microscale flows

The effect of RBC deformability in microscale flows was examined by Passos et al [48] in pressure driven setups for suspensions of healthy and glutaraldehyde-hardened RBCs, which were perfused through straight microchannels at various hematocrits and flow rates. Velocity and hematocrit distributions were obtained simultaneously using μPIV and light transmission methods, and it was found that the velocity profiles of the hardened cells were sharper than the

healthy cells. At lower Hct hardened RBCs were more dispersed compared to healthy ones, whereas at high RBC concentrations, the hardened cells were found to have less blunt velocity profiles, implying a reduction in shear thinning behaviour. In addition, the bluntness of Hct profiles also decreased with hardening of the cells (Figure 1.14)

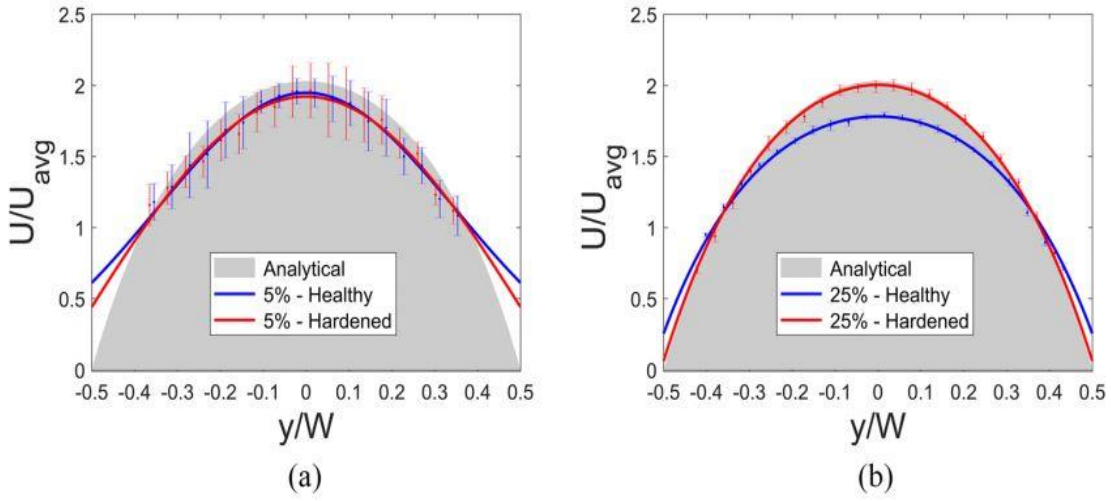

Figure 1.14. Velocity profiles of healthy and hardened (GA 0.08%) RBC samples from a single donor obtained in the square microchannel at feed haematocrit [48]**: (a): 5% and (b) 25%. The grey area indicates the analytical velocity profile for a Newtonian fluid in a square channel.**

The effect of deformability on haematocrit distributions was found to be dependent on the feed haematocrit. In the same study it was observed that with increased number of stiffened RBCs in flow, the stiffened RBCs concentrate more toward the centre-line of the 50μm wide channel compared to a healthy case [48].

Czaja et al [16] also investigated RBC deformability when a significant percentage of stiffened RBCs are present in whole blood. However, it was not observed a significant difference between stiff and healthy haematocrit profiles. It is believed that this effect is more significant in vessels <50μm.

In another study [49] the effect of extensional flow was examined, using a microfluidic device with a hyperbolic-shaped contraction. It was observed that RBCs experience a strong extensional flow with a region of homogeneous strain rate along the centreline. The results showed that the RBCs are highly deformable under strong extensional flows, with the degree of deformability being highly dependent on the flow rate. In addition, the deformability of RBCs seems to be converging to a maximum state as flow rate is increased as shown in Figure 1.15. Moreover, for the range of conditions tested in the study, there was no RBC rupture.

Results also show that for the flow rate ranges covered in this work, the cell-free layer (CFL) thickness downstream of the expansion plane increases significantly (up to ten times).

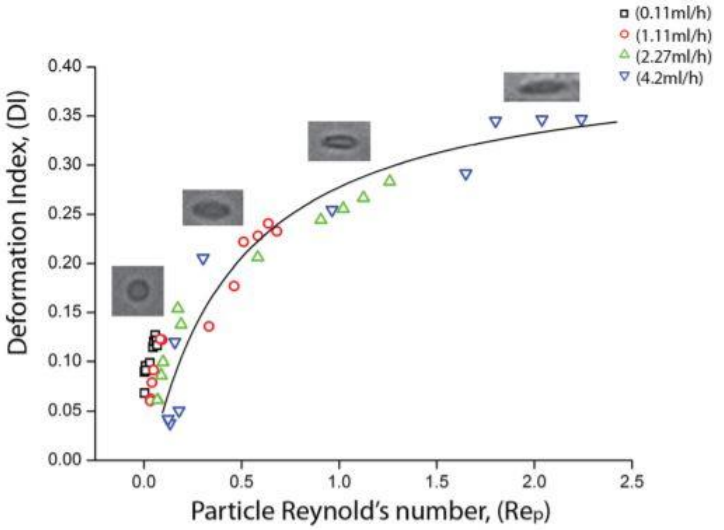

Figure 1.15. RBCs Deformability Index (DI) as a function of the particle Reynolds Number (Re_p) at the centreline of the hyperbolic microchannel for different volumetric flow rates: Q = 0.11 ml/h, Q = 1.11 ml/h, Q =2.27 ml/h and Q = 4.2 ml/h. The Rep was calculated by assuming the average diameter of a human RBC (D_{RBC}) = 8 μm [49]**.**

1.7 Surface tension microfluidic flows

As aforesaid the most popular microfluidic devices for blood flow used in the literature (including the aforementioned studies) are pressure-driven, which also mimic microcirculation. For diagnostic applications, however, using pressure-driven flows, tubing connection problems and dead volume in the tubing, cause difficulties on-site analysis [4,50]. Surface tension driven blood flows is another cheaper and simpler option than the pressure driven choice in microfluidic flows [51]. Surface tension is a material property of a fluid-fluid interface whose origins lie in the different attractive intermolecular forces that act in the two fluid phases. When a fluid is in contact with another surface or fluid it tends to minimize its surface area [52]. This minimization of the surface area is caused by the attraction of the particles in the surface layer by the bulk of the liquid resulting to a tensional force on the fluid-fluid surface. Surface tension is the ratio of the tensional force to the length which the force acts [52,53]. At surface tension driven flows the hydrophilicity/hydrophobicity of the material have a significant effect on the flow. Hydrophilic materials have good affinity with fluids causing them to spread. On the other hand, hydrophobic materials cause repulsion to fluids resulting to droplet formation. Contact angle is the angle measured through the liquid, where a liquid–vapor interface meets a

solid surface. When the static contact angle (θ_s) of water is greater than 90^o material is known to be hydrophilic and when it's lower than 90^o is known to be hydrophobic. Hydrophilic materials result to higher interaction forces than hydrophobic materials enhancing the surface tension driven flow [54,55].

1.7.1 Surface tension driven microscale flows

Surface tension driven flow has also been examined in a passive micro pumping system, in which the dynamics of the pressure-drop generated by droplets at the inlet and exit of the channel were analysed [4]. The results showed that the surface tension mechanism provides a predictive analytical model that accurately characterizes the specific flow. The effect of microchannel aspect ratio on the advancing meniscus velocity in surface tension-driven flows has been examined in various studies [4,50,56]. Chen et al., [56] examined the flow characteristics of surface tension driven flow in open micro channels with sharp turns (45^0 to 135^o) in the vertical plane (downwards) and of different aspect ratios (AR) (0.75 to 3). The working fluids were isopropyl alcohol and silicone oil. The results, similarly to C. F. Kung et al [37], showed that for higher aspect ratio the velocity of the advancing liquid front was higher, although there were no significant changes for aspect ratio channels (AR) greater or near 1.5 (Figure 1.16).

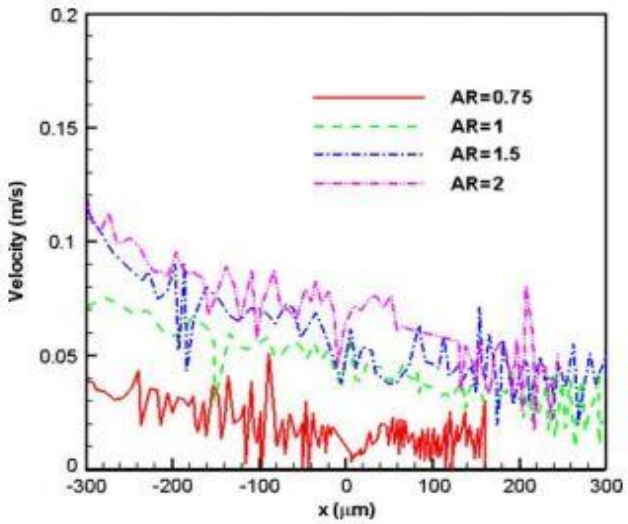

Figure 1.16. Advancing velocity of liquid front as front arriving x-position for the microchannels of different aspect ratios and of turning angle of 60º [56]**.**

Another observation was that the meniscus velocity slowed down close to the turning region and then picked up velocity after turning. For turning angles ranging from 45^0 to 75^0 a small difference in the advancing velocity was observed. However, for turning angles 90^0 to 135^0

advancing velocity accelerated to a slightly higher value than incoming velocity and recovered back to its original incoming velocity. This was explained by the higher centrifugal force developed at the sharper turns leading to greater increase in the advancing velocity. Furthermore, as the liquid front was advancing meniscus was elongated and the radius of curvature was significantly reduced [56].

Ichikawa et al [50] has developed an extended theory of capillary driven motion in a rectangular channel more clearly and compared the new theory with experiments. In this study the exact solution for flow velocity distribution in a cross section of the rectangular channel with the boundary condition of u = 0 at the side and top boundaries of the microchannel from another study Brody et al. [22] was modified, where aspect ratio was also introduced. By balancing driving force caused by hydrostatic pressure and capillary force with viscous drag the following equation resulted:

$$2(1 + \varepsilon)w\sigma\cos(\theta) + \rho g z_o \varepsilon w^2 - \pi^4\mu/8\varepsilon(1 - \frac{2\varepsilon}{\pi}\tanh\frac{\pi}{2\varepsilon})\, s\frac{ds}{dt} = \rho\varepsilon w^2(s\frac{d^2s}{dt^2} + \left(\frac{ds}{dt}\right)^2), \quad 1.4$$

where ε is the aspect ratio, w the width of the channel, z_o the initial height of the liquid in the reservoir and s the distance travelled by the meniscus. Then by applying the initial conditions $s=s_o$ and $ds/dt=0$, at t=0, and non-depersonalizing, the following equation resulted:

$$s*^2 - s_0*^2 = D_f(t^* - 1 + e^{-t*}), \quad 1.5$$

where s and t are the non-dimensional forms of s and t and D_f a constant. Further by differentiation non-dimensional velocity was found as:

$$V^* = \frac{ds^*}{dt^*} = D_f(1 - e^{-t*})/2\sqrt{D_f(t* - 1 + e^{-t*}) + s_0*^2}\,. \quad 1.6$$

In the experimental setup a horizontal channel was placed under a CCD camera where the working fluid was inserted with a pipette. Flow was capillary driven and was captured by the CCD video camera which was used for interface motion measurement. For the experiments glass rectangular tubes with sizes of about 50 to 100 μm square and PDMS micro channels with dimensions of 85 × 68 μm and 75 × 45 μm were used. Working fluids were DI water in the glass channels and Ethanol in the PDMS channels. The experimental results were in

agreement with the theoretical. Furthermore, for higher channel aspect ratio higher velocities occurred as in [37,56].

1.7.2 Surface tension driven Microscale flows using whole blood

Surface tension driven studies involving blood flow include this of Kung et al [37] in which deionised (DI) water and blood flow was characterized in a micro channel at different sloping angles (from -90^o to 90^o). A microchannel was fixed at different slopping angles with a CCD camera to capture the flow. Working fluid was placed at the inlet and driven due to capillary forces, where flow was recorded by the CCD camera. Contrary to DI water, surprisingly it was found that for upward motion (+ve angle) blood flow rate was increased and that for downward flow (-ve angle) blood flow rate was decreased (Figure 1.17). This was explained by the change in frictional force at different sloping angles, due to the haematocrit decrease in the upward case.

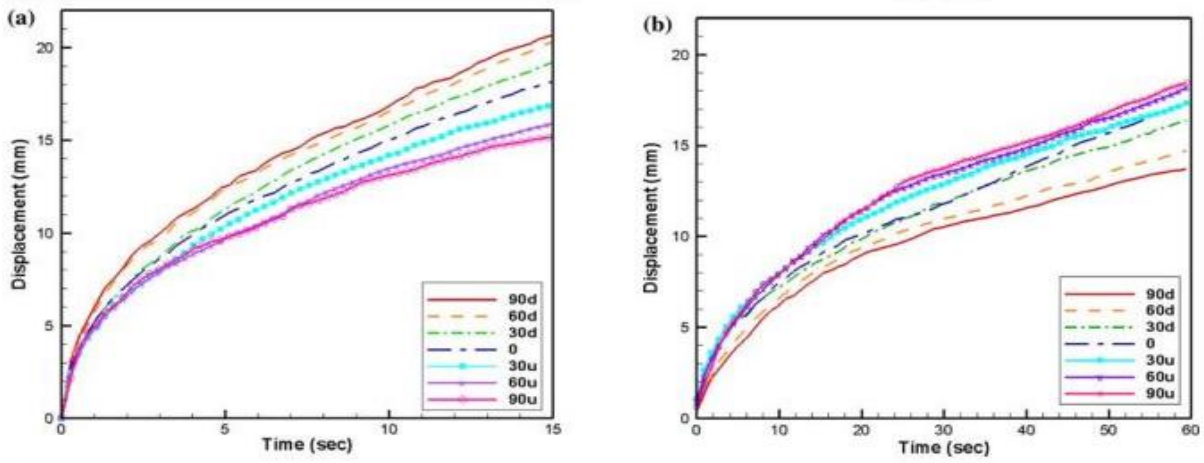

Figure 1.17. Experimental results for DI water and blood flow under different sloping angles in the microchannel [37]**. (a): Experimental results for a DI water. (b): Blood flow under different sloping angles in a microchannel, where channel height h = 3 μm, width w = 100 μm, and total length L = 4 cm. Note that 90d denotes the flow moving downward at 90^o, and 90u denotes the flow moving upward at 90^o.**

Cito et al [51] examined the flow behind the meniscus for water and blood, using rectangular and circular microchannels of various cross sections, and utilizing a spectral-domain Doppler optical coherence tomography technique (SDDOCT). They showed that recirculation regions exist behind the meniscus, with normal to the flow velocities comparable and even higher to the meniscus velocities. The results were then compared with the analytical predictions of the

Lucas–Washburn equation assuming that blood behaves as a power-law non-Newtonian fluid and found to be in an agreement (Figure 1.18) [51].

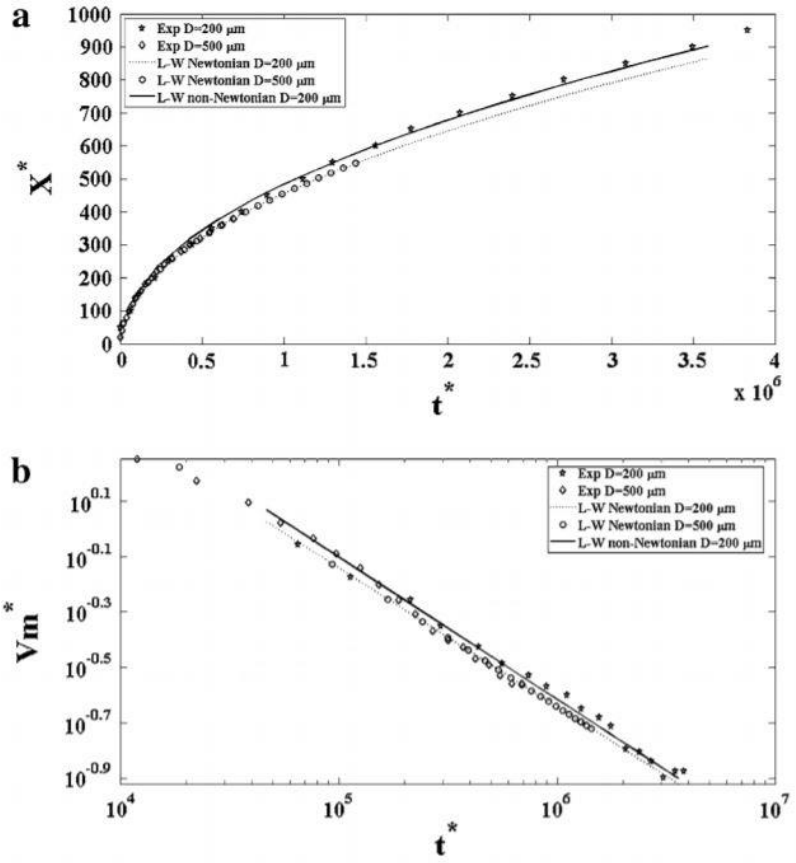

Figure 1.18. (a): Measured and theoretically predicted time evolutions of the non-dimensional position. (b): Averaged velocity of the meniscus for the different microchannels [51]**.**

Berthier et al [57] studied the spontaneous capillary flow (SCF) in a narrow V-groove microchannel. For whole blood the measured velocities were found to be up to 7.5 cm/s. The whole channel of length 1 cm was filled with blood in less than 0.2 s. This observation agreed with their theoretical analysis of spontaneous capillary flows in open channels. The dynamics of the fluid motion were analyzed, using analytical arguments based on a force balance between the capillary forces, which drive the flow, and viscous friction at the walls, which resists it. Computational fluid dynamics were used and the results were compared to show a good agreement. Using force balance, it was shown that the velocities decrease with the distance inside the V-groove, but remains significant throughout the length of the device.

Berthier et al [58] in another study, examined spontaneous capillary flow in curved, open microchannels. In the case of suspended channels contact angles and turn aspect ratio were not found to have any special effect. However, for rectangular open U-grooves turning corners

were found to curve the interfaces depending on the radius of the turn. Furthermore, capillary flow behaviour related in this work is observed to be independent of the liquid. Whole blood, tinted water, and IPA solutions had a similar behaviour.

Gosselin et al [59] have investigated the capillary filling of whole blood within a 50μm-radius cylindrical duct made of borosilicate. They were able to distinguish the two-phase rheological behaviour of blood by plotting the filling distance against time (Figure 1.19).

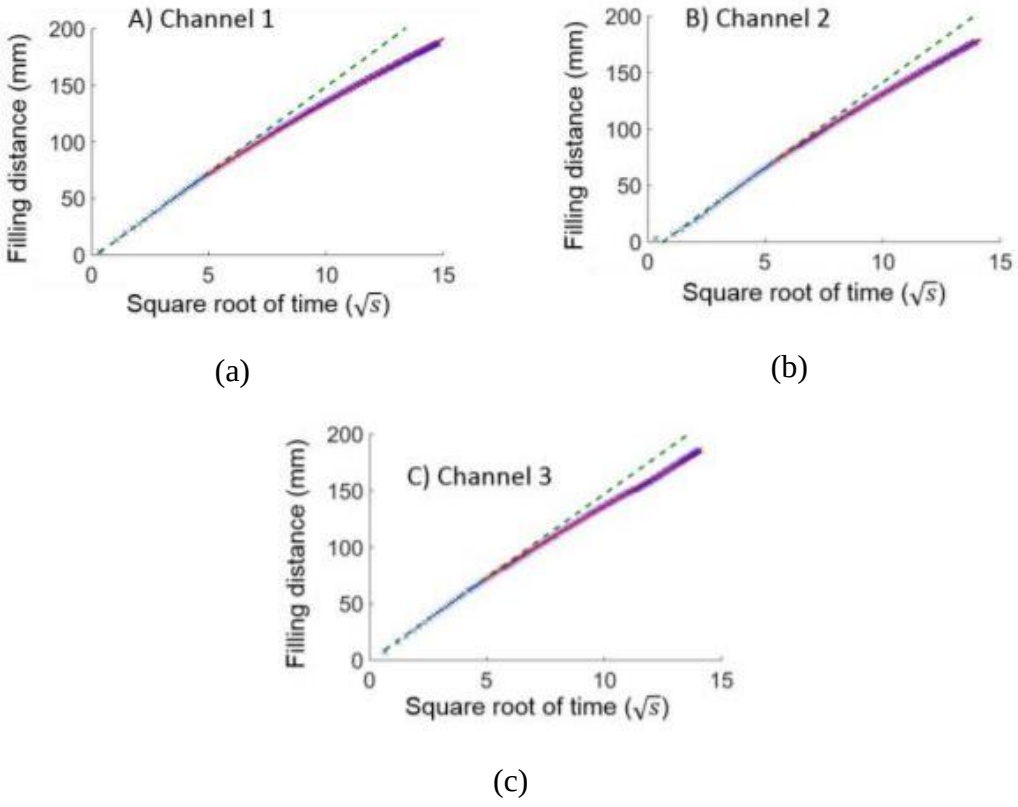

(a) (b)

(c)

Figure 1.19. Comparison between the non-Newtonian model of the capillary flow of whole blood (red solid line) and the experimental data points (blue crosses) [59]**. (a): Channel 1, (b): Channel 2 and (c): Channel 3. The green dashed line shows the Newtonian fit of the first part of the capillary flow.**

Three experiments have been performed, each one with a different channel of the same section (i.e. Channel 1, 2 and 3). Until a certain distance blood follows the Newtonian Lucas-Washburn-Rideal law, i.e. is linear with the square root of time (Figure 1.19). However, after a few centimetres it departs from the LWR law, meaning that it undergoes a transition towards its non-Newtonian behaviour. In addition, differential equation for the dynamics of capillary flow of Herschel-Bulkley fluids was derived from the Navier-Stokes equations. The numerical solution was in good agreement with the experiments (Figure 1.19). It is suggested that this

approach demonstrates the validity of the generalized equation for the dynamics of non-Newtonian capillary flows and confirms the consistency of the Herschel-Bulkley model for the whole blood rheology [59].

1.7.3 Theoretical studies on surface tension driven flows of whole blood

Analytical approaches have been also utilised in the literature to study the STD flow from the theoretical perspective. In a theoretical study by Chakrabotry (2005), a novel mathematical approach was formulated in order to analyse the flow of blood from a droplet into a micro capillary channel [60]. The fluid flow was modelled under the following assumptions: (a): the fluid flow is non-Newtonian and laminar, (b): at the entrance section of the channel (immediately before the droplet is into the channel), the movement of the droplet can be effectively modelled by a potential flow analysis, neglecting local dissipative effects, (c): apparent viscosity of the blood sample may vary due to influence of suspended particles, (d): the contact angle varies dynamically, as per prevailing flow conditions, (e): the flow behaviour can be approximately modelled as one-dimensional, by invoking the area-averaged mean flow velocities at pertinent sections along the channel axis.

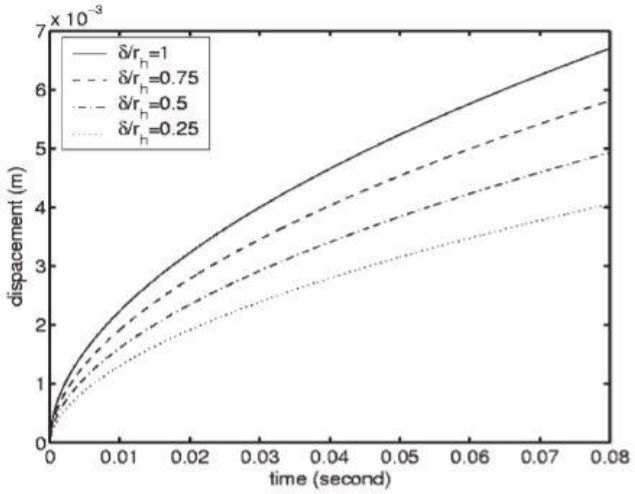

Figure 1.20. Time course of displacement of fluid into the channel, for different values of relative sizes of the particulate matters (RBC) [60]**.**

The fluid flow was then described, by employing suitable governing equations and constitutive models. It was found that the fluid accelerates in the entrance of the channel, and that for higher aspect ratio channels; the velocity of the fluid is increased for the whole length of the channel (Figure 1.20). In addition, axial accumulation of RBCs was found to cause blunting of velocity profiles. Furthermore, they showed that since contact angle reduces with the decrease of velocity, the capillary force increases with time (as it is proportional to the cosine of the contact

angle).In another mathematical approach to analyze the effects of the exit port (i.e., area and location of exit opening) on the flow of blood it was shown that if the capillary tube has an open window at the end, a simplified analytical solution yields results within 5% of the numerical. However, if the capillary tube has a closed end and a window on the side wall, the effect of the air motion in front of the blood-air interface is more significant [61].

1.7.4 Lab on chip set-ups

STD microfluidic configurations are also developed for Lab-Chip devices. Sneha Maria et al [62] performed surface tension driven blood flow experiments in a micro channel with differential wetting properties in order to separate the plasma and detect the glucose levels therein. A rectangular polydimethylsiloxane (PDMS) micro channel with hydrophilic walls (on three sides) and a completely hydrophobic region (all four walls) was constructed by using oxygen plasma exposure. At the entrance of the hydrophobic region blood flow was impeded and the accumulated blood cells in this region formed a filter to facilitate the separation of plasma (Figure 1.21).

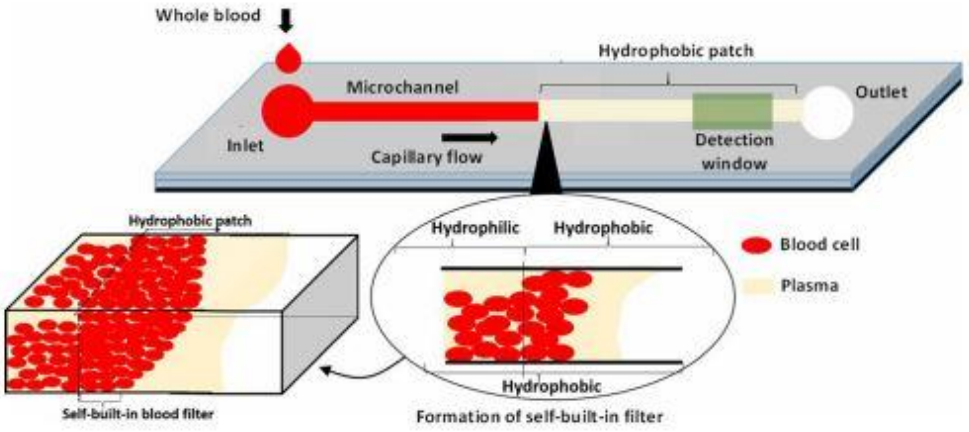

Figure 1.21. Schematic of the capillary driven PDMS microchannel device with a hydrophobic region for the separation of plasma from whole blood and subsequent detection of glucose [62]**.**

The plasma obtained was found to be pure and comparable with that obtained using centrifugation. The detection of glucose was performed in the hydrophobic region. Furthermore, a theoretical model was developed for predicting the flow velocity of blood along the hydrophilic micro channel and validated. The velocity of blood meniscus for normal hydrophilic and asymmetric (only three walls hydrophilic) rectangular micro channels was calculated experimentally and analytically using the following equation:

$$u_{av} = \frac{1}{k_1}\left(k_0 h + \frac{P_0}{x}\frac{h^2}{12}\right) \quad 1.7$$

where h is height of the channel, Po the pressure difference driving the flow and k_1 and k_0 are constants. The above equation was derived using the Navier–Stokes equations for open ended steady fully developed flow of a non-Newtonian fluid given as $\frac{\partial \tau}{\partial y} = \frac{\partial p}{\partial x}$, where τ is the shear stress, in combination with the Young-Laplace equation $P_0 = \sigma\left(\frac{1}{R1} + \frac{1}{R2}\right)$, to account for the pressure driving the flow; where σ is the surface tension of blood, and R_1 and R_2 are the radii of curvature on the top and side walls of the channel. Since the channel was of high aspect ratio, the radius of curvature along the width is much higher as compared to that along the height hence 1/ R_2 was considered negligible. Therefore, P_0 was expressed as $P_0 = \frac{2\sigma cos\theta}{h}$. In addition, shear stress was substituted using Casson model as follows:

$$\sqrt{\tau} = \sqrt{k_o} + \sqrt{k_1 \dot{\gamma}} \quad 1.8$$

and in combination with no slip velocity boundary conditions the aforementioned velocity of blood meniscus equation was derived. The experimental and theoretical results found to be in good agreement (Figure 1.22a).

The effect of waiting time (elapsed time after the oxygen-plasma exposure - T_w), exposure time (time of oxygen-plasma exposure - T_e), and channel AR on the meniscus velocity for the asymmetric capillary flow was also examined. Increasing waiting time was found to decrease velocity, although for waiting time greater than 60mins the decrease in velocity was very small (Figure 1.22b). For exposure time 0.5 to 2 minutes velocity was found to increase and for higher exposure times to decrease (Figure 1.22c). It was observed that the meniscus velocity increased with an increase in the channel height up to 400 μm and then to reduce with further increase in the channel height (Figure 1.22d) [62].

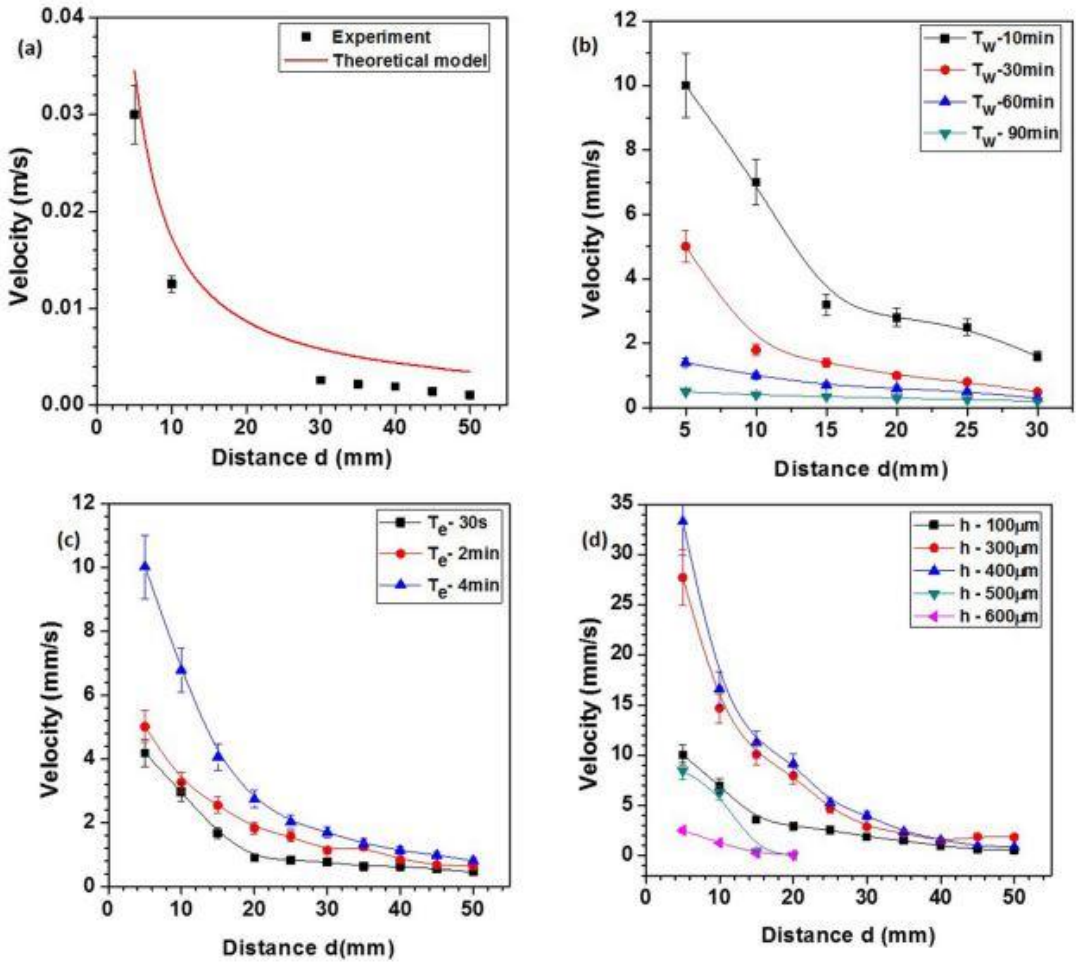

Figure 1.22. (a): Comparison of the velocity of blood meniscus in a microchannel. (b): Velocity versus distance for different waiting times for 2 min exposure time. (c): Velocity versus distance for three different exposure times at a waiting time of 10 min. (d): Velocity versus distance for different channel height for 2 min exposure time and a waiting time of 10 min [62]**.**

In another study [63] an on-chip whole blood/plasma separator was developed using a combination of asymmetric nonporous super-hydrophilic surfaces and patterned hydrophobic patches. An asymmetric capillary force through the micro channel was attained to achieve the separation of plasma from whole blood. Red blood cells were continuously accumulated within the hydrophobic patch working as a naturally organized micro filter. A relatively large amount of blood plasma separation was achieved by utilizing both the asymmetric capillary force and the patterned 10 mm hydrophobic patch [63].

Sakamoto et al [64], also, developed a capillary driven microfluidic device for blood plasma separation, and high-throughput screening from a drop of blood. The device is a straight

rectangular channel with array channels of 2 mm deep to filter the red blood cells from the whole blood. At the inlet of the device, numerous red blood cells get clogged in the microchannel arrays. As the flow proceeded, at 200 mm from the inlet, about 800 cells were observed, which indicated that more than 99% of the cells were separated by the inlet microchannels. Further ahead at more than 600 mm from inlet, no red blood cells were observed. The separation efficiency was estimated to be greater than 99%, and volumes of about 150 nL of blood plasma were isolated in about 3 min. Surface wettability was optimized by O_2 plasma irradiation and by applying poly-L-lysine (PLL) coating in order to increase capillary driving force.

1.8 Surface treatment for enhancing the flow in surface tension driven setups

One very important parameter of capillary driven microfluidics chips are the surface properties of the configuration, since there is no pumping mechanism to drive the flow. Flow is such setups is driven by capillary forces, hence surface properties are important in order to enhance surface tension and hence capillary forces to ensure good flow conditions. The most common treatment techniques are UV treatment and oxygen plasma treatment [65,66]. UV activation was found in previous studies to increase hydrophilicity of glass which results to better flow conditions (Figure 1.23a) [66,67]. In addition, plasma treatment was also found to increase wettability (Figure 1.23b) [65]

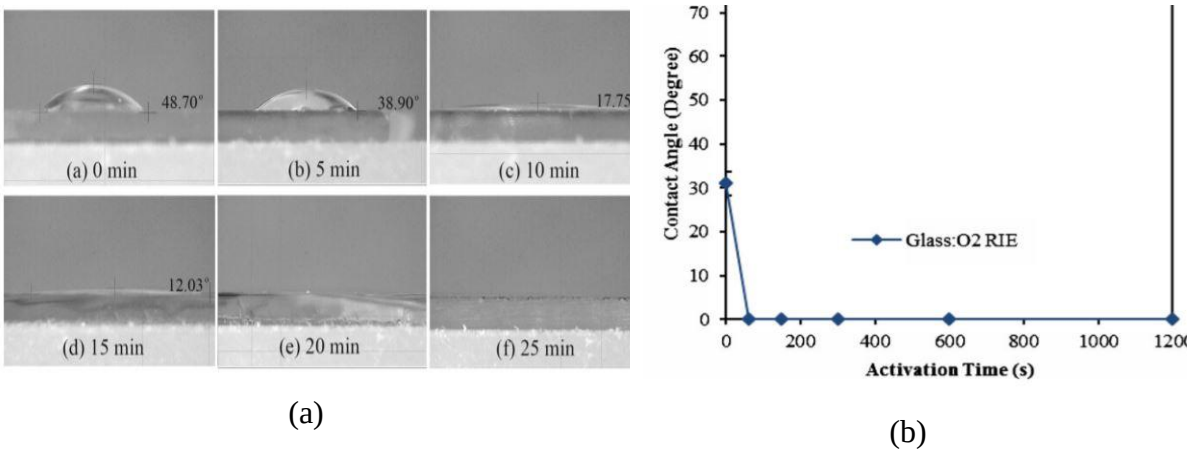

(a) (b)

Figure 1.23. (a): Contact angles between water droplets and silica films with various UV/Ozone exposure times [67]**. (b): Water contact angle glass as a function of oxygen plasma activation time** [65]**.**

Furthermore, titanium oxide (TiO_2) films are found to improve hemocompatibility [68]. Manfred et al [69] examined hemocompatibility on these samples by measuring the adhesion

of blood platelets, their P-selectine expression, and the blood clotting time. The crystalline titanium oxides had a slightly higher activation of the clotting cascade but lower platelet adhesion than nanocrystalline and amorphous titanium oxides. No obvious effect was found for surface roughness below 50 nm. Both, implantation of phosphorous or chromium ions, strongly reduced the activation of the clotting cascade. The phosphorous implanted surface also showed a reduced platelet activation, whereas platelet adhesion and activation were strongly increased on the chromium implanted surfaces. TiO_2 coating has shown to increase its hemocompatibility, both concerning blood platelets and blood clotting cascade.

In another work [70], TiO_2 films were deposited on glass substrates with and without O_2 plasma treatment. The surface structures of TiO_2 films were observed from SEM images and their wettability and photo induced hydrophilic properties were investigated according to the changes in water contact angles under UV light irradiations with intensity of 10 mW/cm^2. Enhanced hydrophilic property occurred using oxygen plasma treatment and TiO_2 films compared to bare glass with TiO_2 film (Figure 1.24). In addition, hydorphilicity was additionally enhanced by UV light irradiations with intensity of 10 mW/cm^2 post plasma and $Ti0_2$ film deposition [70].

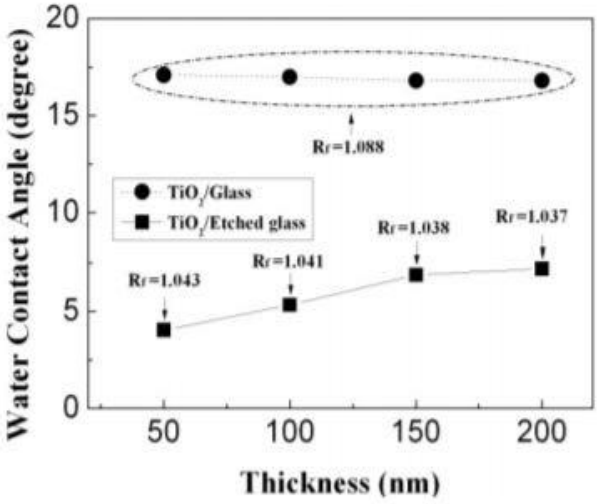

Figure 1.24. Change of water contact angle as a function of thickness for TiO_2 films according to presence (rectangular) or absence (circle) of oxygen plasma etching on the surface of glass substrates [70]**.**

In another work [71] optical properties such as transmittance, as well as the superhydrophilicity and self-cleaning properties of deposited TiO_2 film on glass plates was examined. TiO_2 coating was applied on the glass plates by electrospinning. The electrospinning process on the glass plates was carried out for different time intervals (1 min, 1.5 min, 2 min, 2.5 min and 3 min,

respectively) to have films with different thicknesses (in nm range). Hence the coated glasses were sintered at 450 ^{o}C for 30 min (in air medium) with a ramping rate of 2 ^{o}C per min. The sintering heating process evaporates the polymer and the solvent/acid residues which result in high porosity for the TiO_2. As observed from Figure 1.25a the superhydrophilicity of the TiO_2 coated films increased with an increase in the thickness of the TiO_2. The increase in hydrophilicity with increasing film thickness was attributed to the quick water chemisorption to the inner porous layers.

The optical properties were examined by UV–Vis spectroscopy (Shimadzu UV3600 UV–VIS–NIR spectrophotometer) with a spectral resolution of 1 nm. The transmittance of plain glass and the TiO_2 coated glass were very similar (around 90%) for the entire wavelength range as seen in Figure 1.25b, showing that TiO_2 coating does not affect the light transmittance of the glass.

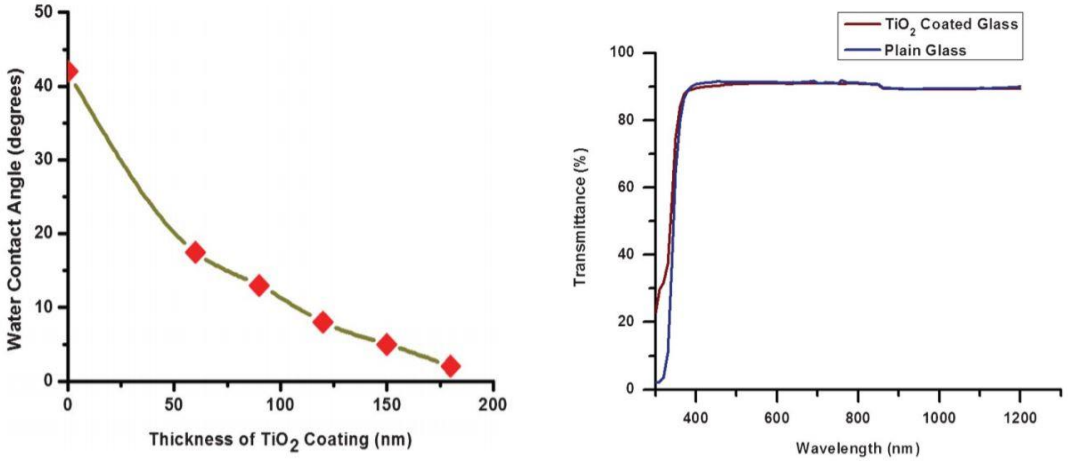

(a) (b)

Figure 1.25. (a): Measured decrease of water contact angle vs thickness of the TiO_2 coating. (b): A comparison of the transmittance of plain and TiO_2 coated glass samples. [71]**.**

1.9 Geometry effects in the surface tension driven flow

In a numerical study [72], simulations of Capillary-Driven Flows in Non-uniform Cross-Sectional Capillaries were performed, showing increased velocity in converging sections compared to straight sections (Figure 1.26). On the other hand diverging sections have shown to decrease velocity [72].

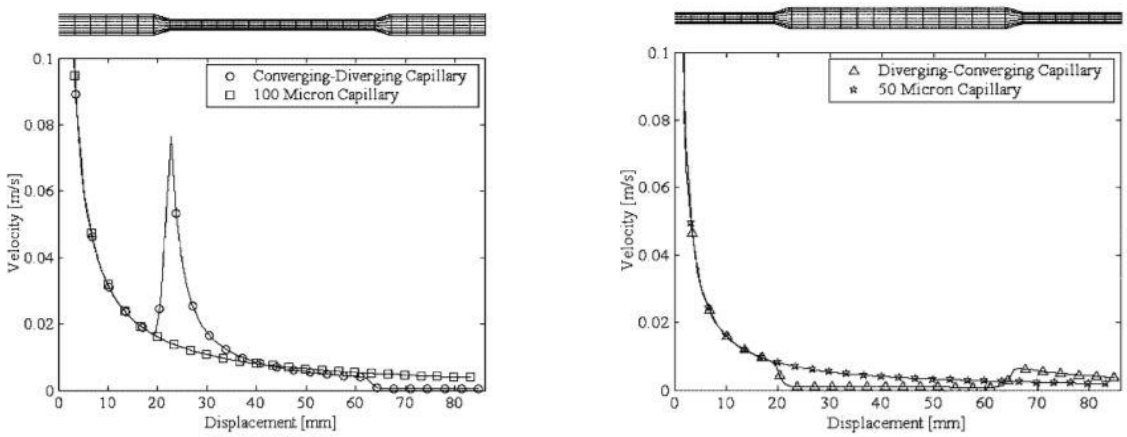

(a) (b)

Figure 1.26. Interface velocities [72]**. (a): For a converging diverging capillary and a 100-µm-diameter straight capillary. (b): For a diverging converging capillary and a 50-µm-diameter straight capillary. Upper image shows irregular capillary layout.**

Saha et al [73] performed experimental and numerical investigation of capillary flow in SU8 and PDMS microchannels with integrated-protruding pillars. The flow within the pillar region was faster at the converging side of the pillar and slowed down at the diverging side, becoming uniform where no pillars existed [73].

The increased velocity in the pillars converging section can be observed from the velocity curve spikes in Figure 1.27 showing meniscus velocity of the working fluid (isopropyl alcohol) in the SU8 and PDMS pillar integrated channels.

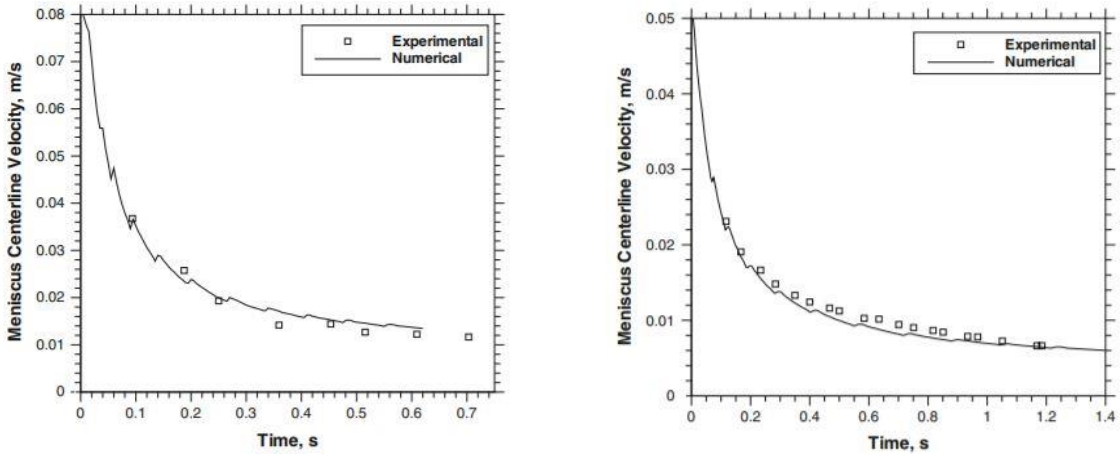

(a) (b)

Figure 1.27. Numerical and experimental comparison of meniscus centerline velocity obtained with isopropyl alcohol [73]**. (a): Using a PDMS channel and (b): Using a SU8 channel.**

The spikes in the curve correspond to the meniscus velocity in the pillar converging section. A higher velocity of the capillary meniscus was obtained with increase in surface area to volume

ratio in the devices. In addition, pillars created uniform meniscus front in the microchannel for the working fluids (ethanol and isopropyl alcohol) [73].

Pillar arrangement was also examined in another study [74], evaluating several permeability models to identify a robust model for optimizing pillar dimensions for maximum fluid flow rate. It was found that there is an optimum L/d (distance between two pillars/diameter of the pillar) for a given H/d (H=height of the pillar), based on the trade-off between viscous losses and capillary pressure. However, machining glass to integrate pillars is difficult and complicated [75]. In another study [76], where a microfluidic valve for capillary flow was developed, the sudden expansion of the microchannel formed a barrier of capillary pressure.

1.10 Summary of the Literature Review findings

In the previous sections of the chapter various aspects of the issue under investigation, namely blood flow in microfluidic applications and the influence of various parameters, were reviewed. Closely related past research work performed from researchers in the field was inspected in order to better understand the issue under investigation. Background material was also provided. A summary of the findings from this review is provided bellow.

Blood is a complex fluid, consisting of various formed elements, with the RBC being the most important as regards the flow and mechanical properties of the fluid. RBC aggregation, deformability and concentration are the three structural properties governing the viscoelastic and flow behaviour of blood.

The significance of microfluidic applications, for blood research or diagnostic purposes, was identified in a number of publications. The benefits, advantages and disadvantages of such systems, as found from the literature review, can be summarized as follows:

- Detailed information regarding the flow characteristics and the influence of hemorheological factors has been extracted in many studies utilizing pressure-driven setups.
- Surface tension driven (STD) setups have offered the possibility to utilize very small volumes of blood, and can be developed at very low cost. Basic characteristics of the blood flow in such devices have been investigated.
- Theoretical studies on the flow behaviour in the STD microfluidics also exist, however basic knowledge has been obtained regarding blood flow.
- The influence of various hemorheological parameters in the flow of blood in surface tension driven setups is not well understood.

- Blood microfluidics offered the possibility to develop Lab-on-Chip systems for the examination of various properties of blood.

Regarding the development of STD microfluidic setups, two parameters found to be related to the flow performance: the surface tension of the surfaces (therefore hydrophilicity) and the geometry of the channel. For the first it was concluded that the TiO2 coating is an effective approach to enhance to flow, whereas for the second it was identified that converging geometries offer an advantage, due the increased velocities observed in the channel.

Generally, the literature review findings point out that there is a fundamental need for deepening our understanding on the influence of basic physiological and pathological phenomena, in the passive microfluidic flow of blood. Additional issues are also further reviewed in the following chapters.

1.11 Rationale and aims of the study

The importance of the study lies on the fact that although a considerable body of work on STD blood flow exists in the literature, the influence of basic physiological (red blood aggregation, deformability, haematocrit, viscosity) and pathological phenomena, which dominate the non-Newtonian nature of blood, have not been thoroughly investigated in passive microfluidic flows.

In the present study, it is aimed to examine the influence of the above mentioned physiological/hemorheological factors in the STD flow, and the possibility for improving/enhancing the passive microfluidic flow, by a) increasing the interfacial surface tension between the fluid and solid walls through surface treatment and b) choosing an appropriate flow geometry.

The flow enhancement will be assessed through detailing the meniscus velocity and the velocity field characteristics in the channel specific hemorheological factors (Hct, viscosity, and RBC aggregation and deformability states). Local structural phenomena, such as RBC aggregation, will be quantified through image processing techniques, and rheological characterization will be performed to extract relevant information.

In addition, shearing conditions within the channel and the meniscus will be examined in detail since no such information exists in the literature, and it is a vital fluid mechanics quantity in blood rheology.

The outcome of this work is expected to produce new knowledge in the fields of Biorheology/Hemorheology, Blood Fluid Mechanics, for blood flows in microfluidic devices. Moreover, it is expected to lead in the development of a preliminary design for a functional point-of-care device for the measurement of RBC aggregation and other blood properties. Non-Newtonian theory would be employed to derive rheological characteristics of blood, such as viscosity, from the STD microfluidic device using appropriate computational models.

CHAPTER 2. Topics of interest, structure of the PhD research and research output

In this Chapter, the general structure of the PhD research is described, according to the topics of interest which were examined in the study. In each topic, the main points and relevant parameters are mentioned and briefly described. The research output resulted by the work in the PhD program is also listed at the end of the section.

2.1 Topics of interest and work structure

a) **Microchannel design parameters and construction, for flow enhancement:**

- Geometry of the channel for flow enhancement: Examination of different geometrical configurations for strengthening the intensity of the flow were performed.
- Fluid-wall interface properties optimisation (wettability, biocompatibility) through surface treatment. The objective was to design/improve/optimize the wall surface properties of the microchannel to achieve the optimum flow conditions for pumpless flow delivery in point of care systems. Biocompatibility of the channel should also be ensured. The following treatment techniques, and their combination, were explored:
  - UV treatment
  - Oxygen plasma treatment
  - Titanium oxide coating on glass surfaces.

Methods techniques: Surface spaying, Spin coating, UV exposure, Air plasma exposure

b) **Flow characterization in the passive microchannel**. The effect of the following parameters on the meniscus and core velocity field were examined:

- Haematocrit
- Fluid viscosity
- RBC aggregation
- RBC deformability

Methods and techniques for flow characterisation: μPIV (JPIV, Classic), MatPiv, analytical, (computational).

c) **Structural characterization of blood**. The following microstructural aspects were examined utilising the commercial instruments:

- Haematocrit.
- RBC aggregation (using Rheoscan A aggregometer). A preliminary design of a capillary driven point of care microfluidic system was developed to measure RBCA through developed algorithms.
- RBC deformability (using Rheoscan D300 instrument).

d) **Rheological characterization.**

- Rheology theory and appropriate models were utilised in order to extract information on basic hemorheological parameters. Analytical and computational, models were developed, in order to estimate the viscosity of blood flowing in the microchannel. Newtonian and Generalised Newtonian theory were utilised. The basic parameters and properties required for the task include:
  1) Surface tension
  2) Contact angles
  3) Meniscus location in the channel during the flow
- Viscosity Measurements. The effect of RBCA, RBCD and HCT on viscosity were examined. Viscosity was measured at different shear rates using commercial instruments (Brookfield DV2T cone-plate viscometer), under different aggregative conditions, HCTs and after decreased RBC deformability, and several viscosity indices were produced.
- Red blood cell aggregation: Measurements performed using a Rheoscan-A200 system and home-made image processing methods.
- Red blood cell deformability: Measurements: performed using a Rheoscan-D300 system.

2.2 Research Output

The following journal publications and conference proceedings have been resulted from the work and contribution of the Author of this Thesis in the present PhD program.

Journal Publications:

[1] **Pasias D**., Koutsokeras L., Passos A., G. Constantinides, Balabani S. and Kaliviotis E. (2022). Effects of biomechanical properties of blood on surface tension driven flows in superhydrophilic channels. Physics of Fluids, Submitted February 2022, Accepted April 2022.

[2] **Pasias D**., Passos A., G. Constantinides, S. Balabani, and Kaliviotis E. (2020). Surface tension driven flow of blood in a rectangular microfluidic channel: effect of erythrocyte aggregation. Physics of Fluids, 32, 071903, doi.org/10.1063/5.0008939.

[3] Kapnisis K., Seidner H., Prokopi M., **Pasias D**., Pitsillides C., Anayiotos A. and Kaliviotis E., (2019). The effects of stenting on hemorheological parameters: an in vitro investigation under various blood flow conditions. Clinical Hemorheology and Microcirculation, 72(4), pp. 375-393.

[4] Kaliviotis E., **Pasias D**., Sherwood J., and Balabani S. (2016). Red blood cell aggregate flux in a bifurcating microchannel. Medical Engineering and Physics, https://doi.org/10.1016/j.medengphy.2017.04.007.

Conference Publications:

[1] Kapnisis K., Seidner H., Prokopi M., **Pasias D**., Pitsillides C., A. Anayiotos and E. Kaliviotis. Blood rheology and flow geometry effects. Proceedings of the 9th International Conference of the Hellenic Society of Rheology, Samos, Greece, 22-27 June, 2019.

[2] Kaliviotis E., Kapnisis K., Seidner H., Prokopi M., **Pasias D**., Pitsillides C., Pavlides S. and A. Anayiotos. In vitro investigation of hemorheological parameters under various flow conditions in stented vessels. *Proceeding of the 8th World Congress of Biomechanics,* Dublin, Ireland, 8-12 July 2018.

[3] **Pasias D**., Kaliviotis E., Velocity and erythrocyte aggregation characteristics for surface tension-driven flow of blood in rectangular microfluidic channels. *Proceedings of the Joint Meeting of the European Society for Clinical Hemorheology, the International Society for Clinical Hemorheology and the International Society of Biorheology.* Krakow, Poland, 2-6 July, 2018.

[4] **Pasias D**., and Kaliviotis E. Surface tension driven microfluidic blood flow: red blood cell aggregation and viscosity effects. *Proceedings of the 8th International Conference of the Hellenic Society of Rheology*, Limassol, Cyprus, 12-14 July, 2017.

[5] Kaliviotis E., **Pasias D**., Sherwood J., and Balabani S. Blood microstructure and viscosity in bifurcating microfluidic flows. *Proceedings of the Blood Flow: Current State and Future Prospects Conference*, 9-11 October, Paris, France, 2017.

CHAPTER 3. Methodology

In this Chapter the methodology adopted in the study will be described. As the work in the study was multi-faceted, methodological details will also be described in the results Chapters 4, 5, 6 and 7, whenever deemed appropriate. Also, some additional, however very relevant, information from the literature is included in the sections of this chapter.

3.1 Hemorheological parameters examined in the study.

The effect of the following parameters on the meniscus and core velocity field were examined in the study.

Haematocrit: It is known in the literature that aggregation parameters are significantly influenced by the haematocrit of the blood samples [77]. Aggregation index has shown an increase with the increase of HCT [77]. In this study aggregation parameters and viscosity were examined at different HCTs. Details on sample treatments to produce different haematocrits are provided further bellow. Furthermore, the effect of HCT was examined in the velocity profiles in the core and meniscus velocity along the channel.

Fluid viscosity: Fluid viscosity, which is also related to aggregation [31,39] was examined under various aggregation levels and shearing conditions. At high shear rates RBCs disperse, hence aggregation is reduced contrary to low shear rates [30]. Viscosity was measured at a range of shear rates (from high shear rates to ensure disaggregation ramping down to low values) using Brookfield DV2T viscometer, producing viscosity indices and hence related with the velocity indices.

RBC aggregation: Velocity profiles in pressure driven flows show an increase in bluntness when aggregation exist [31]. In order to examine the effect of RBCA on surface tension driven flows RBCA indices were extracted for working fluids, at different aggregative conditions using Rheoscan A instrument. The aggregation indices have been correlated with the meniscus flow velocities and the velocity profiles. At low shear rates RBC aggregation is enhanced where, at higher shear rates disaggregation occurs due to higher shear forces [31]. Hence shear rate profiles were calculated and plotted from the channel velocity profiles, to examine whether shear rates in the flow are high enough to ensure disaggregation at the beginning of the flow and examine whether there are good disaggregation conditions within the flow. Moreover, meniscus shear rate curves were produced form the beginning of the flow until meniscus reached the end of the channel, to further examine the shear rates effects in the aggregation characteristics of the flow. In addition, shear rate indices were produced from the shear rate

profiles and meniscus shear curves for three different time steps (beginning, end and whole duration of the flow).

RBC deformability: RBC deformability is known to affect aggregation and viscosity hence giving information about the flow. In pressure driven flows CFL thickness increases with cell deformability, since the membrane deformability allows the cells to deform and create a concentrated core. Since CFL and aggregation increases, core viscosity is also increased. This leads to a decrease in effective viscosity with higher levels of aggregability [78]. Deformability indices were produced using Rheoscan D300 commercial instrument. Heat treatment was applied according to a protocol form another work [79], in order to harden RBCs, hence making them less deformable. Velocity indices and profiles of the working fluids prior and post heat treatment were compared and also related with the deformability indices to examine the effect of decreased RBC deformability on the flow.

3.2 Microchannel design and construction

3.2.1 Rectangular-straight microchannel

The design of the microchannel was examined, in order to develop a functional microfluidic chip were the experiments were performed. Since, RBC aggregation which is examined in this research is a shear dependent phenomenon [45,46] (aggregates form at low flow velocities) as aforementioned, flow conditions should be favourable to the flow. The microchannel was designed to be simple to manufacture, cost effective and user friendly. The microchannel design which has been used in the first experiments, has been developed with xurography techniques. Transparent material is joined though adhesive means, and the desired geometry is cut with blades. Glass slides (Superfrost 75mm x 26mm, 1mm thickness) and double sided tape (3M, 100μm height) were utilised similar to other studies [80].

The geometry of this design (Figure 3.1) was a straight channel due to the simplicity of the geometry. Part of the bottom glass slide was left protruded to accommodate the blood drop. The fluid is placed at the entrance of the channel using a pipette, then it flows through the channel due to capillary forces [81]. The aspect ratio (AR=W/h) was approximately 3, and the channel length 10 mm. In this work the variables x, y and z, are normalized with the width of the channel (W~300 μm) and expressed as x*, y* and z*. The origin of the coordinate system was taken at the midplane of the channel, at the entrance. All measurements were performed in the region from z=600 μm from the entrance of the channel to a distance of ~z=1700 μm to avoid any entrance effects, as in [51]: An entrance length (Le) of 3.5 times the channel height

(350 μm in the present case) for capillary flow in a rectangular channel, is sufficient to ensure fully developed flow [82].

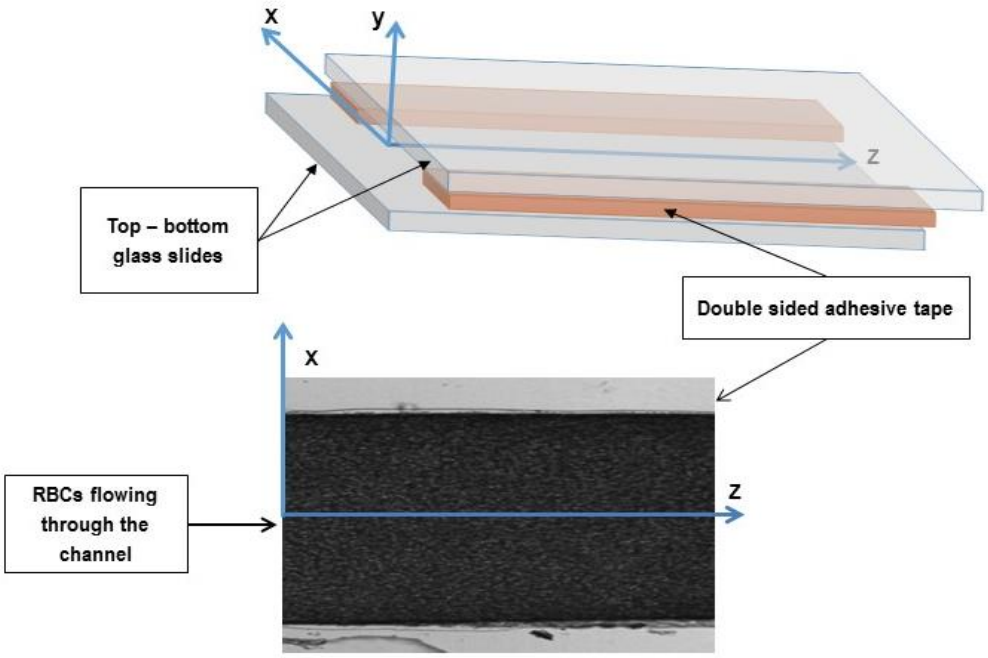

Figure 3.1. Top: Schematic of the microchannel geometry (not in scale) and the coordinate system used. Bottom: Sample image of the RBC flow in the microchannel.

The design met the conditions of simplicity and cost effectiveness. However, as aforementioned, more parameters were examined to further improve the flow conditions such as: a) The channel geometry and b) Surface treatment of the glass slides

3.2.2 Convergent – surface treated rectangular microchannel

3.2.2.1 Geometry

A progressive reduction in the flow area of the channel should enhance the flow according to mass flow conservation, which agrees with a study in numerical simulations of capillary-driven flows for non-uniform cross-sectional capillaries [72], which showed the increase of velocity when the working fluid passed through converging sections of the channel [72,73].

To establish this fact experimentally, the flow in a converging geometry was compared against that in a straight channel, so that the effects of convergence be examined, and hence decide on the final geometry of the channel. The meniscus velocity of a Newtonian fluid (produced as explained later in Section 3.6) in straight microchannels, and channels with converging angles of 3^o and 5^o was compared in order to identify the geometry providing the best flow conditions.

The glass slides were pre-cleaned with HCl-DI water solution in a concentration of 1:2. The micro channels were constructed using double sided adhesive tape (Tessa 100μm height) and glass slides (Superfrost 75mm x 26mm, 1mm thickness) similar to microchannel version 1 (Section 3.2.1). The channel geometries were drawn using CAD software (Solid Works), and then the tapes were cut according to the drawings, and manually transferred on the glass slide in order to create the desired channel geometries. Before placing the top glass, a hole was drilled at one end to form the exit of the channel. The flow was manually controlled by the user, by blocking and opening the exit hole. The length of the channels was 8mm. The 3^o and 5^o channels included a small straight section at the end of convergence leading to the exit hole. The sample was applied at the entrance (bottom glass slide was left protruded to accommodate the blood drop) with a micropipette. The channels design is shown below in Figure 3.2.

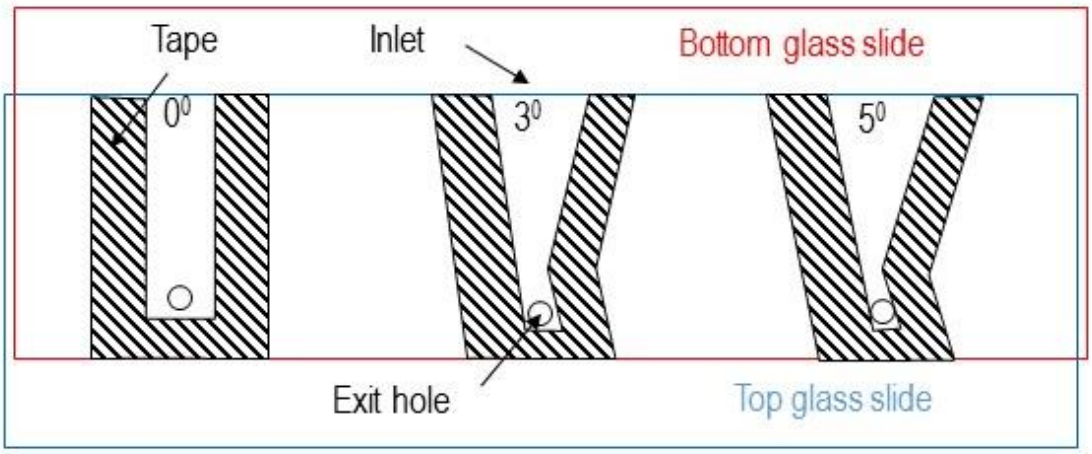

Figure 3.2. The geometries tested for optimizing the geometry of the channel (0^o, 3^o and 5^o convergence). The diagrams are not shown in scale. Double sided tape (shadowed sections) sandwiched between glass slides.

The meniscus position was recorded with a USB camera after the initiation of flow at a frame rate of 20 fps and the data were analysed to track the meniscus position at each frame, using a free tracker software package (https://www.rollapp.com/app/tracker). The velocity was calculated from the position and frame rate data.

The results in Figure 3.3 indicate that converging channels provide higher meniscus velocities compared to straight, and hence more favourable flow conditions. Comparing the two converging channels, the results show similar velocities. However, the 3^o geometry provide a smaller entrance and increased channel length which are practically preferable in the present case. Therefore, the 3^o geometry was adopted in this work.

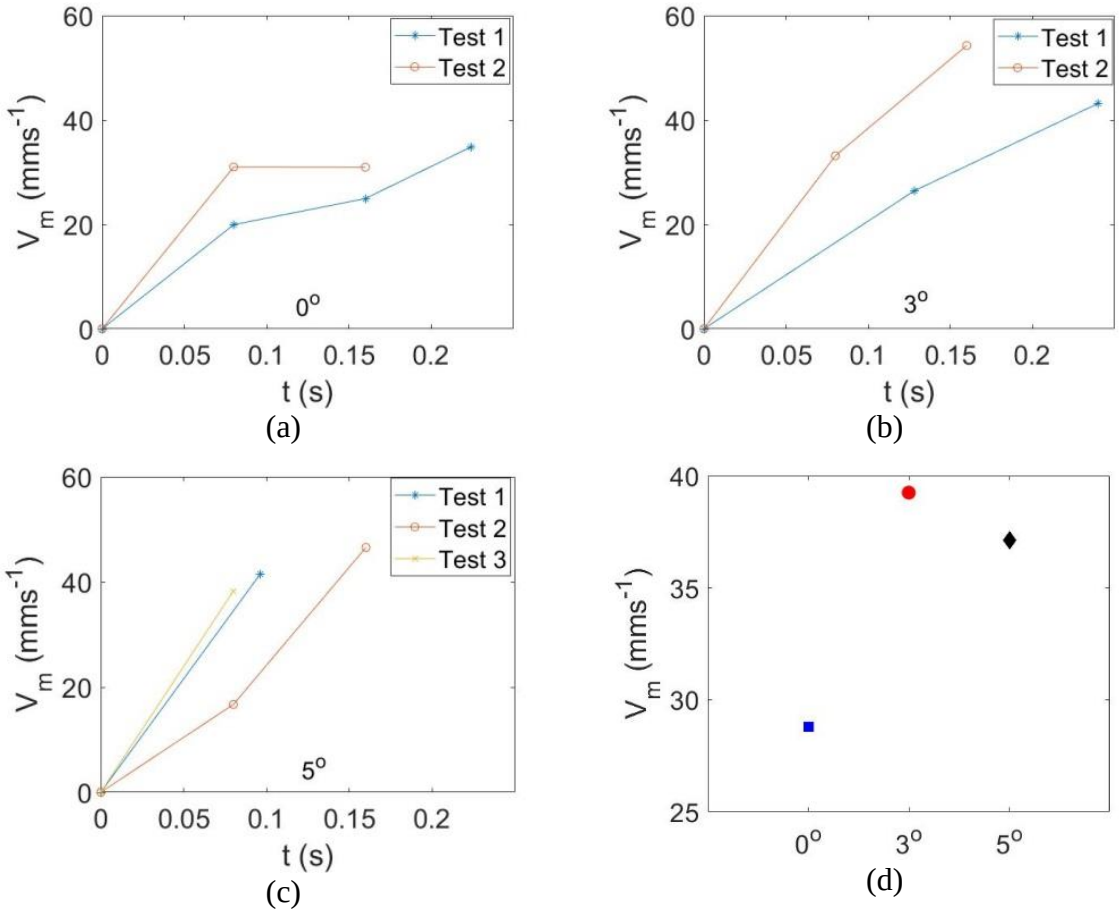

Figure 3.3. Meniscus velocity vs time. (a, b and c): Results of straight channel, 3º and 5º respectively. (d): Mean meniscus velocity of NF at 0º, 3º and 5º geometries.

3.2.2.2 Surface treatment

The surface properties are highly important in surface tension driven flows since there is no pumping mechanism to drive the flow [54,55]. The degree of hydrophilicity shows how favourable to the flow is the material used [54,55]. Hence, to further improve the hydrophilicity, of the microchannel surface treatment was applied on the glass slides. The relevant metric of hydrophilicity is the contact angle (details on measuring contact angles are described in the next Section 3.3).

UV/ozone and Plasma treatment were performed and compared to the cleaned glasses for different treatment times in order to assess their effect on improving glass wettability. UV/ozone was applied for 10, 20 and 30 minutes using Ossila E511 UV/ozone cleaner apparatus. Plasma treatment of the microscope glasses has been performed in a homemade apparatus based on a modified microwave oven and a standard 500ml glass bottle shown in Figure 3.4.

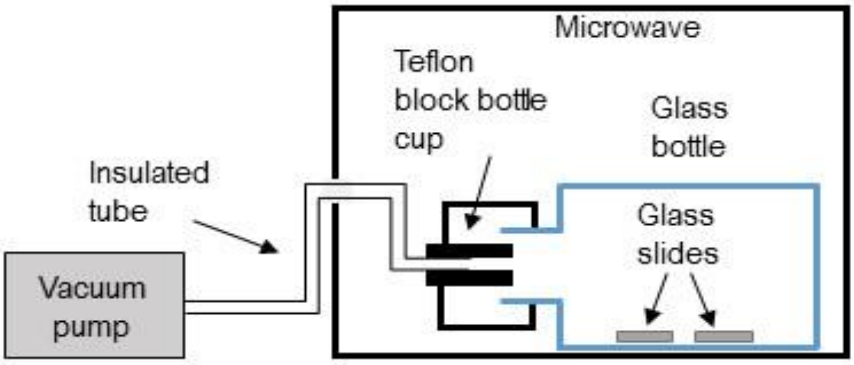

Figure 3.4. Schematic of plasma cleaning setup.

The glass bottle has been converted into a small vacuum chamber by connecting it to a dry-scroll vacuum pump (Agilent, Triscroll) via a custom-made Teflon cap through the walls of the microwave oven. The glass slides were placed into the glass bottle which was sealed and then evacuated to a lower pressure, in the order of 1×10^{-1}Torr. The microwave power selector was at the highest setting and the built-in timer was used to control the treatment time. By turning on the microwave power, a vivid plasma was created in the whole bottle volume, having a red-purple color, indicating that air was the main gas in the bottle. The glasses were treated with Plasma for 5,10, 20 and 30 seconds. Prior to any treatment the contact angle was measured to be approximately 45º.

UV exposure found to have very similar effects for either the 10, 20 or the 30-minute duration, as observed in Figure 3.5a. For all treatment times the contact angle was significantly reduced to ~10º, however a loss in hydrophilicity was observed after 6 hours, when the contact angle increased back to ~20 º. Plasma treatment of 5s and 10s had the smallest contact angles compared to 10s and 30s treatment time (Figure 3.5b). However, plasma treatment for 10s is observed to have better aging time compared to 5s. Comparing the results of Figure 3.5a and Figure 3.5b , although contact angles after UV and plasma treatment are similar, plasma treatment has better aging time and provides slightly lower contact angles. Hence plasma treatment for 10s (which is the most effective plasma treatment time in terms of contact angle and aging time compared to 5s, 20s and 30s) has been chosen instead of UV.

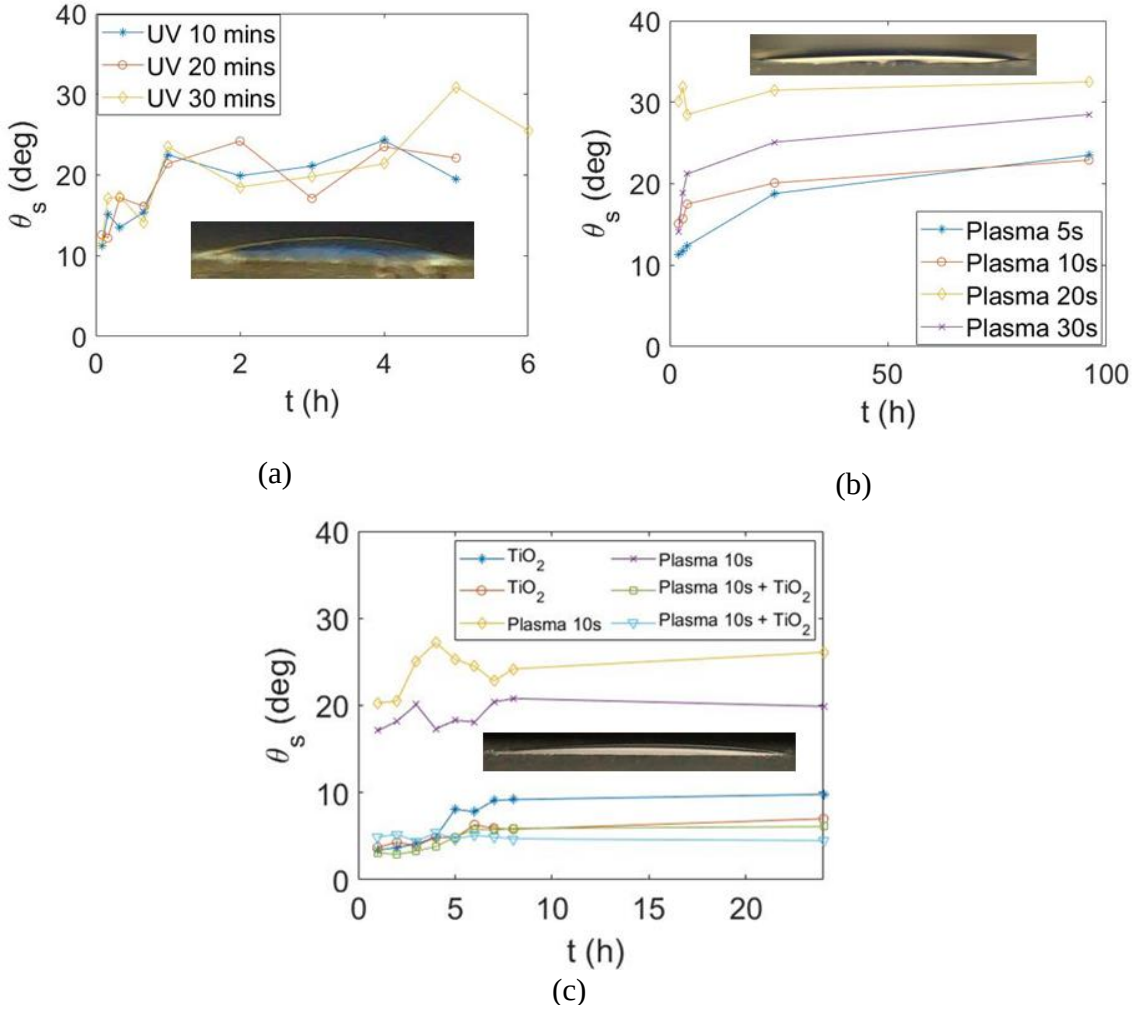

Figure 3.5. Contact angles of DI water on UV, Plasma and Ti0$_2$ treated microscope glasses vs time. (a): Contact angle for UV treated glass slides for 10, 20 and 30mins. (b): Contact angle for Plasma treated glass slides for 5s,10s, 20s and 30s. (c): Contact angle for Ti0$_2$, Plasma 10s and their combination. Inserts show representative image samples from the optimum condition in each case, taken at longest time.

To further improve hydrophilicity application of TiO_2 coating was investigated both without and post plasma treatment similar to another study [70]. TiO_2 coating was applied on the pre-cleaned glasses with two methods. The first method was by using a standard compression spray gun for spray coating as in another work [83]. The second method was spin coating as in [84] at 3000rpm for 1 minute and then left to dry at room temperature for 5 minutes. The fluid used in spin coating was Sufashield G (Ti0$_2$ nano particles suspended in water). Both methods resulted in similar contacts angles. Ti0$_2$ treatment was also performed after plasma treatment for 10s on the pre cleaned glasses. The results of Plasma, TiO_2 treatment, and their combination is compared in Figure 3.5c. Pre cleaned glasses treated in combination with Plasma for 10s and

TiO_2 coating give lower contact angles than plasma or TiO_2 coating alone; hence this method was chosen to be the final treatment of the glasses.

3.2.2.3 Convergent Microchannel fabrication

A convergent microchannel was made of glass slides (Superfrost,75mm x 25mm 1mm thickness) and double sided tape (Tessa, ~100μm height). The glass slides prior to channel fabrication were surface treated (cleaned plasma treatment for 10s and hence coated with TiO_2) as explained above in section 3.2.2.2. The design included a round deposition well, a converging geometry part (as it has shown to enhance flow in section 3.2.2.1-Figure 3.3), and a straight section leading to the exit hole. Figure 3.6 shows the schematic of the microchannel version 2, The adhesive tape was cut according to design using xurography techniques [85], using a commercial Silhouette Portrait 2 cutter. The converging section had a width of ~5 mm at the beginning of the channel, and a length of 20 mm until it converged to a width of ~1mm. The top slide was drilled at the beginning and at the end of the channel creating the deposition well and the exit of the channel.

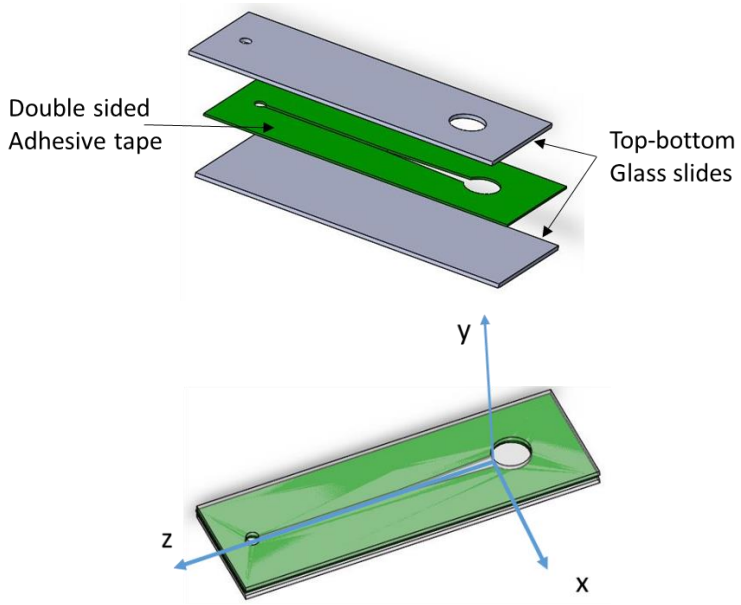

Figure 3.6. The convergent and surface treated microchannel.

3.3 Contact angle measurements

Static contact angle measurements were performed by capturing drop images Figure 3.7(a) at the surfaces of contact (glass and adhesive tape), and then analysing the images using ImageJ software. The contact angle measurement set-up consisted of a USB camera, aligned with the XZ surface plane of the specimen. Both camera and specimen were secured on a horizontally

levelled stand. A drop of 10μl volume was applied with a micropipette on the surface of the specimen. The drop surface and drop contact lines were identified through image processing using the software ImageJ. The contact angle θ_c was defined as the angle between the line of contact and the surface line of the drop, measured counter clockwise (Figure 3.7c and d). When the wettability is high, small contact angles (<<90°) and large base diameters occur (Figure 3.7a-c), whereas when wettability is low large contact angles (>>90°) and smaller base diameters are apparent (Figure 3d) [86]. The static contact angles of the fluids on the hydrophilic glass surfaces were found to be 36°, 38° and 44° for the Non Aggregative Blood (NAB), Whole Blood (WB) and Newtonian Fluid (NF) fluids respectively (Table 3.1), forming a drop base diameter of approximately 5 mm (Figure 3.7a-c). Contact angles on the adhesive tape were found to be 100°, 96°, 110°, for the NAB, WB and NF fluids respectively (Table 3.1), indicating the neutral/hydrophobic nature of the side, as opposed to the top and bottom walls of the channels (Figure 3.7d). The drop base diameters for the aforementioned cases were found to be approximately 3 mm.

(a) (b) (c) (d)

Figure 3.7. Images of drops on the glass surface. (a): From the Newtonian fluid, (b): From the non-aggregating blood and (c): From the whole blood. θ_c is the measured static contact angle. In panel (d): Representative image of whole blood drop on the adhesive tape.

Fluid	Contact angle at each surface
NF	Glass/Tape, 44º/110º
NAB	Glass/Tape, 36º/100º
WB	Glass/Tape, 38º/96º

Table 3.1 Contact angles at different surfaces

3.4 Structural characterization of blood

3.4.1 RBC aggregation

Aggregation indices were derived utilising the Rheoscan-A200 instrument. Aggregometry was performed on the aggregating fluids for both heat- and not heat-treated conditions. Aggregometry was not performed to non-aggregating fluids since these samples show negligible aggregation. The Rheoscan-A200 transmission system consists of a laser diode (LM-

6305MR, Lanics Co., Ltd., Seoul, Korea) and a photodiode (FDS1010, ThorLab, Boston, USA). The transmitted light detected by the photodiode was converted to digital signals by a DAQ card (NI, USA) and transferred to a computer [77,87] (Figure 3.8a).

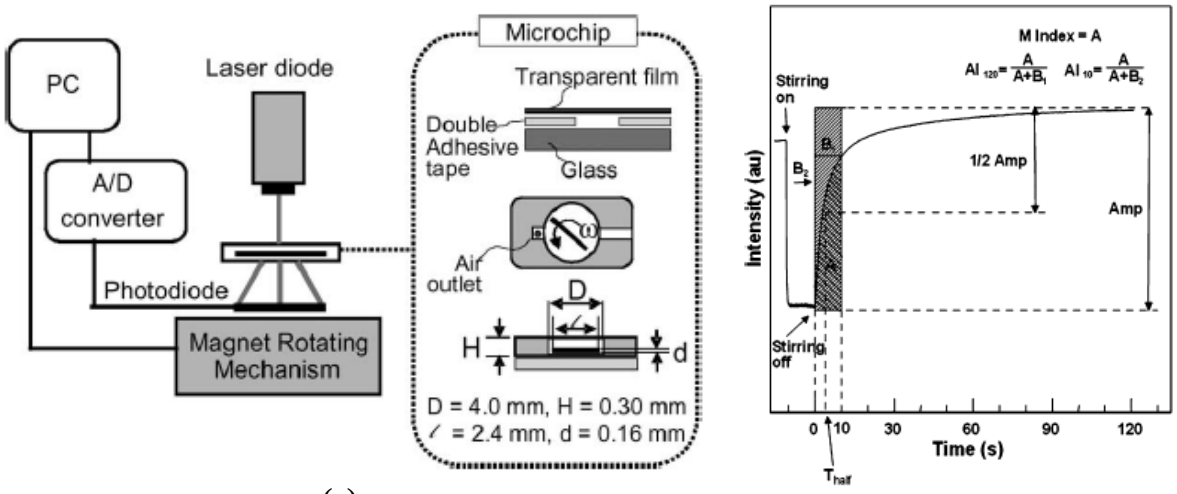

Figure 3.8. (a): The operating principle of the Rheoscan-A200 instrument. (b): The indices produced by the intensity curve of the instrument [77]**.**

Prior to recording the RBCs in the microchip are stirred by a magnetic stirrer for 10s at 900rpm in order to fully disperse the RBC aggregates. The light transmission curve is then analysed to produce various the following aggregation indices [88]:

- AI: The ratio of the area under the Intensity curve (syllectogram) to the total area, for 10 or 120 s in Figure 3.8b.
- Amp: The difference between the I_{min} and the light intensity at either 10 or 120 s, indicating the extent of RBC aggregation.
- $t_{1/2}$: The time required to reach a light intensity of Imin + 1/2 AMP, indicating the characteristic time constant to reach the half level of aggregation for 10 or 120s.
- M index: The area below the syllectogram over either 10 s time period (M), indicating the degree of the accumulated aggregation during 10s.

The abovementioned indices were obtained at each experiment for each type of working fluid tested and then averaged to find a mean index.

Moreover, red blood cell aggregation was measured in the microchannel using specially made algorithms and Matlab software (provided complete in Appendix 1). The RBCA algorithm calculated the light intensity from captured images, and Intensity/Time curves were produced,

from which aggregation indices were derived, and compared with the indices of the commercial aggregometer Rheoscan A.

3.4.2 RBC deformability

Working fluids were heat-treated to reduce RBCs deformability. Deformability indices of aggregative and non-aggregative working fluids both prior and post heat treatment were found using commercial instrument Rheoscan-D300 (Sewon Meditech, Inc., Seoul, Korea). The RheoScan-D instrument consists of a disposable fluidic element, a laser, a CCD camera sensor, a pressure sensor and a vacuum-generating mechanism. The working principle of the instrument is illustrated in Figure 3.9.

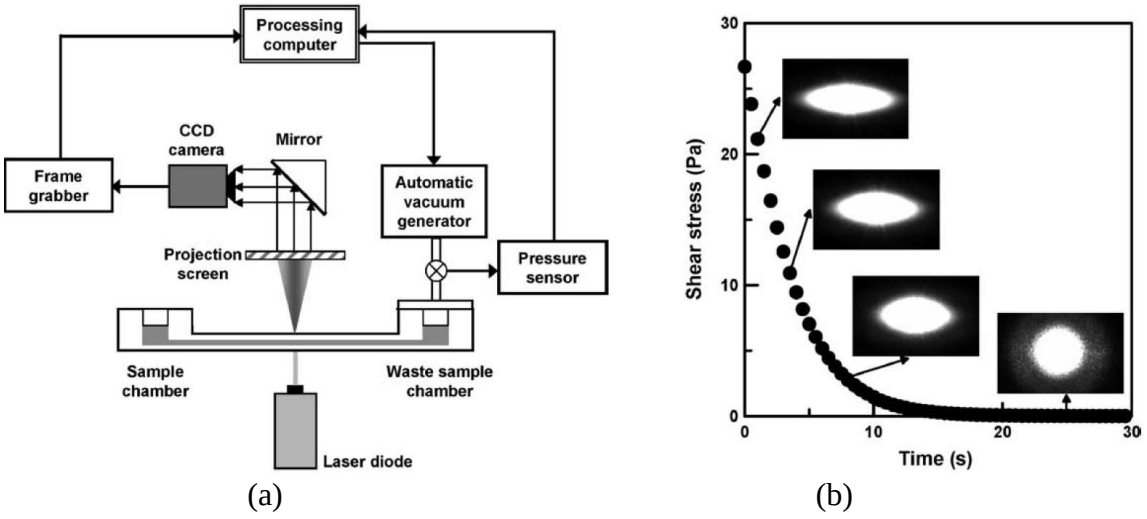

(a) (b)

Figure 3.9 (a): The working principle of the Rheoscan-D300 instrument. (b): The laser diffraction patterns produced in the system for various shear stresses [89]**.**

The disposable element, which is made of transparent plastic receives the sample in the inlet reservoir (sample chamber) [90]. Blood of 6μl volume is aspirated in a mixing tube, which is gently shacked, and the mixture is transferred in the fluidic element, which is finally then inserted in the instrument. The dilute RBC suspension is perfused in the microchannel under vacuum, which pressure decreases from approximately 20 to 0.5 Pa. A laser beam aims through the sheared sample which is diffracted by the deformed cells. The diffracted beam is captured by a CCD camera and analyzed by the computer. Based on captured diffraction patterns elongation index (EI) is determined for each shear stress [90]. The deformability indices used in this study are the following:

- Elongation index: EI, defined as $EI = \frac{A-B}{A+B}$, shown in Figure 5.6a as a function of the applied stress (A and B are the length and the width of the diffraction pattern),

- Half Shear Stress ($SS_{1/2}$), which is the shear stress required for half-maximal deformation
- Ratio, defined as $R = \frac{EI}{SS_{1/2}}$.

By comparing deformability indices prior and post heat treatment, the effect of RBC hardening on deformability was examined. In addition, deformability and aggregation indices were compared, to examine how the suspension medium (Plasma, Dextran, PBS) used to alter aggregation conditions of the working fluids, affected RBCs deformability.

3.5 Rheological characterization

Viscosity measurements were performed, utilising a Brookfield DVIIT instrument, which is a cone-plate geometry viscometer. Samples were loaded in the plate of the viscometer with a micropipette (0.6 ml volume) and tests were initiated approximately 30 seconds afterwards. Viscosities were measured by ramping down from high shear rates of the order of 10^2 (to ensure RBC aggregate dispersion) to low shear rates of the order or $10s^{-1}$ (30 seconds measurement time at each shearing point), without pre-shearing between shear points. The duration of a complete viscosity test was 8.5 minutes (17 points of measurement, 30 seconds each), and the viscosity measurement was performed at the end of the shearing period at each point. The maximum shear stress that cells were exposed at the highest shear rate was approximately 2 Pa for 30 seconds, hence much lower from stress/duration causing membrane damage and hemolysis [91]. All measurements were performed at room temperature (25 ± 0.5 ^{o}C).

Further, rheology theory and appropriate models were utilised in order to extract information on basic hemorheological parameters. Analytical models were developed in order to estimate the viscosity of blood flowing in the microchannel using matlab software. Newtonian and Generalised Newtonian theory was utilised. The basic parameters and properties required for the task included:

a) Surface tension
b) Contact angles
c) Meniscus location in the channel during the flow

Details of the analytical approach are given in relevant Results Chapters 4.1 and 4.4.

3.6 Flow characterization

3.6.1 PIV and Brightfield µPIV

Particle image velocimetry (PIV) is a common technique used in fluid dynamics for providing the velocity field of a flow. The fluid flow is captured and imaged, through the light scattered by liquid or solid particles, which are illuminated by a laser light sheet. These particles have to be artificially seeded to the flow as tracing particles, since they do not naturally exist in the flow. In addition, their size has to be small enough to follow the streamlines and not affect the flow significantly. A common standard two-component PIV (2C-PIV) setup is illustrated in Figure 3.10, which shows a typical PIV setup in standard PIV. Though several types of laser sources are suitable, the most commonly used is the pulsed Neodyme-YAG (Nd:YAG) laser, doubled in frequency (532 nm). Pulse duration is typically 5-10 ns, and repetition rate is on the order of 10 Hz. Laser energy can reach 400 mJ/pulse. PIV systems are made of two independent laser cavities, but the laser beams should be superimposed in the near- and far-fields so that the two laser sheets illuminate the exact same area. In most cameras, digital image recording is done via a CCD (Charge-Coupled Device) sensor which converts photons to an electric charge based on the photoelectric effect. The CCD sensor consists of many individual sensors that are arranged in a rectangular array. Each pixel has a size on the order of 10x10 µm. Their repetition rate in PIV double frame mode is on the order of 10 Hz

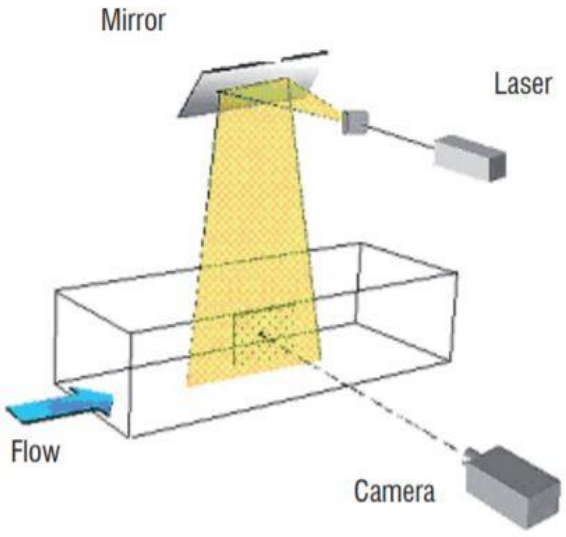

Figure 3.10. Typical PIV setup [92].

The desired plane in the flow is illuminated twice by utilizing two superimposed laser light sheets. Light is scattered by the particles and recorded on two separate frames on a special

cross-correlation CCD camera sensor. The captured images are then separated into smaller regions called interrogation windows (IW). Hence, by cross-correlation functions the location of each IW in the next frame is found. The correlation of two functions f(x) and g(x) is defined as the integral of the product of f (x) with g(x), the latter shifted over some distance Δx. i.e.

$$f * g = C_{fg} = \int_{-\infty}^{+\infty} f(x)g(x + \Delta x)dx \qquad 3.1$$

For each shift Δx the correlation is calculated. This means that if a structure moves as awhole, besides random and offset correlations, a correlation maximum will be found at the shift corresponding to the translation. As an example let us take two delta functions:

$$f(x) = \delta(x - x_f) \qquad 3.2$$

$$g(x) = \delta(x - x_g) \qquad 3.3$$

Then the correlation C_{fg} is: $C_{fg}(\Delta x) = \delta(x - x_{fg})$ where $x_{fg} = x_g - x_f$. The correlation shows a peak at x_{fg} and is zero elsewhere. This situation is illustrated in Figure 3.11.

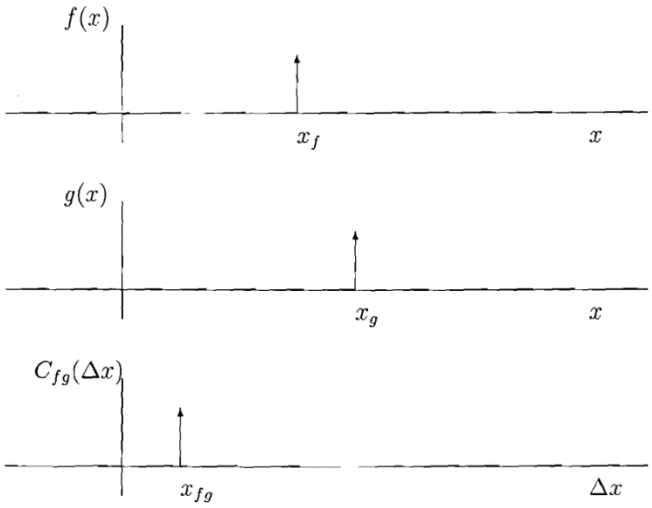

Figure 3.11. Example of cross-correlation with two Dirac-functions [92]**.**

In this way the local 2 component-displacement vector (horizontal and vertical direction) of the particle images between the two illuminations is determined for each IW. By taking into account the time interval between the two laser pulses and the image magnification obtained from camera calibration, the projection of the local flow velocity vector is determined, attributed to the centre of the interrogation window [92].

The correlation concept can also be shown visually using Figure 3.12. Figure 3.12a and Figure 3.12b show instantaneous images taken from a particle field at two consecutive times, with a time separation of Δt. If the second particle field is translated horizontally, superposition of the translated image with the first (Figure 3.12c) allows for visual detection of horizontal particle motions. Likewise, if the second particle field is rotated, superposition of the rotated image with the first (Figure 3.12d) allows for visual detection of rotating motions [93].

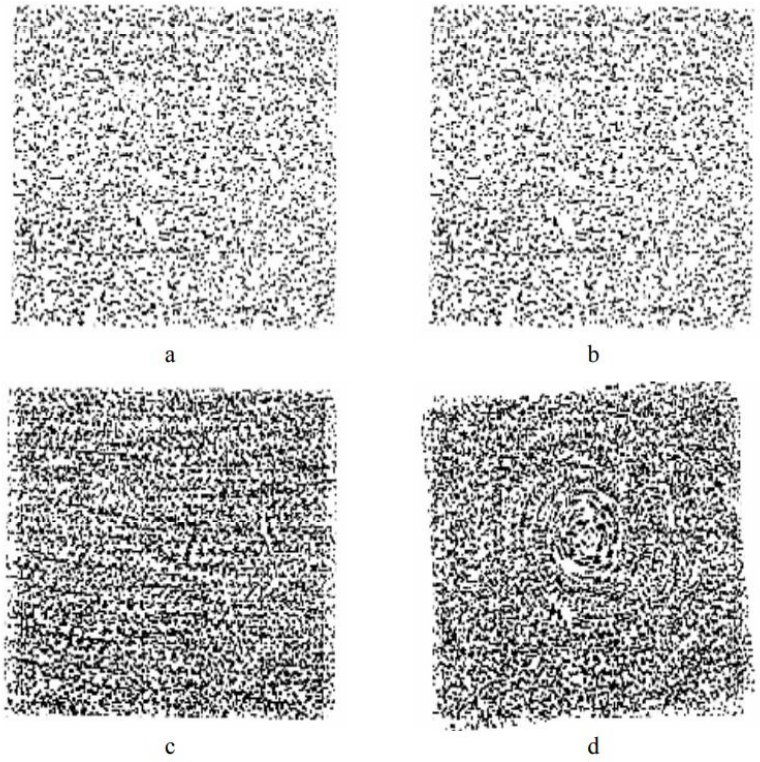

Figure 3.12. (a) and (b) are sample particle images. By translating a with respect to (b) and overlaying the two, a simulated translational shift is obtained and shown in (c). By rotating a with respect to (b) and overlaying the two, a rotational shift is obtained and shown in (d) [93]**.**

To obtain a quantitative two-dimensional vector field from such images, particle images must be systematically interrogated. To do so, these recorded images as abovementioned are sampled using an interrogation window (see Figure 3.13a, left), the dimensions of which determine the spatial resolution of the measurement. The interrogation regions can be adjacent to each other, or more commonly, have partial overlap with their neighbours that will allow for increased spatial resolution. The image subsamples, f(i,j) and g(i,j), are extracted at the same location within the images from the interrogation window (Figure 3.13a). Then, a cross-correlation procedure is performed on these two interrogated regions. Figure 3.13b shows a

cross-correlation algorithm. This procedure results in a cross-correlation distribution with the pixel domain within the interrogated regions with a dominant peak corresponding to the shift of the particles, (see Figure 3.13c and Figure 3.14) designated by (dx,dy). Lastly, the pixel shift (dx,dy) is converted into a velocity through calibration parameters (see Figure 3.13d). Details of these steps from a theoretical foundation to practical implementation are described in the following sections [93].

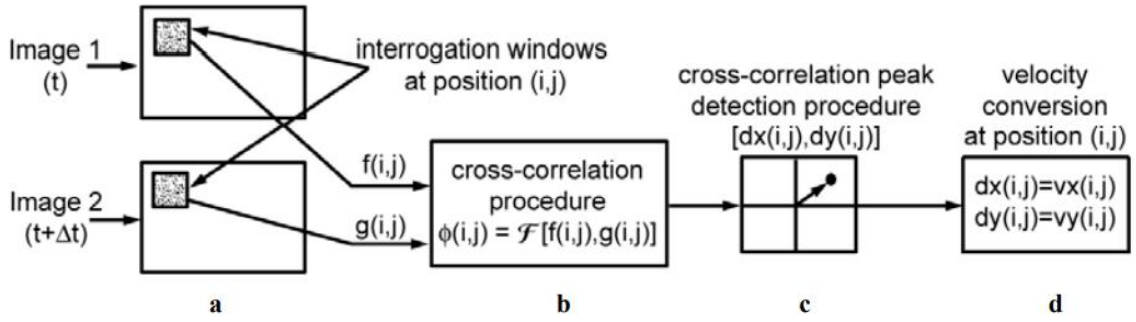

Figure 3.13: Cross-correlation data processing procedure [93]**. (a): An interrogation window subsamples the main sequential image pairs; (b): a cross-correlation procedure is performed; (c): within the cross-correlation domain, the peak's location corresponding to the average shift of particles within the interrogation windows is identified; (d): this shift is converted to physical space, providing a velocity vector.**

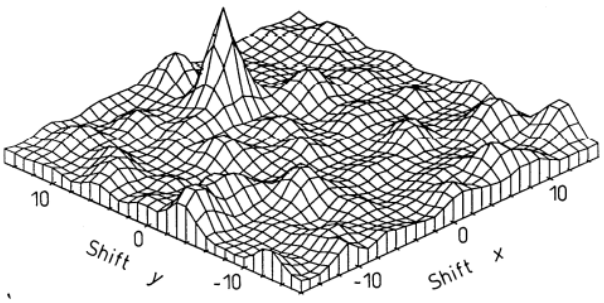

Figure 3.14. Sample cross-correlation peak showing single dominant peak corresponding to the magnitude and direction of particle shifts [93]**.**

In the experiments of this work an alternative approach was applied that is often used in blood flows. Instead of classic PIV, the method used in these experiments to produce displacement vectors and velocity fields, was brightfield μPIV configuration as in [94]. Instead of using seeding particles, RBCs were used as the tracer particles as in Kaliviotis et al [94]. Therefore, in these experiments the velocity field of the RBCs was examined rather than the suspending medium, as in other works [48].

The sample was placed horizontally on an upright microscope stage (OLYMPUS BX51). Images of the flow were recorded with a CMOS camera (IDT X3) attached on the microscope (10X-objective NA=0.25) (Figure 4.1) and analysed using JPIV (www.jpiv.vennemann-online.de), MatPiv and Matlab software. The spatial resolution of the optics was 1.65 μm/pixel. In this case, images instead of be taken in pairs like the classic PIV (i.e two images per time interval of lighter pulse), images are taken consecutively in the frequency of the CCD camera attached on the microscope. By cross correlation functions the location of each IW in the next frame is found. Hence again by considering time interval between two images found from the frequency of the camera on the microscope (instead of time interval between the two laser pulses as in classic PIV) and image magnification, velocity vectors are obtained for each IW.

3.6.1.1. Validation of the micro-PIV technique

In order to assess the validity of the μPIV technique three methods were used. A plate-plate system (CSS450 LINKAM SCIENTIFIC – for a diagrammatic representation see Figure 3.15) was placed horizontally on an upright microscope stage (OLYMPUS BX51). Images were captured with a CMOS camera (IDT X3, at 625 or 1250 fps) attached on the microscope (10X-objective NA=0.25). The velocity of RBCs in the plate-plate system was measured experimentally by using the μPIV approach and compared with the analytical solution for the particular flow. A thin film (~150 μm) of whole blood was applied on the bottom plate of the plate-plate system, which then was rotated at two different constant rotational speeds ($\omega = 0.13$ and 0.8 rad s^{-1}). The linear velocity of the plate at the area of observation is given by $v=\omega r$ for a range of radius r, from r=7.1mm to r=7.9mm and constant angular velocity ω. The captured images were analysed using JPIV (www.jpiv.vennemann-online.de), Matlab PIV and Matlab software. The spatial resolution of the optics was 1.65 μm/pixel.

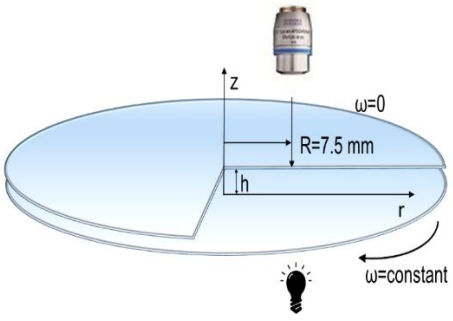

Figure 3.15. Schematic of plate-plate system.

In the second method, simple Couette flows were generated between the bottom and the upper plate of the system (with gap between plates h=100μm). The blood sample was placed between

the plates and the microscope was focused at a height of 50μm from the bottom plate. The bottom plate was rotated again at two angular speeds (ω = 0.13, 0.8 rad s^{-1}) and images where captured with the CMOS camera as described above.

Three passes with interrogation windows (IW) of height and width of 32, 16 and 8 pixels were used for the μPIV processing on the acquired images. Invalid vectors were replaced by the median of the neighbouring vectors. Displacement vector fields (2-D horizontal and vertical dimensions) of the images captured were produced from processing in Jpiv software. Then velocity vector fields were calculated using:

$$\mathrm{V} = \frac{\text{Pixel location in frame i} + 1 - \text{Pixel location in frame i}}{\text{frame i} + 1 - \text{frame i}} \qquad 3.4$$

Further velocity vector fields were converted from pixel/frame to μm/s by using:

$$\left(\frac{\mu\mathrm{m}}{\mathrm{s}}\right) = \mathrm{f}\left(\frac{1}{\mathrm{s}}\right) \times \mathrm{V}\left(\frac{\text{pixels}}{\text{frame}}\right) \times \mathrm{res}\left(\frac{\mu\mathrm{m}}{\text{pixel}}\right) \qquad 3.5$$

where f is the frequency which the images were images were captured i.e. f = 625/1250 fps and res is the spatial resolution i.e. res = $1.65\frac{\mu m}{pixel}$. Hence the velocity vectors were averaged spatially in the z-direction and temporally for the duration of the flow (ensemble averaging) using matlab software to yield the velocity profile. Brightfield micro-PIV techniques, however, suffer from relatively large depth of fields (D) [95] which lead to an underestimation of the velocity magnitude. Poelma et al [96] have shown that for relatively low magnifications in the μPIV set-up the velocity was found 33% lower than the actual flow velocity [96]. D can be estimated using the equation [97]:

$$D = 2\left\{\frac{\left(1-\sqrt{\varepsilon}\right)}{\sqrt{\varepsilon}}\left[\frac{n^2 dp^2}{4NA^2}\right] + \left[\frac{5.95(M+1)^2 L^2 n^4}{16M^2 NA^4}\right]\right\}^{\frac{1}{2}} \qquad 3.6$$

Where d_p is the particle diameter, L in the wavelength of illumination light, M is the image magnification, n is the refractive index of air and NA the numerical aperture of the lens. E is the relative threshold over which particles no longer contribute to the evaluation of displacement-correlation peak which normally takes the value of 0.01. Hence, it can be considered that the measured velocity information represents the mean velocity of RBCs in the depth D as the latter was calculated to be 99 microns.

The expected velocity profile for a narrow gap of h=50μm was also calculated analytically for the lower plate rotating at an angular velocity ω and the upper plate being stationary using the equation:

$$v = r\omega - \frac{z}{h} r\omega \qquad 3.7$$

with z = 50 μm, and r from 7.1 to 7.9mm. Therefore, the above equation provides the velocity values at each point in the radial direction, at z=50μm, which is the average theoretical velocity in the flow configuration.

Figure 3.16a and b compare the measured velocity profiles (using Jpiv software for analysis) against the theoretical one for the first validation method (thin film of blood rotating on plate), illustrating good qualitative agreement (velocity data have been normalized with their values at the centre of the flow). Absolute velocity values were lower than theoretical ones by ~ 10% and ~ 30% for the 0.13 and 0.8 rad s^{-1} angular velocities respectively. Figure 3.16c and d show the comparison between measured and analytical normalized velocities for the Couette flow developed in the gap of the shearing system.

The angular velocities were kept the same as in the previous test case, 0.13 and 0.8 rad s^{-1}, resulting in shear rates of 10 s^{-1} and 60 s^{-1}. The observed velocity underestimation using Jpiv software for analysis was ~ 20% and ~ 30% respectively. In addition, the observed velocity underestimation using MatLab Piv software for analysis was ~ 14.5% for plate angular velocity 0.8 rad s^{-1}.

The underestimation in the velocity magnitude calculated with the μPIV technique is ~30% maximum, in agreement with discrepancies reported in other studies [96]. The large depth of field, D, also means that the flow regions closer to the objective will contribute more to the PIV analysis, than the regions further away. The velocities in these regions are smaller (since they are closer to the top, fixed plate) which might further bias the measured (underestimated) velocities [96].

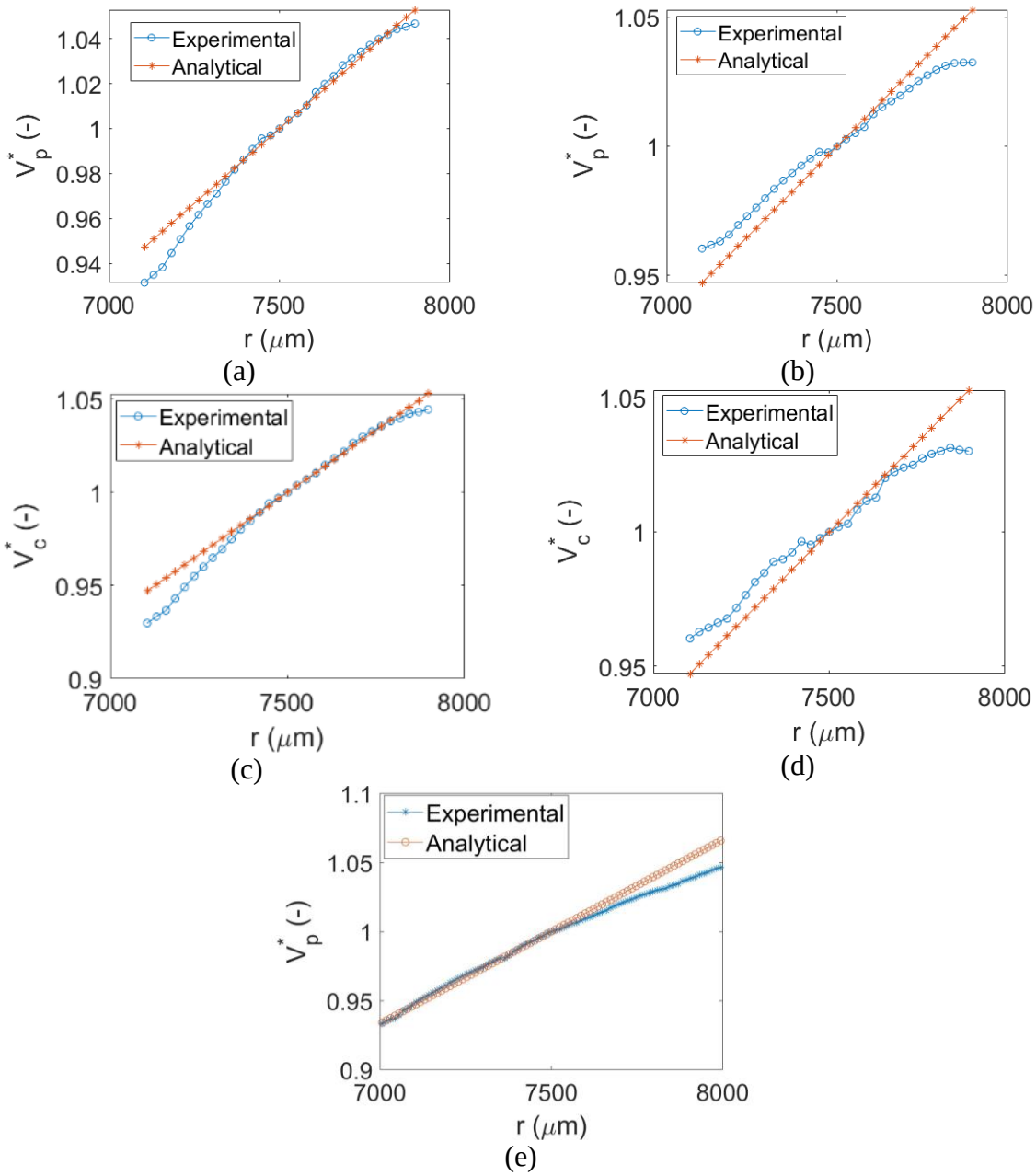

Figure 3.16. Experimental vs analytical velocities. Panel (a): V_p^* (normalised with velocity values at the centre of the flow) for whole blood rotating on the bottom plate (ω=0.13 rad/s) and (b): at ω= 0.8 rad/s. Absolute velocities differ by 10.30% and 30.52% respectively. V_c^* (normalised with velocity values at the centre of the flow) derived from the Couette flow at shear rates 10 s^{-1} (ω=0.13 rad/s) (c), and 60 s^{-1} (ω=0.8 rad/s) (d). Absolute velocities differ by 21.06% and 28.46 % respectively. (e): V_p^* for whole blood rotating on the bottom plate at ω=0.8 rad/s using Matlab Piv for analysis (absolute velocities differ by 14.5%).

In a third validation exercise, the velocity field of the Newtonian STD flow in a microchannel (AR~3.7) was measured, utilising a laser based micro-PIV technique using fluorescent particles

as tracers (Nile Red, ~1 μm size, at 1% concentration) suspended in distilled water, and compared against brightfield μPIV measurements (JPIV software) using milk particles as tracers in a 1:3 milk/water Newtonian solution. The experimental setup for the fluorescent μPIV experiments is also described in previous studies by Zhang *et al*. [98,99] The system comprised a 16 Hz Nd-YAG laser source at 532 nm (Litron Laser, UK) for illumination, and a CMOS camera (Xyla 5.5, Andor, UK) integrated on a bespoke microscope assembly (10X objective, NA = 0.28), for image acquisition. The spatial resolution of the technique was 0.56 μm/pixel and the depth of correlation was estimated to cover the entire flow depth.

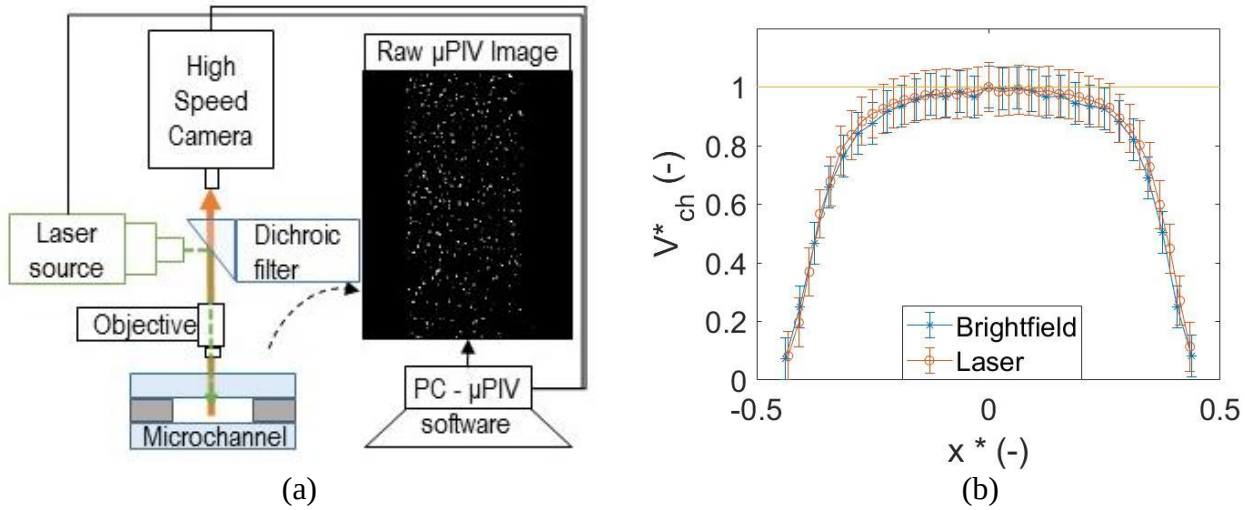

Figure 3.17. (a): Annotated schematic of the laser microPIV, and an enhanced raw PIV image. (b): Normalized velocity profiles of a Newtonian fluid flow measured with brightfield (blue stars) and laser micro-PIV (orange circles).

Figure 3.17a shows an annotated schematic of the laser based μPIV system, and b compares the measured velocity profiles (both profiles are normalized by the maximum measured velocity). Qualitatively the two profiles show very good agreement. The slightly increased bluntness of the velocity profile measured with the laser micro-PIV technique, could be attributed to technique-specific issues (differences in correlation depth, etc.). The decrease in the velocity gradient near the side-walls of the channel is mainly due to the non-uniformity of the side-walls of the channels (adhesive tape), in which existing micro-pockets created regions of persistently low velocity. Direct comparison of velocity magnitudes between the measurement techniques show a maximum difference of ~15% with the velocity in fluorescent μPIV being higher.

The Stokes number (St) of the tracer particles can be calculated from $St = \frac{t_p}{t_f}$, where t_p is the particle characteristic response time, given by $t_p = \frac{\rho_p d_p^2}{18 \mu_{NF}}$, with particle density ρ_p=1050 kg m^3, particle nominal diameter d_p=1μm and Newtonian fluid viscosity $\eta_{NF} \approx 1.5\ 10^{-3}$ Pa s (see later section 4.3 on viscosity measurements). T_f is a flow characteristic time defined as $t_f = \frac{d_h}{\bar{V}_{PIV}}$. $\bar{V}_{PIV}$ is the mean velocity of the flow, here calculated by the PIV technique and found to be in the order of 3 mm s^{-1}, and d_h is a characteristic diameter (hydraulic) of the channel equal to 150 microns. St was found to be in the order of 10^{-8}, indicating a negligible particle response time to the dynamics of the flow [100].

3.6.3. High resolution meniscus velocity characterization

The flow meniscus was tracked at the core of the channel from images captured using the CMOS camera (IDT X3, at 625 fps) attached on a microscope (10X-objective NA=0.25) (Figure 4.1 and 4.2) using matlab image processing algorithms. The meniscus position in the z-direction was found at each time-step, (see Figure 4.3 for the results from 45 images of a representative WB sample). The meniscus velocity V_m was then calculated by computing the distance covered by the meniscus (Δz) at each time-step (Δt): $V_m = \frac{\Delta L}{\Delta t}$, with $\Delta t = \frac{1}{625}$, based on the frame rate used in image capturing. The mean velocity, $\bar{V}_m$, of the advancing meniscus (Figure 4.3) was calculated as the average in the x-direction.

3.6.4. Meniscus velocity characterization in the whole channel

A side camera (JVC TK-C1380 colour, with a 60mm Panasonic lens) was introduced (Figure 5.1) in order to capture the meniscus flow in the microchannel. After the sample deposition and the initiation of the flow, the meniscus position was recorded with the side camera at a frame rate of approximately 20 fps (Figure 5.1). Hence from the images captured from the side camera meniscus flow was tracked using free tracker software package (https://www.rollapp.com/app/tracker). Therefore, the tracked time-dependent meniscus location (L_m) was fitted using a power law equation $L_m = Ct^n$ (R-square close to 1, C and n are constants) as shown in Figure 3.18a. The meniscus velocity as a function of time was derived by differentiating the position function $V_m = \frac{dL_m}{dt} = Cnt^{n-1}$ (Figure 3.18b), for all tests (n=10) and for the different samples. Figure 3.18c shows the results for the WB samples from all experiments (n =10) and their mean curve.

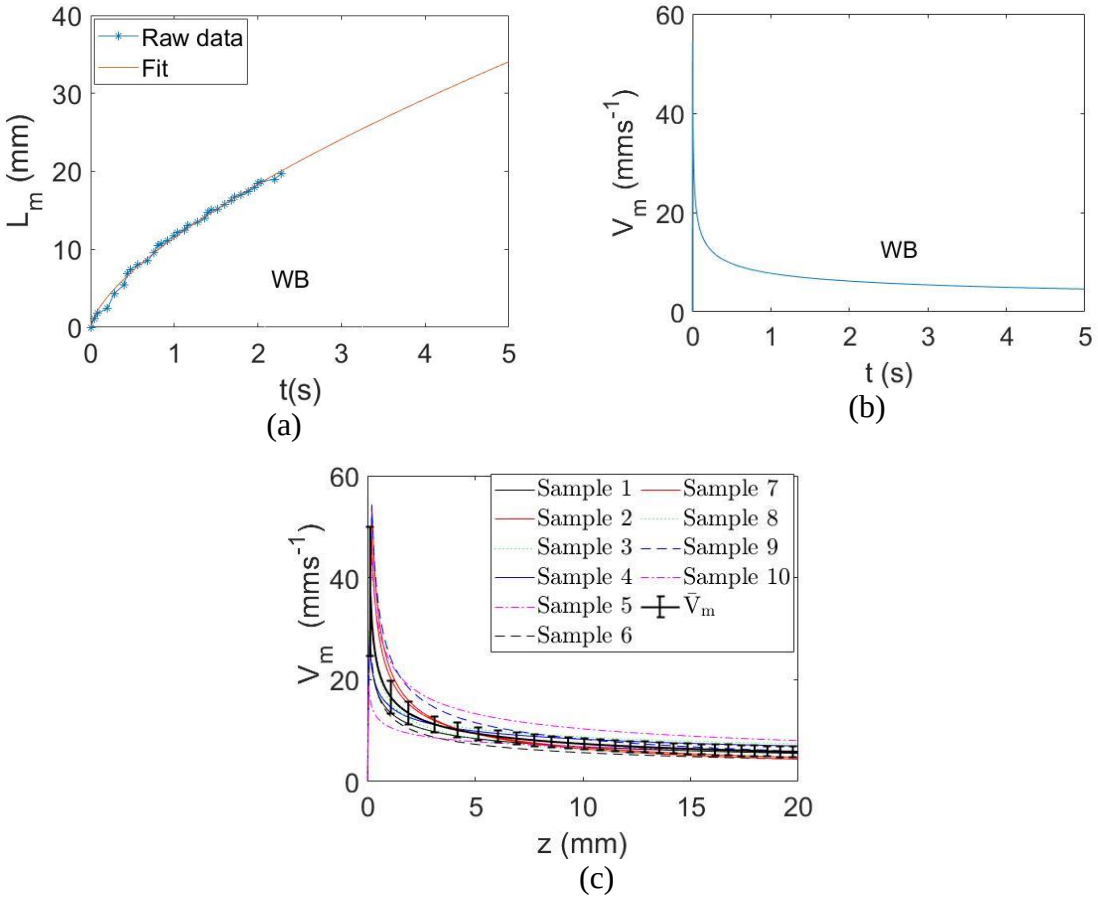

Figure 3.18. (a): Raw data from a representative sample of WB (symbols) with the fitted power law function L_m. (b): Mensicus velocity ($V_m = Cnt^{n-1}$) vs time for the WB sample. (c): Results for V_m as a function of position, for WB (10 tests from different donors) and their mean curve.

3.6.5. Shearing conditions

RBC aggregation is a shear and time dependent phenomenon and therefore it is of interest to estimate the shearing conditions in the channel. The shear rate magnitude in the microchannel can be evaluated from the individual shear strain components [101]:

$$|\dot{\gamma}| = [2(\frac{\partial u}{\partial x})^2+2(\frac{\partial w}{\partial z})^2+2(\frac{\partial v}{\partial y})^2+\left(\frac{\partial w}{\partial x}+\frac{\partial u}{\partial z}\right)^2+\left(\frac{\partial v}{\partial z}+\frac{\partial w}{\partial y}\right)^2+\left(\frac{\partial u}{\partial y}+\frac{\partial v}{\partial x}\right)^2]^{\frac{1}{2}}. \quad 3.8$$

If it is assumed that the u and v components are negligible (i.e. one-dimensional flow) and flow is fully developed ($\frac{\partial}{\partial z} = 0$) then the equation for $|\dot{\gamma}|$ becomes

$$|\dot{\gamma}| = [\left(\frac{\partial w}{\partial x}\right)^2+\left(\frac{\partial w}{\partial y}\right)^2]^{\frac{1}{2}} \quad 3.9$$

The first term (the in-plane shear rate component) can be calculated from the experimental velocity profile as follows; $\dot{\gamma}_{i\text{-}p} = \frac{\partial w}{\partial x} = \frac{dV_{ch}}{dx}$. The out-of-plane shear rate component ($\dot{\gamma}_{o\text{-}p} = \frac{\partial w}{\partial y}$) was estimated as $\frac{V_{max}}{H}$ where V_{max} is the maximum velocity in the experimental velocity profile (V_{ch}), and H the channel height (100μm in the channels used for this work).

3.7 Subjects of the study

Regarding the number and gender of the participants, it should be noted that females and males have differences in hemorheological properties (RBC aggregation, blood viscosity etc.) [102]. Therefore, for consistency researchers opt to utilise samples from a specific group of people. As regards the number of participants, studies report various populations. In the study of Shin etal., [103] 6 healthy volunteers (aged 25-40 males and females) were used and 30 repeated measurements on the aliquots of the same blood sample were performed to calculate the mean, standard deviation (SD) and CV of various aggregation parameters. In another [88] venous blood samples were obtained from 10 healthy male volunteers aged between 25 and 52 years were used. Ten (10) repeated measurements on the same sample form each donor were performed. In an earlier study [77] blood was taken from only one healthy volunteer and each experiment was performed 5 times.

In this study viscosity, deformability and aggregation measurements were performed using commercial instruments, and their effects were assessed in the surface tension driven microchannel flow. Blood from 10 different healthy volunteers of both genders (8 males and 2 females ages 27-44) was used in this study. It was aimed for 5 repetitions (similar to another study [77]) of each measurement (viscosity, deformability and aggregation) for each sample. The receptions were within one working day since after 6 hours blood properties are affected by change in blood composition [104] as aforementioned. Hence due to time restriction only 2 repetitions were performed for aggregation and viscosity measurements.

3.8 Ethical issues, sample collection and treatment

All experiments were performed according to the guidelines for hemorheological measurements as endorsed by the Endorsed by International Society for Clinical Hemorheology and European Society for Clinical Hemorheology and Microcirculation [Baskurt etal 2009 New Guidlines for the assesment of hemorheological parameters, Baskurt 2005 Guidlines for the assesment of hemorheological parameters, Journal of Clinical Pathology 1993;46:198-203, 1993, Journal of Clinical Pathology. PRACTICE GUIDELINE ICSH

recommendations for measurement of erythrocyte sedimentation rate. International Council for Standardization in Haematology (Expert Panel on Blood Rheology) [published erratum appears in J Clin Pathol 1993 May;46(5):488]]]

Volunteers prior to giving sample are given a form to read and understand the procedure which the sample will be taken. At least 24 hours' time is given to them to understand and ask questions about sample taking, the purpose of the experiment or any other relevant. Hence if they decide to participate they sign the participation form. Samples were acquired with the approval of the Cyprus Bioethics Committee (ref: ΕΕΒΚ/ΕΠ/2016/18). Blood was collected into vacuum tubes (BD) preloaded with 1.8 mg/ml EDTA from healthy volunteers. The working fluids tested in the present study were whole blood in its native state (WB), non-aggregative blood and aggregative blood suspensions. The non-aggregative blood samples (NAB) were prepared by washing RBCs twice in Phosphate Buffered Saline (PBS), centrifuging at 3600 rpm for 10 minutes, and re-suspending them in the PBS. Washed RBCs were suspended in Dextrans (500000-2000000 mw) to produce additional aggregative samples (termed DEX). Different hamatocrits (40% and 45%) were produced for the NAB and DEX samples by adjusting the fluid mediums (PBS or DEX solution) to the RBC volume. Portions of the five aforementioned working fluids (WB, DEX 45%, DEX 40%, NAB 45%, NAB40%) were inserted in a water bath for heat treatment at 50 ^{o}C for 7 minutes, in order to alter the deformability of the RBCs, similarly to previous studies [79]. Newtonian flows were also examined by producing a Newtonian fluid (NF) using milk/water solutions (1:3 concentrations respectively).

CHAPTER 4. Haemodynamics in the rectangular straight microchannel*

In the following chapters of the thesis the results from all aspects of work in the PhD program will be presented. In Chapter 4 the part of the work elaborating on the haemodynamics in the STD flow of aggregating, non-aggregating RBC, and Newtonian suspensions, in a rectangular straight microchannel is presented. Some additional methodological aspects, specific to the work are also given in more detail.

The velocity fields were obtained using micro-PIV techniques (described in section 3.6.1) and an analytical solution for blood velocity in the channel was developed utilising the Power Law model for blood viscosity. Velocity fields were produced, and the velocity profiles at the beginning and at the end of the flow were derived to examine the effect of aggregation on the velocity profiles. The meniscus position in the microchannel, and the mean velocity in the core were derived using specialised algorithms (Matlab and other software, described in section 3.6.3) and compared with the developed analytical solution for blood velocity.

The structural characteristics of the samples were examined by utilising specialised algorithms developed to give an index of aggregation during the flow (as explained in section 3.4). Viscosity measurements were performed using a Brookfield DVIIT instrument in order to examine the effect on aggregation on fluid viscosity (Section 3.5).

4.1 Sample Preparation

For these experiments, five (5) blood samples were acquired from healthy volunteers into 4ml vacuum tubes (BD) preloaded with 1.8 mg/ml EDTA. Whole blood (WB) was used for aggregating blood experiments whereas non-aggregative blood samples (NAB) were produced at a haematocrit of 45% as explained in section 3.8. The consistency of the tests was examined by duplicating/triplicating tests where appropriate. Newtonian flows were also examined using

* Part of the work presented in this section has been published in the journal Physics of Fluids:

Pasias D., Passos A., G. Constantinides, Balabani S. and Kaliviotis E. (2020). Surface tension driven flow of blood in a rectangular microfluidic channel: effect of erythrocyte aggregation. ***Physics of Fluids***, 32, 071903 (2020); https://doi.org/10.1063/5.0008939.

The above publication has been selected as the Editors Peek for the specific issue.

Newtonian Fluids (produced as explained in section 3.8). Milk particles where used as tracers for the μPIV-based analysis of NF, as in previous studies [105].

4.2 Experimental set up

Figure 4.1 shows a schematic of the experimental setup used for the initial experiments, utilizing the brightfield μPIV system. The microchannel was constructed as described in section 3.2.1 and it was placed horizontally on an upright microscope stage (OLYMPUS BX51) as described in section 3.6.1.

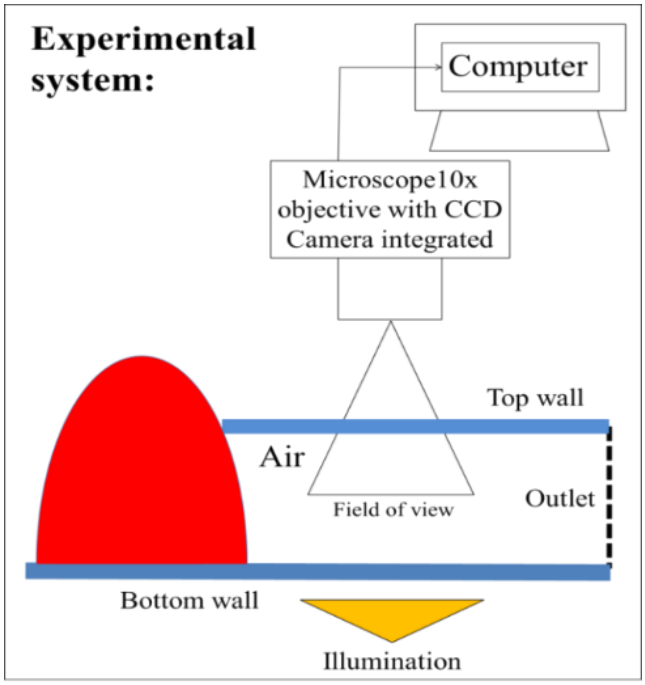

Figure 4.1. Annotated schematic of the capillary driven micro channel flow, and the μPIV measurement set up: the gap (2h) between the top and bottom walls of the channel was 100 μm, respectively (diagram not to scale) [106].

Sample images of the surface tension driven microchannel flows of WB and NF, at different time points are shown in Figure 4.2 together with the region of interest (where the μPIV analysis was performed) and the schematic showing the dynamic contact angle. The angle that the marching meniscus forms with the side walls of the channel (the adhesive tape) is the dynamic contact angle, denoted by θ_d, which is also an index of wettability [86].

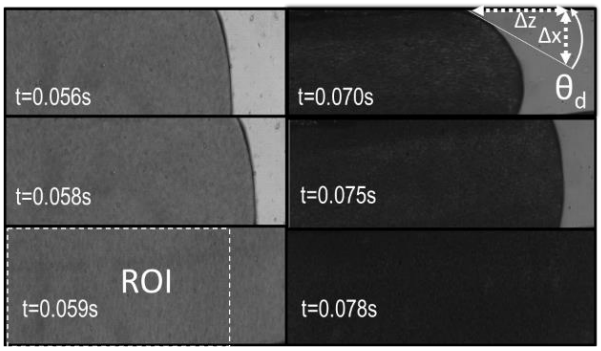

Figure 4.2. Images of drops from the Newtonian fluid are shown in the left panels and of the NAB in the right panels, and whole blood Dynamic contact angle θ_d (in degrees) as a function of time.

Dynamic contact angle was calculated for the initial stages of the flow (approximately 0.07 seconds and L ~ 1.7mm, z* = L(z) / 1.7), where the meniscus z position was found at each frame, using Matlab image processing algorithms. Figure 4.3 illustrates the meniscus shape from 45 images of a representative WB sample).

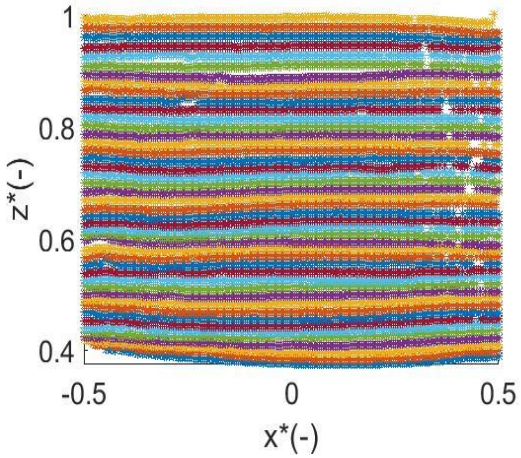

Figure 4.3. Typical meniscus distance from the entrance of the channel vs width of the channel.

A best line of fit was created at the meniscus profile close to the side-wall (Figure 4.4), and θ_d was evaluated using: $\theta_d = \tan^{-1}\frac{\Delta x}{\Delta z}$. The meniscus is seen, to have a slight paraboloid, or even a uniform shape, due to the non-hydrophilic properties of the side walls (double sided adhesive tape).

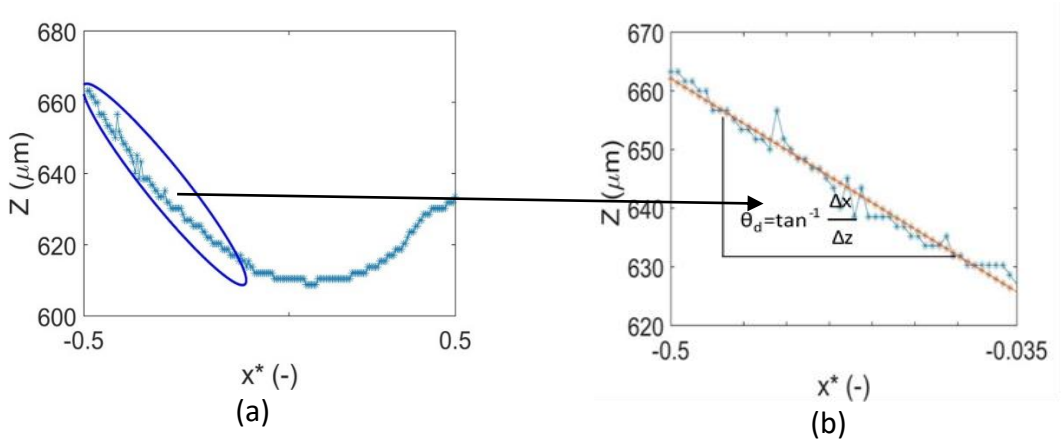

Figure 4.4. (a): Advancing meniscus velocity profile at a random time-step. (b): Points of meniscus curvature with their best fit line.

Figure 4.5a shows a representative dynamic contact angle θ_d against time, illustrating that the meniscus profile becomes nearly flat as the dynamic contact angle reaches ~85^o very shortly.

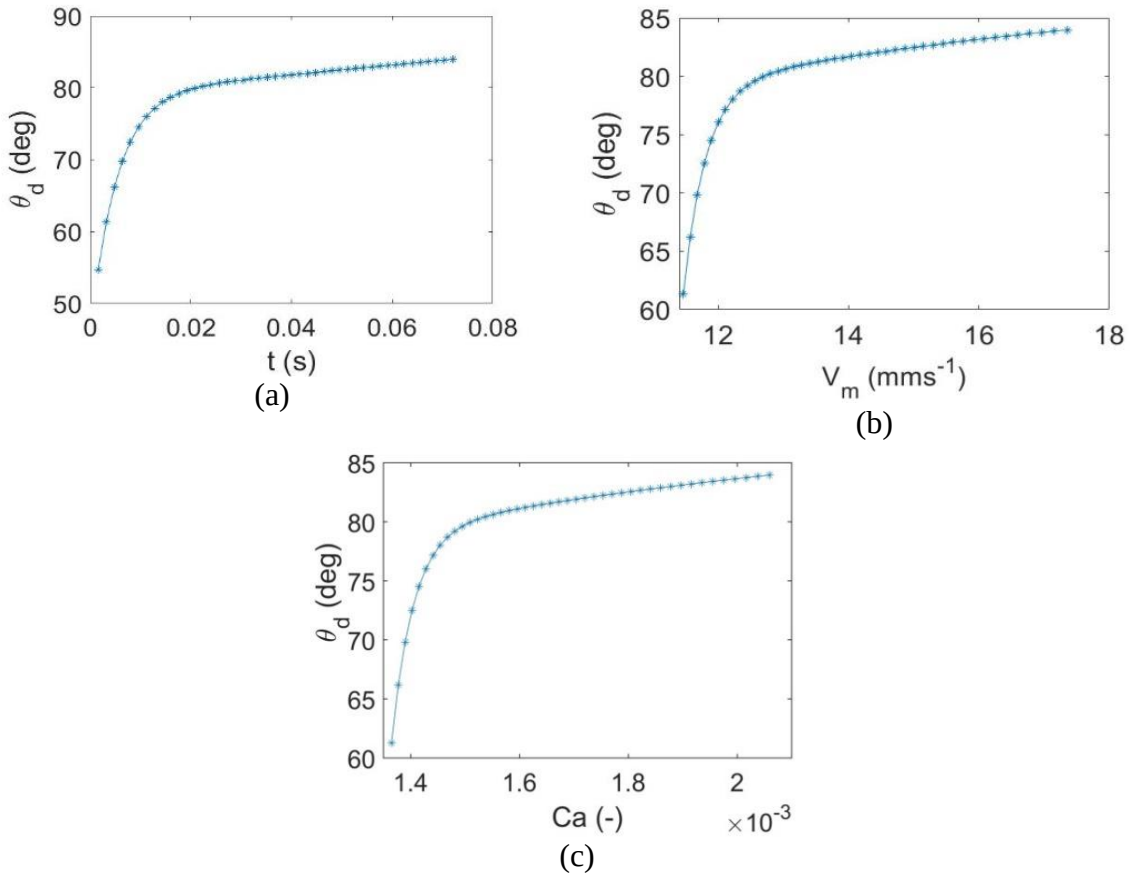

Figure 4.5. (a): θ_d vs time (b): θ_d vs marching meniscus velocity and (c): θ_d vs capillary number.

The hydrophobicity/neutrality of the side boundaries does not promote the meniscus flow, which is driven by the surface tension forces developed at the top and bottom boundaries; it

should be noted that the top/bottom dynamic contact angles could not be measured in the current set-up.

The capillary number $Ca = \frac{\mu \bar{V}_m}{\sigma}$ (where μ is the dynamic viscosity, $\bar{V}_m$ is mean meniscus velocity and σ the surface tension), represents the relative effect of viscous forces versus surface tension acting across an interface between a liquid and a gas, or between two immiscible liquids [107,108]. In Figure 4.5b, θ_d is shown as function of $\bar{V}_m$ and in Figure 4.5c as a function of the capillary number. However, since WB is a Non-Newtonian fluid the value of μ used for Ca calculation, was a constant value of μ, at the mean shear rate on which WB viscosity was tested (explained in the later section 4.3). θ_d increases proportionally with the rate of change of velocity in the beginning of the flow, and hence Ca reaching a nearly flat profile (θ_d~90^o) agreeing with the experimental data of other works [107]. This might be due to the initial capillary forces that drive the meniscus being very high (much higher than viscous forces impending the flow as illustrated on Figure 4.5c, where Ca is very small). These forces accelerate the flow [81,109,110], and hence result to forcing the flow of RBCs along the boundaries [29,30], countering the impending flow conditions there. As a result, a nearly flat meniscus profile with contact angle close to 90 degrees appears in the measurements.

4.3 Sample Viscosities

Viscosity measurements were performed, utilising a Brookfield DVIIT instrument as explained in section 3.5. Viscosities were measured by ramping down shear rates from 400 to 12.5 s^{-1}. Moreover, a power law model was used to fit the data from the viscosity measurements ($\mu_{P\_L} = k\dot{\gamma}^{n-1}$) [111].

Viscosity curves of the three working fluids are shown in Figure 4.6 for shear rates ranging from 12.5 s^{-1} to 400 s^{-1}. As expected, WB exhibits a shear thinning behaviour mainly due to RBC aggregation. The non-aggregating sample (RBCs in PBS medium) exhibits a smaller decrease in viscosity with increasing shear rate, which is mainly due to the deformation of RBCs. The viscosity of NF is effectively constant at ~1.68 mPa s.

The power law viscosity model ($\mu_{P\_L} = k\dot{\gamma}^{n-1}$) was used to fit the viscosity data for both the WB and NAB blood suspensions, similarly to other studies [111]. The consistency indices *k* and the exponent *n* for the WB and NAB cases are shown in Table 4.1 and are in agreement with reported values in the literature [111].

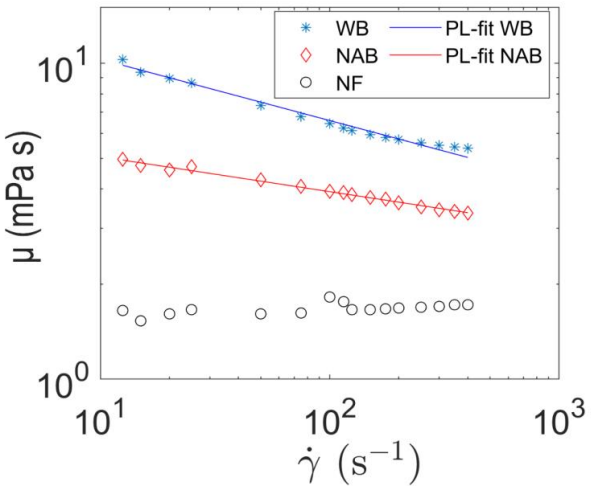

Figure 4.6 Viscosity of WB (blue stars), NAB (red diamonds) and NF (black circles) at shear rates from 12.5 s^{-1} to 400 s^{-1}.

Power law coefficients and R^2 values of blood samples.			
Sample	k [mPa s^n]	n [-]	R^2
WB	26.200	0.302	0.973
NAB	7.134	0.123	0.991

Table 4.1 Power law coefficients and R^2 values of blood samples.

4.4 Analytical solution for the mean meniscus velocity

The theoretical mean axial (z-direction) meniscus velocity in STD flows can be calculated analytically as in previous studies [51,112], using the incompressible Navier-Stokes (N-S) equations, under the assumptions that the flow is fully developed, and one-dimensional, influenced mainly by the smaller dimension of the geometry (i.e. the height, 2h, of the channel, in the y direction for the coordinate system chosen for this study – please see Figure 3.1). The latter is due to the smaller radius of the meniscus curvature in the y-direction, compared to the one in the width direction (x). Under these assumptions, the continuity and z-momentum equations in the N-S equations reduce to:

$$\frac{\partial V_{z\text{-}\sigma}}{\partial z} = 0 \qquad 4.1$$

and

$$-\frac{1}{\rho}\frac{\partial P}{\partial z}+\frac{\mu}{\rho}\frac{\partial^2 V_{z\text{-}\sigma}}{\partial y^2}=0 \qquad 4.2$$

μ is the dynamic viscosity of the fluid, and $\partial P = P_1 - P_0$ is the differential pressure difference. However, since the chancel is open ended P_1 is equal to atmospheric pressure resulting to $\partial P = -P_0$ leading to $\frac{\partial P}{\partial z} = \frac{-P_0}{L}$. L is the meniscus position from the entrance. ∂P can be approximated with the Young-Laplace pressure drop**:**

$$\Delta P = \sigma\left(\frac{1}{R_1}+\frac{1}{R_2}\right) \qquad 4.3$$

R_1 and R_2 are the radii of curvature on the top and side walls of the channel respectively. As mentioned above, due to the high aspect ratio of the channel, the radius of curvature along the width W is much higher, compared to that along the height 2h, hence the term $1/R_2$ is small compared to $1/R_1$ and considered negligible. This assumption results to $\Delta P_{Y\text{-}L} = \frac{2\sigma\cos(\theta_c)}{2h}$ and therefore:

$$-\frac{\partial P}{\partial z} = \frac{\sigma\cos(\theta_c)}{hL} \qquad 4.4$$

Inserting Eq.4.4 into Eq.4.2:

$$\frac{\sigma\cos(\theta_c)}{hL}+\mu\frac{\partial^2 V_{z\text{-}\sigma}}{\partial y^2}=0 \qquad 4.5$$

Integrating Eq.4.5 once, and applying the condition $\frac{\partial V_{z\text{-}\sigma}}{\partial y} = 0$ at y = 0, for a velocity maximum at the centre of the channel yields: $\mu\frac{\partial V_{z\text{-}\sigma}}{\partial y} = -\frac{\sigma\cos(\theta_c)}{hL}y$. By using the power law shear stress $\mu\frac{\partial V_{z\text{-}\sigma}}{\partial y} = k\left[\frac{\partial V_{z\text{-}\sigma}}{\partial y}\right]^n$ the equation becomes $k\left[\frac{\partial V_{z\text{-}\sigma}}{\partial y}\right] = -\left(\frac{\sigma\cos(\theta_c)}{hkL}\right)^{1/n}$ and can be solved using the no-slip boundary condition at the wall $V_{z\text{-}\sigma} = 0$ at y = h:

$$V_{z\text{-}\sigma} = \left(\frac{n}{n+1}\right)\left[\frac{\sigma\cos(\theta_c)}{khL}\right]^{\frac{1}{n}}\left[h^{1+\frac{1}{n}} - y^{1+\frac{1}{n}}\right] \qquad 4.6$$

For n=1, the parabolic Newtonian profile is recovered. The flow rate can be calculated from the velocity profile $V_{z\text{-}\sigma}$:

$$Q = 2W\int_0^h V_{z\text{-}\sigma}dy \;=\; 2W\left(\frac{n}{n+1}\right)\left[\frac{\sigma\cos(\theta_c)}{khL}\right]^{\frac{1}{n}}\left[h^{\frac{2n+1}{n}}\;(1-\frac{n}{2n+1})\right] \qquad 4.7$$

The mean velocity in the core of the flow can be calculated as $V_{mean} = Q / hW$:

$$V_{mean} = \left(\frac{n}{n+1}\right)\left[\frac{\sigma\cos(\theta_c)}{hkL}\right]^{\frac{1}{n}}\;\left[h^{\frac{n+1}{n}}\;(1-\frac{n}{2n+1})\right] \qquad 4.8$$

Assuming that the mean velocity of the meniscus (V_m) is equal to the mean velocity in the core of the flow (i.e. $V_m = V_{mean}$), the meniscus position as a function of time (L=L(t) can be estimated using:

$$\frac{dL(t)}{dt} = V_{mean} \qquad 4.9$$

Therefore, by integrating Eq.4.9 with respect to t,

$$L(t) = h\left[\frac{\sigma\cos(\theta_c)}{hk}\right]^{\frac{1}{n+1}}\left[1-\frac{n}{2n+1}\right]^{\frac{n}{n+1}}\;t^{\frac{n}{n+1}} \qquad 4.10$$

The time dependent marching meniscus velocity can be estimated analytically from the position L(t):

$$V_{m\text{-}an} = \frac{dL(t)}{dt} = h\,t^{\left(\frac{-1}{n+1}\right)}\;\left[\frac{\sigma\cos(\theta)}{kh}\right]^{\frac{1}{n+1}}\;\left[\frac{n}{n+1}\right]\left[1-\frac{n}{2n+1}\right]^{\frac{n}{n+1}} \qquad 4.11$$

The solution for the mean meniscus velocity (V_{m-an}) is similar to other solutions in the literature [51] for the flow in the circular capillary duct.

4.5 Analytical solution for the two-dimensional velocity profile in the core of the flow

The mean meniscus velocity was derived in the previous section based on Eq.4.8, assuming negligible influence from the side boundaries (i.e., $V_{z\text{-}\sigma} = V_{z\text{-}\sigma}(y)$). For the analysis of the velocity field in the core of the flow, however, a complete analytical solution in both x and y directions is required for comparison with the experimental data. The 2-dimensional analytical solution for the velocity of pressure-driven flows in straight rectangular microchannels exists for a Newtonian fluid [112].

The equation solution for the velocity of the pressure-driven flows in straight rectangular microchannels for Newtonian fluid was derived from the Navier-Stokes equations for steady state Poiseuille-flow [112].

The boundary conditions are: $V_z = 0$ at the boundary i.e. $V_z = 0$ at $x = \pm w/2$, $y = 0$, $y = h$. The Navier-Stokes equation for steady state Poiseuille-flow with associated boundary conditions is given by:

$$\left(\frac{\partial^2}{\partial x^2} + \frac{\partial^2}{\partial y^2}\right) V_z = -\frac{\Delta P}{nL} \qquad 4.12$$

for, $-w/2 < x < w/2$ and $-h < y < h$. where Δp is the pressure drop along length L and n is the viscosity. Since the flow was surface tension driven Young-Laplace Eq.4.3 was used for Δp, for high channel aspect ratio; the radius of curvature along the width is much higher as compared to that along the height. $1/R_2$ was therefore considered negligible similar to the aforementioned study [62]. Hence, Δp can be expressed as:

$$\Delta p = \frac{2\sigma\cos\theta}{2h} = \frac{\sigma\cos\theta}{h} \qquad 4.13$$

Inserting 4.13 to 4.12:

$$\left(\frac{\partial^2}{\partial x^2} + \frac{\partial^2}{\partial y^2}\right) V_z = -\frac{\sigma\cos\theta}{nhL} \qquad 4.14$$

Hence, all functions in the problem were expanded as Fourier series along the short vertical y direction. In order to make sure that the boundary conditions V_z (x,-h) = V_z (x, h) = 0 are satisfied, only terms proportional to $\sin(n\pi z/h)$, where n is a positive integer were used.

Expanding the right-hand side of Eq.4.14 results to a series containing only odd integers n.

$$-\frac{\sigma\cos\theta}{nhL} = \frac{\sigma\cos\theta}{nhL}\frac{4}{\pi}\sum_{n,odd}^{\infty}\frac{1}{n}\sin\left(n\pi\frac{y}{2h}\right) \qquad 4.15$$

The coefficients $f_n(x)$ of the Fourier expansion in the y co-ordinate of the velocity are constants in y, but functions of x, and hence,

$$V_z(x,y) = \sum_{n=1}^{\infty} f_n(x) \sin\left(n\pi \frac{y}{2h}\right) \quad 4.16$$

Inserting Eq.4.16 in the left-hand side of Eq.4.14 leads to:

$$\left(\frac{\partial^2}{\partial x^2} + \frac{\partial^2}{\partial y^2}\right) V_z = \sum_{n=1}^{\infty} [f_n''(x) - \frac{n^2\pi^2}{4h^2} f_n(x) \sin\left(n\pi \frac{y}{2h}\right)] \quad 4.17$$

A solution to the problem must fulfil that for all values of n, the nth coefficient in the pressure term Eq.4.15 must equal the nth coefficient in the velocity term in Eq. 4.17. The functions $f_n(x)$ are therefore given by:

$$f_n(x) = 0 \text{ for n even} \quad 4.18$$

$$f_n''(x) - \frac{n^2\pi^2}{4h^2} f_n(x) = -\frac{\sigma\cos\theta}{nhL} \frac{4}{\pi} \frac{1}{n} \text{ for n odd} \quad 4.19$$

Then by solving the inhomogeneous second-order differential Eq.4.19 results to the solution for $f_n(x)$ that satisfies no-slip boundary conditions $f_n\left(\pm\frac{w}{2}\right) = 0$:

Hence the solution for the velocity along the channel width (w) and height (2h) is resulting to:

$$V_{z-c}(x,y) = 16h^2 \frac{\sigma\cos\theta}{\pi^3\mu hL} \sum_{n,odd}^{\infty} \frac{1}{n^3} \left[1 - \frac{\cosh\left(n\pi\frac{x}{2h}\right)}{\cosh\left(1-n\pi\frac{w}{4h}\right)}\right] \sin\left(n\pi \frac{y}{2h}\right) \quad 4.20$$

where μ is the dynamic viscosity [113].

The value of L can be set from the experimental data or from Eq.4.10 above, and will affect the behaviour of $V_{z\text{-}c}$ quantitatively. The analytical solution $V_{z\text{-}c}$ will be used to assess the deviation of the experimental velocity profiles from the Newtonian behaviour. The viscosity values used were 1.68, 4.41 and 8 mPa s, i.e. the mean values for the NF, NAB and the WB samples respectively.

4.6 Pressure-viscosity ratio

The main factors influencing the velocity of the flow are the surface tension σ, the viscosity of the fluids μ, and the wettability of the top-bottom channel surfaces quantified by the contact angle θ_c. Surface tension σ and wettability (contact angle θ_c) can be used to calculate the Young-Laplace pressure difference $\Delta P_{Y\text{-}L}$ using $\Delta P_{Y\text{-}L} = \frac{\sigma\cos(\theta_c)}{h}$. The ratio $\Delta P_{Y\text{-}L}/\mu$ could

provide meaningful information about the interrelationships between the aforementioned factors.

Young-Laplace pressure and pressure/viscosity ratio for the three working fluids.					
Sample	σ (Nm^{-1})	θ_c (^{o})	μ (mPa s)	ΔP_{Y-L} (Pa)	$\Delta P_{Y-L} / \mu$ (s^{-1})
WB	0.020	38	8	315.2	$39.4\ 10^3$
NAB	0.023	36	4.41	372.1	$84.4\ 10^3$
NF	0.022	44	1.68	316.5	$188.4\ 10^3$

Table 4.2. Young-Laplace pressure and pressure/viscosity ratio for the three working fluids.

Table 4.2 shows that the pressure/viscosity ratio is found to be higher in the NF fluid ($188.4\ 10^3\ s^{-1}$), compared to NAB and WB ($84.4\ 10^3$ and $39.4\ 10^3\ s^{-1}$ respectively). Thus, the flow of NF is expected to be favoured compared to the other fluids, with WB been affected mostly by the higher viscosity. Table 4.2 also shows the measured and aforementioned quantities in comparison.

4.7 Meniscus velocity

The meniscus velocity (V_m) was calculated for the initial stages of the flow until approximately 0.07 seconds, and L between 0.68 and 1.7 mm as explained in section 3.6.4. The mean velocity, $\overline{V}_m$, of the advancing meniscus (Figure 4.3) is shown in Figure 4.7 (black rectangles) against the analytical solution $V_{m\text{-}an}$ (solid blue line). The experimental parameters n, k, σ, h and θ_c (Table 4.1 and Table 4.2) have been used in $V_{m\text{-}an}$ for the WB sample in Figure 4.7. Figure 4.7 shows that the flow accelerates during the initial observation time (~ 0.07 s). This acceleration is mainly due to the capillary forces, which dominate over other competing, mainly viscous, forces at the initial stages of the flow. This initial flow acceleration has been confirmed by previous numerical and experimental studies in the literature [81,109,110].

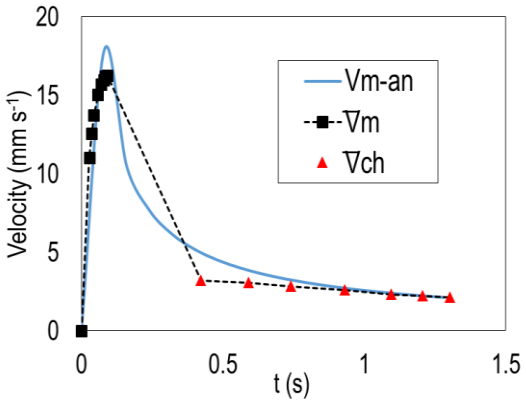

Figure 4.7. Mean velocity values, $\bar{V}_m$ (black rectangles) and $\bar{V}_{ch}$ (red triangles) as a function of time. The solid blue line represents the analytical solution $V_{m\text{-}an}$ (Eq.4.11), with first non-zero value at 0.08 s. The black dashed line connects the experimental data (not a fitted line). Data produced from a representative.

It should be noted here, that the analytical solution for the meniscus velocity ($V_{m\text{-}an}$ in Eq.4.11), can capture the initial acceleration observed in the present, and in other studies, only due to the initial zero velocity value at time t = 0: for very small, but non-zero, values of time, the velocity magnitude will be substantially elevated to infinite values, as it is inversely proportional to this variable. For plotting purposes of $V_{m\text{-}an}$ in the present case the choice of the initial time point after the zero value (t=0.08 s) was made to avoid infinite velocities.

The dominance of the surface tension forces in the initial part of the flow is indicated by the capillary number, which was estimated using the high shear viscosity ($\mu \approx 0.006$ Pa s, Figure 4.6), a mean value of 14 mm s^{-1} (from the meniscus velocity $\bar{V}_m$ in the initial stages of the flow -Figure 4.7) and the surface tension σ for WB (0.020 Nm^{-1}): $Ca = \frac{\mu \bar{V}_{m\text{-}mean}}{\sigma} = 4.2\ 10^{-3}$. There are other forces which potentially contribute to this initial transient behaviour. The fluid drop volume placed at the entrance of the channel was considerably larger than the channel volume (50 μL to 0.3 μL, respectively) and the diameter of the droplet was approximately 6 mm. Therefore, it is reasonable to expect that an extra, albeit small, surface tension-dependent pressure contribution exists, due to the formed drop at the entrance [4,114]. Furthermore, a height difference (~ 3 mm) between the centres of the channel and the blood drop imply a slight hydrostatic pressure contribution (typically negligible). The aforementioned forces although negligible may contribute positively to the flow and may explain the meniscus acceleration during the initial stages of the flow in this particular case and in general.

When deriving the analytical solution for the meniscus velocity $V_{m\text{-}an}$ (Eq.4.11) it was stated that the mean velocity in the core of the flow ($\overline{V}_{ch}$) should be equal to the meniscus velocity ($\overline{V}_{m}$). $\overline{V}_{ch}$ was calculated from the μPIV-measured velocity profiles (the velocity profiles, V_{ch}, are presented in the next section). $\overline{V}_{ch}$ is a good approximation of the meniscus velocity, and was calculated by integrating the velocity profile along the x direction, divided by the width of the channel: $\overline{V}_{ch}=\frac{1}{W}\int_{-W/2}^{W/2} V_{ch}\,dx$. $\overline{V}_{ch}$ was compared to the analytical solution V_{m-an} for the meniscus velocity in the graph of Figure 4.7 (red triangles). Quantitative differences exist between the experimental observations and analytical solution, however, a very good agreement is observed for times beyond 1s.

4.8 Velocity profiles in the core of the flow

Velocity profiles were extracted from the measured velocity vectors, within the region of interest shown in Figure 4.2. The velocity vectors were averaged spatially in the z-direction and temporally for the duration of the flow (ensemble averaging) to yield the velocity profile. The resulting velocity profiles (V_{ch}) are shown in Figure 4.8 for all the fluids tested. All profiles have been normalised with their maximum values ($\overline{V}^{*}_{ch}$) and the Newtonian analytical solution $V_{z\text{-}c}$ (Eq.4.20) is also included for comparison. In general, the velocity profiles in the core of the flow followed the expected paraboloid behaviour for all the fluids investigated, due to the no-slip conditions at the boundaries, in agreement with other capillary- and pressure-driven microfluidic studies [4,32,39]. Zero velocity at the side-walls has been assumed, and the velocity profiles in Figure 4.8 have been extended to this value.

In Figure 4.8a the ensemble average profiles have been calculated for the whole duration of the test (~1.6 s) and as the figure illustrates no significant differences exist between the cases. A difference, however, is apparent between the experimental and the analytical curves. Panels b, c, and d in Figure 4.8 show the ensemble average of the velocity profiles for different time periods in the flow.

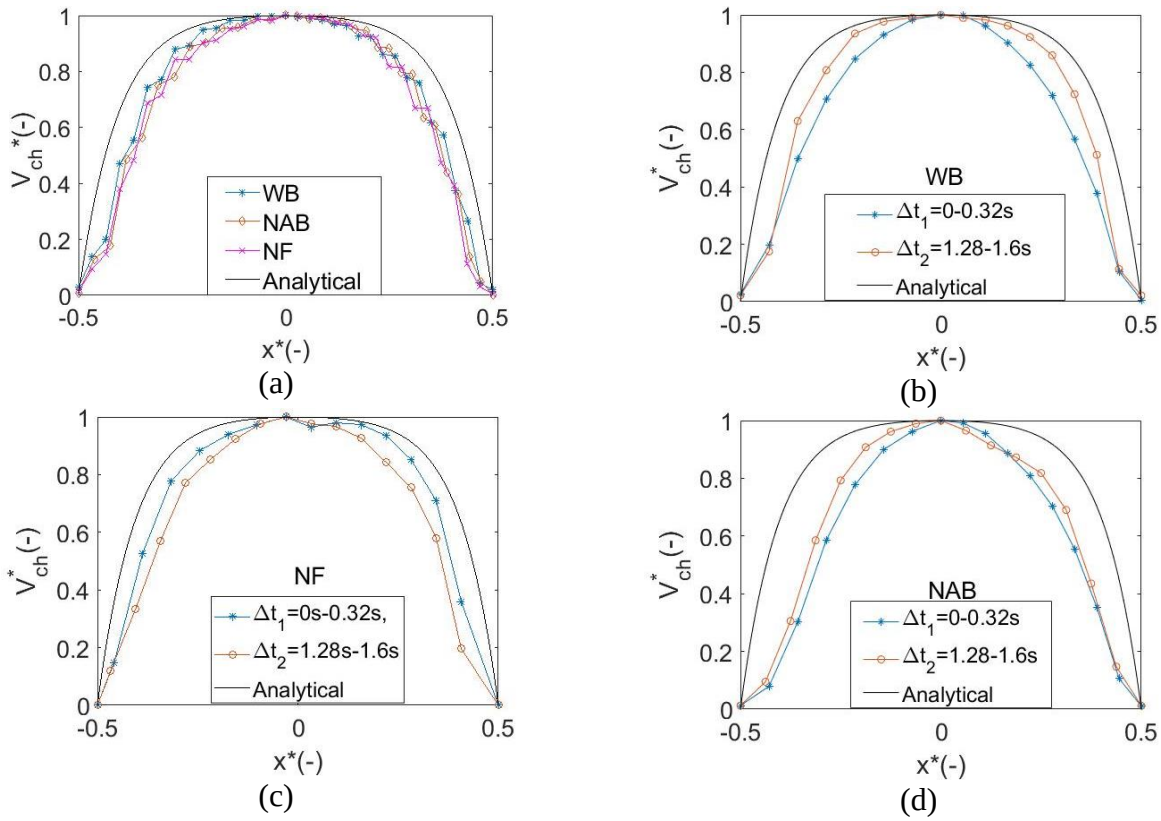

Figure 4.8. Normalized velocity profiles for WB, NAB, and NF samples at a microchannel aspect ratio of 3.5 at Δt_1 and Δt_2. (a): Ensemble average of the profiles of all samples for the whole duration of the flow. (b, c and d): Results for WB, NAB, and NF samples respectively for different time periods in the flow (Δt_1 and Δt_2). The analytical solution is also shown in all graphs for comparison. A zero velocity at the side walls has been assumed in all profiles. The analytical solution is also plotted for comparison.

As Figure 4.7 illustrates the velocity of the fluids decreases with time and therefore it is of interest to assess any time influence on the velocity profile, as it is well known that RBC aggregation is a time and shear-depended phenomenon [115]. The velocity profile calculated by the analytical solution is used as the reference condition. Inspecting the WB case (panel Figure 4.8b) it is observed that the profile for the late time period (Δt_2) is blunter, when compared to the one calculated at an earlier time period Δt_1. The difference is significant for part of the channel width, and can be explained by the influence of the red blood cell aggregation phenomenon which is more intense at the lower shearing conditions. For the non-Newtonian fluids, the shearing forces are proportional to the velocity gradient in the flow in a non-linear manner (the power law model used in this study is an example) resulting in higher flow resistance at regions of lower shear. Smaller differences between the profiles at the

different time periods (Δt_1 and Δt_2) are observed in the other two fluids (NF and NAB, Figure 4.8c and Figure 4.8d respectively).

The velocity profiles for the NF case approaches the analytical one as expected. A comparison between the WB and NAB profiles, shows that the velocity profile of WB is closer to the blunter, analytical profile. This is in agreement with the behaviour of aggregating blood observed in previous studies [30]: in a pressure driven flow of an aggregating blood sample in a rectangular microchannel, the velocity profile is blunter than that of the non-aggregating blood, in both simulated (CFD) and experimental flows.

4.9 Structural characteristics of blood in the rectangular straight microchannel

In order to estimate the extend of RBC aggregation in the measured WB flows the intensity coefficient of variation, CV_I, was calculated as the ratio between the Intensity standard deviation (SD_I) and the mean intensity ($\bar{I}$) in the ROI of the image: $CV_I = \frac{SD_I}{\bar{I}}$. RBC aggregation causes changes in the image intensity characteristics, which can be captured by the statistical variance and illustrated with CV_I.

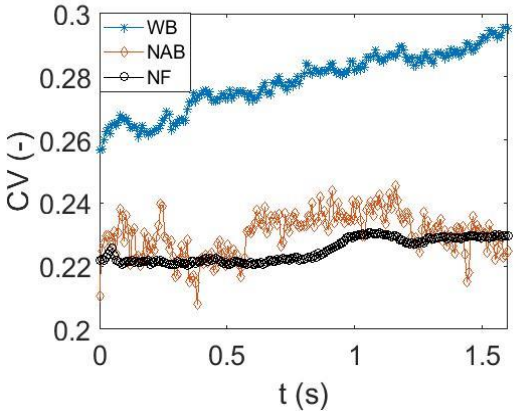

Figure 4.9. Coefficient of variation of image intensity as a function of time for flow of WB, NAB and NF samples respectively.

Figure 4.9 shows a clear difference between the aggregating case (WB) and the other two cases (NF and NAB). The CV_I for the NAB and the NF cases fluctuate around 0.23, whereas the CV of the WB case increases from 0.26 to 0.29 almost monotonically. This increase is expected as it is well known that RBC aggregation is a shear and time-dependent function [116]. As flow propagates viscous forces balance the capillary forces resulting to deceleration [81] as

aforementioned and seen in Figure 4.7 As velocity decreases causes shear rates to be smaller hence RBCs aggregation increases.

4.10 Shearing conditions

Shear rate magnitude was evaluated as explained is section 3.6.5 using Eq.3.9. Shear rate magnitude $|\dot{\gamma}|$ is shown in Figure 4.10 as fitted curves on the experimental data.

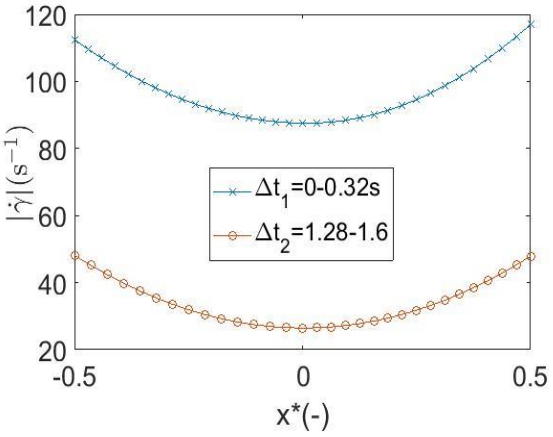

Figure 4.10. Profiles of $|\dot{\gamma}|$ across the width of the channel at two different time periods Δt_1 and Δt_2 (lines fitted on experimental data).

Moderate to strong shear conditions occur in the channel, specially closer to the walls reaching magnitudes of more than 90 s^{-1}, indicating good disaggregation conditions, according to disaggregation shear rates suggested in the literature [12,13]. Furthermore, since the μPIV technique underestimates the calculated velocities, the actual shearing conditions are expected to be further elevated [96].

Therefore, the shear conditions developed in the microchannel, especially close to the walls and during the initial time periods, are sufficiently strong to keep RBC aggregation at low levels. The value of CV_I (Figure 4.9) of the aggregating sample increased approximately 15% compared to the PBS value at the initial stages of the flow, reaching a difference of approximately 27% at the final stages.

4.11 Remarks on the experiments in the straight microchannel

The influence of red blood cell aggregation on surface tension driven flows in a rectangular micro channel was examined. Newtonian fluid, non-aggregating and aggregating blood samples were tested and the flow characteristics in the micro channel were analysed and compared, through micro-PIV based techniques and analytical solutions.

Aggregates at the centre result to an increase in viscosity therein having higher viscosity than near the walls [30]. This was verified by the higher viscosities of WB compared to the viscosities of NAB and NF (Figure 4.6). The increased viscosity at the centre causes a decrease in velocity therein. This effect has as a result the viscous characteristics of the core of the flow to influence more those in the regions of the side walls, and consequently a blunter profile compared to the non-aggregating sample [30]. This decrease in velocity balances with the smaller velocity further away from the centre resulting to a blunter velocity profile. The increased bluntness can be observed, form aggregative working fluid (WB) velocity profiles at the beginning and at the end of the flow (Figure 4.8). This effect has as a result the viscous characteristics of the core of the flow to influence more those in the regions of the side walls, and consequently a blunter profile compared to the non-aggregating sample [30].

In addition, high velocities were observed in the core of the flow (Figure 4.8) and hence, moderate to strong shear rates were observed in the initial stages of the flow (Figure 4.9) determining the extent of aggregation present in the channel.

The high shear rates result to high enough shear forces to break the RBC aggregates resulting, to low RBC aggregation and hence a similar flow behaviour with non-aggregative fluids. The low aggregation can be confirmed as aforementioned from coefficient of variation (CV) of the fluids (Figure 4.9). Whole blood has higher and increasing CV with or all times as expected since as stated above RBC aggregation is a shear and time-dependent function [12]. Although the difference in CV with the other fluids is small showing low aggregation. The present results illustrate that red blood cell aggregation should be considered as an influencing factor in passive microchannel blood flows akin to those used in many point of care diagnostics.

CHAPTER 5. Surface tension driven haemodynamics in the convergent, and heat-treated, microchannel[*]

In this Chapter three major parts of the PhD work are described:

1) The first regards the use of the novel microchannel setup, which includes the convergent geometry, and the surface treatment, for enhancing the flow and achieve the appropriate flow conditions for blood testing.
2) The second regards the extensive rheological characterisation of blood samples, including the heat-treated whole blood samples, which is a novel approach for altering the membrane properties of the RBCs, minimising the uncertainty and effects of sample handling and treatment.
3) The third is the systematic examination of haemodynamics, as influenced by the hemorheological factors.

STD flows have shown to have good potential for examining blood rheology, being simple/easy to handle, without any pumping mechanism, capable of examining and giving important information about the rheological and flow properties of blood. As observed from the experiments in the straight microchannel (Section 4) shear rates within the channel were high enough to expect good RBC disaggregation conditions prior to any measurements, showing that STD configuration setups can be used for examining blood flows, whereas being simpler and cheaper than pressure driven setups. Hence, the experimental methods were further revised and improved, in order to examine in more detail, the effect of red blood cell aggregation and other biomechanical properties of blood under capillary driven flows.

The effect of the following biomechanical properties of blood in the STD flow were examined: Blood viscosity, hematocrit, erythrocyte aggregation and deformability. Blood samples tested included: native whole blood WB, erythrocyte suspensions at different aggregative conditions (utilising Dextran and phosphate buffer saline, for aggregative and non-aggregative respectively), at different haematocrits (native, 40% and 45%) and their heat treated counterparts. The aforementioned samples were produced as explained in section 3.8.

[*] The largest part of the work presented in this Chapter has been submitted for publication in *Physics of Fluids*:

Pasias D., Passos A., G. Constantinides, Balabani S. and Kaliviotis E. (2022). Effects of biomechanical properties of blood on surface tension driven flows in superhydrophilic channels. Submitted February 2022, Physics of Fluids, accepted April 2022.

The construction of the microchannel with a convergent-rectangular geometry and surface treated, was explained in Section 3.2.2. As shown in Section 3.2.2 converging channels provide higher meniscus velocities compared to straight, and hence provide better flow conditions. Moreover, the glass slides were treated with plasma and TiO_2 coating as explained in Section 1.8 becoming super hydrophilic, hence the flow conditions were further improved.

Therefore, the microchannel version 2 is expected to have more favourable flow conditions than the straight geometry-untreated microchannel (version 1) used in the experiments in Section 4, and hence resulting to even better initial disaggregating conditions.

For the present experiments an additional external side camera (JVC TK-C1380 colour, with a 60mm Panasonic lens) was introduced on the initial experimental setup explained in Section 4 (Figure 5.1), developing a two-camera and microscope arrangement. By introducing the side camera in the new setup, meniscus flow in the microchannel could be captured, which was not possible with the initial setup (Figure 4.1) where only the microscope CCD camera was utilized, capturing only the flow in the core. Core and meniscus flow were captured, compared and characterised using micro-PIV and tracking techniques. Velocity profiles in the core, were produced for three different flow periods (at the beginning, at the end and for the whole duration of the flow Δt_1=0-0.16s, Δt_2=0.64-0.8s and Δt_3=0-0.8s respectively) whereas, velocity indices, where also produced for the aforementioned time periods. Furthermore, meniscus velocity was analysed in the entire channel, producing indices for the three Δt_s. In addition, shearing conditions within the channel were found from the velocity profiles produced from the μPIV analysis of the images from the CCD camera. Further, shearing history was calculated from the meniscus velocity curves produced from analysis of the side camera images.

5.1 Sample preparation

Blood was collected into vacuum tubes (BD) preloaded with 1.8 mg/ml EDTA from 10 healthy volunteers. The working fluids tested in these experiments were whole blood in its native state (WB), non-aggregative blood (NAB40% and NAB45%), aggregative blood (AB) suspensions (DEX40% and DEX45%) and their heat-treated counterparts. The aforementioned working fluids were produced as explained in Section 3.8.

5.2 Experimental setup

Figure 5.1 shows a schematic of the experimental setup, which was similar to the setup of the initial experiments explained in Section 4 (Figure 4.1), with the addition of a side camera in order to capture the meniscus flow. The micro channel was placed horizontally on the

microscope stage. A 25µl drop of fluid was placed at the entrance, using a micropipette and the fluid was then set in motion through the channel by capillary forces. The flow was recorded with a CMOS camera (IDT X3, 2000 images were captured at 1250 fps) attached on the microscope (upright BX51 OLYMPUS, 10X-objective, NA=0.25) and images were analysed using Matlab. The spatial resolution of this optical setup was 1.65 µm/pixel. The side camera (JVC TK-C1380 colour, with a 60mm Panasonic lens) was fixed at the maximum angle possible (47^o to the y-axis) to capture the meniscus on the horizontal plane.

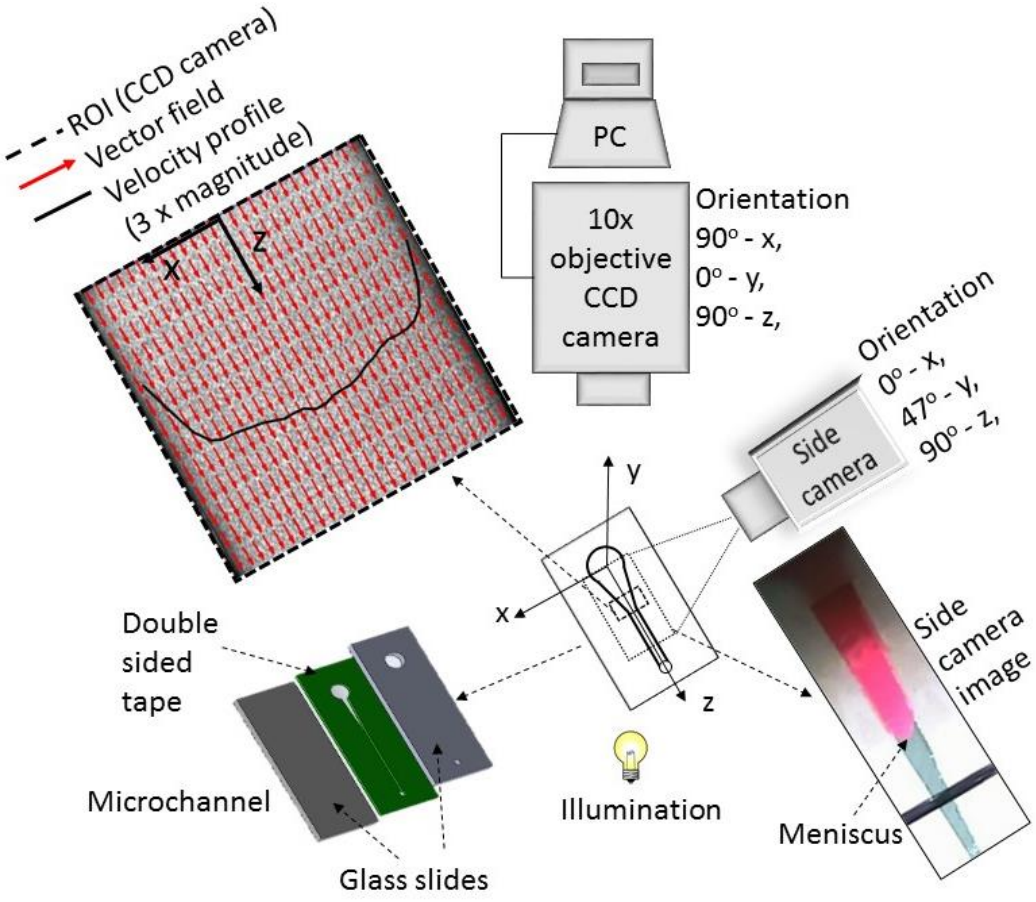

Figure 5.1. New experimental setup Annotated schematic of the capillary driven micro channel flow, and the PIV measurement set up: the width (W) and depth (h) of the channel were W = 5mm at the beginning converging to ~ 1mm at the end of the converging section and h ~ 100 µm, respectively (diagrams not to scale).

5.3 µPIV processing

The images were processed using Matlab PIVLab software as explained in section 3.6.1 to resolve the velocity field, and to analyse/plot the velocity profile in the channel (Figure 5.1). RBCs were used as tracing particles as in the experiments using microchannel version 1 in section 4. The velocity profiles were calculated by axially averaging all of the velocity vectors in a region of interest (ROI) in the channel after the meniscus had progressed. The choice for averaging the velocity vectors in the channel, and not the z-component of velocity only, was based on the fact that the convergent geometry resulted in a negligible increase of the cross-flow velocity components. In addition, of particular importance in the present work is the magnitude of the shear rate, which is calculated including an estimation of the out-of-plane shear component. The latter is calculated using the maximum velocity of the profile and the channel height (a detailed description is provided section 3.6.5).

5.3.1 Validation of the µPIV analysis

In addition to the validation procedure explained in section 3.6.1.1 another method was used to validate Matlab PIV software analysis. The validity of the µPIV approach adopted in this part was assessed by comparing the mean flow velocity in the channel, $\bar{\bar{V}}_{ch}$ (measured at a distance of 15mm from the entrance to avoid any entrance effects) with the tracked mean meniscus velocity $\bar{\bar{V}}_m$ for each sample (calculation of $\bar{\bar{V}}_m$ and $\bar{\bar{V}}_{ch}$ is explained in later sections-5.4 and 5.5). Indeed $\bar{\bar{V}}_{ch}$ and $\bar{\bar{V}}_m$ were calculated for a period of 0.16 s (200 images) at two different time points in the flow: Δt_1 is a period at the beginning of the flow (i.e. 0-0.16s) and Δt_2 is at the end of the flow from 0.64-0.8s. Another calculation was performed for the whole duration of the flow (Δt_3) i.e. 0 - 0.8 s (1000 images). Indeed, comparing $\bar{\bar{V}}_m$ with $\bar{\bar{V}}_{ch}$ (Figure 5.2) for the periods Δt_1, Δt_2, and Δt_3 a general qualitative and quantitative agreement is observed, indicating that the µPIV technique utilised is valid for the present analysis. More specifically, Figure 5.2 shows that the results are consistent with: a) the decrease of velocity which is expected from the period Δt_1 to the period Δt_2 (see the meniscus velocity in Figure 5.3c and d), b) the expected higher velocity of $\bar{\bar{V}}_m$ compared to $\bar{\bar{V}}_{ch}$ for the overall period Δt_3, due to the µPIV underestimation, and c) the expected discrepancy in velocities between the normal and hardened (heat-treated) samples. In some cases, (i.e. WB, DEX45%) $\bar{\bar{V}}_{ch}$ and $\bar{\bar{V}}_m$ appear very close and in the case of the WB-HT sample, $\bar{\bar{V}}_{ch}$ appears higher than $\bar{\bar{V}}_m$.

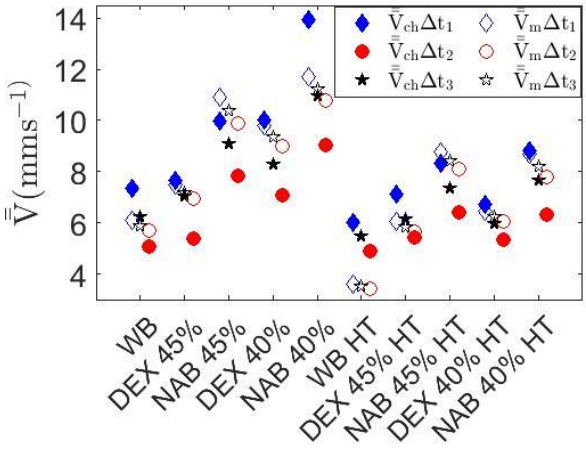

Figure 5.2. Comparison of $\bar{\bar{V}}_m$ with $\bar{\bar{V}}_{ch}$ for each different sample and for the 3 different time periods $\Delta t_{1.2.3}$.

5.4 Meniscus Velocity calculation

The meniscus velocity curves were produced for all samples as explained in section 3.6.4. The mean meniscus velocity $\bar{V}_m$ curves from all tests and for each sample type are shown in Figure 5.3. In addition, $\bar{\bar{V}}_m$ was calculated as a time-average velocity within the different time periods (Δt_1, Δt_2, and Δt_3) as: $\bar{\bar{V}}_m = \frac{\sum_1^n \bar{V}_m(z)}{n}$

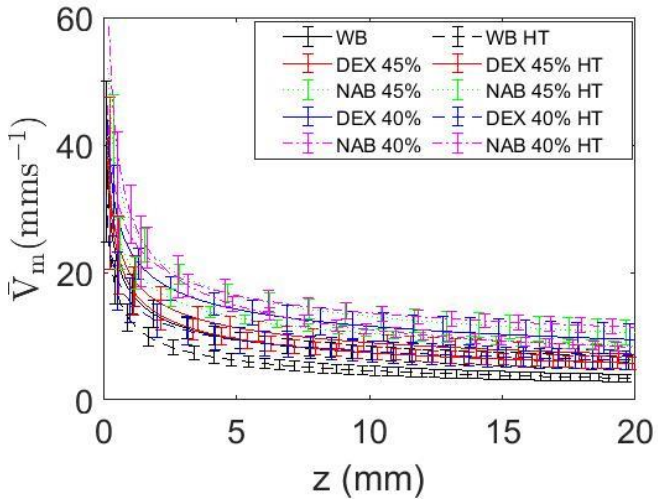

Figure 5.3. Mean meniscus velocity, as a function of position, from all tests (n=10) in each different sample.

5.5 Velocity profiles in the core of the flow

Velocity profiles, $\bar{V}_{ch}$, were extracted from the measured velocity vectors, as described in the previous section, in an ensemble-average manner. For the velocity profile derivation, it was assumed that any velocity component in the x-direction, due to the 3-degree converging width and any fabrication uncertainties at the walls, is negligible in the core of the flow. Indeed, examining the vector components u and w (produced by the microPIV technique for the x and z directions of the flow respectively), revealed a presence of u, as < 1% maximum of the w component (Figure 5.4).

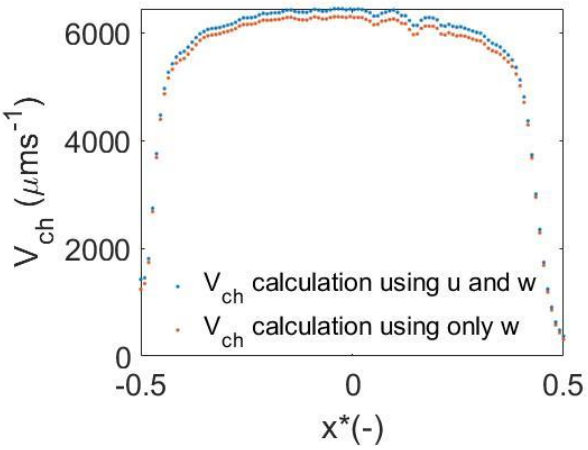

Figure 5.4. Representative velocity profiles calculated using only u component and u, w components.

The region of interest used for the micro PIV analysis was rectangular, and was positioned to cover the entire channel (see in Figure 5.1). Therefore, the flow analysis domain included a small portion of the walls in which zero velocity was expected to appear. Due to refraction effects at the walls the first line of vectors near the end of the vector field was neglected, so the field was reduced by 13.2 μm in each side. Therefore, the portion of the vector field affected by the zero velocities due to the wall, was significantly minimised.

For presentation and comparison purposes the x-direction in each mean velocity profile was normalized with its width, to produce limits of $-0.5 \leq x^{*} \leq 0.5$. Due to small variations in the dimensions between the constructed microchannels, velocity points could appear at slightly different x* positions in the V_{ch} profiles. Therefore, in order to minimize errors when averaging the V_{ch} profiles to produce the mean $\bar{V}_{ch}$ velocity profiles (for the three Δts), the position of the velocity points from the centreline were used rather than x*. Finally, the mean channel flow

velocity was calculated from the velocity profiles $\bar{V}_{ch}$, of all samples (n = number of samples) as follows: $\bar{\bar{V}}_{ch} = \frac{1}{n}\sum_1^n \left[\frac{1}{x^*}\int_{-0.5}^{0.5} \bar{V}_{ch-n}\, dx^*\right]$.

5.6 RBC aggregation and deformability

The aggregation indices AI, Amp, $t_{1/2}$, and M were obtained at each experiment using the Rheoscan-A200 instrument, for each type of working fluid tested and then averaged to find a mean index. Light transmission intensity over time was plotted for each sample type for all experiments (data from a representative sample from all tests (n=10) is shown in Figure 5.5a) illustrating the behaviour of the process. Hence the intensity curves (n=10) of each sample type were averaged and a mean light transmission intensity ($\bar{I}$) curve for each tested working fluid was produced as shown in Figure 5.5b.

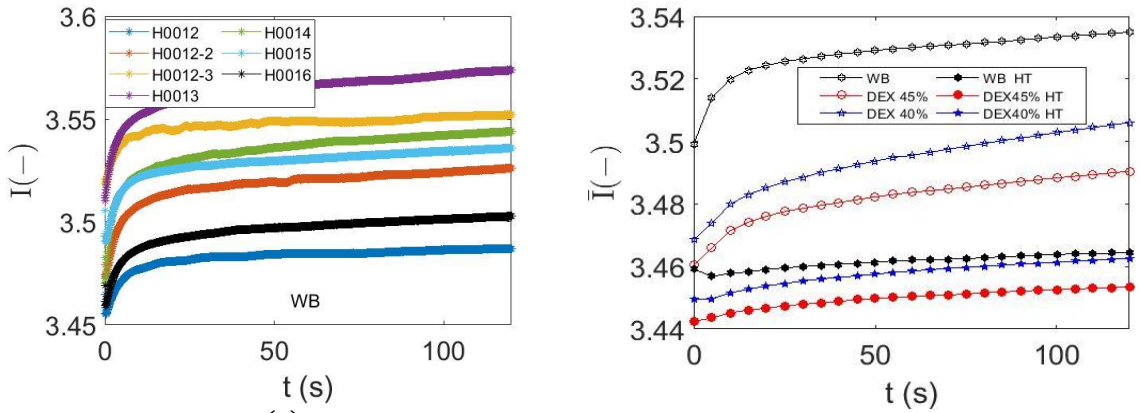

(a) (b)

Figure 5.5. (a): Aggregation index of WB samples. (b): Mean aggregation index syllectogram for WB, DEX45%, DEX40% heat and non-heat treated samples.

Deformability measurements were performed using the Rheoscan-D300 instrument, for the WB and DEX45% and NAB45% samples, and for their heat-treated counterpart cases. The deformability indices used in this study were the Elongation index: EI, the Half Shear Stress ($SS_{1/2}$), and Ratio, defined as $R = \frac{EI}{SS_{1/2}}$, as explained in Section 3.4.2. The same procedure as with the aggregation intensity curves was followed to produce the mean $\overline{EI}$ curves over shear stress (Figure 5.6b).

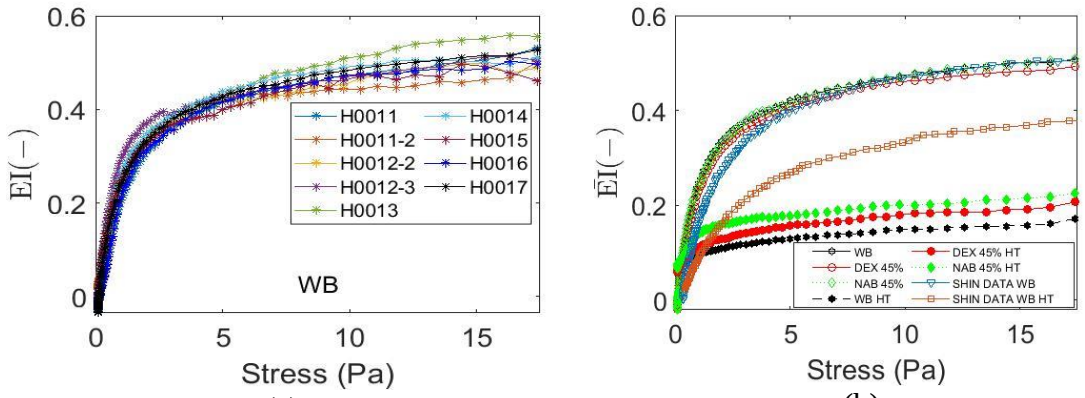

Figure 5.6. (a): Elongation index curve of WB samples. (b): Mean Elongation index syllectogram for WB, DEX45%, NAB45% heat and non-heat treated.

For a clearer presentation the curves in Figure 5.6 error bars are not included. However, the average standard deviation in the steady state part of each ĒI curve has been evaluated for each case, and it was found to be less than 4% of the $\overline{EI}$ values (3.44% in the DEX45% case).

5.7 Viscosity measurements

Viscosity measurements were performed using a Brookfield DVIIT instrument as explained in section 3.5. In this part of the work the viscosities were measured by ramping down shear rates from 251.2 to 1s^{-1}, without pre-shearing between shear points (Figure 5.7) and including points 15.82 s^{-1} and 7.785 s^{-1}. The analysis of the data was restricted to the shear range of 251.2 - 7.785 s^{-1}, since the torque sensitivity of the viscometer was at its lower limit near the shear rate of 7.785 s^{-1}. The three aforementioned shear rate points (251.2,15.82 and 7.785s^{-1}) were selected for the presentation of viscosity.

An average viscosity ($\bar{\mu}$) was calculated at each shear rate from all tests (n=10) and for each sample type and shown in Figure 5.7 with the standard deviation. Furthermore, $\bar{\bar{\mu}}$ has been included as an average value of $\bar{\mu}$, to indicate the viscosity levels within shear rates from 251.2 up to 7.815s^{-1} since as abovementioned at this shear rate the torque sensitivity of the viscometer was near the lower limit.

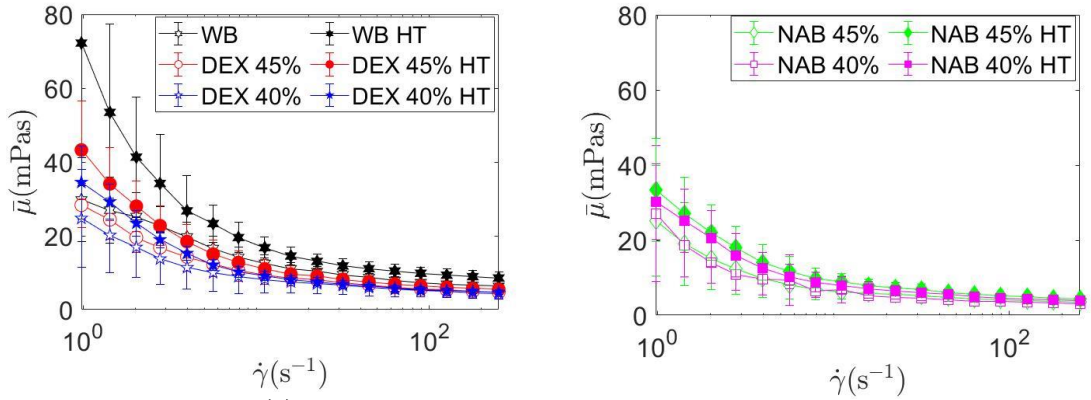

Figure 5.7. Mean viscosity. (a): Aggregative samples. (b): Non-aggregative samples.

From the mean viscosity $\bar{\mu}$ data, the relative viscosity ($\bar{\mu}_{rel}$) was produced as the ratio of the measured sample viscosity to the viscosity of the suspending medium at the three shear points (251.2 s^{-1},15.82 s^{-1} and 7.785s^{-1}). Suspending medium viscosities included those of plasma (μ_{pl}), Dextran (μ_{Dex}) and PBS (μ_{pbs}). Therefore, the WB samples viscosity were normalised with μ_{pl}, the Dextran ones with (μ_{dex}) and the NAB ones with μ_{pbs}.

Furthermore, $\bar{\mu}_{rel}$ was normalized with the $\bar{\mu}_{rel}$ value at maximum shear rate, resulting to the normalized low-to-high shear viscosity ratio $\bar{\mu}^{*}_{rel}$ for the 15.82 s^{-1} and 7.785s^{-1} shear rates, as an index of the shear thinning behaviour of the fluid. In addition the virial viscosity index (μ_{vir}), was calculated similarly to another study [117], as:

$\mu_{vir} = \frac{\bar{\mu}(\text{at } \dot{\gamma}=7.88 \text{ or } \dot{\gamma}=15.82\ ) - \bar{\mu}\ (\text{at } \dot{\gamma}=251.2)}{\bar{\mu}\ (\text{at } \dot{\gamma}=251.2)}$, in order to examine the extent of shear thinning behaviour of the working fluids.

5.8 Rheological characteristics of the samples used in the study

The rheological properties of blood are influenced by specific factors including RBC aggregation and deformability, haematocrit, and plasma viscosity. Therefore, in order to better understand the behaviour of the fluid in the surface tension driven flow these factors were taken into consideration in the design of experiments. The characteristic indices for the aforementioned quantities are given in this section to assist the discussion and analysis of the results thereafter. In addition, there is a particular interest in this part of the work, since for particular samples used, namely the WB heat-treated samples, there is no relevant information in the literature regarding their rheological behaviour.

It should also be noted, that this part of the work is particularly extensive and required a substantial effort in the PhD program to be completed. This work is embedded in Chapter 4.2 due to the relevance on the specific topic.

5.8.1 Structural characteristics (Aggregation and Deformability indices)

As regards RBC aggregation (RBCA), the averaged indices (all repetitions in each sample category) derived from the curves in Figure 5.5 are shown in Figure 5.8.

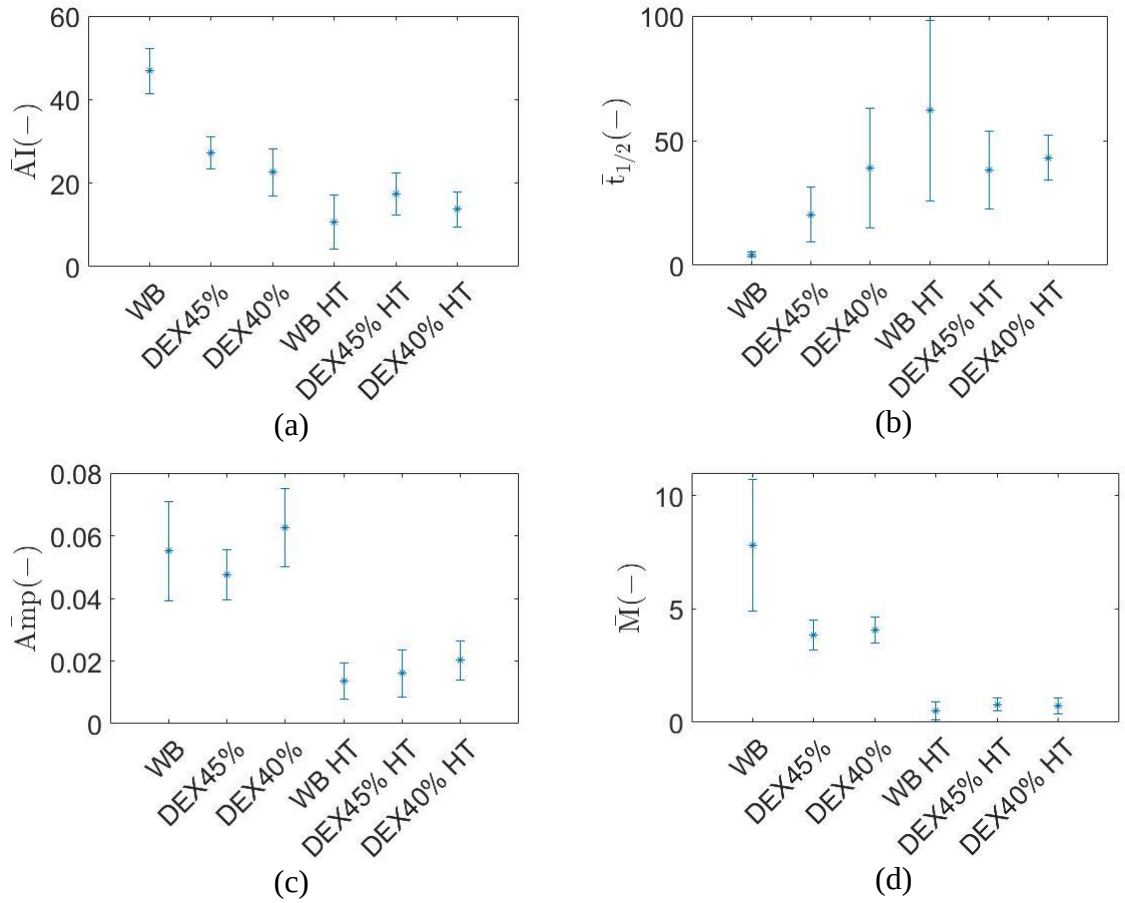

Figure 5.8. Mean Rheoscan-A200 indices for WB and DEX samples. (a): $\overline{\mathbf{AI}}$, (b): $\bar{\mathbf{t}}_{1/2}$, (c): $\overline{\mathbf{AMP}}$ and (d): $\overline{\mathbf{M}}$ index.

From the intensity curves in Figure 5.5 and the $\overline{AI}$, indices in Figure 5.8, it is observed that RBCA in whole blood is higher than the Dex45% and Dex40% for both heated-treated and normal cases. The higher aggregation tendency in WB compared to DEX45% and DEX40% was expected, since the dextran concentration was low/moderate in terms of influence in RBCA [118]. RBCA in Dex45% is higher than Dex40% as expected, due to the higher haematocrit [119].

The heat treatment had an obvious effect on RBCA, suppressing the phenomenon in agreement with other studies [120], however the decrease does not appear systematic. Jovtechv et al [120] examined role of electrical and mechanical properties of red blood cells for their aggregation. Since aggregation forces require a deformation of the cell membrane in order to form a stable contact between two cells, decrease of RBC membrane deformability due to hardening caused by the heat treatment, result to weakening of RBC aggregation mechanism [120].

This is illustrated in Table 5.1 where the percentage difference of the indices prior and post heat-treatment, is shown calculated as $\mathrm{AI_{max}}\ \Delta\% = \frac{\mathrm{AI_{max\,(prior\,HT)}} - \mathrm{AI_{max\,(post\,HT)}}}{\mathrm{AI_{max\,(prior\,HT)}}} \times 100$. It can be seen that both Dextran samples exhibit the same change in aggregation post heat treatment whereas WB shows a more pronounced decrease in $\overline{\mathrm{AI}}$; this can be probably attributed to the heat-treatment also affecting the plasma proteins responsible for the RBCA phenomenon to a greater extent than the Dextran molecules. According to Lerche et al [121] the bridging energy of Dextran molecules (4g% of D70 in that study) is higher than for this of the fibrinogen found in normal plasma, and therefore an increased rigidity of RBCs, or/and a heat-altered macromolecule-glycocalyx interaction can have a greater impact in the case of WB compared to Dextran samples.

Sample	WB	Dex45%	Dex40%
AI_{max} % difference	-77.2%	-36.2%	-39.3%
$t_{1/2}$ % difference	1320.3%	87.2%	10.1%
Amp % difference	-75.2%	-66.3%	-75.2%
M% difference	-93.4%	-79.5%	-82.3%

Table 5.1. Difference in aggregometry indices between heat and not heat-reated working fluids

The $t_{1/2}$ RBCA index provides information on the RBCA kinetic characteristics, since is a transient index. The more aggregative the fluid the smaller the $t_{1/2}$ is observed. Furthermore, comparing $\bar{t}_{1/2}$ of DEX45% with DEX40% the sample with higher haematocrit has smaller $\bar{t}_{1/2}$ which might shows that higher haematocrit results to faster aggregation transient behaviour, agreeing with the results in other studies [122]. This specific index increases after heat treatment as expected implying a suppressed dynamic behaviour of RBCA. For WB the percent difference in $\bar{t}_{1/2}$ appears also higher compared to the other aggregative samples, due to heat treatment affecting plasma proteins as discussed above. It is worth noting that the

changes in $\bar{t}_{1/2}$ (i.e. of the transient characteristics in RBCA) prior and post heat-treatment appear higher for DEX45% compared to DEX40%, despite their similar $\overline{AI}$ percent changes. Similar trends were also observed with other quantified RBCA indices (Amplitude and M index).

The deformability of the RBCs has been assessed for all samples and the relevant indices are provided in Figure 5.9. The maximum mean elongation index ($\overline{EI}_{max}$) for the three normal (pre-heat) working fluids tested (both aggregative and non-aggregative) is approximately the same. Therefore, the treatment of the samples for altering RBCA, and the medium fluid properties (suspension in plasma, PBS, and Dextran solutions) do not seem to have a significant impact on cell deformation.

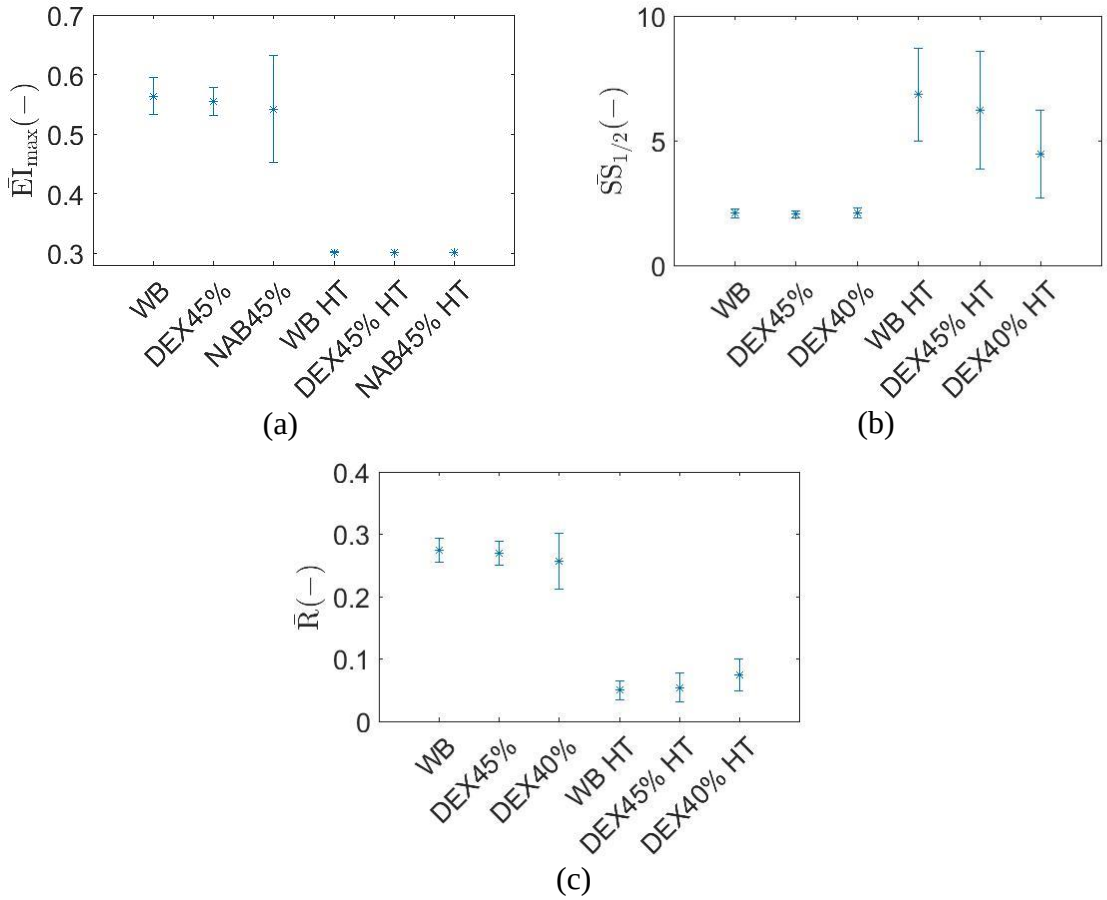

Figure 5.9. Mean Rheoscan D indices. (a): $\overline{EI}_{max}$ for all working fluids. (b): $\overline{SS}_{1/2}$ for all working fluids. (c): $\overline{R}$ for all working fluids.

The heat-treatment, however, reduces significantly the elongation index for all working fluids tested as observed in Figure 5.9 and Table 5.2; all working fluids exhibit the same $\overline{EI}_{max}$ following heat-treatment and hence the $\overline{EI}_{max}$ percent difference is almost the same for all

working fluids (Table 5.2). This indicates that suspending mediums (plasma, PBS, and Dextran) did not any effect on deformability due to heating.

Other deformability indices ($\overline{SS}_{1/2}$ and $\overline{R}$) show consistent changes, with some differences between the NAB and the aggregative samples. As expected, after the heat-treatment the $\overline{EI}_{max}$ index decreased whereas the $\overline{SS}_{1/2}$ has been increased, and the Ratio index is decreased. The $\overline{SS}_{1/2}$ index provides information on how the application of stresses influences the deformability of the RBCs.

Sample	WB	Dex45%	NAB45%
$\overline{EI}_{max}$ % difference	-46.5%	-45.7%	-44.5%
$\overline{SS}_{1/2}$ % difference	228.2%	205.3%	112.2%
$\overline{R}$ % difference	-79.4%	-85.4%	-70.8%

Table 5.2. Difference in deformability indices between heat and non heat-treated working fluids

As observed in Table 5.2, the $\overline{SS}_{1/2}$% - difference is significantly higher for the aggregative fluids indicating a difference in how the RBC deforms at various stresses. Comparing the aggregative samples with each other WB, which shows the highest aggregation, shows also slightly higher $\overline{SS}_{1/2}$ percentage difference from the DEX45% samples. This might imply that aggregation increases the stress needed for the cell to deform. Indeed, higher viscosity is observed at high aggregation, and hence higher shear stress needs to be applied for cell deformation.

5.8.2 Viscosity

As observed in Figure 5.10, aggregative samples have higher $\bar{\bar{\mu}}$ than non-aggregative (Figure 5.10d), which agrees with other studies where aggregation increases viscosity [123]. The same implies for the heat-treated working fluids. However, their non-Newtonian behaviour seems not significantly affected, as indicated by the viscosity ratio $\bar{\mu}^*_{rel}$ and the $\bar{\mu}_{vir}$ index (Figure 5.10b), i.e. the $\bar{\mu}^*_{rel}$ and $\bar{\mu}_{vir}$ for the HT samples is similar to that of the normal ones, even though the aggregation and deformability of the RBCs has been reduced in the HT cases. Indeed, since RBC deformability (Figure 5.9 and Table 5.2) and aggregation, (Figure 5.8 and Table 5.1) have been reduced post HT, the shear thinning behaviour would be expected to be

less obvious. However, RBC aggregation and deformability are still not negligible: there is a ~37% reduction in AI for the DEX cases (and a larger reduction of ~77% in the WB case) and ~ 45% reduction in the deformability of the RBCs ($\overline{EI}_{max}$ index).

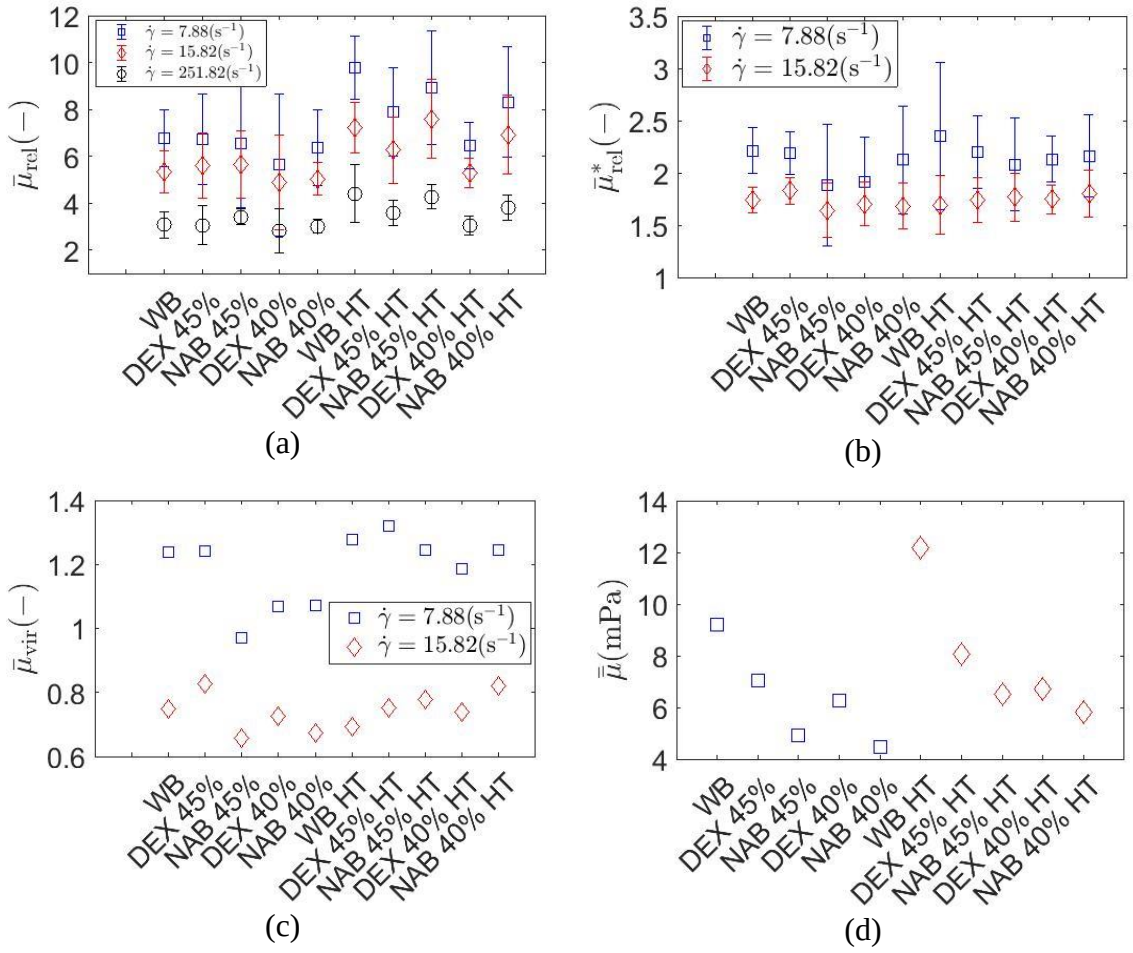

Figure 5.10 (a): Mean relative viscosity $\bar{\mu}_{\mathrm{rel}}$ of all working fluids at shear rates $\dot{\gamma}$=7.88s^{-1}, $\dot{\gamma}$=15.82s^{-1} and $\dot{\gamma}$=251.82s^{-1}. (b): Mean normalized relative viscosity ($\bar{\mu}^*_{rel}$) of all working fluids at shear rates $\dot{\gamma}$=7.88s^{-1} and $\dot{\gamma}$=15.82s^{-1}. (c): The virial viscosity index $\bar{\mu}_{\mathrm{vir}}$. (d): The bulk viscosity index $\bar{\bar{\mu}}$.

Furthermore, it has been reported in the literature [79], that when the deformability of RBCs is reduced by heat treatment, the disaggregating shear stress (i.e. the minimum shear-stress required to disperse the aggregates) is increased, depending on the concentration of the aggregating factor (fibrinogen in that case). Increased disaggregating shear stress (DSS) implies both increased viscosity, and non-Newtonian behaviour of the fluids [13]. Another cause of the high viscosity and persisting non-Newtonian behaviour of the HT samples, might be the tumbling of red blood cells in the flow instead of the less energy demanding rolling

motion [124]. It is therefore apparent, that the loss of deformability balances out the effect of reduced AI, and hence the samples retain their shear thinning behaviour.

In addition, as abovementioned, the general trend observed in Figure 5.10 is that the more aggregative the working fluid is, the higher its viscosity appears. In order to demonstrate this more clear, the $\overline{AI}$ of the aggregative samples was normalized with WB mean aggregation index ($\overline{AI}_{WB}$, which has the more aggregation and hence the higher viscosity) i.e. $\overline{\mathrm{AI}}^{*}_{\mathrm{sample}} = \frac{\overline{\mathrm{AI}}_{\mathrm{sample}}}{\overline{\mathrm{AI}}_{\mathrm{WB}}}$ and plotted against the normalized viscosity index i.e. $\bar{\bar{\mu}}^{*}_{\mathrm{sample}} = \frac{\bar{\bar{\mu}}_{\mathrm{sample}}}{\bar{\bar{\mu}}_{\mathrm{WB}}}$.

From Figure 5.11a it is obvious that for higher aggregation indices ($\overline{\mathrm{AI}}^{*}$) higher viscosity indices ($\bar{\bar{\mu}}^{*}$) are observed for both heat and non-heated samples expect from the WB HT sample. This is because, as aforementioned, heat treatment affects significantly plasma proteins which are responsible for RBCA, resulting to further decreased aggregation post heat treatment than the dextran samples [121]. Moreover, as expected and shown in Figure 5.10d, after heat treatment viscosity has increased similar to other studies [79].

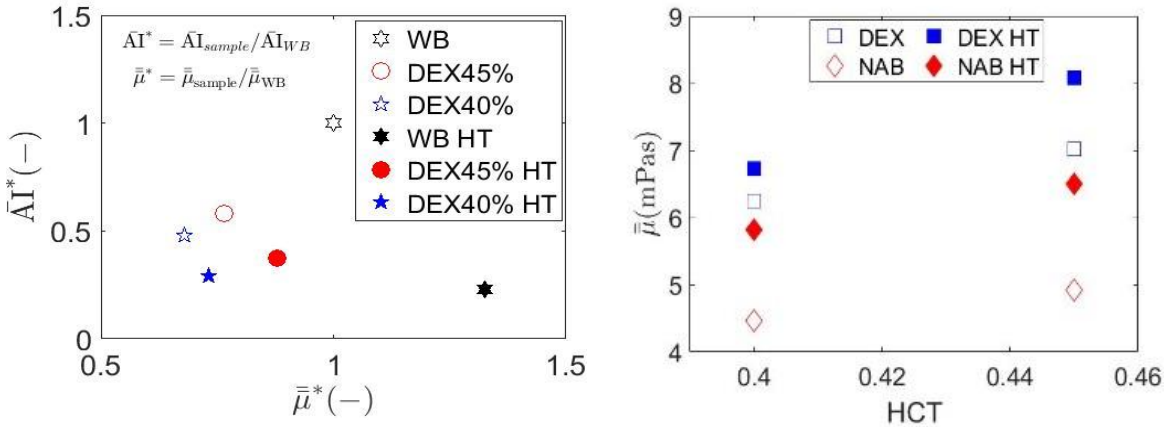

Figure 5.11 (a): Mean normalized Aggregation index ($\overline{AI}^{*}$) vs mean normalized viscosity index ($\bar{\bar{\mu}}^{*}$). (b): Bulk viscosity index $\bar{\bar{\mu}}$ of Dex and NAB samples at Hct40% and Hct45%.

The relative and normalized relative viscosities tend to be increased for working fluids with Hct = 45% compared to the working fluids with Hct = 40%. This is observed both prior and post heat treatment. This might indicate that increased hct tends to increase relative viscosity. Table 5.3 provides information on the percentage differences of $\bar{\mu}_{\mathrm{rel}}$ prior and post heat-treatment. In addition, no particular trend is observed in $\overline{\mu_{\mathrm{rel}}}^{*}$ and in $\bar{\mu}_{\mathrm{rel}}$ indices in terms of working fluid aggregability condition.

Further, the viscosity indices ($\bar{\bar{\mu}}$) of aggregative (DEX) and non-aggregative (NAB) working fluids of Hct=40% and Hct=45% were compared (Figure 5.11b). From Figure 5.11b it is observed that both aggregative and non-aggregative samples have increased $\bar{\bar{\mu}}$ at the higher Hct value (Hct45%), both prior and post heat treatment showing that increased Hct increases viscosity [125]

	Shear rate (s^{-1})		
	7.875	15.82	251.2
Working fluid	**$\overline{\mu_{rel}}^{*}$ difference**		
WB	43.26%	34.96%	44.21%
DEX 45%	16.56%	11.86%	35.18%
NAB 45%	25.22%	34.38%	47.31%
DEX 40%	7.41%	8.06%	37.79%
NAB 40%	26.68%	37.65%	45.25%
$\bar{\mu}_{rel}$ difference after heat treatment for shear rates 7.875 s^{-1} ,15.82 s^{-1} and 251.2 s^{-1}			

Table 5.3. $\bar{\mu}_{rel}$ difference after heat treatment for shear rates 7.875 s^{-1}, 15.82 s^{-1} and 251.2 s^{-1}.

5.9 Meniscus Velocity

The meniscus velocity characteristics are shown in Figure 5.12. Figure 5.12a shows the mean meniscus velocity $\bar{V}_m$ along the axial direction for all working fluids, while Figure 5.12b an average velocity value $\bar{\bar{V}}_m$, calculated from z = 5 mm to 20mm, i.e. excluding the non-linear decelerating part of the flow in order to facilitate comparisons.

The velocity data in Figure 5.12b and the sample aggregation tendency in Figure 5.8 show that the more aggregative the sample is, the greater the negative effect on the velocity. The heat-treated samples (Figure 5.12b) also exhibit lower mean meniscus velocity $\bar{\bar{V}}_m$ compared to normal non heated ones probably due to the increased viscosity ($\bar{\bar{\mu}}$).

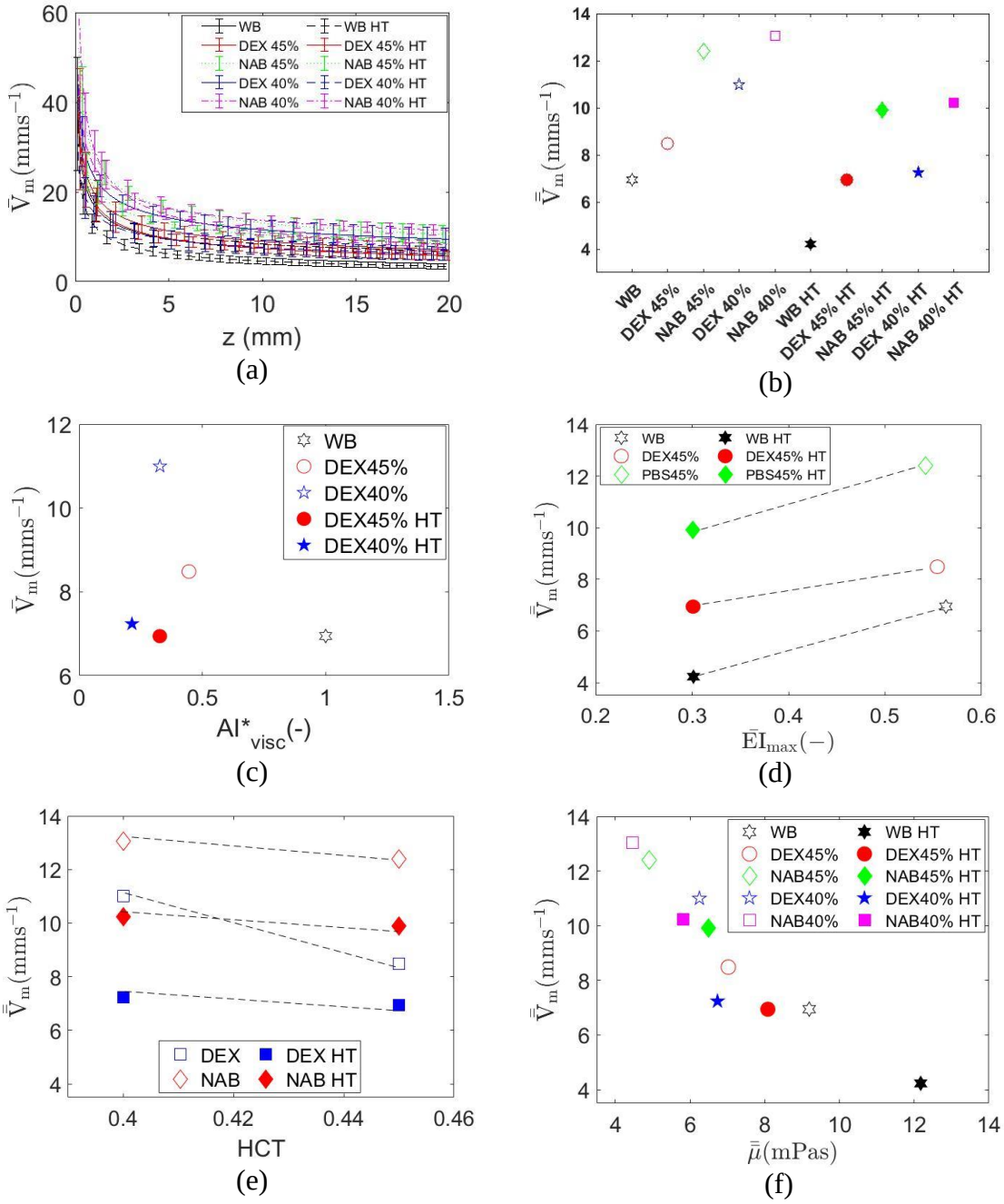

Figure 5.12 (a): Meniscus velocity, $\bar{V}_m$, from all sample categories tested. (b): Meniscus velocity of all working fluids, $\bar{\bar{V}}_m$, averaged from z=5mm until end of the channel (z=20mm). (c): Combined effect of aggregation and viscosity on meniscus velocity ($\bar{\bar{V}}_m$ vs AI^*_{visc}) for the aggregative fluids. (d): Effect of deformability on meniscus velocity ($\bar{\bar{V}}_m$ vs $\overline{EI}_{max}$). (e): $\bar{\bar{V}}_m$ vs HCT. (f): Effect of viscosity on meniscus velocity ($\bar{\bar{V}}_m$ vs $\bar{\bar{\mu}}$).

The velocity $\bar{\bar{V}}_m$ can be correlated with $\overline{AI}$ and the $\bar{\bar{\mu}}$, as it is observed that the more aggregative the fluid is, the higher its viscosity, and hence less its velocity. In order to demonstrate this more clearly an aggregation-viscosity index (AI^*_{visc}) was introduced as $AI^*_{visc} = \overline{AI}^* \times \bar{\bar{\mu}}^*$. As

previously observed at Figure 5.11a, aggregation and viscosity indices are somehow proportional, hence AI^*_{visc} is expected to increase as aggregation viscosity increases. Figure 5.12c presents, the effect of aggregation and viscosity on the meniscus velocity (WB-HT was excluded since as aforementioned, HT significantly affects plasma proteins responsible for aggregation [121] resulting to abnormal behaviour). From Figure 5.12c can be observed that, as AI^*_{visc} increases, it has a negative effect on $\bar{\bar{V}}_m$ for both heat and non-heat treated samples. As abovementioned an increase in AI^*_{visc} implies increase in aggregation and viscosity. Hence from the results in Figure 5.12c the negative effect on velocity due to increased aggregation, and hence viscosity, is clearly demonstrated. In addition, the negative effect of increased viscosity on meniscus velocity is also observed in Figure 5.12f.

The reduced deformability from heat-treatment (Figure 5.9) influences negatively the mean velocity $\bar{\bar{V}}_m$ for all working fluids (Figure 5.12d). In this case the viscosity ($\bar{\bar{\mu}}$) also is found increased (Figure 5.10). In addition, $\bar{\bar{V}}_m$ of aggregative (DEX) and non-aggregative samples (NAB) for Hcts40% and 45% were compared (Figure 5.12a) to examine the effect of Hct in the flow. Reduced velocities are found at the higher Hct value (Hct = 45%) [37] for the working fluids tested (Figure 5.12a), in agreement with the results in Figure 5.10f were for higher Hct, increased viscosities were observed hence lower $\bar{\bar{V}}_m$ (Figure 5.12f).

5.10 Velocity profiles in the core of the flow

The channel velocity profiles $(\bar{V}_{ch}$ and $\bar{\bar{V}}_{ch})$ shown in Figure 5.13 demonstrate the role of RBC aggregation similarly to the meniscus velocities ($\bar{V}_m$ and $\bar{\bar{V}}_m$ in Figure 5.3 and Figure 5.12c). This is apparent when comparing the DEX 45% to NAB 40% sample and is attributed to the elevated viscosity found in the DEX samples (Figure 5.10). The impact of the reduced RBC deformability is also evident in the reduced velocity profiles of the heat-treated samples in Figure 5.13.

Heat-treated samples exhibit smaller differences in channel velocities compared to normal ones; however, the standard deviation between samples appears much higher. Figure 5.13a and c indicate significant differences in channel velocities between samples, with the velocity of the NAB40% appearing higher than the other cases. The maximum velocity of WB samples appears at the lower end of velocities observed in both $\Delta t_{1,}$ and $\Delta t_{2.}$ periods of measurement, and the same applies for the heat-treated counterparts.

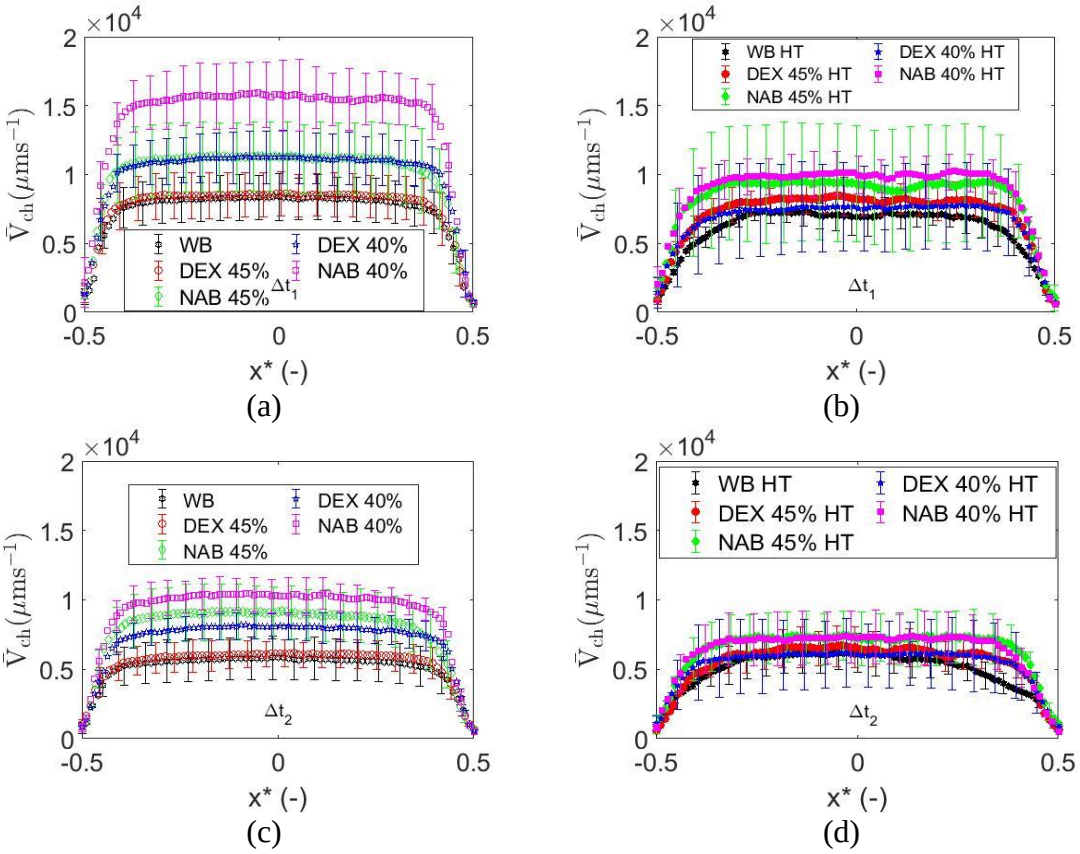

Figure 5.13 (a), and (b): $\bar{V}_{ch}$ at Δt_1 for normal and HT samples respectively. (c) and (d): $\bar{V}_{ch}$ at Δt_2 for normal and HT samples respectively.

For the velocity profiles in heat-treated samples (Figure 5.13b and d) the minimum velocity is within approximately 30% of the highest velocity, compared to normal ones; however, the standard deviation between samples appears much higher, and no statistically significant differences can be detected between samples.

The decelerating behaviour of the meniscus velocity is also apparent in Figure 5.14a, and b, comparing $\bar{\bar{V}}_{ch}$ at different periods Δt_1, and Δt_2. The velocity values are lower in the Δt_2 period, in agreement with the plots in Figure 5.12a.

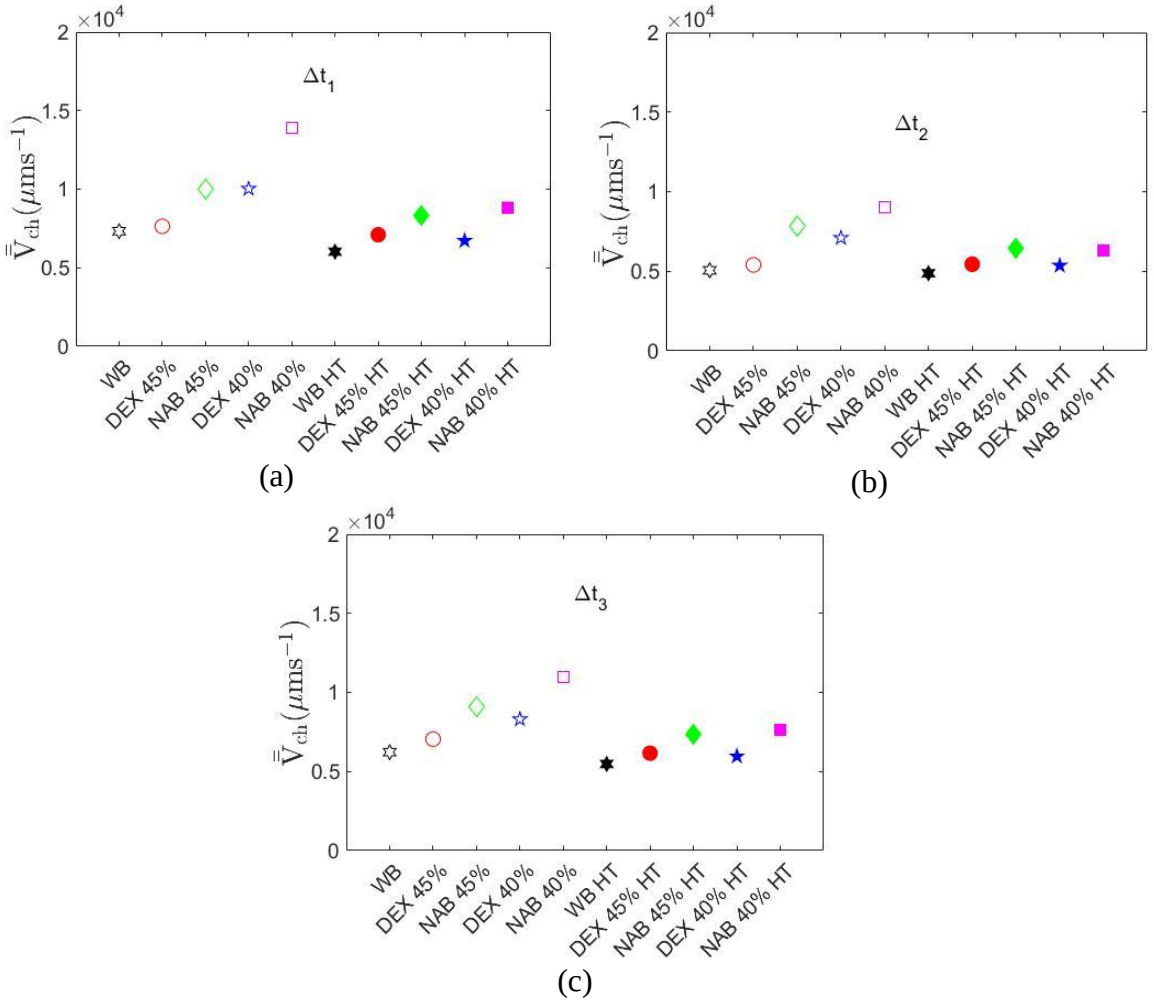

Figure 5.14. $\bar{\bar{V}}_{ch}$ at each Δt. (a): at Δt1, (b): at Δt2 and (c): at Δt3

Figure 5.15 represent $\bar{\bar{V}}_{ch}$ and $\bar{\bar{V}}_{m}$ in comparison for the three Δt periods and for normal and heat-treated samples. It is observed for all Δt, $\bar{\bar{V}}_{ch}$ and $\bar{\bar{V}}_{m}$ have a similar trend for both heat and not heat treated samples. That is the velocity of all samples has been decreased after heat-treatment, irrespectively of the nature of the sample (WB, Dextran or RBC suspension in PBS). The dispersion of the data is higher in the $\bar{\bar{V}}_{ch}$, than in the $\bar{\bar{V}}_{m}$ velocities, however their mean values are close.

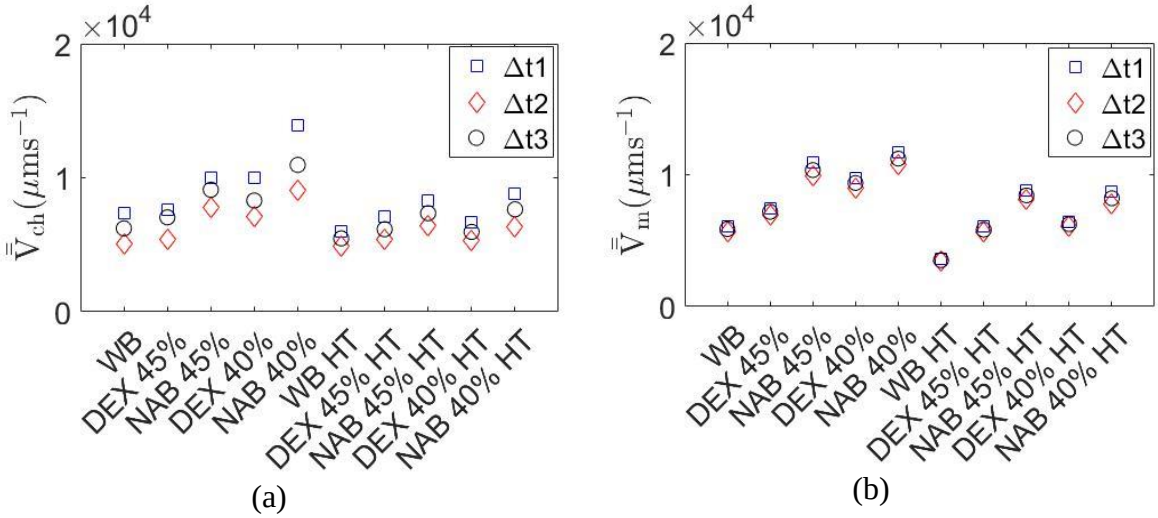

Figure 5.15. Velocities $\bar{\bar{V}}_{ch}$ and $\bar{\bar{V}}_{m}$ (panels (a) and (b) respectively) for the three periods Δt_1, Δt_2 and Δt_3 and for normal and heat-treated samples.

5.10.1 Velocity ratio

Another important characteristic of the velocity field, is the shape of the velocity profiles. It appears from Figure 5.13 above that the heat-treated samples show a slightly smaller flat area in their profile, compared to the normal samples, which could imply a higher maximum to mean velocity ratio. To quantify these characteristics a velocity ratio index was defined, similar to previous studies [31,39,48], which could allow assessing also the effects of aggregation and RBC deformability: $V_{RI} = \frac{\bar{\bar{V}}_{ch}}{\bar{V}_{ch-max}}$. The maximum velocity $\bar{V}_{ch-max}$ was utilised for the normalization of the mean channel velocity. Hence, V_{RI} will be closer to a value of 1 when larger population of RBCs approaching the maximum velocity in the channel. The resulted V_{RI} indices calculated for the overall period Δt_3 are shown in Table 5.4.

Sample	WB	WB HT	Dex 45%	Dex 45% HT	NAB 45%	NAB 45% HT	DEX 40%	DEX 40% HT	NAB 40%	NAB 40% HT
V_{RI} (-)	0.87	0.80	0.86	0.83	0.87	0.87	0.88	0.87	0.86	0.86
ΔV_{RI}%	-8.50		-1.06		-0.13		-0.75		-0.52	

Table 5.4. V_{RI} calculated for the Δt_3 period, for all samples and conditions. The difference between the normal and the HT cases are also shown.

V_{RI} was found to be slightly decreased in the HT samples, particularly for WB and aggregative samples; comparing WB, DEX45% and DEX40% shows that the higher the aggregation the

largest the reduction in velocity ratio. This is more obvious in Figure 5.16, which also illustrates the effect of haematocrit: the higher the haematocrit, the greater the effect of HT on the bluntness of the profiles. Non-aggregative samples NAB45% and NAB40% exhibit a much smaller decrease in V_{RI} compared to aggregative ones. However, although a decrease in velocity ratio is observed post HT, for both aggregative and non-aggregative samples, the change is not statistically significant.

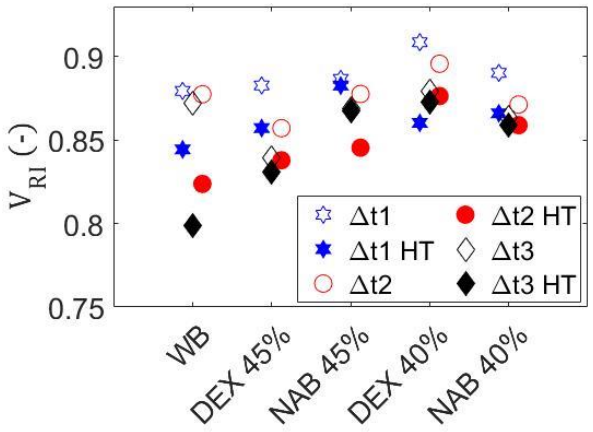

Figure 5.16. Comparison of V_{RI} between all samples, conditions and periods of time.

5.10.2 Shearing conditions

The shear rate magnitude in the microchannel was evaluated similarly to section 4.10 and other studies [106,109], as explained in Section 3.6.5. Therefore, the mean shear rate $\bar{\dot{\gamma}}_{ch}$ was obtained using Eq.3.9 as $\bar{\dot{\gamma}}_{ch}(x^*) = \sqrt{\left(\frac{d\bar{V}_{ch}}{dx}\right)^2 + \left(\frac{\bar{V}_{ch\,max}}{h}\right)^2}$.

An average shear rate in the channel flow, $\bar{\bar{\dot{\gamma}}}_{ch}$, was obtained by integrating $\bar{\dot{\gamma}}_{ch}(x^*)$ in the x^* and dividing by Δx^*as: $\bar{\bar{\dot{\gamma}}}_{ch}(x^*) = \frac{1}{\Delta x^*}\int_{-0.5}^{0.5} \bar{\dot{\gamma}}_{ch}\, dx^*$.

Figure 5.17 shows the $\bar{\dot{\gamma}}_{ch}$ profiles obtained for all samples and for the two measuring periods Δt_1, and Δt_2. From the $\bar{\dot{\gamma}}_{ch}$ profiles can be extracted that the shearing conditions developed in the microchannel, for both Δt periods, seem sufficiently intense to keep RBC aggregation at low levels. Furthermore, as aforementioned, μPIV underestimates the velocity field, therefore the shearing conditions were also underestimated. Shear rates in these experiments ($\bar{\dot{\gamma}}_{ch}$ and $\bar{\bar{\dot{\gamma}}}_{ch}$) were underestimated by approximately 15%. This gives indication that the shearing conditions should be even stronger leading to further disaggregation.

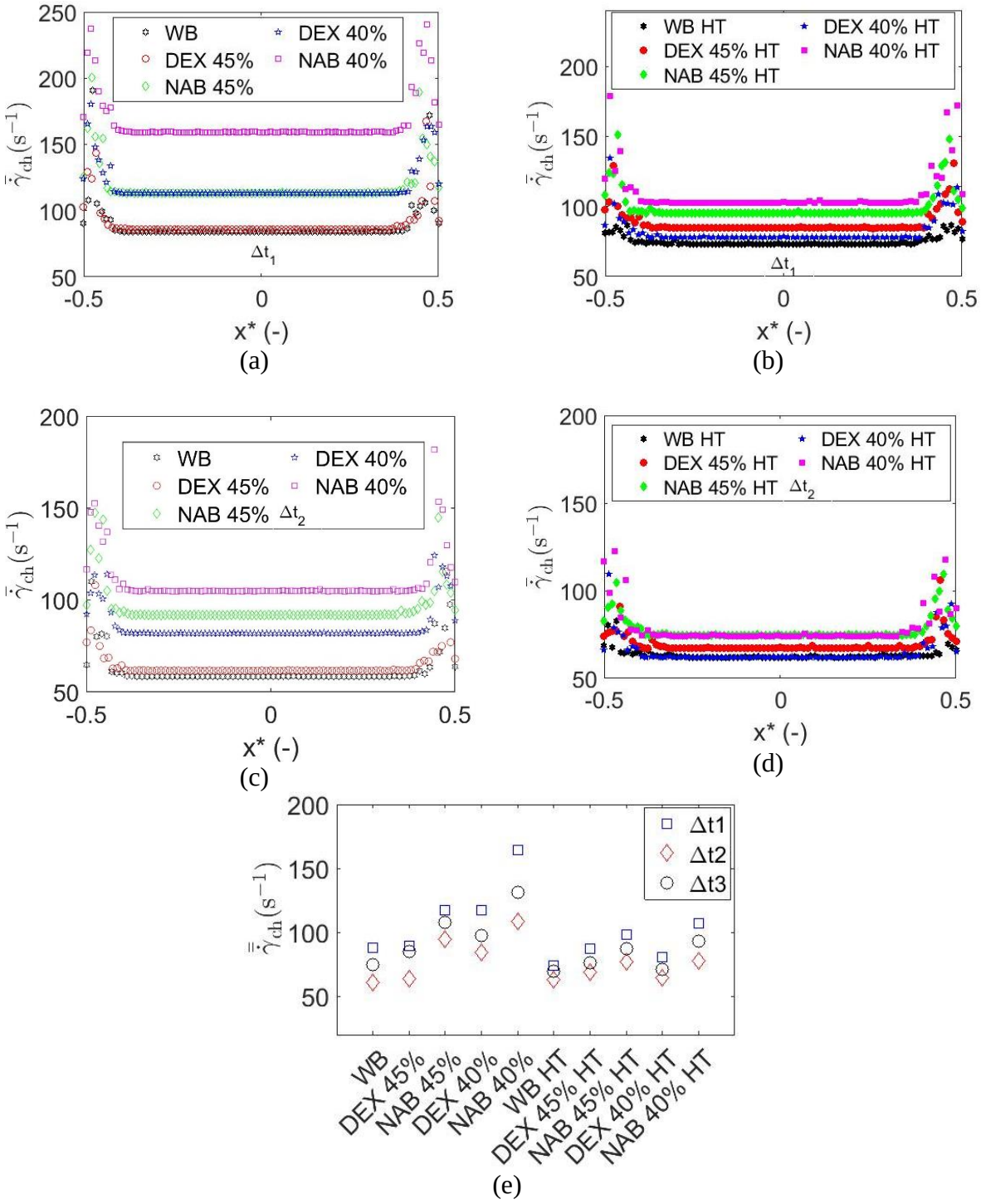

Figure 5.17. (a) and (b): $\overline{\dot{\gamma}}_{ch}$ at Δt_1 for normal and heat-treated samples. (d) and (e): $\overline{\dot{\gamma}}_{ch}$ at Δt_2 for normal and heat-treated samples. (e): The mean shear value $\overline{\overline{\dot{\gamma}}}_{ch}$ for Δt_1, Δt_2 and the overall period Δt_3.

For the WB case which is the most viscous and aggregative, and hence having the smallest velocity and shear rates, $\overline{\overline{\dot{\gamma}}}_{ch}$ is ~ $90s^{-1}$ at Δt_1 decreasing to ~ $60s^{-1}$ at Δt_2. It should be noted

also, that for the overall duration of the flow (Δt_3), when averaging the $\bar{\dot{\gamma}}_{ch}$ profiles into $\bar{\bar{\dot{\gamma}}}_{ch}$, the shear rate values are within disaggregation shear rates mentioned in section 3.6.5 [12,13].

The meniscus mean shear rate ($\bar{\dot{\gamma}}_m$) was calculated only using $\left(\dot{\gamma}_{o-p} = \frac{\bar{V}_m}{h}\right)$ since data to the in-plane direction could not be obtained by using the side camera with which the meniscus flow was captured. Hence, $\bar{\dot{\gamma}}_m$ at each meniscus position was found from the velocity curves ($\bar{V}_m$ vs z curves: Figure 5.12a), as: $\bar{\dot{\gamma}}_m(\mathrm{z}) = \frac{\bar{V}_m(z)}{h}$. Further another bulk shearing parameter was calculated for the three time periods ($\Delta t_{1,2,3}$), from the produced shear rate curves (Figure 5.18a), as the mean of the $\bar{\dot{\gamma}}_m(\mathrm{z})$ data, i.e: $\bar{\bar{\dot{\gamma}}}_m = \frac{\sum_1^n \bar{\dot{\gamma}}_m(\mathrm{z})}{n}$, to indicate the overall shear strain that the fluid is exposed to throughout the duration of the STD flow. Shear rate index, $\bar{\bar{\dot{\gamma}}}_m$, was calculated from z = 5mm until the end of the channel z = 20mm i.e in the linear region in order to avoid the initial fast deceleration rate for better clarity.

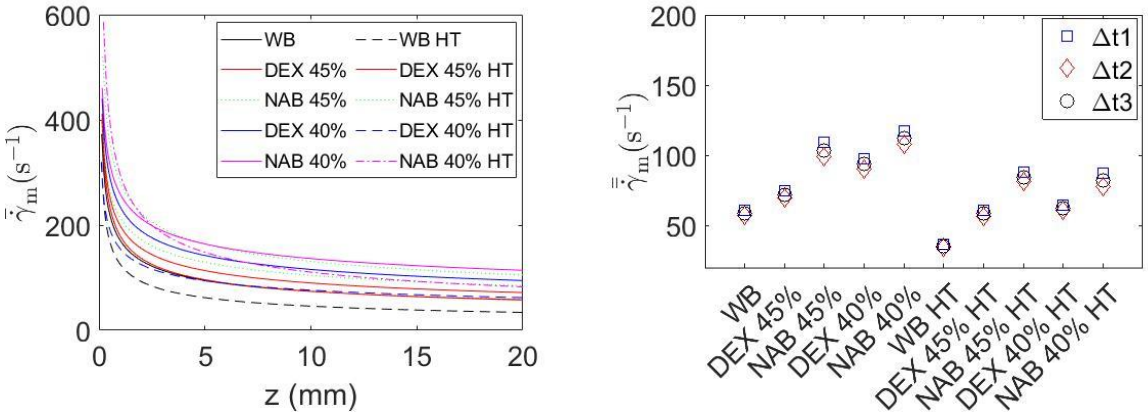

(a) (b)

Figure 5.18. (a): $\bar{\dot{\gamma}}_m$ for all cases, and (b): $\bar{\bar{\dot{\gamma}}}_m$ for the three time periods Δt_1, Δt_2 and Δt_3.

The initial shearing conditions near the entrance of the channel will influence the aggregation state in the area, which consequently may affect the rheological properties of the samples downstream (shearing history). Figure 5.18 illustrates the shear behaviour in the flow as calculated from the meniscus velocity. Very high shear rates are observed at the beginning of the flow (> 400 s^{-1}), which decrease, as the flow decelerates, to approximately 100 s^{-1} until about L_m ~ 5mm. The rate of decrease of the shear rate after the length of 5 mm, until the meniscus reaches the end of the channel (L=20mm) appears low, with moderate shearing conditions ($\bar{\bar{\dot{\gamma}}}_m$ > 50s^{-1}) in relation to reported disaggregation shear rates in Section 3.6.5 [12,13].

When considering the larger meniscus velocities in the initial part of the channel (Figure 5.12) and the calculated shear rates $\bar{\dot{\gamma}}_m(z)$ in Figure 5.18a, it is obvious that intense shearing (>100 s^{-1}) occurs for a significant part of the flow.

For the WB case shear rates (which is the most aggregative and more viscous, hence having less favourable flow conditions than the other samples) larger than $300s^{-1}$ are observed at the beginning of the flow with much larger values for the other samples. This suggests that intense disaggregation takes place at the initial stages of the flow and may continue for the largest portion of the flow for the normal samples. Further, Figure 5.18b indicates that the general shearing level that the samples are exposed, are within the abovementioned disaggregation shear rates. The exact shear rate values are subject to errors due to the assumptions made and the velocity measurements and hence should be treated with caution.

5.11 Discussion on the convergent microchannel study

This work examined systematically the impact of important mechanical properties of blood, namely aggregation and deformability under STD flow, in a converging rectangular super hydrophilic channel. This study, according to our knowledge so far, is the first systematic study examining the abovementioned blood mechanical properties in STD flows.

The microfluidic chips were designed for simplicity, and low manufacturing cost, having improved surface properties to favour the generated STD flow, resulting in pumpless flow delivery channels. The channels (Figure 5.1) were manufactured using xurography techniques for the cutting of the channel boundaries, followed by sandwiching the cut double sided adhesive tape between the treated glass slides as explained in Section 3.2.2. This approach ensured the rapid production of the test chips.

The increased hydrophilicity of the channel surfaces had a favourable impact on the flow, as seen in the flow of the WB sample for example. For the particular case the mean velocity increased from approximately 2 mm s^{-1} (observed in the experiments in section 4.1 (Figure 4.7) using microchannel version 1 i.e, untreated, straight geometry) to approximately 8 mms^{-1} (an approximately 4-fold increase) in the present experiments (Figure 5.12a at z = 10 mm). Part of this increase however, is attributed to the convergent geometry of the channels adopted in this work, compared to the straight configuration used in section 4.1. Indeed, it was found that the velocity of the Newtonian fluids tested were higher in the convergent section compared to the straight one (section 3.2.2.1 Figure 3.2 and Figure 3.3) in agreement with previous works [72,73].

The influence of rheological parameters in the flow of blood is relatively well understood, and a plethora of works exists in the literature for pressure drive flows. Much less is known for surface tension driven flows of blood; reports in the literature present mostly information on the velocity of the meniscus, and in certain cases, the local velocity field ([37,57–59,62,106]), with little reference to the haemorheological factors.

The present work confirmed that the increased haematocrit, elevates the viscosity of the fluid (Figure 5.7 and Figure 5.10a-d and f), in both aggregative and non-aggregative cases, and in the normal and the heat-treated conditions also. This results in smaller channel and meniscus velocities, according to Figure 5.15 for both normal and heat-treated samples.

RBC aggregation (RBCA) was measured in the aggregating working fluids (WB and DEX samples), and was found higher in WB samples, since the Dextran concentrations used in the experiments resulted in a moderate aggregation intensity (Figure 5.8). The most aggregative samples produced a higher viscosity and apparent viscosity (Figure 5.7, Figure 5.10a-d and f) [123], resulting in reduced mean meniscus and channel velocities (Figure 5.12c,f and Figure 5.15)

RBC deformability was found similar in both aggregative and non-aggregative working fluids, within the normal and the heat-treated sample groups (Figure 5.9). As already mentioned the sample treatment, and the medium fluids (PBS, and Dextran solutions) do not seem to have a significant effect on the cell deformability. The heat-treatment, however, reduced significantly the cell deformability for all working fluids tested (Figure 5.9 and Table 5.2). The decrease in RBC deformability in the HT samples results in an increase in the viscosity (Figure 5.7 and); this is illustrated in the mean relative/virial viscosity and the bulk viscosity index $\bar{\bar{\mu}}$ plotted in Figure 5.10a-d. This is in agreement with other studies in the literature [79] and results in a decreased mean meniscus and channel velocities (Figure 5.12a).

The aforementioned observations are also reflected in the relations between the hemorheological parameters with the mean meniscus velocity (Figure 5.19). As expected the most consistent (negative) trend is this of the viscosity on the mean velocity of the fluid in the channel (top-left panel in Figure 5.19). The impact of the reduced deformability is also apparent between the normal and the heat treated samples (top-right panel in Figure 5.19), whereas the effect of the haematocrit is not very clear when examined explicitly (Figure 5.19, bottom-right panel), mostly due to the relatively narrow haematocrit range (40 – 45%). The aggregation intensity in the samples appears to have a non-monotonic effect on the meniscus velocity; it

seems to promote the flow in the heat-treated samples, whereas the opposite is apparent in the normal samples (Figure 5.19 bottom-left panel). For the former, aggregation is very low in the heat-treated samples due to RBC hardening, whereas in the latter case normal aggregation appears for the physiological WB sample and decreased in the Dextran cases. From the trends illustrated in Figure 5.19, this of the viscosity and velocity (Figure 5.19 top-left panel) seems the most consistent, with a correlation found to be -0.92 having an R^2 value of 0.85.

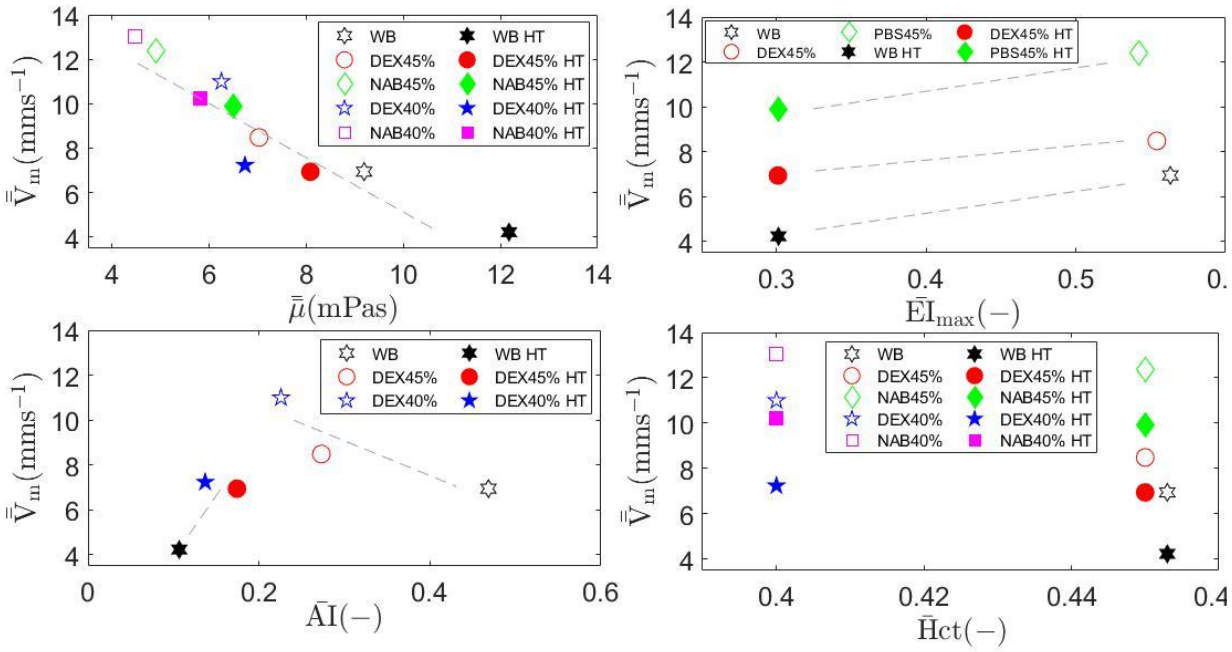

Figure 5.19. Trends between the various hemorheological factors and the velocity of the meniscus (lines are not fitted on the data).

When examining the local velocity characteristics (Figure 5.13) it appears that the heat-treated samples exhibit a higher V_{RI} index, which implies less blunted velocity profiles (Figure 5.16), similarly to those observed in Passos et al [48], where the flow of hardened RBCs was examined in straight microchannel pressure driven flows. The highest V_{RI} index is observed for the normal aggregative DEX40% sample, whereas the largest difference in the V_{RI} between normal and heat-treated samples is obviously in the WB sample. Another important result stemming out from the velocity analysis is the shear characteristics in the channel. High enough shear rates are observed during the flow (Figure 5.17 and Figure 5.18) which should cause intense disaggregation conditions in the channel. For the WB case shear rates larger than $300s^{-1}$ are observed at the beginning of the flow with much larger values for the other samples. Moreover, the values of $\bar{\bar{\gamma}}_m$ in Figure 5.18 indicate that the overall shearing exposure is above

50 s^{-1} suggesting good disaggregation conditions since its very close to the disaggregation shear rates known in the literature [12,13].

The favourable flow and shearing conditions developed in the current configuration are also important for the measurement of hemorheological parameters such as the RBC aggregation. The initial conditions for such measurements require the blood sample to be at dispersed state. Commercial aggregometers (including Rheoscan A used in the present study) utilise mechanical techniques to achieve the disaggregated state, whereas in the present configuration this is achieved in a passive manner. Hence the developed channel can be potentially used to measure RBCA, using a very small volume of blood (similar to volume produced by finger prick), and by utilising image processing algorithms, similarly to previous works [106].

5.12 Remarks on the flow within the convergent microchannel.

The present study investigated the surface tension driven flow of blood in a superhydrophilic rectangular microchannel with a slightly converging geometry. The influence of RBC aggregation, deformability and haematocrit, and consequently the sample viscosity, on the flow were examined using microPIV and image processing techniques. The study was motivated by the popularity of the particular flow mechanism for point of care diagnostics, and the lack of a systematic approach to assess the effect of important rheological characteristics of blood on the flow performance of such microfluidic set ups.

The treatment of the microchannel surfaces with $Ti0_2$ in combination with the 3-degree convergent channel, significantly improved the flow conditions compared to previous studies in similar geometries. The more aggregative samples were found to have smaller meniscus and channel core velocities than the non-aggregative ones, due to their higher viscosity. The reduced RBC deformability in the heat-treated samples also decreased the velocity of the samples, despite a reduction in the extent of aggregation with heat treatment; an increase in viscosity was also observed in these cases. The haematocrit was also found to have an effect as expected; increasing the haematocrit decreased the velocity of the samples which can be attributed to the higher viscosity of denser samples. No significant variation was observed in the velocity profile characteristics between the normal and heat treated samples, with the exception of WB, which showed a notable decrease in the V_{RI} index following heat treatment.

Very high shear rates were observed upon initialization of the flow suggesting high disaggregation in the inlet sections of the geometry. The shear rate gradually decreases as the flow proceeds; however, it remains sufficiently high until the flow reaches the end of the

channel. The shear conditions developed in the microchannel, especially close to the walls appear sufficiently strong to keep RBC aggregation at low levels for the duration of the flow.

The heat-treatment of the samples (in particular in the case of WB) could also relate to the direct effects of thermal injuries on blood physiology, and the consequences this may have on the circulatory flow. The importance and role of blood flow in the thermal injury (e.g. heat stroke or exposure to extremely high temperatures) is well documented in the literature. This includes the transport of heat from the body core to the skin surface, and a great increase in cutaneous blood flow. Nevertheless, experimental studies of thermally exposed blood flow in the microscale are scarce in the literature and little is known about the local flow characteristics in these cases. The present results suggest a significant influence of the heat effect, not only on blood physiology, but in the local flow characteristics (bulk velocity magnitude and profile).

The results of the present study provide important information regarding the surface-tension driven blood flow in converging microchannels with rectangular cross-section, which could aid the design of relevant devices and experiments. Future work should address issues regarding cell distribution and sedimentation, as well as flow extension and duration.

CHAPTER 6. Blood microstructural characteristics assessed in the straight microchannel[*].

In this Chapter the assessment of blood's major microstructural property, namely RBC aggregation (RBCA), in a square microchannel will be described. The aim was to further explore the possibility for using the microchannel as a testing-chip in a Point of Care Device (POC) device for assessing RBCA. Indeed, in the experimentation using the straight microchannel (Chapter 4), an initial estimation of RBCA was performed, using the coefficient of variation as an RBCA index (Figure 4.9). RBCA in a square microchannel was also examined as part of the work described in Kapnisis et al., [126] and in the present chapter the details from the aforementioned work [126] for RBCA characterization will be described. Other parts from the work in the specific publication will briefly mentioned.

6.1 Red blood cell aggregation and viscosity in the stented tube

The detailed examination of the effects of various biomechanical properties of blood under surface-driven flow shown in Chapters 4 and 5, illustrated that the particular setup is suitable for use in order to detect alteration in blood properties in the micro scale as a result of external factors. Therefore, the RBC aggregation alterations (and other mechanical and physiological properties of blood), as a result of flow through stented vessels were examined.

For the part of the work described below, the blood samples used, were prior subjected to flow through a stented microtube, which was used in order to assess the effects of the particular condition in the RBC aggregation phenomenon and other hemorheological properties. Aggregating and non-aggregating samples were subjected to various flow rates within and above the physiological range, in a clear (not-stented) tube and in a stented-tube. Self-expanding nitinol stents were inserted in clear perfluoroalkoxy alkane tubing. The tube was connected to a syringe, and the latter was integrated in a syringe pump. The samples were tested at flow rates of 17.5, 35 and 70 ml/min. The flow in the non-stented vessels was regarded as

[*] Parts of this work have been published in:

- Pasias D., Passos A., G. Constantinides, L. Koutsokeras, S. Balabani, and Kaliviotis E. (2020). Surface tension driven flow of blood in a rectangular microfluidic channel: effect of erythrocyte aggregation. Physics of Fluids, 32, 071903, doi.org/10.1063/5.0008939.
- Kapnisis K., Seidner H., Prokopi M., Pasias D., Pitsillides C., Anayiotos A. and Kaliviotis E., (2019). The effects of stenting on hemorheological parameters: an in vitro investigation under various blood flow conditions. Clinical Hemorheology and Microcirculation, 72(4), pp. 375-393.

the control case. The effect of stenting for each flow rate on red blood cell aggregation and viscosity was examined using commercial instruments, Rheoscan-A200 and BrookfieldDV2T viscometer respectively. A preliminary design of a microfluidic POC system, incorporating the capillary driven flow configuration (the microchannel) to measure red blood cell aggregation was developed. Aggregation indices under the various flow conditions in the experiments were measured with the developed POC microfluidic system (termed Capillary Driven Microfluidic Aggregometer - CDMA) and compared with commercial aggregometer Rheoscan-A200.

6.2 Specific methodological issues

6.2.1 Sample preparation

The study protocol was approved by the Cyprus National Bioethics Committee (ref:EEBK/E_/2016/18). Samples were collected from a healthy population (9 humans, 25–46 years) into vacuum tubes (BD) containing 1.8 mg/ml EDTA, using a 21G needle. After collection, one portion of the blood donation from each participant was centrifuged at ~1350g, for 10 minutes, in order to remove the buffy coat and to adjust the haematocrit (45% by adding/subtracting plasma). This portion of the sample was kept as the normally aggregating blood (AB) sample. Another portion of the blood donation was used in order to produce non-aggregating blood samples (NAB) as explained in Section 3.7. All samples were oxygenated by rolling in the 50 ml syringes, for approximately 1/2 minute prior to extracting the air from the syringe. Hemorheology tests were performed immediately after collection and treatment, and within 4 hours, except for a small number of tests for which the samples were kept at 4 ^{0}C until testing.

6.2.2 Tube stenting experimental setup

The experimental set-up is shown in Figure 6.1. Self-expanding nitinol stents (1.0×3.3 mm, closed-cell design with diamond-shaped pattern, Figure 6.1a) were inserted in clear perfluoroalkoxy alkane (PFA) tubing of internal diameter 0.75mm (Figure 6.1b). The tubing was connected to a syringe (50 ml) through a 20G needle, and placed on a syringe pump (KDS 200) as shown in Figure 6.1c. The internal diameters of the 50 ml syringe tip (2 mm), the 20G needle tip (0.603 mm) and the PFA tubing (0.75 mm) were larger than the (minimum) deployed stent diameter (0.570 mm) - all internal diameters were larger than the internal diameter (0.514 mm) of the 21G needle used in the blood sampling. The perfused samples were collected at the exit of the tube in 1.5 ml Eppendorf tubes (Figure 6.1c). An identical tube-needle set up,

without stenting, was also used for comparison as the control cases. All tests were performed at identical flow conditions in both tube set ups.

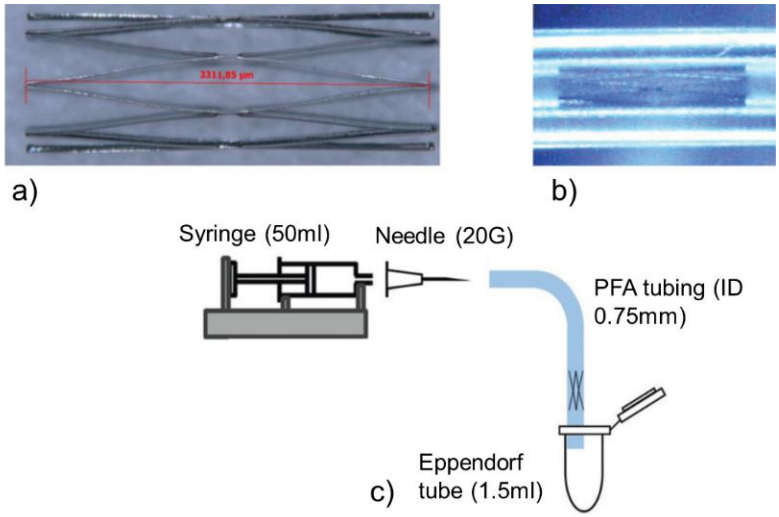

Figure 6.1. Tube stenting experimental setup [126]**. (a): The nitinol stent used in the study. (b): The inserted stent in the PFA tubing. (c): A diagrammatic representation of the flow configuration (not drawn to scale).**

6.2.3 Flow conditions

The aggregating and non-aggregating blood samples (referred to as AB and NAB respectively) were infused in both set ups (stented and non-stented tubes) at three flow rates (Q = 17.5, 35 and 70 ml/min) to reflect a range of physiological flow conditions. A triple exposure of the samples to Q = 70 ml/min was set as an extreme flow condition, for the stented case only; this was achieved by infusing/withdrawing/infusing the same volume of the sample. The aforementioned flow cases will be referred to as Q17.5, Q35, Q70 and 3XQ70 respectively, for convenience. Hemorheological tests were also performed in samples that did not undergo any infusion in the tube set-ups and served as the baseline cases (referred to as BL cases). BL samples were placed in the Eppendorf tubes prior to transportation in the syringe/tube set up.

6.2.4 Microchannel design and fabrication

The microchannel needed to fulfil the following requirements: a) to be simple to manufacture and b) be cost effective. As aforementioned, RBCA is a shear dependent phenomenon [13], hence prior to any measurements appropriate shearing and hence disaggregation conditions should be ensured as in other commercial instruments [88]. The Straight Microchannel (see Section 3.2.1) was used, as shown in Figure 3.1 and Figure 6.2 (fabrication is explained in Section 3.2.1). The specific design was chosen due to the simplicity, the ease of manufacturing,

and the good disaggregating conditions within the channel, as seen in the experiments in Section 4.10 (Figure 4.10). However, in terms of dimensions an aspect ratio (AR) of 20 was used instead of AR = 3 as in the initial design. A large AR was deemed appropriate due to the low resolution USB camera used in the CDMA device, hence a large Region of Interest (ROI) is needed for image processing. Nevertheless, for AR higher than 1.5 no considerable changes in flow conditions are observed in a capillary driven flow [56]. Hence, moderate/high shear rates and good disaggregation conditions in the beginning of the flow are expected in the channel used in the CDMA device with increased AR. This is observed in the experiments in Section 4.1 for AR=3 (Figure 4.9 and Figure 4.10).

6.2.5 Red blood cell aggregation assessment

Various methods for the assessment of RBC aggregation have been demonstrated in the literature, including mainly optical based methods, and other approaches such as electrorheology techniques [127]. In the aforementioned work it was shown that optical (image processing) techniques agree with electrorheology results for experiments performed at similar conditions. In the electrorheology approach the conductivity of the blood samples was measured for various flow conditions (shear rates), reflecting the restructuring taking place within the sample, as a result of the aggregation dynamics.

Optical techniques were adopted in the present part of the work. RBC aggregation was measured with a Rheoscan A200 instrument described in Section 5.6. In addition, RBC aggregation measurements were performed in the capillary driven microfluidic aggregometer (CDMA) developed in the laboratory and described below.

6.2.6 Capillary driven microfluidic aggregometer (CDMA)

The capillary driven microfluidic aggregometer (CDMA) consisted of a USB camera (XIMEA 1fps capturing images with dimensions 640 x 480 pixels) positioned directly above a microchannel and an Arduino microprocessor connected to a PC (Figure 6.2). Illumination was provided by the USB camera integrated LEDs. A blood drop of 50μl was placed at the channel entrance using a micropipette and the flow was driven by capillary forces in the channel. The device was controlled by the Arduino microprocessor connected to the PC, using python software. Images of the flow where captured by the USB camera after the meniscus has reached the end of the channel, and when the flow was stopped. The images where captured for 120s in 1 fps as in the Rheoscan-A200 commercial instrument [88].

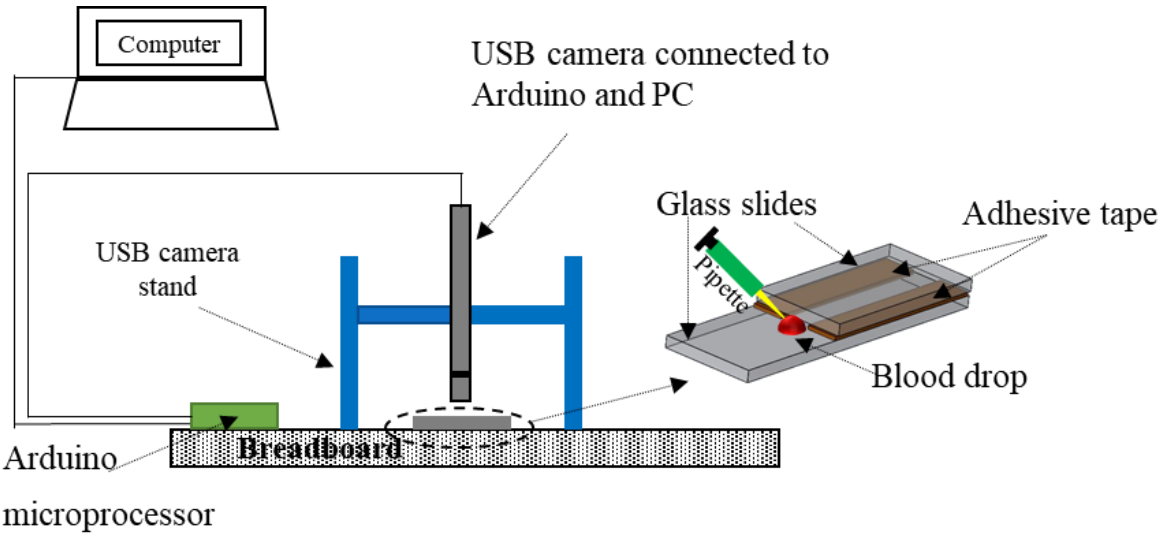

Figure 6.2. The Capillary Driven Microfluidic Aggregometer (CDMA) setup.

6.2.7 RBCA assessment in the CDMA

The images captured in the CDMA setup were analysed using Matlab software. RBC aggregation was measured taking into account the intensity differences between the captured images. Mean intensity of each image was found by enable average and plotted against time to produce intensity curves. RBCA causes changes in the image intensity characteristics, which result to variation in the intensity of each image.

The mean intensity ($\bar{I}$) of the 120 images was found as an ensemble average of the image intensity variation. Hence it was plotted against time producing intensity curves (Figure 6.3) similarly to the commercial aggregometer Rheoscan-A200. Technical issues, such as sudden reduction in the light intensity of the USB camera, resulted to dropped magnitudes of the $\bar{I}$ and hence a correction of the intensity curve was performed when such condition was detected (Figure 6.3a and Figure 6.3b). The correction was performed, using specific Matlab algorithms (Appendix 1). The intensity curves were normalized with the minimum intensity for better presentation, i.e., $I^* = \frac{I}{I_{min}} - 1$, and shown in Figure 6.3c.

A double exponential fit was also performed on I^* and plotted with the raw data (Figure 6.3d). The double exponential equation is given bellow:

$$I_f^* = ae^{bt} + ce^{dt} \qquad 6.1$$

where a, b, c and d are constants.

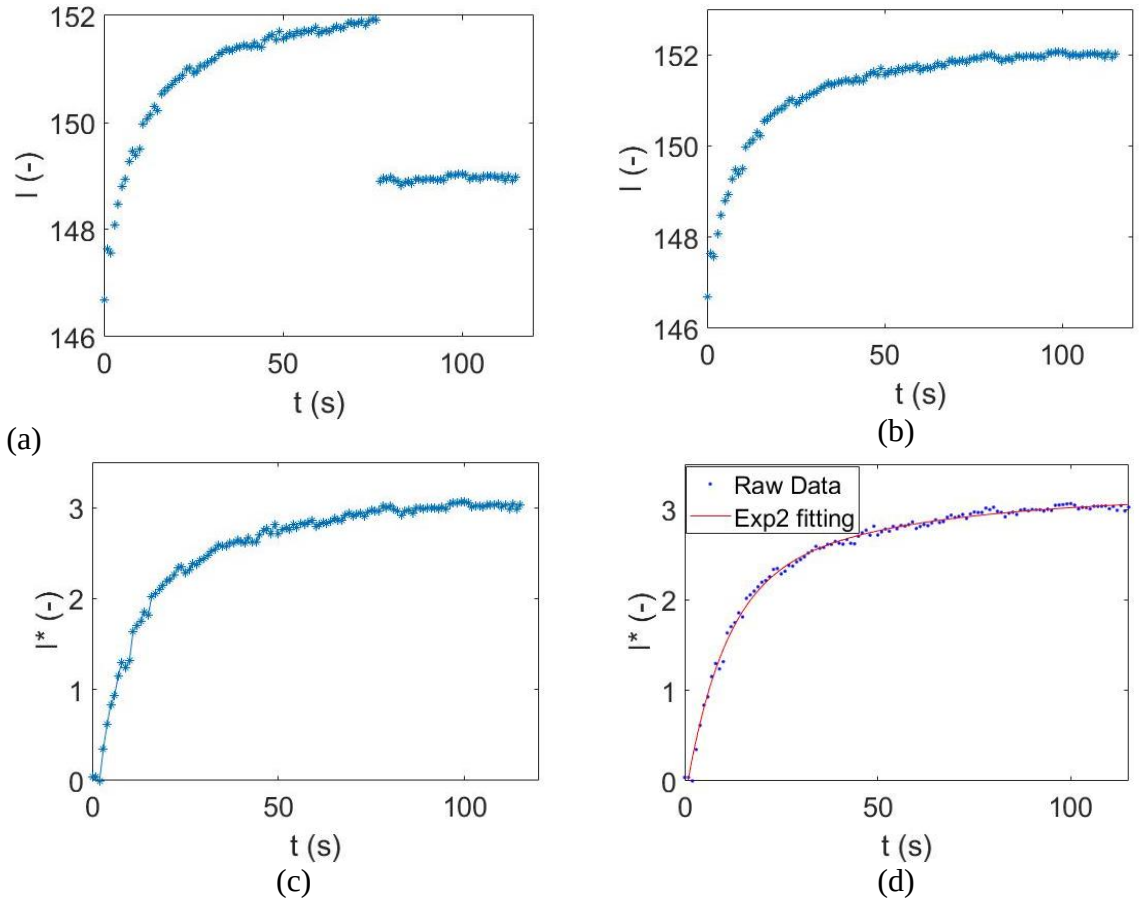

Figure 6.3. Representative results from the CDMA for a representative sample. (a): Intensity curve (raw data). (b): Corrected intensity curve. (c): Intensity curve normalized. (d): Normalized intensity curve with double exponential fitting.

The RBC aggregation indices AI, half time $t_{1/2}$, and AMP were calculated for the AB samples from the final intensity curves (Figure 6.3d), similarly to the methodology used by the Rheoscan-A200 commercial instrument (explained in section 5.4), for a direct comparison. The RBCA indices were produced for all flow rates and for both stented and baseline cases. The mean values of the indices (AI, $t_{1/2}$ and AMP) at each flow rate and sample condition, produced from the CDMA device final intensity curves, was compared with the results from Rheoscan-A200.

6.2.8 Viscosity of the utilised samples

Viscosity measurements were performed to assist the analysis of the results. The Brookfield DV2T instrument was used for the viscosity measurements as described in Section 4.3 and section 5.7). Samples were transported immediately after infusion in the stented (or non-stented) tubes using Eppendorf tubes and gently loaded with a micropipette (0.6 ml volume) in the plate of the viscometer. Viscosity tests were initiated after approximately 1 minute from

perfusion in the tubes. AB and NAB sample viscosities were measured for shear rates between 251.2 and 1.4 s^{-1} in this order. Plasma viscosity was also measured for all samples prior to perfusion in the tube set-ups.

Sample viscosity results were normalised by their plasma (or PBS medium) viscosities to obtain the dimensionless relative viscosity i.e: $n_{r-p} = n_{sample}/n_{plasma/medium}$. Hence n_{r-p} values at three distinct shear rates (2.275, 7.878 and 15.820 s^{-1}) were chosen, in order to compare the results from the tested cases. The measured n_{r-p} values at those shear rates were further normalised by the highest shear rate n_{r-p} value. The double normalisation of the viscosity values (referred to as η_r) was deemed necessary in order to mediate the effects of inter-donor variation in viscosity, and to account for the differences in the plasma/medium viscosities of the samples.

6.3 Results

6.3.1 Red blood cell aggregation measurements

The indices produced from the Rheoscan-A200 and CDMA system where normalized with their baseline values for better comparison and shown in Figure 4.33a, c, and e. The percentage difference of the indices produced from the Rheoscan-A200 and the CDMA was found as: $100 \times (CDMA_{index} - Rheoscan_{index}) / CDMA_{index}$ and are shown in Figure 6.4b, d and f. Figure 6.4a illustrates that both the Rheoscan-A200 (in the graph is refer to as "Rheo" for space economy) and the CDMA device show a decrease in AI* as the flow rate Q increases.

The Rheoscn-A200 shows a further decrease in AI* in the extreme condition 3XQ70, although no further change is detected by the CDMA system in the particular condition. The decrease of RBCA as Q increases might be due RBC deformability changes as stronger collisions and shear forces are expected to develop in the stented area. In the specific cases the deformability of the RBCs has been found to be affected (decreased) by the increasing flow rate [126]. It is known in the literature that RBC deformability affect aggregation; reduced deformability decreases aggregation [128].

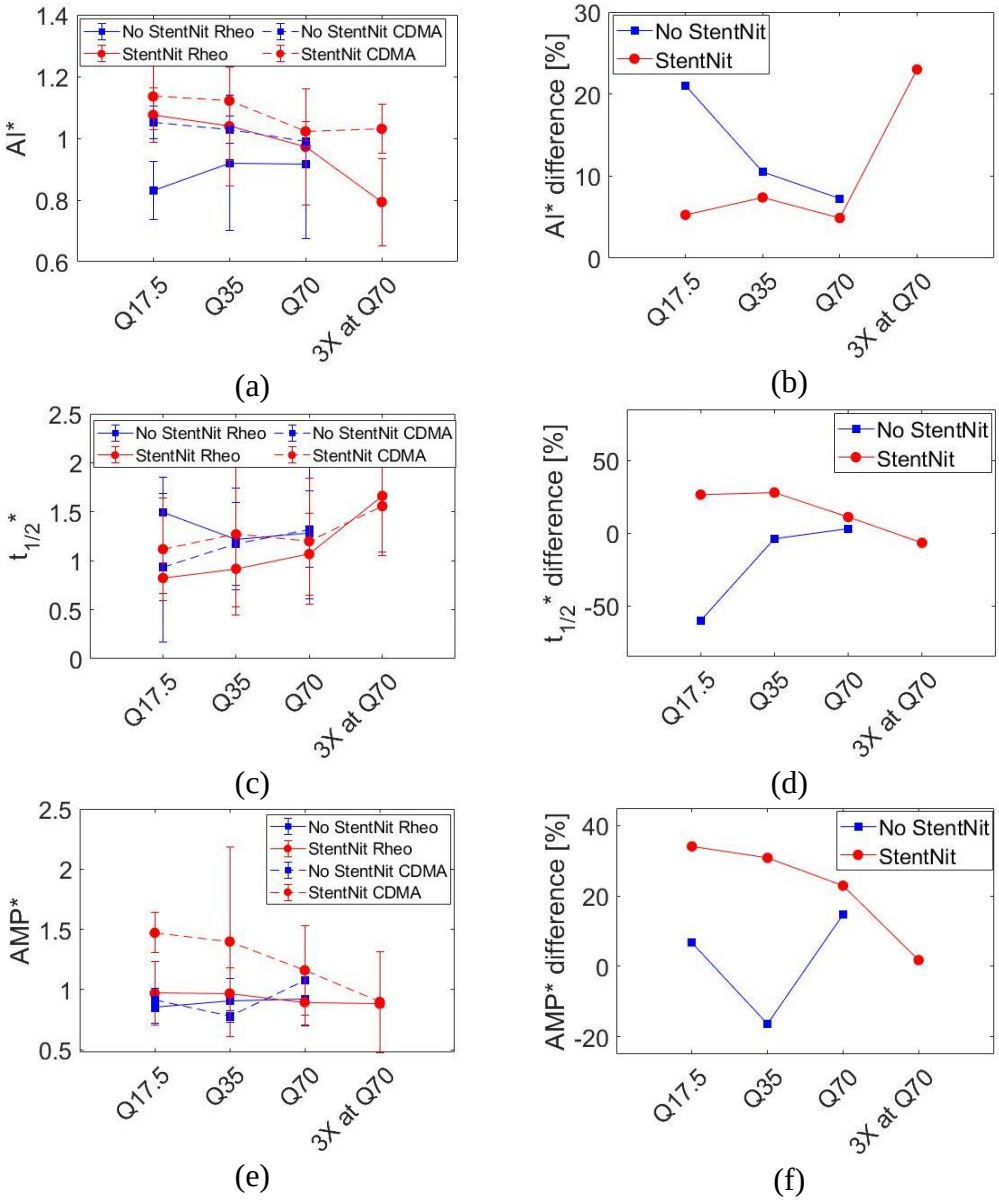

Figure 6.4. Rheoscan-A200 and CDMA normalized indices for Q=17.5, Q=35, Q=70 and Q=70 3X are shown in (a): AI* index, (c): $t^*_{1.2}$ and (e): AMP*. The percentage differences between Rheoscan-A200 and CDMA are shown in (b), (d) and (f).

Observing the data in Figure 6.4a for the stented tube condition (termed StentNit in the legend of the graph) a good qualitative agreement between devices, and for the three flow rates is apparent. A deviation in this agreement is observed in the extreme, Q70X3, case. The percentage difference between devices is approximately 5% for Q17.5, 35 and 70 ml/min, and increases to approximately 20% in the Q70X3 case (Figure 6.4b).

Smaller changes in AI* as Q increases, are observed for the not stented cases (termed No StentNit in Figure 6.5), compared to the stented case. This is apparent in the results from both the instruments (Rheoscan-A200 and CDMA). In terms of flow influence in RBCA, this

implies that Q does not affect AI* when stents are not present. As regards the discrepancy between devices (Figure 6.4b) the largest difference appears in the data of the Q17.5 flow rate and reaches approximately 20%. This seems to be the maximum discrepancy in AI* for all cases, implying a promising prospect for the particular method.

An increase in AI* is observed in the stented, comparted to the not-stented, conditions and it is similar in both Rheoscan-A200 (Figure 6.4a) and the CDMA system (10 to 20% increase in both cases). This increase may occur for the changes in deformability of the RBCs as a result of the collisions and stresses developed with the stent area, resulting to an increase in RBCA [78,120].

A similar behaviour for the $t^*_{1/2}$ index of RBCA is apparent in Figure 6.4c. The Rheoscan-A200 results show that $t^*_{1/2}$ follows the AI* behaviour, that is for the stented case $t^*_{1/2}$ increases with Q, implying that aggregation decreases, which is what is observed in AI*. The same trend appears for the not stented case. The inverse relationship between AI* and $t^*_{1/2}$ is similar in the results of the CDMA system for both, not stented and stented case. However, in the latter case the $t^*_{1/2}$ index decreases slightly at Q70. This may be due to the fact that in the CDMA device the pre-shearing shear rate magnitude depends on the flow characteristics of the sample tested, since the flow is capillary driven. For the samples at higher Q condition the viscosity of the sample is lower as explained in the next section and shown in Figure 7.1b, hence the shear rate during the flow is higher. For the higher pre shearing shear rate the $t_{1/2}$ index might decrease, although AI can increase as observed in the work of Kim et al [129] agreeing with the slight decrease of $t^*_{1/2}$ at Q70 observed at the results from the CDMA.

For the stented conditions, the $t^*_{1/2}$ index is lower than the not stented condition for both systems (except for the CDMA device at Q17.5 and Q35, which appears slightly higher). Furthermore, as in the Rheoscan results $t^*_{1/2}$ increases significantly in the extreme case (3XQ70), implying reduced RBCA response. The $t^*_{1/2}$ index discrepancy between systems appears to be higher than the AI* index: Figure 6.4d shows a difference between -50 and 25% in the particular case.

Regarding the AMP* index in Figure 6.4e it is observed that there is a good consistency for the Rheoscan-A200 and the CDMA system when compare with the AI* index. it is observed from Figure 6.4f that the percentage difference of AMP* is relatively low between devices (~5%-30%) indicating good qualitative agreement of the results.

In order to investigate the performance of the CDMA system against the Rheoscn-A200 instrument, the results of the present work were correlated and shown in Figure 6.5.

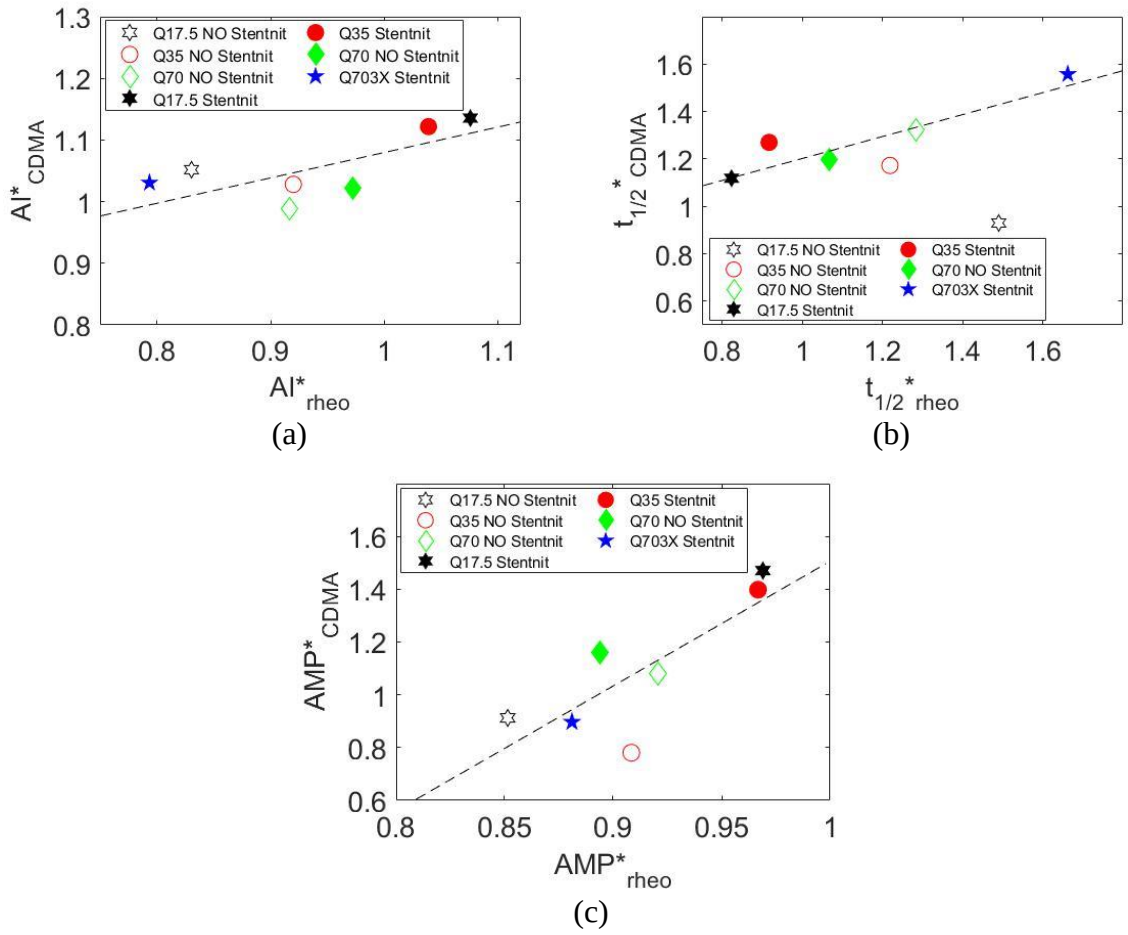

Figure 6.5. Correlation of the normalized indices produced by CDMA and Rheoscan. (a): AI*, (b): $t_{1/2}^*$ and (c): AMP*.

A correlation appears in the AI*, $t_{1/2}^*$ and AMP* index, with an R-Square value of 0.45,0.74 and 0.65 (Figure 6.5a,c) and a linearity as y = 0.35x + 0.72, y = 0.45x + 0.75 and y = 4.87x - 3.85 respectively. The discrepancies between devices may be explained by looking in to the different mechanisms incorporated in each system. Differences exist on the illumination mechanism. In CDMA (Figure 6.2) illumination occurs through the camera LED and the image is captured by the USB camera. The Rheoscan-A200 transmission system consists of a laser diode and a photodiode in a transmission arrangement (see section 3.4.1). For transmission through a thick layer of blood, it is expected that the transmitted intensity decreases in accordance with the Beer-Lambert law: $I = I_0 e^{-\lambda D}$ where I is the transmitted intensity when a light beam of intensity I_0 falls on the suspension of red cells. D is the thickness of the blood

layer, and λ represents the attenuation coefficient of blood in the bulk [130]. Therefore, the difference in the light transmission/illumination mechanism, and the difference in blood layer thickness (100μm in CDMA microchip and 300μm in Rheoscan-A200 microchip) between the two devices may cause discrepancies in the results.

Moreover, RBC aggregates in the CDMA microchip were dispersed prior to measurements by shear rates of the order of 10^2 s^{-1} for a period of ~ 1s due to the capillary forces driving the flow. In the Rheoscan-A200 aggregometer, pre-shearing is achieved by a magnetic stir bar with in the microchip rotates at 900 RPM (resulting to a shear rate of the order of $10^3 s^{-1}$) for 10 s [77,87]. The difference is pre-shearing time and shear rate is known to affect aggregation results [129]. In a study where effects of rational speed of the magnetic stirrer were examined, AI was increased with the rotational speed and reached its maximum at 2800 pm. Further increasing the stirring speed resulted a slight decrease of the AI at 3800 rpm [129]. In addition, the effect of shearing time was examined. For a relatively low shear (1000 rpm), the AI values gradually increased with the shearing time but did not show significant changes up to 60s [129].

6.3.2 Viscosity of the utilised samples

The viscosity is the major parameter affecting the velocity, the shearing conditions and therefore the aggregate dispersion in the testing channel. Figure 6.6 shows the viscosity of the samples at three different shear rates. The viscosity of the aggregative blood (AB) samples in the not stented case does not show considerable changes with Q. This is observed in all shear rates tested. In the stented condition however, the viscosity of the AB samples increases with Q (Figure 6.6a and b) compared to the Baseline value, whereas RBCA decreases with Q, when considering the baseline value (Figure 6.6a). At the low shear rate where aggregation is expected to be more apparent, a decrease in viscosity occurs in the stented case of the AB sample as Q increases from 35 to 70 ml/min and to 3XQ70 condition. This might be due to the decreased RBCA at higher Q conditions (see the AI* in Figure 6.5a).

As observed in Figure 6.6a the NAB sample viscosity in the not stented case does not show any considerable difference for all Qs.

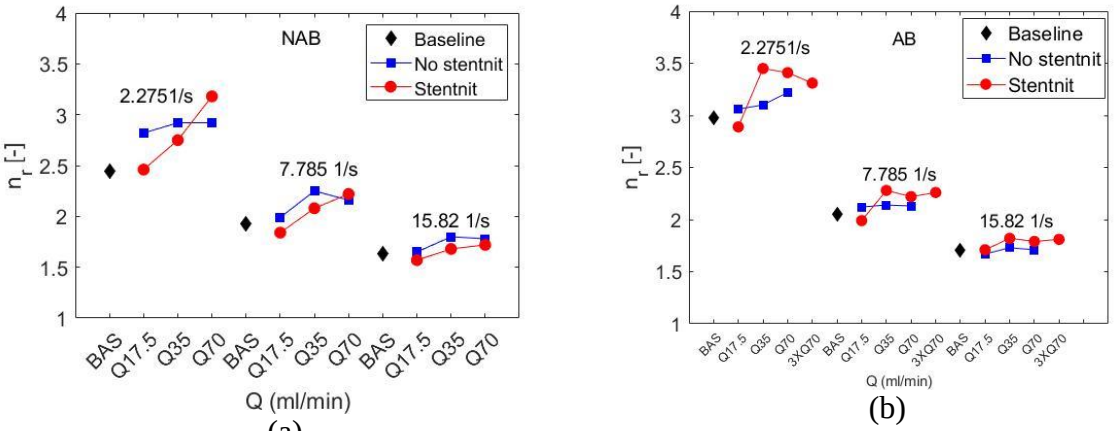

Figure 6.6. Relative viscosity η_r against all flow conditions (BL, Q17.5 Q35, Q70 and 3XQ70), for the two flow configurations (stented and non-stented tubes), and for three distinct shear rates (2.275, 7.878 and 15.820 s^{-1}) [126]**. (a): Results for the NAB. (b): Results for the AB samples (presented separately for clarity).**

In the stented case, and as Q increases, the viscosity also shows a small increase. This increase might be due to RBC deformability changes due to stronger shear stresses in the stented area as Q increases. A decrease in deformability is known in the literature [124], and as observed from the results in this study (Sections 4 and 5), increases the of the sample viscosity. This is more obvious in the lower shear rate (Figure 6.6).

The present results show that the AI* and AMP* indices more reliable from $t^*_{1/2}$ index. The changes in viscosity for the different cases discussed above, might play a part in the measurements of the RBCA by the CDMA device, and it might affect the RBCA indices differently. For example, any residual aggregation at the testing starting time, due to insufficient shearing, would affect the time constant of the double exponential equation, used to extract the RBC indices, differently than the AI index. The AI index is the ratio of the area below the curve with the total area, hence a small error in the fitting due to a residual aggregation will not have much effect on the result. However, for the half time index ($t_{1/2}$), which is the time needed for half of the maximum amplitude to be reached, much less data are used in its calculation. Hence any error in the fitting will give higher error in the half time than AI where all the data are used for its calculation. Nevertheless, it was shown in Section 5 that an improved testing channel can significantly improve the velocity and the shearing conditions in the testing channel. This fact alone could improve the accuracy and robustness of the approach.

6.4 Remarks on the structural characterization via the CDMA device

This part of the study examined the possibility of assessing the RBC aggregation phenomenon on the square microchannel using the CDMA device. For this purpose, data from experiments on the effects of stenting on the rheology of blood were utilised [126]. Aggregating and non-aggregating samples were subjected to various flow rates within physiological and extreme ranges, in a stented tube and a non-stented tube configuration. It was found that in the stented condition the increased flow rates and further exposure to the highest flow rates, had an effect on the rheological properties of blood, such as reduced aggregation and increased viscosity. This might be due to decrease in deformability of RBCs due to stronger shear stresses developed within the stented area at higher Qs, which is known to increase viscosity [124].

Further, a preliminary POC system was produced (CDMA) to measure RBC aggregation. The intensity curves produced by the CDMA device give promising results showing similar behaviour as Rheoscan-A200 commercial instrument for specific indices. Further investigation and development would ensure a better performance of the CDMA device. In addition, the optimization of the channel such as this presented in Section 5 is expected to further enhance the flow and shearing conditions in the channel and improve the validity of the RBCA indices.

CHAPTER 7. Blood viscosity estimation in the convergent microchannel

Chapter 7 elaborates on the viscosity estimation using the data produced in the microfluidic device. The shear viscosity can be calculated as a function of the flow rate Q and pressure drop through a straight capillary of known dimensions [131], where some commonly used geometries are axisymmetric or planar slit. For a rectangular channel with width w and depth d (with aspect ratio w>>d), low values of wall shear stress can be measured at a given shear rate as $\dot{\gamma} \sim Q/(wd^2)$. For steady fully developed flow in a rectangular channel with w >> d and L >> d (where L is the channel length) the pressure drop is given by the force balance as $wd\Delta P = 2Tl(w + d)$. Hence pressure difference is found as: $\Delta P = \frac{2Tl(w+d)}{wd} \sim \frac{2Tl}{d}$.

Capillary viscometry can be very practical due to the inherent simplicity of the design combined with the ease of microfabricating straight planar channels with small depths compared to the channel length. The fundamental principle employed by microfluidic capillary viscometers is identical to their macroscale counterparts and the shear viscosity is found from the pressure drop ΔP and flow rate Q for a capillary of length L. A key difference between conventional and microfluidic capillary viscometers, however, is that the former are often gravity-driven resulting in measurements of the kinematic shear viscosity while the latter give the dynamic shear viscosity directly. Viscosity in capillary driven microfluidic devices is found by taking into account the position of the meniscus as the flow proceeds in combination with Y-L pressure [132,133]. A detailed explanation on viscosity measurements using capillary driven microfluidic devices is given in the section 7.1.

The aim of the work presented in this chapter, was to utilise fluid mechanics and rheology theory to model the flow behaviour of blood, in terms of the viscous effects, in the STD microchannel flow. This could further enhance the function of the POC capillary driven aggregometer, described in Chapter 6, so that the viscosity of blood from the recorded meniscus position during the flow in the microchannel could be estimated. Data from the STD flow (meniscus position as flow propagates) in the version 2 microchannel (Section 5) were used. Analytical solution for the viscosity was produced and values were compared with the viscosity curves produced using commercial instrument Brookfield DVIIT viscometer (section 4.3.5) to examine the validity the method.

7.1 Analytical method for the calculation of viscosity within the microchannel

In order to calculate the viscosity of blood, from the meniscus flow in the microchannel version 2, a method was developed similar to other works [110,134]. The analytical equation for meniscus velocity under STD flow in a rectangular channel (Eq.4.8) was used in combination with the recorded meniscus position and velocity at each time step. Eq.4.8 was derived in Section 4.4 from the incompressible Navier Stokes continuity and momentum equations, using the power-law viscosity model i.e. ($\mu = k[\frac{\partial V_{z\text{-}\sigma}}{\partial y}]^{n-1}$, where $\frac{\partial V_{z\text{-}\sigma}}{\partial y} = \dot{\gamma}$), and assuming that the flow is fully developed, one-dimensional, and influenced mainly by the smaller dimension of the geometry. Hence, by rearranging Eq.4.8 with respect to V^n and assuming V and L as functions of t (i.e V(t) as the meniscus velocity at each timestep and L(t) the meniscus position at each timestep), the following equation was found:

$$V(t)^n = \left(\frac{n}{n+1}\right)^n \left[\frac{\sigma\cos(\theta_c)}{hkL(t)}\right] \left[h^{\frac{n+1}{n}} \left(1 - \frac{n}{2n+1}\right)\right]^n \qquad 7.1$$

Further by substituting for $\sigma\cos(\theta_c)/h$ the YL pressure ΔP (i.e $\Delta P = \frac{2\sigma\cos(\theta_c)}{2h} = \frac{\sigma\cos(\theta_c)}{h}$ and rearranging:

$$V(t)^n = \left(\frac{n}{n+1}\right)^n \left[\frac{\Delta P}{Kl(t)}\right] \left[h^{\frac{n+1}{n}} \left(\frac{n+1}{2n+1}\right)\right]^n \qquad 7.2$$

Then, by solving for 1/L(t) the following equation was found similar to other works:

$$\frac{1}{L(t)} = \left(\frac{2n+1}{n}\right)^n \frac{k}{\Delta P} \frac{1}{h^{n+1}} V(t)^n = CV(t)^n \qquad 7.3$$

Where the constant $C = \left(\frac{2n+1}{n}\right)^n \frac{k}{\Delta P} \frac{1}{h^{n+1}}$ and ΔP is Y-L pressure i.e $\Delta P = \frac{\sigma\cos\theta}{h}$.

L(t) and V(t) of each sample were measured in the experiments in section 5 (n = 10 for each sample) in convergent rectangular channels and the mean values were found.

Hence Eq7.3 was modified in logarithmic scale as:

$$\log\left(\frac{1}{L(t)}\right) = \log(CV(t)^n) = \log C + \log V(t)^n = \log C + n\log V(t) \quad 7.4$$

and by using the mean L(t) and V(t) values a log-log plot 1/L(t) vs V(t) was plotted for each sample. Therefore, from the log-log plot 1/L(t) vs V(t) (shown in Figure 7.1 for WB), the power law exponent n, can be found from the slope and logC, hence k from the y axes interception as observed from Eq.7.4 [95,118]. Further, by substituting the calculated PL constants k and n, in the power law viscosity model ($\mu=k\dot{\gamma}^{n-1}$), experimental viscosity values could be calculated and hence plotted and compared with the mean viscosity curves (Figure 5.7) found in section 5.

7.2 Results and Discussion

Figure 7.1 shows the log-log plot 1/L(t) vs V(t) for WB. As observed from Figure 7.1 for WB, the power law constant n = 0.99 (that is the slope in Figure 7.1) is very close to the Newtonian value of 1. Similar values have been calculated for the other samples. This is due to the fact that the meniscus velocity (and consequently shearing) in the present work (Figure 5.18) appear to be elevated for the largest part of the flow. The moderate/high shearing conditions result in the Newtonian nature of the flow to dominate for the largest part of the fitting.

As blood is a shear thinning fluid (decrease in viscosity with increase in shear rate) the PL constant *n* is reported to be close to 0.7 [8,111]. Viscosity calculations in similar setups have given an *n* value close to 0.7. In the aforementioned works [110,134] a rectangular channel with L~10cm was used, having a spiral like shape in order to accommodate a large channel length for meniscus flow (Figure 7.2). In addition, in these studies [110,134], the flow duration (from start until meniscus has reached the end of the channel) was for 120s, instead of only ~2.5s as in the present work. Furthermore, in the present work channels with length of 2cm were used.

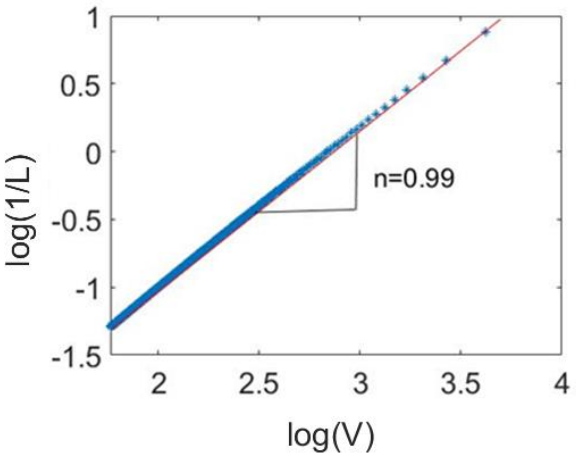

Figure 7.1. The log-log plot of (1/L) with V.

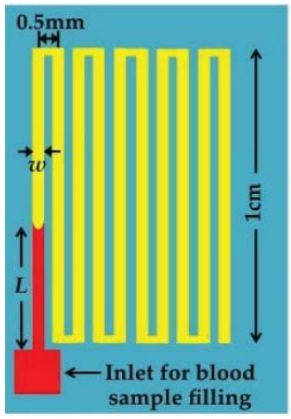

Figure 7.2. Geometry of capillary driven non/Newtonian fluid viscometer used by Kang et al [134]**.**

As abovementioned RBCA is the main cause for the shear thinning behaviour of blood [14]. As mentioned and explained in Section 5.10.2, the flow shearing conditions (shown in Figure 5.18) are very high at the beginning of the flow, (much higher than the disaggregation shear rates reported in literature [12,13]) expecting very high disaggregation. For the whole duration of the flow, shearing conditions are high enough to keep RBCA at low levels (Figure 5.18). These shear rates are higher than the shear rates in the aforementioned studies [110,134], hence supressing the shear thinning behaviour of blood.

In addition, comparing the measured RBCA index $t_{1/2}$ for WB (~4s, using the Rheoscan-A200, Figure 5.8) with the duration of the flow in the channel (t_{flow} ~2.5s) there is not sufficient time for aggregation, and hence the shear thinning behaviour to occur. In other relevant studies [110,134] the duration of the flow (120s) suffice for RBCA to occur.

As aforementioned in Section 5.10.2 the WB sample is more aggregative (with smaller $t_{1/2}$) and viscous than the other samples used in this study. Therefore, better shearing conditions are observed in the flow of the other samples. Hence, RBCA and the shear thinning behaviour of the rest of fluids are also supressed. This is confirmed from the viscosity curves in Figure 4.6, where it is observed that for shear rates greater than ~50s^{-1}, which is the minimum mean shear rate observed in the cannel (Figure 5.18), the fluids follow a more Newtonian behaviour, which can only occur due to good disaggregation conditions. Therefore, the value of the PL index *n* found for the samples tested being close to 1 suggesting Newtonian like behaviour, and is expected due to the good disaggregation conditions for the whole duration of the flow.

The viscosity percentage difference (μ_d) between the analytical and experimental results for various shear rates are shown in Table 7.1 calculated as $\mu_d = (\mu_{\text{analytical viscosity}} - \mu_{\text{experimetal viscosity}})/\mu_{\text{experimetal viscosity}}$ X 100.

	Sample viscosity difference μ_d (%)				
Shear rate (s^{-1})	WB	DEX45%	NAB45%	DEX40%	NAB40%
251.2	-8.94	-18.67	-12.03	10.98	3.5
125.9	-19.97	-29.7	-20.68	-4.71	-11.33
63.07	-33.45	-40.22	-28.65	-19.36	-22.6
31.58	-46.75	-51.95	-39.42	-35	-39.91
15.82	-56.39	-60.39	-46.18	-45.69	-48.73
7.875	-67.43	-68.7	-54.59	-56.5	-60.44
3.975	-77.6	-77.51	-67.55	-67.07	-74.99
2.025	-83.27	-84.01	-78.95	-78.71	-83.48

Table 7.1. Sample viscosity difference μ_d (%) at various shear rates.

As observed from the Table 7.1 for the non HT samples the viscosity difference (μ_d) (%) decreases as shear rate increases. For high shear rates, as aforementioned, blood behaves like a Newtonian fluid due to strong shearing preventing RBCA which causes the shear thinning behaviour of blood [14].

The dependence of the PL index k (the consistency index – related to the dynamic viscosity μ) on the surface tension (σ) was examined by calculating k for surface tension increments of 0.001N/m, starting from a value σ = 0.02 N/m, which was measured using a Kruss 100 surface tenσion meter for the WB sample, up to σ = 0.05N/m. Plots of σ against k are shown in Figure 7.3, from which is observed that k varies linearly with σ, increasing with a rate of 20% (i.e.

dk/dσ = 0.2). The value of k has increased 2.5 times for the range of σ examined (0.02N/m < σ < 0.05N/m) showing that surface tension affects k and hence the analytical viscosity values since $\mu = k\dot{\gamma}^{n-1}$.

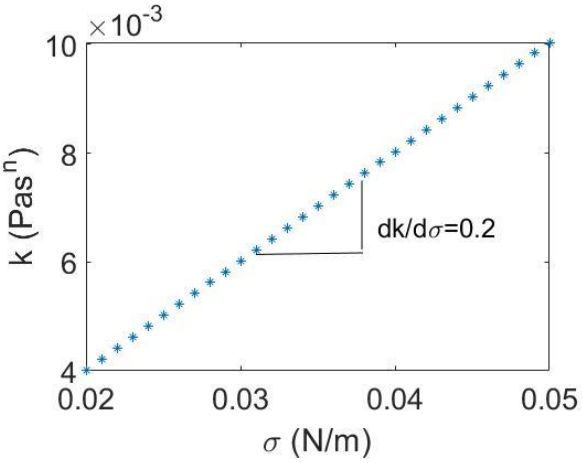

Figure 7.3. Dependence of K on surface tension.

Furthermore, k was also calculated for a range of contact angles $5^o < \theta < 20^o$ in increments of 0.01^o shown in Figure 7.4.

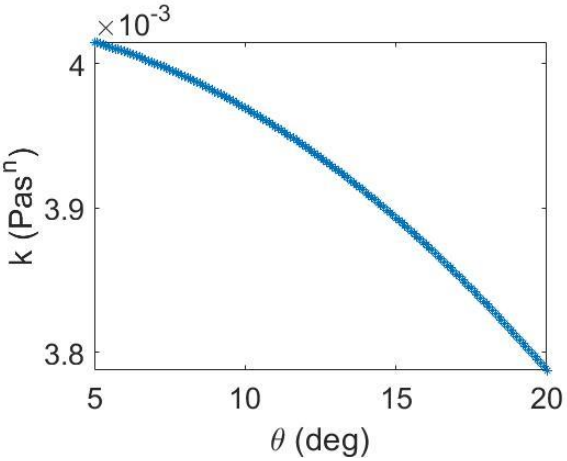

Figure 7.4. Dependence of K on contact angle.

As observed from Figure 7.4 k has only decreased about 5% from $\theta = 5^o$ to $\theta = 20^o$ showing that θ does not significantly affect the value of k and hence of the analytical viscosity. This is a positive result since it implies that any surface imperfections (such as hydrophobic recovery) may have minimal effects on the calculation of μ.

For the analytical calculation of the viscosity of blood from the meniscus flow within the channel, a method was developed based on the non-Newtonian equation for meniscus velocity under STD flow in a rectangular channel (Eq.4.8). Eq.4.8 was rearranged to Eq.7.4 and by

substituting the recorded meniscus position data and the calculated velocity at each time step an estimation of viscosity power law constants, and hence viscosity, values at different shear rates could be derived.

The value of the ability to calculate the high-shear viscosity of blood from a POC device is illustrated in other studies. The physiological shear rates in most parts of the circulation fall along the plateau part of the blood viscosity curve, where blood shows near-Newtonian behaviour. Hence, measuring blood viscosity at high shear rates is also important. As the non-Newtonian behaviour of blood becomes apparent, at shear rates mostly below the physiological range, in many clinical studies the viscosity is measured at two relatively shear rates (e.g. 230^{-1} and 23 sec^{-I} in [135]).

Fons et al [136] have tested the accuracy and the usefulness of the MT90 (falling ball) viscometer as an alternative to more expensive and sophisticated devices for physiological and clinical investigations. The MT90 viscometer measured blood viscosity from the velocity of a ball falling through a syringe filled with less than 1 ml of blood or plasma at a shear rate of 1000 s^{-1} (within the shearing range where blood behaves as a Newtonian fluid). The measured viscosities were compared with the commercial instrument's Carri-Med rheometer. The results of the MT90 viscometer and the Carri-Med rheometer were in good agreement suggesting that the MT90 viscometer is useful and accurate for physiological and clinical studies [136].

7.2.1 Extensional viscosity

Extensional flow can be observed in situations where there are abrupt changes in the flow geometry. In converging flows such as the present, extensional flow can be produced due to the changes of velocity in the direction of the flow. The behaviour of the RBC in extensional flow differs from that in the shear flow, in that there is not tumbling motion and intense RBC interactions [49,137,138]. In this work, due to the converging geometry of the channel and the decelerating behaviour of the flow, velocity gradients in the direction of the flow are expected, hence the effect of the extensional flow was examined. The extensional strain rate $\dot{\epsilon}$ (i.e velocity gradient in the direction of the flow) and viscosity μ_{ext} (i.e. the resistance of a fluid to extensional flow) of WB were calculated for the capillary driven flow within the convergent surface treated channel. Extensional strain rate (or elongational rate) and viscosity were calculated respectively similar to other works [49,137,138] as:

$$\dot{\epsilon} = \mathrm{Q}\frac{w_1 - w_2}{Lhw_1w_2} \qquad 7.5$$

Q is the flow rate and w_1, w_2 the widths of the channel at the beginning (z = 0) and at the end of the flow (z = 20mm) respectively, and L the length of the channel. The flow rate, Q, was found as $\mathrm{Q} = \overline{\mathrm{V}}_{\mathrm{m}}\mathrm{A}_{\mathrm{channel}}$, with $\mathrm{A}_{\mathrm{channel}}$ the mean cross-sectional area of the converging channel. An approximate extensional viscosity can therefore be calculated based on entrance flow theory [139] as:

$$\mu_{ext} = \frac{\Delta \mathrm{P}}{\dot{\epsilon}} \qquad 7.6$$

where ΔP is the Young Laplace pressure was used for the pressure difference.

The elongational rate and extensional viscosity are shown in Figure 7.5. From the graphs in Figure 7.5a and b, it can be observed that the elongational rate $\dot{\epsilon}$ is a decreasing function of the flow direction (z), becoming very low as the flow proceeds, and that $\dot{\epsilon}$ it is not constant in time (unsteady). The magnitude of $\dot{\epsilon}$ is very low, ranging from approximately 4 to 0.2 s^{-1}, therefore a very small elongational effect is expected. This is to say that RBC aggregation and deformability will not be affected by the elongational nature of the flow. Indeed, it has been shown [49] that for significant RBC deformation to take place, $\dot{\epsilon}$ magnitudes of more than 30 s^{-1} should be created. Therefore, no significant RBC deformation is expected due to extensional flow effects. In terms of RBC aggregation behaviour in the elongational flow no substantial information exists in the literature. However, it is known that a disaggregating shear stress of approximately 0.2 Pa (and a $\dot{\gamma}$ of approximately 50 s^{-1}) is needed in order to effectively disperse an aggregate, and that a shear stress of approximately 1 Pa (and ~300 s^{-1}) is required for the initiation shear deformation of the RBC [140,141]. By inspecting the values of $\dot{\epsilon}$ and $\dot{\gamma}$ for RBC deformation, an approximate 10-fold difference is observed. Further, considering that there is a 6-fold difference between the RBC deforming and disaggregating $\dot{\gamma}$ values (300 to 50 s^{-1}), it would be suggested that the disaggregating $\dot{\epsilon}$ lies lower, in the vicinity of ~6 s^{-1}. Therefore, disaggregating effects due to the elongational nature of the flow should be expected only in the beginning of the flow and at the entrance of the channel.

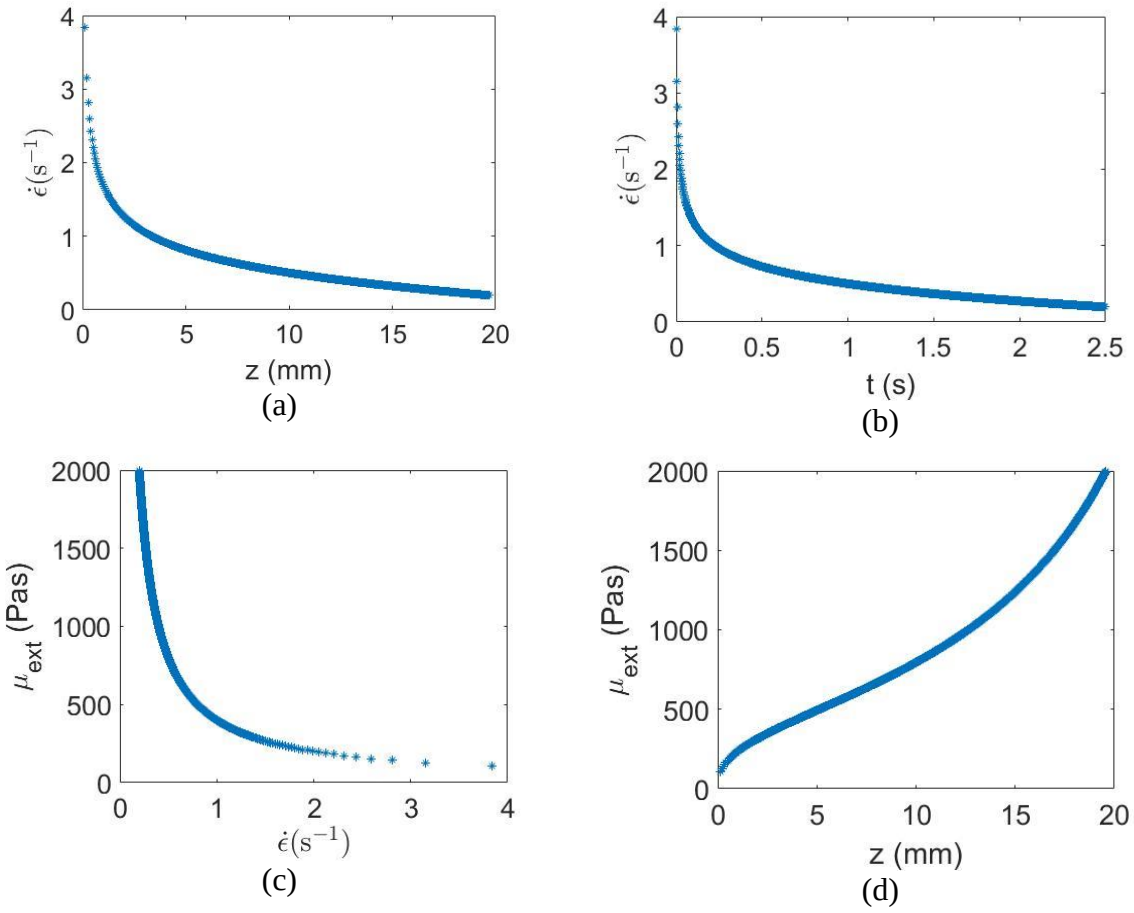

Figure 7.5. Extensional strain rate and extensional viscosity, for the whole length of the flow for WB: (a) and (b) extensional rate, as a function of space and time respectively, (c) Extensional viscosity vs the extensional rate and (d) Extensional viscosity as the flow proceeds in the flow direction.

Figure 7.5 also shows that the extensional viscosity increases as the flow proceeds, and that the magnitude ranges from approximately 100 Pas to 2000 Pas. This behaviour agrees qualitatively with other works in terms of the order of magnitude of the estimated μ_{ext}. Kolbalsov etal, [142], reported μ_{ext} magnitudes in the vicinity of ~45 Pas for elongational rates ė of ~50 s^{-1}. For the same ė value (50 s^{-1}), and by extrapolating μ_{ext} (from the values of ė in Figure 7.5c), a value of μ_{ext} ~ 40 Pas is found, indicating the validity of approach.

7.3 Remarks on the viscosity calculations

Due to the high shearing conditions in the flow, in combination with the small channel length resulting ($t_{1/2} > t_{flow}$), RBCA was found suppressed for the duration of the measured flow. Therefore, it was possible to estimate the Newtonian viscosity of blood, which can provide information about the general viscous status of the fluid. Comparing the analytical viscosity

results with the experimental (Table 7.1), the viscosity values were close for the higher shear rates ($\dot{\gamma}$ > 63.07s^{-1}) were the fluids follow a Newtonian behaviour due to reduced RBCA under these shearing conditions [12,13].

The estimated μ_{ext} shows a shear thinning behaviour of WB, which is similar with the dynamic viscosity calculations shown earlier. The magnitude of μ_{ext} is in the range shown by other works in the literature, although the approximation of the Equation 7.6 provides a crude estimation of μ_{ext}. Indeed, the flow in the channels is far from the steady and shear free condition, complicating the analysis. Shear effects could be incorporated by using the Goswell approximation which includes non-Newtonian properties (power law index n) also, $\mu_{ext} = \frac{3}{8}(n+1)\frac{\Delta P}{\dot{\epsilon}}$. The resulted μ_{ext} using the Goswell approximation [139] is in the vicinity of the results using Equation 7.6, in terms of order of magnitudes. The elongational effects in the particular configuration could be strengthened more by altering the geometry of the microchannel, and by concentrating the analysis in the entrance region.

CHAPTER 8. Limitations and uncertainties of the study

In this Chapter a discussion on the limitations and uncertainties in the various parts of the study is presented. The purpose is to illustrate and clarify all issues that may have affected the experimental and analytical procedures adopted in this work.

8.1 Rectangular straight and convergent, surface treated microchannel

In the bright field μPIV techniques, due to the large depth of correlation of the microscope objective, a certain degree of error occurs [106]. This finite depth of correlation leads to an underestimation of the velocity magnitude, the extent of which was assessed in the present study and agrees with previous reports [96,106,143]. However, the velocity underestimation is found to be consistent across the largest part of the flow field (Figure 3.16e) and therefore the shape of the velocity profile should be qualitatively preserved. In addition, the comparison of channel and meniscus velocities shown in Figure 5.2 provide evidence for the relatively good validity of the velocity measurements.

The side walls of the channel are constructed by a double-sided adhesive tape, which introduces an apparent roughness on the side wall-flow interface. In addition, due to small variations in the dimensions between the constructed microchannels, velocity points could appear at slightly different x* positions in the V_{ch} profiles. Therefore, to account for this V_{ch} profiles were averaged by considering the velocity values according to their position from the centerline, in order to produce the mean $\overline{V}_{ch}$ velocity profile.

The sample deposition at the entrance of the channel is conducted with great care by the trained operator using a micropipette. The sample volume is consistently controlled using the micropipette, however, uncertainties due to sample handling might be possible. In the present work, cases showing abnormal behaviour (specially in channel and meniscus velocity due to side walls having small air bubbles hence blood flowing through the side walls), have been excluded from the analysis. Viscosity values at the lowest shear rate (12.5 s^{-1}) were close to the lower sensitivity limit of the viscometer (accepted at the 5% of the transducer torque range). Nevertheless, the viscosity of the Newtonian fluid measured in this low-end of the torque sensitivity, shows no significant deviation from the rest of values indicating valid readings of viscosity for WB, NAB and DEX working fluids.

The heat treatment is known to have a slight effect on the optical properties of blood [144], which may affect slightly the RBC aggregation and PIV velocity results. The Dextran

suspending medium is expected also to have been affected by the heat treatment. More specifically, the stability of Dextran is decreased with increasing temperature, since thermal degradation increases at higher temperatures. However, the initial decomposition temperature (T_i) for dextran occurs at T_i ~283ºC, hence at 50^{O}C which dextran was heated in these experiments no thermal degradation is expected [145]. In addition, the intrinsic viscosity of Dextran (which is also depended on the solvent medium-water in this study) reduce with increasing solution temperature [146]. The intrinsic viscosity of Dextran2000000 with water as solvent, which was used in this work, is expected to have been decreased by ~27% by heating from room temperature ~25 ^{O}C prior to heat treatment to ~50 ^{O}C post heating [146].

8.2 Microstructural characterization in the CDMA device

Sample handling (PBS washing and resuspension, transportation between tubes and syringes, oxygenation, mixing for aggregate dispersion, etc.) could affect the RBC mechanical properties (through osmotic effects) and introduce uncertainty in the quantities measured. For this reason, a strict protocol on sample handling and experimental procedures was put in place and followed as closely as possible. It is expected that any influence of sample handling will be systematic, affecting all samples similarly.

Viscosity values at the lowest shear rate (2.275 s^{-1}) were closest to the lower validity limit of the viscometer (in this study set at 5% of the transducer torque range); data that deviated abnormally from the previous shear rate point were discarded as outliers. The uncertainty in the viscosity measurements was approximately 3-4%, according to the torque calibration of the instrument. Validation tests using standard viscosity fluids showed a similar discrepancy for the valid range of the transducer torque range.

In addition, the Rheoscan A200 RBC aggregometer shows an acceptable intra-assay variation of less than 5%, and an acceptable sensitivity to aggregation differences [88].

Moreover, technical issues, such as sudden reduction in the light intensity of the USB camera, resulted to dropped magnitudes of the mean intensity. Therefore, a correction of the intensity curve was performed when such condition was detected using specific Matlab algorithms.

Furthermore, outliers of intensity values in the CDMA intensity curves at the initial measurements could significantly affect the indices calculations. A very low or high intensity value at the beginning of the intensity curve will significantly change the area ratio below and above the curve resulting errors in AI index measurement. Furthermore, an outlier with a very high or low intensity value could significantly affect AMP which is the difference between

maximum and minimum intensity. Hence half time index ($t_{1/2}$) which is the time needed for minimum intensity to reach half of the AMP is also significantly affected. For this reason, outliers have been discarded using Matlab algorithms.

8.3 Analytical viscosity

The short channel length resulting in a $t_{1/2} > t_{flow}$ and the high shear rates within the flow suppressed RBCA and hence the shear thinning behaviour of blood. Therefore, it was possible to estimate mainly the Newtonian viscosity of blood, which can provide information about the general viscous status of the fluid. The Power law constant k is dependent on the contact angle θ, which was not measured as flow proceeded in the channel. However, k was calculated for a range of contact angles $5^o < \theta < 20^o$ in increments of 0.01^o (Figure 7.4), showing no significant variation within this range of contact angles.

For the analysis of the extensional viscosity, it should be noted that in the present case the elongational rate $\dot{\epsilon}$ is not constant, and that the flow is not purely elongational. As discussed, the shear effects could be incorporated by using the Goswell approximation, which includes non-Newtonian properties (power law index n) also, $\mu_{ext} = \frac{3}{8}(n+1)\frac{\Delta P}{\dot{\epsilon}}$. Indeed, the resulted μ_{ext} using the Goswell approximation found in the vicinity of the results when using Equation 7.6. The hydrophobic sidewalls, affect the calculations also, as the effective channel surface tension was not possible to be defined with accuracy.

CHAPTER 9. Conclusions

The broader aim of the PhD program was to elaborate on specific aspects of blood fluid mechanics, with emphasis in microscale surface tension driven flow. These aspects were stated in Section 2.1 and included in the investigation of the following topics:

a) Microchannel design parameters and construction for flow enhancement.

b) Flow characterization in the passive microchannel.

c) Structural characterization of blood.

d) Rheological characterization.

The work described in each section of the Chapter 3, investigated one or more of the above topics and the results were presented in Chapters 4, 5, 6 and 7. Four journal and five conference publications have been produced from the work described in this Thesis. In the paragraphs bellow, the main conclusions from each piece of work will be given, as well as a note on the general contribution of the work in the scientific area of blood fluid mechanics.

9.1 Rectangular straight microchannel

The initial part of the work included experiments on straight hydrophilic rectangular microchannels, constructed using xurography techniques, as explained in Section 3.2 in more detail. Newtonian fluids, and blood samples were utilised, and the flow characteristics in the micro channel were analysed. Viscosity measurements were also performed. Higher viscosities were found for WB compared to the viscosities of NAB and NF (Figure 4.6), verifying that aggregates at the centre of the microfluidic chamber result to an increase in viscosity therein and impeding the flow [30]. The velocity profile of WB was found to be blunter compared to the non-aggregating sample since the abovementioned effect causes the viscous characteristics of the core of the flow to influence more than those in the regions of the side walls. In the beginning of the flow high velocities were observed, resulting to high shear rates, and hence good disaggregating conditions. The low aggregation at the initial stages of the flow can be confirmed from the coefficient of variation (CV) calculated from the image intensity of the fluids (Figure 4.9). The value of this part of the work lies on the fact that aggregating blood was specifically investigated in the surface tension driven flow, approach which was lacking in the literature.

9.2 Convergent, surface treated microchannel

The work described previously set the basis for the next part of the work, which regarded the systematic examination of the effects of blood properties in the STD flow. To fulfil that aim, the first task was to consider approaches in order to enhance the flow in the microchannel. This included the adoption of a convergent geometry and the coating of the channel surfaces with TiO_2 (Section 1.8). The flow conditions have been significantly improved by the treatment of the microchannel surfaces with $Ti0_2$ in combination with the ~3 - degree convergent geometry, compared to the straight untreated microchannel used in the initial work and other studies with similar geometries.

Another important aspect in this part of the work, was the examination of the main hemorheological parameters affecting blood mechanical properties, in the STD microchannel flow. For this purpose, various samples were produced to reflect in the best and more effective manner, the changes in those hemorheological conditions. Namely, aggregative and non-aggregative samples, samples with altered deformability, and samples of different haematocrit. The results confirmed some known aspects of blood fluid mechanics and added new knowledge on some other. The more aggregative samples had higher viscosity and therefore smaller meniscus and channel core velocities than the non-aggregative ones. The reduced RBC deformability due to heat-treatment, although it resulted to a reduction in the extent of aggregation, it has also caused a decrease in the velocity of the samples, since an increase in viscosity was observed in these cases. In addition, as expected the haematocrit was also found to have an effect; increasing the haematocrit decreased the velocity of the samples which can be attributed to the higher viscosity of denser samples. No significant variation was observed in the velocity profile characteristics between the normal and heat-treated samples, with the exception of WB.

In terms of the shearing conditions in the STD blood flow, high shear rates were observed upon initialization of the flow, suggesting high disaggregation in the inlet sections, of the geometry. As the flow proceeded the shear rate gradually decreases, however, it remained sufficiently strong until the flow reaches the end of the channel. The shear conditions developed in the microchannel, especially close to the walls appear sufficiently strong to keep RBC aggregation at low levels for the duration of the flow. This is an important outcome in this study, since it establishes the fact that STD microfluidic devices could be utilised for the measurement of RBCA. Another important outcome from this part of the study is the counter-intuitive influence

of RBCA on the flow velocity as it appears that there is an initial beneficial effect (increasing velocity) before a flow impedance occur (Figure 5.19).

9.3 Effects of the stented tube and structural characterization by the CDMA device

The capability of the STD microfluidic setup for use as an RBCA measuring system (CDMA device) was illustrated by constructing a prototype using a simple USB camera-based system. The system was used to assess RBCA in the study by Kapnisis et al., [126]. In this study, alterations in the aggregation tendency of blood samples were examined for samples subjected to various flow rates, in a stented tube configuration. Both the CDMA and the Rheoscan-A200 instrument were used for comparison. In terms of the stent influence, it was observed that for the samples subjected to flow through stented tube (StentNit condition), at the higher flow rates, and at further exposure to these flow rates, the rheological properties of blood were affected (decreasing aggregation and increasing viscosity). Decrease in the deformability of RBCs was also observed, which might occur due to stronger shear stresses developing within the stented area.

The intensity curves produced by the CDMA device give promising results, as they show similar behaviour as Rheoscan-A200 commercial instrument. The produced indices from Rheoscan-A200 and CDMA curves follow a similar trend (Figure 6.4a, c and e). Moreover, although both devices use light transmission techniques in order to obtain the intensity curves, and measurements are performed after the flow is ceased, the values of the indices differ slightly (Figure 6.5b, d and f). This may be due to different shearing time, illumination, blood layer thickness and light detection mechanism. However, there is a good correlation between the indices produced from the CDMA and Rheoscan-200 instrument (Figure 6.5). Further optimization of the microchannel can be pursued in order to further enhance the flow conditions.

9.4 Analytical viscosity estimation

The analysis of flow behaviour, as influenced by the most important haemorheological and flow factors, was performed from a theoretical basis. The Navier-Stokes equations, in combination with blood constitutive equations (Power Law) and surface tension dynamics, were used to provide additional insight in understanding the results of the present work. Moreover, the high-shear blood viscosity modelling approach would add to further enhance the

functions of the CDMA. To estimate the viscosity of blood analytically the recorded meniscus position during the flow in the microchannel can be utilised in the analytical solution. The analytical viscosity values were compared with the measured by viscometry and literature results and reasonable agreement was found.

9.5 General conclusions

In general, the results of this work provide important information regarding the surface-tension driven blood flow in converging microchannels with rectangular cross-section. The effects of the biomechanical properties of blood, such as erythrocyte concentration (haematocrit), deformability and aggregation in such flows are explained in detail which could aid the design of microfluidic devices and experiments. Hence, the present analysis could serve as a guide for the design of surface tension driven flow microfluidics, regarding geometry and flow conditions. Furthermore, the present work has set the basis for pursuing an advanced CDMA device design, which can be of lost cost and more used friendly. Such device could be used by patients for assessing inflammation levels using a fingerpick blood drop.

9.6 Future work

Future work should address issues regarding, advanced methods of characterising erythrocyte aggregation, microchannel haematocrit and erythrocyte sedimentation, as well as flow extension and duration periods. The aforementioned characteristics require image processing-based techniques. The following approaches could be assessed:

- Frequency domain processing. Pre-processing in the frequency domain can be used in order to emphasize on specific aspects of the blood structure. Fourier can be used for the development of shape descriptors to characterize global structural features in the aggregating blood.
- Wavelet transforms can be utilised for the detection of fibrin features in the microstructure.
- Image entropy is another approach for statistically measuring the randomness of the texture of an image. The main characteristic of the basic element of RBCA, the rouleaux, is the local order they introduce; image entropy could detect changes caused by the formation of aggregates.

- Proper orthogonal decomposition (POD) is a powerful data analysis technique used in turbulent fluid flows, which could be utilized for the characterization of RBC aggregation.

Flow related issues that worth special attention include the analysis of the flow in the complex front of the advancing meniscus. Small amount of work exists in the literature regarding this aspect. Further, experimental studies of thermally exposed blood flow in microcirculatory mimicking microchannels is also of interest. Both the aforementioned issues deserve immediate attention.

References

[1] Sackmann EK, Fulton AL, Beebe DJ. The present and future role of microfluidics in biomedical research. Nature. 2014;507(7491):181–9. 10.1038/nature13118.

[2] Weigl B, Domingo G, Labarre P, Gerlach J. Towards non- and minimally instrumented, microfluidics-based diagnostic devices. Lab Chip. 2008;8(12):1999–2014. 10.1039/b811314a.

[3] Tsui JH, Lee W, Pun SH, Kim J, Kim DH. Microfluidics-assisted in vitro drug screening and carrier production. Vol. 65, Advanced Drug Delivery Reviews. 2013. p. 1575–88. 10.1016/j.addr.2013.07.004.

[4] Berthier E, Beebe DJ. Flow rate analysis of a surface tension driven passive micropump. Lab Chip. 2007;7(11):1475–8. 10.1039/b707637a.

[5] Mathew J, Bhimji SS. Physiology, Blood Plasma. StatPearls. 2018.

[6] Khairy K, Foo J, Howard J. Shapes of Red Blood Cells: Comparison of 3D Confocal Images with the Bilayer-Couple Model. Cell Mol Bioeng. 2008;1(2–3):173–81. 10.1007/S12195-008-0019-5.

[7] Burkhart JM, Vaudel M, Gambaryan S, Radau S, Walter U, Martens L, et al. The first comprehensive and quantitative analysis of human platelet protein composition allows the comparative analysis of structural and functional pathways. Blood. 2012; 10.1182/blood-2012-04-416594.

[8] Alves MM, Rocha C, Gonçalves MP. Study of the rheological behaviour of human blood using a controlled stress rheometer. Clin Hemorheol Microcirc. 2013;53(4):369–86. 10.3233/CH-121645.

[9] Dao M, Lim CT, Suresh S. Mechanics of the human red blood cell deformed by optical tweezers. In: Journal of the Mechanics and Physics of Solids. 2003. p. 2259–80. 10.1016/j.jmps.2003.09.019.

[10] Mehri R, Niazi E, Mavriplis C, Fenech M. An automated method for dynamic red blood cell aggregate detection in microfluidic flow. Physiol Meas. 2018; 10.1088/1361-6579/aaa0ad.

[11] Flormann D, Schirra K, Podgorski · Thomas, Wagner · Christian, Wagner C. On the rheology of red blood cell suspensions with different amounts of dextran: separating the effect of aggregation and increase in viscosity of the suspending phase. Rheol Acta. 2016;55:477–83. 10.1007/s00397-015-0882-7.

[12] Firsov NN, Priezzhev A V., Ryaboshapka OM. Study of erythrocyte-aggregation kinetics in shear flow in vitro by light-scattering technique. In: Proceedings of SPIE - The International Society for Optical Engineering. 1993.

[13] Snabre P, Bitbol M, Mills P. Cell disaggregation behavior in shear flow. Biophys J. 1987;51(5):795–807. 10.1016/S0006-3495(87)83406-9.

[14] Foresto P, D'Arrigo M, Carreras L, Cuezzo RE, Valverde J RR. Evaluation of red blood cell aggregation in diabetes by computerized image analysis. . Med (B Aires). 2000;60(5):570.

[15] Kim Y, Kim K, Park Y. Measurement Techniques for Red Blood Cell Deformability: Recent Advances. In: Blood Cell - An Overview of Studies in Hematology. InTech; 2012. 10.5772/50698.

[16] Czaja B, Gutierrez M, Závodszky G, De Kanter D, Hoekstra A, Eniola-Adefeso O. The influence of red blood cell deformability on hematocrit profiles and platelet margination. PLoS Comput Biol. 2020; 10.1371/journal.pcbi.1007716.

[17] Pozrikidis C. Axisymmetric motion of a file of red blood cells through capillaries. Phys Fluids. 2005;17(3):031503. 10.1063/1.1830484.

[18] Limtrakarn W, Muengtaweepongsa S, Phakdeesan P, Eiamaram P, Pratumwal Y, Duangburong S, et al. Whole blood viscosity modeling using power law, Casson, and Carreau Yasuda models integrated with image scanning U-tube viscometer technique Cerebral Embolus Detection with TCD View project Dynamic cerebral autoregulation, neurovascular coupling and cereb. Artic Songklanakarin J Sci Technol. 2017;39(5):625–31. 10.14456/sjst-psu.2017.77.

[19] OK B, HJ M. Blood rheology and hemodynamics. Semin Thromb Hemost. 2003;29(5):435–50. 10.1055/S-2003-44551.

[20] Karsheva M, Dinkova P, Pentchev I, Ivanova T. Blood rheology-a key for blood circulation in human body. J Univ Chem Technol Metall. 2009;44:50–4.

[21] Shibeshi SS, Collins WE. The Rheology of Blood Flow in a Branched Arterial System. Appl Rheol. 2005;15(6):398. 10.1901/JABA.2005.15-398.

[22] Kaliviotis E, Yianneskis M. An energy-rate based blood viscosity model incorporating aggregate network dynamics. Biorheology. 2009; 10.3233/BIR-2009-0555.

[23] Giannokostas K, Dimakopoulos Y, Anayiotos A, Tsamopoulos J. Advanced constitutive

modeling of the thixotropic elasto-visco-plastic behavior of blood: Steady-state blood flow in microtubes. Materials (Basel). 2021;14(2):1–37. 10.3390/ma14020367.

[24] Giannokostas K, Moschopoulos P, Varchanis S, Dimakopoulos Y, Tsamopoulos J. Advanced constitutive modeling of the thixotropic elasto-visco-plastic behavior of blood: Description of the model and rheological predictions. Materials (Basel). 2020;13(18). 10.3390/ma13184184.

[25] Varchanis S, Dimakopoulos Y, Wagner C, Tsamopoulos J. How viscoelastic is human blood plasma? Soft Matter. 2018;14(21):4238–51. 10.1039/c8sm00061a.

[26] Lima R, Wada S, Takeda M, Tsubota K ichi, Yamaguchi T. In vitro confocal micro-PIV measurements of blood flow in a square microchannel: The effect of the haematocrit on instantaneous velocity profiles. J Biomech. 2007; 10.1016/j.jbiomech.2007.01.012.

[27] LIma R, Wada s., Tanaka S, Takeda M, Ishikawa T, Tsubota K, et al. In vitro blood flow in a rectangular PDMS microchannel: experimental observations using a confocal micro-PIV system. Biomed Microdevices. 2007;10(2):153–67.

[28] Lima R, Wada S, Tanaka S, Takeda M, Ishikawa T, Tsubota KI, et al. In vitro blood flow in a rectangular PDMS microchannel: Experimental observations using a confocal micro-PIV system. Biomed Microdevices. 2008;10(2):153–67. 10.1007/s10544-007-9121-z.

[29] Lima R, Ishikawa T, Imai Y, Takeda M, Wada S, Yamaguchi T. Radial dispersion of red blood cells in blood flowing through glass capillaries: The role of hematocrit and geometry. J Biomech. 2008;41(10):2188–96. 10.1016/j.jbiomech.2008.04.033.

[30] Sherwood JM, Dusting J, Kaliviotis E, Balabani S. The effect of red blood cell aggregation on velocity and cell-depleted layer characteristics of blood in a bifurcating microchannel. Biomicrofluidics. 2012; 10.1063/1.4717755.

[31] Sherwood JMJM, Kaliviotis E, Dusting J, Balabani S. Hematocrit, viscosity and velocity distributions of aggregating and non-aggregating blood in a bifurcating microchannel. Biomech Model Mechanobiol. 2014;13(2):259–73. 10.1007/s10237-012-0449-9.

[32] Pries AR, Neuhaus D, Gaehtgens P. Blood viscosity in tube flow: dependence on diameter and hematocrit. Am J Physiol. 1992;263(6 Pt 2):H1770–8.

[33] Thomas B, Sumam KS. Blood Flow in Human Arterial System-A Review. Procedia Technol. 2016;24:339–46. 10.1016/j.protcy.2016.05.045.

[34] Alapan Y, Matsuyama Y, Little JA, Gurkan UA. Dynamic deformability of sickle red blood cells in microphysiological flow. TECHNOLOGY. 2016;04(02):71–9. 10.1142/S2339547816400045.

[35] Chebbi R. Dynamics of blood flow: modeling of the Fåhræus–Lindqvist effect. J Biol Phys. 2015;41(3):313–26. 10.1007/s10867-015-9376-1.

[36] Toksvang LN, Berg RMG. Using a classic paper by Robin Fåhraeus and Torsten Lindqvist to teach basic hemorheology. Am J Physiol - Adv Physiol Educ. 2013;37(2):129–33. 10.1152/advan.00009.2013.

[37] Kung CF, Chiu CF, Chen CF, Chang CC, Chu CC. Blood flow driven by surface tension in a microchannel. Microfluid Nanofluidics. 2009;6(5):693–7. 10.1007/s10404-008-0345-x.

[38] Kaliviotis E, Sherwood JM, Balabani S. Partitioning of red blood cell aggregates in bifurcating microscale flows. Sci Rep. 2017; 10.1038/srep44563.

[39] Sherwood JMJM, Holmes D, Kaliviotis E, Balabani S. Spatial distributions of red blood cells significantly alter local haemodynamics. PLoS One. 2014;9(6). 10.1371/journal.pone.0100473.

[40] Kaliviotis E, Dusting J, Sherwood JM, Balabani S. Quantifying local characteristics of velocity, aggregation and hematocrit of human erythrocytes in a microchannel flow. Clin Hemorheol Microcirc. 2016;63(2):123–48. 10.3233/CH-151980.

[41] Kaliviotis E, Pasias D, Sherwood JM, Balabani S. Red blood cell aggregate flux in a bifurcating microchannel. Medical Engineering and Physics. 2016; 10.1016/j.medengphy.2017.04.007.

[42] Kaliviotis E, Pasias D, Sherwood JM, Balabani S. Red blood cell aggregate flux in a bifurcating microchannel. Med Eng Phys. 2017; 10.1016/j.medengphy.2017.04.007.

[43] Tomaiuolo G, Lanotte L, Ghigliotti G, Misbah C, Guido S. Red blood cell clustering in Poiseuille microcapillary flow. Phys Fluids. 2012;24(5). 10.1063/1.4721811.

[44] D'Apolito R, Taraballi F, Minardi S, Liu X, Caserta S, Cevenini A, et al. Microfluidic interactions between red blood cells and drug carriers by image analysis techniques. Med Eng Phys. 2016;38(1):17–23. 10.1016/j.medengphy.2015.10.005.

[45] Mehri R, Laplante J, Mavriplis C, Fenech M. Investigation of blood flow analysis and red blood cell aggregation. J Med Biol Eng. 2014;34(5):469–74. 10.5405/jmbe.1695.

[46] Mehri R, Mavriplis C, Fenech M. Red blood cell aggregates and their effect on non-Newtonian blood viscosity at low hematocrit in a two-fluid low shear rate microfluidic system. PLoS One. 2018; 10.1371/journal.pone.0199911.

[47] Reinhart WH, Piety NZ, Shevkoplyas SS. Influence of red blood cell aggregation on perfusion of an artificial microvascular network. Microcirculation. 2016;DOI: 10.1111/micc.12317. 10.1111/micc.12317.

[48] Passos A, Sherwood JM, Kaliviotis E, Agrawal R, Pavesio C, Balabani S. The effect of deformability on the microscale flow behavior of red blood cell suspensions. Phys Fluids. 2019; 10.1063/1.5111189.

[49] Yaginuma T, Oliveira MSN, Lima R, Ishikawa T, Yamaguchi T. Human red blood cell behavior under homogeneous extensional flow in a hyperbolic-shaped microchannel. Biomicrofluidics. 2013; 10.1063/1.4820414.

[50] Ichikawa N, Hosokawa K, Maeda R. Interface motion of capillary-driven flow in rectangular microchannel. J Colloid Interface Sci. 2004;280(1):155–64. 10.1016/j.jcis.2004.07.017.

[51] Cito S, Ahn Y-C, Pallares J, Duarte RM, Chen Z, Madou M, et al. Visualization and measurement of capillary-driven blood flow using spectral domain optical coherence tomography. Microfluid Nanofluidics. 2012;13(2):227–37. 10.1007/s10404-012-0950-6.

[52] Navascues G. Liquid surfaces: theory of surface tension. Reports Prog Phys. 1979;42:1131–86. 10.1088/0034-4885/42/7/002.

[53] Rosenthal A. Demonstration of Surface Tension. J Chem Educ. 2001;3(78):332. 10.1021/ed078p332.

[54] Krause P. A demonstration of surface tension and contact angle. J Chem Educ. 2000;77(1):58–9. 10.1021/ed077p58.

[55] Definitions for Hydrophilicity, Hydrophobicity, and Superhydrophobicity: Getting the Basics Right. J Phys Chem Lett. 2014;5:686–8. dx.doi.org/10.1021/jz402762h |.

[56] Chen YF, Tseng FG, ChangChien SY, Chen MH, Yu RJ, Chieng CC. Surface tension driven flow for open microchannels with different turning angles. Microfluid Nanofluidics. 2008;5(2):193–203. 10.1007/s10404-007-0237-5.

[57] Berthier J, Brakke KA, Furlani EP, Karampelas IH, Poher V, Gosselin D, et al. Whole

blood spontaneous capillary flow in narrow V-groove microchannels. Sensors Actuators, B Chem. 2015;206:258–67. 10.1016/j.snb.2014.09.040.

[58] Berthier J, Brakke KA, Gosselin D, Navarro F, Belgacem N, Chaussy D. Spontaneous capillary flow in curved, open microchannels. Microfluid Nanofluidics. 2016; 10.1007/s10404-016-1766-6.

[59] Gosselin D, Huet M, Cubizolles M, Rabaud D, Belgacem N, Chaussy D, et al. Viscoelastic capillary flow: The case of whole blood. AIMS Biophys. 2016; 10.3934/biophy.2016.3.340.

[60] Chakraborty S. Dynamics of capillary flow of blood into a microfluidic channel. Lab Chip. 2005;5(4):421. 10.1039/b414566f.

[61] Jun W, Wei H, Raghbir S. B, Pin T. Modeling of Surface-Tension-Driven Flow of Blood in Capillary Tubes. Tech Sci Press. 2004;1(2):161–7.

[62] Sneha Maria M, Rakesh PE, Chandra TS, Sen AK. Capillary flow of blood in a microchannel with differential wetting for blood plasma separation and on-chip glucose detection. Biomicrofluidics. 2017;10(5).

[63] Lee K, Kinnunen M, Khokhlova MD, Lyubin E V, Priezzhev A V, Meglinski I, et al. Optical tweezers study of red blood cell aggregation and disaggregation in plasma and protein solutions. J Biomed Opt. 2016;21(3):35001.

[64] Sakamoto H, Hatsuda R, Miyamura K, Sugiyama S. Plasma separation PMMA device driven by capillary force controlling surface wettability. Micro Nano Lett. 2012; 10.1049/mnl.2011.0627.

[65] Alam AU, Howlader MMR, Deen MJ. The effects of oxygen plasma and humidity on surface roughness, water contact angle and hardness of silicon, silicon dioxide and glass. J Micromechanics Microengineering. 2014; 10.1088/0960-1317/24/3/035010.

[66] Luo S, Wong CP. Effect of UV/ozone treatment on surface tension and adhesion in electronic packaging. IEEE Trans Components Packag Technol. 2001; 10.1109/6144.910801.

[67] Noonuruk R, Sritharathikhun J, Pecharapa W. Surface Wettability of Silica Films Modified by UV/Ozone Treatment. Vol. 16, KMITL Sci. Tech. J. 2016.

[68] Topala I, Dumitrascu N, Pohoata V. Influence of plasma treatments on the hemocompatibility of PET and PET + TiO 2 films. Plasma Chem Plasma Process. 2008; 10.1007/s11090-008-9136-0.

[69] Maitz MF, Pham MT, Wieser E, Tsyganov I. Blood compatibility of titanium oxides with various crystal structure and element doping. J Biomater Appl. 2003; 10.1177/0885328203017004005.

[70] Kim, Hwa-Min, Sung Bo Seo, Dong Young Kim, Kang Bae and SYS. Enhanced Hydrophilic Property of TiO2 Thin Film Deposited on Glass Etched with O2 Plasma. Trans Electr Electron Mater. 2013;14(3):152–5. 10.4313/teem.2013.14.3.152.

[71] Ganesh VA, Nair AS, Raut HK, Walsh TM, Ramakrishna S. Photocatalytic superhydrophilic TiO 2 coating on glass by electrospinning. RSC Adv. 2012;2(5):2067–72. 10.1039/c2ra00921h.

[72] Erickson D, Li D, Park CB. Numerical simulations of capillary-driven flows in nonuniform cross-sectional capillaries. J Colloid Interface Sci. 2002; 10.1006/jcis.2002.8361.

[73] Saha AA, Mitra SK, Tweedie M, Roy S, McLaughlin J. Experimental and numerical investigation of capillary flow in SU8 and PDMS microchannels with integrated pillars. Microfluid Nanofluidics. 2009;7(4):451–65. 10.1007/s10404-008-0395-0.

[74] Hale RS, Bonnecaze RT, Hidrovo CH. Optimization of capillary flow through square micropillar arrays. Int J Multiph Flow. 2014; 10.1016/j.ijmultiphaseflow.2013.08.003.

[75] Van Toan N, Toda M, Ono T. An investigation of processes for glass micromachining. Micromachines. 2016; 10.3390/mi7030051.

[76] Hitzbleck M, Delamarche E. Advanced capillary soft valves for flow control in self-driven microfluidics. Micromachines. 2013; 10.3390/mi4010001.

[77] Shin S, Yang Y, Suh JS. Measurement of erythrocyte aggregation in a microchip stirring system by light transmission. Clin Hemorheol Microcirc. 2009; 10.3233/CH-2009-1172.

[78] Zhang J, Johnson PC, Popel AS. Effects of erythrocyte deformability and aggregation on the cell free layer and apparent viscosity of microscopic blood flows. Microvasc Res. 2009;77(3):265–72. 10.1016/j.mvr.2009.01.010.

[79] Xue S, Lee BK, Shin S. Disaggregating shear stress: The roles of cell deformability and fibrinogen concentration. Clin Hemorheol Microcirc. 2013; 10.3233/CH-2012-1627.

[80] Juncker D, Schmid H, Drechsler U, Wolf H, Wolf M, Michel B, et al. Autonomous microfluidic capillary system. Anal Chem. 2002;74(24):6139–44. 10.1021/ac0261449.

[81] Cavaccini G, Pianese V, Jannelli A, Iacono S, Fazio R. One-dimensional mathematical

and numerical modeling of liquid dynamics in a horizontal capillary. J Comput Methods Sci Eng. 2009;9(1–2):3–16. 10.3233/JCM-2009-0252.

[82] Cito S, Pallares J, Fabregat A, Katakis I. Numerical simulation of wall mass transfer rates in capillary-driven flow in microchannels. Int Commun Heat Mass Transf. 2012;39(8):1066–72. 10.1016/j.icheatmasstransfer.2012.06.013.

[83] La Notte L, Salamandra L, Zampetti A, Brunetti F, Brown TM, Di Carlo A, et al. Airbrush spray coating of amorphous titanium dioxide for inverted polymer solar cells. Int J Photoenergy. 2012; 10.1155/2012/897595.

[84] Suciu RC, Roşu MC, Silipaş TD, Biriş AR, Bratu I, Indrea E. TiO2 thin films prepared by spin coating technique. In: Revue Roumaine de Chimie. 2011.

[85] Bartholomeusz DA, Boutté RW, Andrade JD. Xurography: Rapid prototyping of microstructures using a cutting plotter. J Microelectromechanical Syst. 2005; 10.1109/JMEMS.2005.859087.

[86] Yuan Y, Lee TR. Contact Angle and Wetting Properties. In: Surface Science Techniques. 2013. p. 3–5. 10.1007/978-3-642-34243-1.

[87] Baskurt OK, Uyuklu M, Ulker P, Cengiz M, Nemeth N, Alexy T, et al. Comparison of three instruments for measuring red blood cell aggregation. Clin Hemorheol Microcirc. 2009; 10.3233/CH-2009-1240.

[88] Baskurt OK, Uyuklu M, Ulker P, Cengiz M, Nemeth N, Alexy T, et al. Comparison of three instruments for measuring red blood cell aggregation. Clin Hemorheol Microcirc. 2009;43(4):283–98. 10.3233/CH-2009-1240.

[89] Shin S, Hou JX, Suh JS, Singh M. Validation and application of a microfluidic ektacytometer (RheoScan-D) in measuring erythrocyte deformability. Clin Hemorheol Microcirc. 2007;37(4).

[90] Baskurt OK, Hardeman MR, Uyuklu M, Ulker P, Cengiz M, Nemeth N, et al. Comparison of three commercially available ektacytometers with different shearing geometries. Biorheology. 2009; 10.3233/BIR-2009-0536.

[91] Horobin JT, Sabapathy S, Simmonds MJ. Red blood cell tolerance to shear stress above and below the subhemolytic threshold. Biomech Model Mechanobiol. 2020;19:851–60. 10.1007/s10237-019-01252-z.

[92] Brossard C, Monnier J-C, Barricau P, Vandernoot F-X, Sant Y Le, Champagnat F, et al. Principles and applications of particle image velocimetry. Onera AerospaceLab J. 2009;

[93] Dabiri D. Cross-Correlation Digital Particle Image Velocimetry-A Review.

[94] Kaliviotis E, Sherwood JM, Dusting J, Balabani S. Quantification of local blood flow characteristics in microfluidic applications. Ser Biomech. 2016;

[95] C. J. Bourdon, M. G. Olsen, and A. D. Gorby. The Depth of Correlation in Micro-PIV for High Numerical Aperture and Immersion Objectives. J Fluids Eng. 2006;128:883–6.

[96] Poelma C, Kloosterman A, Hierck BP, Westerweel J. Accurate Blood Flow Measurements: Are Artificial Tracers Necessary? PLoS One. 2012;7(9). 10.1371/journal.pone.0045247.

[97] Bourdon CJ, Olsen MG, Gorby AD. The Depth of Correlation in Micro-PIV for High Numerical Aperture and Immersion Objectives. J Fluids Eng. 2006;128(4):883. 10.1115/1.2201649.

[98] Zhang S, Cagney N, Balabani S, Naveira-Cotta CP, Tiwari MK. Probing vortex-shedding at high frequencies in flows past confined microfluidic cylinders using high-speed microscale particle image velocimetry. Phys Fluids. 2019; 10.1063/1.5111817.

[99] Zhang S, Neil C, Lacassagne T, Balabani, Stavroula Naveira-Cotta CP, Tiwaria MK. Mixing in flows past confined microfluidic cylinders: effects of pin and fluid interface offsetting. Chem Eng J. 2020;Accepted.

[100] Crowe CT, Schwarzkopf JD, Sommerfeld M, Tsuji Y. Multiphase Flows with Droplets and Particles. Multiphase Flows with Droplets and Particles. 2011. 10.1201/b11103.

[101] Kaliviotis E, Dusting J, Balabani S. Spatial variation of blood viscosity: Modelling using shear fields measured by a μPIV based technique. Med Eng Phys. 2011; 10.1016/j.medengphy.2010.09.004.

[102] Kameneva M V, Watach MJ, Borovetz HS. Gender difference in rheologic properties of blood and risk of cardiovascular diseases. Clin Hemorheol Microcirc. 1999;

[103] Shin, S., Jang, J. H., Park, M. S., Ku, Y. and Suh J. Optical detection of red blood cell aggregation in a disposable microfluidic channel. J Mech Sci Technol. 2005;19(3):887–93. 10.1007/bf02916137.

[104] Uyuklu M, Cengiz M, Ulker P, Hever T, Tripette J, Connes P, et al. Effects of storage

duration and temperature of human blood on red cell deformability and aggregation. Clin Hemorheol Microcirc. 2009; 10.3233/CH-2009-1178.

[105] Kowalczyk W, Zima BE, Delgado A. A biological seeding particle approach for μ-PIV measurements of a fluid flow provoked by microorganisms. Exp Fluids. 2007;43(1):147–50. 10.1007/s00348-007-0324-0.

[106] Pasias D, Passos A, Constantinides G, Balabani S, Kaliviotis E. Surface tension driven flow of blood in a rectangular microfluidic channel: Effect of erythrocyte aggregation. Phys Fluids. 2020;32(7). 10.1063/5.0008939.

[107] Heshmati M, Piri M. Experimental investigation of dynamic contact angle and capillary rise in tubes with circular and noncircular cross sections. Langmuir. 2014; 10.1021/la501724y.

[108] Shi Z, Zhang Y, Liu M, Hanaor DAH, Gan Y. Dynamic contact angle hysteresis in liquid bridges. Colloids Surfaces A Physicochem Eng Asp. 2018; 10.1016/j.colsurfa.2018.07.004.

[109] Szekely J, Neumann AW, Chuang YK. The rate of capillary penetration and the applicability of the washburn equation. J Colloid Interface Sci. 1971; 10.1016/0021-9797(71)90120-2.

[110] Srivastava N, Burns MA. Analysis of non-Newtonian liquids using a microfluidic capillary viscometer. Anal Chem. 2006;78(5):1690–6. 10.1021/ac0518046.

[111] Elblbesy MA, Hereba AT. Computation of the Coefficients of the Power law model for Whole Blood and Their Correlation with Blood Parameters. Appl Phys Res. 2016; 10.1177/003591571200501117.

[112] Bruus H. Theoretical microfluidics. USA: Oxford University Press; 2008.

[113] Bruus H. Theoretical microfluidics. Vol. 18, Physics. USA: Oxford University Press; 2008. 10.1111/j.1574-6968.2009.01808.x.

[114] Zaitsev S. Dynamic surface tension measurements as general approach to the analysis of animal blood plasma and serum. Advances in Colloid and Interface Science. 2016. 10.1016/j.cis.2016.06.007.

[115] Kaliviotis E, Yianneskis M. On the effect of microstructural changes of blood on energy dissipation in Couette flow. Clin Hemorheol Microcirc. 2008;39(1–4):235–42. 10.3233/CH-2008-1087.

[116] Kaliviotis E, Yianneskis M. An energy-rate based blood viscosity model incorporating

aggregate network dynamics. Biorheology. 2009;46(6):487–508. 10.3233/BIR-2009-0555.

[117] Gillissen JJJ, Papadopoulou A, Balabani S, Tiwari MK, Wilson HJ. Suspension rheology of adhesive particles at high shear-rates. Phys Rev Fluids. 2020; 10.1103/PhysRevFluids.5.053302.

[118] Chien S, Jan K. Ultrastructural basis of the mechanism of rouleaux formation. Microvasc Res. 1973;5(2):155–66. 10.1016/0026-2862(73)90068-X.

[119] Kitamura H, Sigel B, Machi J, Feleppa EJ, Sokil-Melgar J, Kalisz A, et al. Roles of hematocrit and fibrinogen in red cell aggregation determined by ultrasonic scattering properties. Ultrasound Med Biol. 1995; 10.1016/0301-5629(95)00022-J.

[120] Jovtchev S, Djenev I, Stoeff S, Stoylov S. Role of electrical and mechanical properties of red blood cells for their aggregation. Colloids Surfaces A Physicochem Eng Asp. 2000; 10.1016/S0927-7757(99)00345-3.

[121] Lerche D, Baumler H. Moderate heat treatment of only red blood cells (RBC) slows down the rate of RBC-RBC aggregation in plasma. Biorheology. 1984; 10.3233/BIR-1984-21308.

[122] Yamamoto M. Effects of Fibrinogen, Globulin, Albumin and Hematocrit on the Kinetics of Erythrocyte Aggregation in Man. Angiology. 1986;37(9):663–71. 10.1177/000331978603700908.

[123] Merrill EW, Gilliland ER, Lee TS, Salzman EW. Blood rheology: effect of fibrinogen deduced by addition. Circ Res. 1966; 10.1161/01.RES.18.4.437.

[124] Dupire J, Socol M, Viallat A. Full dynamics of a red blood cell in shear flow. Proc Natl Acad Sci U S A. 2012; 10.1073/pnas.1210236109.

[125] Brooks DE, Goodwin JW, Seaman G V. Interactions among erythrocytes under shear. J Appl Physiol. 1970;28(2):172–7. 10.1152/jappl.1970.28.2.172.

[126] Kapnisis K, Seidner H, Prokopi M, Pasias D, Pitsillides C, Anayiotos A, et al. The effects of stenting on hemorheological parameters: An in vitro investigation under various blood flow conditions. Clin Hemorheol Microcirc. 2019;72(4):375–93. 10.3233/CH-180540.

[127] Kaliviotis E, Ivanov I, Antonova N, Yianneskis M. Erythrocyte aggregation at non-steady flow conditions: A comparison of characteristics measured with electrorheology and image analysis. Clin Hemorheol Microcirc. 2010;44(1):43–54. 10.3233/CH-2009-1251.

[128] Ju M, Ye SS, Low HT, Zhang J, Cabrales P, Leo HL, et al. Effect of deformability difference between two erythrocytes on their aggregation. Phys Biol. 2013; 10.1088/1478-3975/10/3/036001.

[129] Kim J-H, Lee H, Lee B, Shin S. Influence of shear stress on erythrocyte aggregation. Clin Hemorheol Microcirc. 2016;62(2):165–71. 10.3233/CH-151969.

[130] Gaspar-Rosas A, Thurston GB. Erythrocyte aggregate rheology by transmitted and reflected light. Biorheology. 1988;25(3):471–87. 10.3233/BIR-1988-25308.

[131] White F. Viscous Fluid Flow (McGraw-Hill Mechanical Engineering). 2005;640.

[132] Macosko CW. Rheology Principles. Meas Appl. 1996;568.

[133] Pipe CJ, McKinley GH. Microfluidic rheometry. Mech Res Commun. 2009;36(1):110–20. 10.1016/J.MECHRESCOM.2008.08.009.

[134] Dongyang K, Wang W, Lee J, Tai YC, Hsiai TK. Measurement of viscosity of unadulterated human whole blood using a capillary pressure-driven viscometer. In: 2015 IEEE 10th International Conference on Nano/Micro Engineered and Molecular Systems, NEMS 2015. Institute of Electrical and Electronics Engineers Inc.; 2015. p. 1–4. 10.1109/NEMS.2015.7147343.

[135] Dormandy JA. Clinical significance of blood viscosity. Ann R Coll Surg Engl. 1970;47(4):211–28.

[136] Fons C, Brun JF, Supparo I, Mallard C, Barnet L, Orsetti A. Evaluation of blood viscosity at high shear rate with a falling ball viscometer. Clin Hemorheol Microcirc. 1993;13(5):651–9. 10.3233/CH-1993-13509.

[137] Trouton FRT. On the coefficient of viscous traction and its relation to that of viscosity. Proc R Soc London Ser A, Contain Pap a Math Phys Character. 1906;77(519):426–40. 10.1098/RSPA.1906.0038.

[138] Różańska S, Różański J, Ochowiak M, Mitkowski PT. Extentional viscosity measurments of concentrated emulsions with the use of the opposed nozzles device. 31(01):47–55.

[139] Padmanabhan M, Macosko CW. Extensional viscosity from entrance pressure drop measurements. Rheol Acta. 1997;36(2). 10.1007/bf00366820.

[140] Jung J, Lee B-K, Shin S. Yield shear stress and disaggregating shear stress of human

blood. Korea Aust Rheol J. 2014;26(2):191–8. 10.1007/s13367-014-0020-6.

[141] Simmonds MJ, Meiselman HJ. Prediction of the level and duration of shear stress exposure that induces subhemolytic damage to erythrocytes. Biorheology. 2016; 10.3233/BIR-16120.

[142] Kolbasov A, Comiskey PM, Sahu RP, Sinha-Ray S, Yarin AL, Sikarwar BS, et al. Blood rheology in shear and uniaxial elongation. Rheol Acta. 2016;55(11–12). 10.1007/s00397-016-0964-1.

[143] KUOK KK, CHIU PC. Application of Particle Image Velocimetry (PIV) for Measuring Water Velocity in Laboratory Sedimentation Tank. IRA-International J Technol Eng (ISSN 2455-4480). 2017; 10.21013/jte.v9.n3.p1.

[144] Nilsson AM, Lucassen GW, Verkruysse W, Andersson-Engels S, van Gemert MJC. <title>Optical properties of human whole blood: changes due to slow heating</title>. In: Laser-Tissue Interaction and Tissue Optics II. SPIE; 1996. p. 24–34. 10.1117/12.260746.

[145] Amin M, Hussain MA, Shahwar D, Hussain M. Thermal Analysis and Degradation Kinetics of Dextran and Highly Substituted Dextran Acetates. Vol. 37, J.Chem.Soc.Pak. 2015.

[146] Masuelli MA. Dextrans in Aqueous Solution. Experimental Review on Intrinsic Viscosity Measurements and Temperature Effect. J Polym Biopolym Phys Chem. 2013;1(1):13–21. 10.12691/jpbpc-1-1-3.

Appendices

Appendix 1 CDMA Matlab algorithm for the calculation of the RBCA index CV.

```
clear all;
close all;
clc;
%% reding of images
%diff from image 1 and in cvembiov9 from image 5
%%%%%%%%%%%%%%%%%%%%%%H007 WB
cd('F:\Stent Flow\Aggregation_EMBIO\Experiments\2017-12-8_EMBIO Aggregometry\H007_WB_0');
% read jpiv (.jvc) files in matlab
% f=625
% imread(...,'PixelRegion',{ROWS, COLS})
%a=imread('ImgA000001.tif');
%%%%%%%%%%%%boundaries for roi, tlb=top left boundary , lrb=lower right
%%%%%%%%%%%%
%%%%%%%%%%%%boundary and variables
%cols get x and rows get y
tlbrstart=10;%start for rows in pixelregion in imread
tlbcstart=10;%start for collumns in pixelregion in imread
lrbrlast=10;%end for rows in pixelregion in imread
lrbclast=10;%end for collumns in pixelregion in imread
startimage=4;%%first image after meniscus has passed
lastimage=119;
twb=0:(lastimage-startimage);
threshold_differenceper=0.005*100;
frns=inf;%flowrate no, stent inf if flow is with stent, both frns and frs zero if baseline
frs=17.5;%flow rate stent,inf if flow is with no stent,both frns and frs zero if baseline
%%%%reading of images from curent folder to matlab insert the name of the
%%%%image at imread(sprintf('name_of_image.png',k))
for k=startimage:lastimage%%%%%number of images
    images{k} = imread(sprintf('H007_WB_0_%01d.png',k));%,'PixelRegion',{[tlbrstart,lrbrlast],[tlbcstart,lrbclast]});
%     images{k} = imread(sprintf('H007_WB_0_nostent_%01d.png',k),'PixelRegion',{[tlbrstart,lrbrlast],[tlbcstart,lrbclast]});
end
%%%%%%%%%%%%%
figure
imshow(images{1,startimage})
%%%%%%%%%%convert images form colour to greyscale
for i=startimage:lastimage%%%%%number of images
   imagesgrey{1,i}=rgb2gray(images{1,i});%coverts images from colour to grey
end
imagesgreym = cat(3, imagesgrey{:});%%%images from cell to matrix
% imagesgreym=imagesgreym(1:480,1:600,:); PIXELREGION
%% standard deviation
%%%%%%%%%%%%standaard deviation of each image
imagesnumber=k-startimage+1;%number of images
%standard deviation calculation
stdimagesgreym=zeros(1,1,imagesnumber);%std of images matrix formation

for i=1:imagesnumber
   stdimagesgreym(1,1,i)=std2(imagesgreym(:,:,i));%calculation of std of each image
end
%% mean intensoty
%%%%%%%%%%%%%%%%%%%%%%mean intensity of each image
meanimagesgreym=zeros(1,1,imagesnumber);
for ii=1:imagesnumber
     meanimagesgreym(1,1,ii)=mean2(imagesgreym(:,:,ii));%calculation of intensity of each image
end
%% concentration variation
%%%%%%%%%%%%%%%%%%%%%%concenteation variation
cvimagesgreym=zeros(1,1,imagesnumber);%cv atrix formation
cvimagesgreym=  stdimagesgreym./meanimagesgreym;%cv calculation std/cv of each image
cvimagesgreym2d=cat(3, cvimagesgreym(:));%cvimagesgreym from 3d to 2d
cvimagesgreym2dwb= cvimagesgreym2d';
dt=1;%%time diference between each image
meancvwb=mean(cvimagesgreym2dwb);%mean cv calculation
%% raw data intensity plot
% twb=(((startimage-1):(lastimage-1))).*dt;%t=0 when meniscus has passed
twb=0:(lastimage-startimage);
 meanimagesgreym2d = permute(meanimagesgreym,[1 3 2]);%meanimagesgreym2d=meanimagesgreym(i.e. mean intansity of each grey image) from 3d to 2d
%%%plot intensity of raw data vs time
figure
plot(twb,meanimagesgreym2d,'*')
%title('whole blood intensity vs time','fontsize',14')
xlabel('t (s)')
ylabel('I (-)')
set(gca,'Fontsize',20)
xlim([0 120])
% subplot(5,2,1)
%
% plot(twb,meanimagesgreym2d,'*')
% %title('whole blood intensity vs time','fontsize',14')
% xlabel('time (s)')
% ylabel('I (-)')

 %%%%%%%%%%%%%%%%%%%%%%
%% raw data corrected intensity plot
%%%%%corrected intensity
%corrected intensity is corection of intensity if illumination of
%microscope intensity sometimes suddenly changes during the experiment
%to correct the intensity set a thresold difference betweeen two readings.
% if the difference between two points is greater than this correct the
% points with the reduced intensity by this difference (correct not only the
% points with the difference greeater than one, correct all the following
% points with reduced intensity)
% diffa=abs(diff);
% dufffav=mean(diffa(1,50:100))
% threshold_difference=1;
for q=1:(length(meanimagesgreym2d)-1)
   for w=q+1;
      diff(1,q)= meanimagesgreym2d(1,q)-meanimagesgreym2d(1,w);
   end
end
diffper=(diff(:,:)./meanimagesgreym2d(1,1:(end-1)))*100;
threshold_differenceper=0.005*100;%i.e. 0.5 tis ekato
if max(diffper)> threshold_differenceper;
   f1=find(diffper(1:end)>threshold_differenceper)+1-1;%find position od difference greater than 1 ignoring the first 10 values
   for r=1:length(f1)

meanimagesgreym2d(1,f1(r)+1:end)=meanimagesgreym2d(1,f1(r)+1:end)+diff(1,f1(r));
      f2=find(diffper>threshold_differenceper);
   end
elseif max(diffper)<threshold_differenceper
```

```
    f1=0;

meanimagesgreym2d(1,f1+1:end)=meanimagesgreym2d(1,f1+1:end);
end

mean(meanimagesgreym2d)
figure
plot(twb,meanimagesgreym2d,'*')
set(gca,'Fontsize',20)
xlim([0 120])
ylabel('I (-)')
xlabel('t (s)')
%title('whole blood intensity corrected vs time 1st','fontsize',14')

 %% 2ND CORRECTION
for q=1:(length(meanimagesgreym2d)-1)
    for w=q+1;
        diff(1,q)= meanimagesgreym2d(1,q)-meanimagesgreym2d(1,w);
    end
end
diffper=(abs(diff(:,:))./meanimagesgreym2d(1,1:(end-1)))*100;
threshold_differenceper=0.005*100;%i.e. 0.5 tis ekato
if max(diffper)> threshold_differenceper;
    f1=find(abs(diffper(1:end))>threshold_differenceper)+1-1;%find
position od difference greater than 1 ignoring the first 10 values
    for r=1:length(f1)

meanimagesgreym2d(1,f1(r)+1:end)=meanimagesgreym2d(1,f1(r)+1:e
nd)-abs(diff(1,f1(r)));
        f2=find(diffper<threshold_differenceper);
    end
elseif max(diffper)<threshold_differenceper
    f1=0;

meanimagesgreym2d(1,f1+1:end)=meanimagesgreym2d(1,f1+1:end);
end
%%

%%%plot corrected intensity vs time
mean(meanimagesgreym2d)
figure
plot(twb,meanimagesgreym2d,'*')
%title('whole blood intensity corrected vs time 2nd','fontsize',14')
% return
% subplot(5,2,2)
% plot(twb,meanimagesgreym2d,'*')
% %title('whole blood intensity corrected vs time','fontsize',14')

figure
plot(twb,meanimagesgreym2d,'*')
%title('whole blood intensity corrected vs time','fontsize',14')
xlabel('time (s)')
ylabel('I (-)')

% subplot(5,2,3)
% plot(twb,meanimagesgreym2d,'*')
% %title('whole blood intensity corrected vs time','fontsize',14')
% xlabel('time (s)')
% ylabel('I (-)')

%% normalized raw data corrected intensity plot
%normalized corrected intensity
%normalize corrected intensity with minimun of corrected intensity
meanimagesgreym2dnorm= ((meanimagesgreym2d/min(
meanimagesgreym2d))-1)*100;
figure
plot(twb,meanimagesgreym2dnorm,'-*');
%title('whole blood intensity corrected normalized vs time','fontsize',14')
xlabel('t (s)')
% ylabel('Intensity Normalized with minimum(-)')
ylabel('I* (-)')
set(gca,'Fontsize',20)
xlim([0 120])
% subplot(5,2,4);
% %%%plot normalized corrected intensity vs time
% plot(twb,meanimagesgreym2dnorm,'-*');
% %title('whole blood intensity corrected normalized vs
time','fontsize',14')
% xlabel('time (s)')
% ylabel('Intensity Normalized with minimum(-)'

%% polyfit
%%%%%%%%%%%%%%%%%% polynomial fit
n=3;%order of polynomial

pfit=polyfit(twb,meanimagesgreym2d,3);
polyfitint=polyval(pfit,twb);
%r square of polynomial fit
correlation_coeff_exnorm = corr2(polyfitint,meanimagesgreym2d);
r_sqr_p = power(correlation_coeff_exnorm,2);
%polynomial fit of the first 10 seconds
twb10=(startimage-1):10+startimage-1;%%% first 10 valid seconds
if startimage==1

meanimagesgreym2d10=meanimagesgreym2d((startimage):10+startim
age);
elseif startimage>1
    meanimagesgreym2d10= meanimagesgreym2d((startimage-
1):10+startimage-1);
end
twb10=twb(1:11);
meanimagesgreym2d10=meanimagesgreym2d(1:11);
pfit10=polyfit(twb10,meanimagesgreym2d10,n);
polyfit10=polyval(pfit10,twb10);
%r square of polyfit of first 10 valid seconds
correlation_coeff_p10 = corr2(polyfit10,meanimagesgreym2d10);
r_sqr_p10 = power(correlation_coeff_p10,2);
%plot polyfit of first 10 valid seconds of corrected intensity
figure
% subplot(5,2,5)
plot(twb10,polyfit10,'-*')
%title('whole blood polynomial fit of 10s')
xlabel('time (s)')
ylabel('I (-)')

%%%%%%%%%%%%%%%%%%%%%%%%%%%%%%%%%%%
%%%%%%%%%%%%%%%%%%%%%%%%%%%%%%%%%%%
%%%%%%
%%%%polynomial fit of first 10 seconds on normalized corrected
intensity
n=3;%order of polynomial
pfitnorm=polyfit(twb,meanimagesgreym2dnorm,3);
polyfitnormint=polyval(pfitnorm,twb);
%r square of polynomial normalized data of corrected intensity
correlation_coeff_pnorm = corr2(
polyfitnormint,meanimagesgreym2dnorm);
r_sqr_pnorm = power(correlation_coeff_pnorm,2);
%%polyomial fit of the first 10 seconds
n=3;%order of polynomial
% twb10=(startimage-1):10+startimage-1;%% 10 seconds after the
meniscus has passed (if some of the first points are discarded due to
error readings the time values will be 10 seconds form the valid point)
% %%%intensity of 10 secoonds after the meniscus has passed (if
some of the first points are discarded due to error readings the intensity
values will be 10 seconds form the valid point)
% if startimage==1
%
meanimagesgreym2dnorm10=meanimagesgreym2dnorm((startimage):
10+startimage);
% elseif startimage>1
%     meanimagesgreym2dnorm10=
meanimagesgreym2dnorm((startimage-1):10+startimage-1);
% end
meanimagesgreym2dnorm10= meanimagesgreym2dnorm(1,1:11);
pfitnorm10=polyfit(twb10,meanimagesgreym2dnorm10,n);
polyfitnorm10=polyval(pfitnorm10,twb10);
%r square of polynomial normalized data of the first valid 10 seconds of
corrected intensity
correlation_coeff_pnorm10 = corr2(
polyfitnorm10,meanimagesgreym2dnorm10);
```

```
r_sqr_pnorm10 = power(correlation_coeff_pnorm10,2);
%%%plot of polynomial fit of the first valid 10 secinds intensity
%%%values vs time
figure
plot(twb10,polyfitnorm10,'-*')
%title('whole blood polynomial normaized fit of 10s vs time')
xlabel('time (s)')
ylabel('Intensity Normalized with mimimum (-)')

 % subplot(5,2,6)
% plot(twb10,polyfitnorm10,'-*')
% %title('whole blood polynomial normaized fit of 10s vs time')
% xlabel('time (s)')
% ylabel('Intensity Normalized with mimimum (-)')

%%%%%%%%%%%%%%%%%%%%%%%%%%%%%%%%%%%
%%%%%%%%%%%%%%%%%%%%%%%%%%%%%%%%
%% expotential fit second order
%%second order expotenial fit for all data
%%%second order expotential fit  of normalized corrected intensity in
cfit form
exfit = fit(twb',meanimagesgreym2d','exp2');
coef=coeffvalues(exfit);

%%%%%%%%%%%%plot second order expotential fit vs time
figure
plot(exfit,twb,meanimagesgreym2d)
%title('double expotential fit')
xlabel('time (s)')
ylabel('I (-)')

% subplot(5,2,7)
% plot(exfit,twb,meanimagesgreym2d)
% %title('double expotential fit')
% xlabel('time (s)')
% ylabel('I (-)')

%%%second order expotential fit  of normalized corrected intensity
form cfit form to matrix
for i=startimage:lastimage
   exfitintensity(1,i)=exfit(i);
end
exfitintensity=exfitintensity(1,startimage:lastimage);
%%%%r square of secind order expotential fil
correlation_coeff_ex = corr2(exfitintensity,meanimagesgreym2d);
r_sqr_ex = power(correlation_coeff_ex,2);

% tfast=-1/coef(1,2);
% tslow=-1/coef(1,4);
%%%%%%%%%%%%%%%%%%%%%%%%%%%%%%%%%%%
%%%%%%%%%%%%%%%%%%%%%%%%%%%%%%%%%%%
%%%%%%%%%%%%%%%%%%%%
%%%second order expotential fit  of normalized corrected intensity
%%second order expotenial fit for all data normalized
%%%second order expotential fit  of normalized corrected intensity in
cfit form
exfitnorm = fit(twb',meanimagesgreym2dnorm','exp2');
coefnorm=coeffvalues(exfitnorm);
% tfastnorm=-1/coefnorm(1,2);
% tslownorm=-1/coefnorm(1,4);
figure
plot(exfitnorm,twb,meanimagesgreym2dnorm)
%title('double expotential fit normalized')
xlabel('time (s)')
ylabel('Intensity Normalized with minimum(-)')

 % subplot(5,2,8)
% %%%plot corrected intensity vs time
%
% plot(exfitnorm,twb,meanimagesgreym2dnorm)
% %title('double expotential fit normalixed')
% xlabel('time (s)')
% ylabel('Intensity Normalized with minimum(-)')

% % figure
% % plot(exfitnorm,twb,meanimagesgreym2dnorm)
% % xlabel('t(s)')
% % ylabel('I(-)')
% % set(gca,'fontsize',20)
%%%from cfit form to matrix
for i=startimage:lastimage
   exfitintensitynorm(1,i)=exfitnorm(i);
end
exfitintensitynorm=exfitintensitynorm(1,startimage:lastimage);
%r square of polynomial normalized data of corrected intensity
correlation_coeff_exnorm = corr2(
exfitintensitynorm,meanimagesgreym2dnorm);
r_sqr_exnorm = power(correlation_coeff_exnorm,2);
%%%%%%%%%%%%%%%%%%%%%%%%%%%%%%%%%%%
%%%%%%%%%%%%%%%%%%%%%%%%%%%%%%%%%%%
% %%%%%%double expotential fit new normalized
% myfitc = fittype('a+b*exp(-(1/c)*x)+d*exp(-(1/e)*x)')
myeq='a+b*exp(-(1/c)*x)+d*exp(-(1/e)*x)';
x=twb;
y=meanimagesgreym2dnorm;
 %%%second order expotential fit new of  corrected intensity in cfit
form
% startpoints=[0 -0.1 1 -0.1 10];
% startpoints=[0 -inf 1 -inf 1];
startpoints=[0 -100 1 -100 1];
lowerlimits=startpoints;
f1 = fit(x',y',myeq,'lower',lowerlimits,'upper',[inf inf 120 inf 120],'Start',
startpoints);
coeff1=coeffvalues(f1);
%% tfast and tslow
t(1,1)=coeff1(1,3);
t(1,2)=coeff1(1,5);
tfast=min(t);
tslow=max(t);
% %%%%%%%%%%%plot second order expotential fit vs time
figure
plot(f1,twb,meanimagesgreym2dnorm)
%title('Double expotential fit new normalized')
xlabel('t (s)')
ylabel('I* (-)')
set(gca,'fontsize',20)
ylim([0 3.5])
legend('Raw Data','Exp2 fitting')
% subplot(5,2,9)
figure
plot(f1,twb,meanimagesgreym2dnorm)
%title('Double expotential fit new normalized')
xlabel('time (s)')
ylabel('Intensity Normalized with minimum(-)')
for i=startimage:lastimage
   exf1(1,i)=f1(i);
end
exf1=exf1(1,startimage:lastimage);
%r square of expotential new  data of corrected intensity
correlation_coeff_exf1 = corr2(exf1,meanimagesgreym2dnorm);
r_sqr_exnewnorm = power(correlation_coeff_exf1,2);

 % aggregation indices

%% aggregation index of raw data
f10=find(twb==10);%find col where twb=10s
areaard=meanimagesgreym2d(1,f10)*(twb(1,f10))-
meanimagesgreym2d(1,1)*(twb(1,f10));%calculates area a of corrected
raw data=intensity at t=10s
areabrd=trapz(twb(1:f10),meanimagesgreym2d(1:f10))-
(meanimagesgreym2d(1,1)*twb(1,f10));%integrates area under raw
data corrected curve at the boundaies of twb
Mrd=areabrd;%M inddex of raw data
AIwbrd=areabrd/(areaard);%+areab);%raw data aggregation index
AUCrd=areabrd;
AAcrd=areaard-areabrd;
AMPrd=max(meanimagesgreym2d)-min(meanimagesgreym2d);
%% Aggregation index calculation of raw data normalized
f10=find(twb==10);%find col where twb=10s
```

```
areaardnorm=meanimagesgreym2d(1,f10)*(twb(1,f10))-
meanimagesgreym2d(1,1)*(twb(1,f10));%calculates area a of corrected
raw data=intensity at t=10s
areabrdnorm=trapz(twb(1:f10),meanimagesgreym2d(1:f10))-
(meanimagesgreym2d(1,1)*twb(1,f10));%integrates area under raw
data corrected curve at the boundaies of twb
Mrdnorm=areabrdnorm;%M inddex of raw data
Alwbrdnorm=areabrdnorm/(areaardnorm);%+areab);%raw data norm
aggregation index
AUCrdnorm=areabrdnorm;
AAcrdnorm=areaardnorm-areabrdnorm;
AMPrdnorm=max(meanimagesgreym2dnorm)-
min(meanimagesgreym2dnorm);
%% aggregation index for polyfit first 10 valid secinds
f10=find(twb==10);%find col where twb=10s
areaap10=polyfit10(1,f10)*(twb(1,f10))-
polyfit10(1,1)*(twb(1,f10));%calculates area a of corrected raw
data=intensity at t=10s
areabp10=trapz(twb(1:f10),polyfit10(1:f10))-
(polyfit10(1,1)*twb(1,f10));%integrates area under raw data corrected
curve at the boundaies of twb
Mp10=areabp10;%M index of fit data of polyfit of first 10 seconds
Alwbp10=areabp10/(areaap10);%;%aggregation of polyfit data of first
10 seconds
AUCp10=areabp10;
AACp10=areaap10-areabp10;
AMPp10=max(polyfit10)-min(polyfit10);
%% aggregation index for polyfit first 10 valid seconds normalized
f10=find(twb==10);%find col where twb=10s
areaap10norm=polyfitnorm10(1,f10)*(twb(1,f10))-
polyfitnorm10(1,1)*(twb(1,f10));%calculates area a of corrected raw
data=intensity at t=10s
areabp10norm=trapz(twb(1:f10),polyfitnorm10(1:f10))-
(polyfitnorm10(1,1)*twb(1,f10));%integrates area under raw data
corrected curve at the boundaies of twb
Mp10norm=areabp10;%M index of fit data of polyfitnorm of first 10
seconds
Alwbp10norm=areabp10norm/(areaap10norm);%;%aggregation of
polyfitnorm data of first 10 seconds;
AUCp10norm=areabp10norm;
AACp10norm=areaap10norm-areabp10norm;
AMPp10norm=max(polyfit10)-min(polyfit10);

%% aggregation index for expotential fit
f10=find(twb==10);%find col where twb=10s
areaaex=exfitintensity(1,f10)*(twb(1,f10))-
exfitintensity(1,1)*(twb(1,f10));%calculates area a of corrected raw
data=intensity at t=10s
areabex=trapz(twb(1:f10),exfitintensity(1:f10))-
(exfitintensity(1,1)*twb(1,f10));%integrates area under raw data
corrected curve at the boundaies of twb
Mex=areabex;%M inddex of raw data
Alwbex=areabex/(areaaex);%+areab);%exp data aggregation index
AUCex=areabex;
AACex=areaaex-areabex;
AMPex=max(exfitintensity)-min(exfitintensity);
%% aggregation index for expotential fit bormalized
f10=find(twb==10);%find col where twb=10s
areaaexnorm=exfitintensitynorm(1,f10)*(twb(1,f10))-
exfitintensitynorm(1,1)*(twb(1,f10));%calculates area a of corrected raw
data=intensity at t=10s
areabexnorm=trapz(twb(1:f10),exfitintensitynorm(1:f10))-
(exfitintensitynorm(1,1)*twb(1,f10));%integrates area under raw data
corrected curve at the boundaies of twb
Mexnorm=areabexnorm;%M inddex of raw data
Alwbexnorm=areabexnorm/(areaaexnorm);%+areab);%exp norm
aggregation index
AUCexnorm=areabexnorm;
AACexnorm=areaaexnorm-areabexnorm;
AMPexnorm=max(exfitintensitynorm)-min(exfitintensitynorm);
%% aggregation index for expotential fit normalized new
f10=find(twb==10);%find col where twb=10s
areaaexf1=exf1(1,f10)*(twb(1,f10))-exf1(1,1)*(twb(1,f10));%calculates
area a of corrected raw data=intensity at t=10s
areabexf1=trapz(twb(1:f10),exf1(1:f10))-
(exf1(1,1)*twb(1,f10));%integrates area under raw data corrected curve
at the boundaies of twb
Mexf1=areabexf1;%M inddexf1 of raw data
Alwbexf1=areabexf1/(areaaexf1);%+areab);%exf1p data aggregation
indexf1
AUCexf1=areabexf1;
AACexf1=areaaexf1-areabexf1;
AMPexf1=max(exf1)-min(exf1);
%% thalf

%% interpulation and thalf of corrected raw data
xqrd=0:0.1:(length(twb)-1);
int=interp1(twb,meanimagesgreym2d,xqrd);
roundint=round(int,1);
intensityhalf=min(meanimagesgreym2d)+((max(meanimagesgreym2d)-
min(meanimagesgreym2d))/2);
roundintensityhalf=round(intensityhalf,1);
[row col] =find(roundint==roundintensityhalf);
dt=(lastimage-startimage+1)/length(int);
thalfrd=col(1,1)*dt;

%% interpulation and thalf of corrected raw data norm
xqrdnorm=0:0.1:(length(twb)-1);
intnorm=interp1(twb,meanimagesgreym2dnorm,xqrdnorm);
roundintnorm=round(intnorm,1);
intensityhalfnorm=min(meanimagesgreym2dnorm)+((max(meanimages
greym2dnorm)-min(meanimagesgreym2dnorm))/2);
roundintensityhalfnorm=round(intensityhalfnorm,1);
[row col] =find(roundintnorm==roundintensityhalfnorm);
dt=(lastimage-startimage+1)/length(intnorm);
thalfrdnorm=col(1,1)*dt;
%% interpulation and thalf of expotential
xqex=0:0.1:(length(twb)-1);
int=interp1(twb,exfitintensity,xqex);
roundint=round(int,1);
intensityhalf=min(exfitintensity)+((max(exfitintensity)-
min(exfitintensity))/2);
roundintensityhalf=round(intensityhalf,1);
[row col] =find(roundint==roundintensityhalf);
dt=(lastimage-startimage+1)/length(int);
thalfex=col(1,1)*dt;
%% interpolation and thalf of expotantial data norm
xqexnorm=0:0.1:(length(twb)-1);
intnorm=interp1(twb,exfitintensitynorm,xqexnorm);
roundintnorm=round(intnorm,1);
intensityhalfnorm=min(exfitintensitynorm)+((max(exfitintensitynorm)-
min(exfitintensitynorm))/2);
roundintensityhalfnorm=round(intensityhalfnorm,1);
[row col] =find(roundintnorm==roundintensityhalfnorm);
dt=(lastimage-startimage+1)/length(intnorm);
thalfexnorm=col(1,1)*dt;
%% interpolation and thalf of expotantial data new norm
xqexf1norm=0:0.1:(length(twb)-1);
intnorm=interp1(twb,exf1,xqexf1norm);
roundintnorm=round(intnorm,1);
intensityhalfnorm=min(exf1)+((max(exf1)-min(exf1))/2);
roundintensityhalfnorm=round(intensityhalfnorm,1);
[row col] =find(roundintnorm==roundintensityhalfnorm);
dt=(lastimage-startimage+1)/length(intnorm);
thalfexf1norm=col(1,1)*dt;
%% interpulation and thalf of polyfit
xqp=0:0.1:(length(twb)-1);
int=interp1(twb,polyfitint,xqp);
roundint=round(int,1);
intensityhalf=min(polyfitint)+((max(polyfitint)-min(polyfitint))/2);
roundintensityhalf=round(intensityhalf,1);
[row col] =find(roundint==roundintensityhalf);
dt=(lastimage-startimage+1)/length(int);
thalfp=col(1,1)*dt;

%% interpolation and thalf of polyfit data norm
xqpnorm=(startimage-1):0.1:(length(twb)-1);
intnorm=interp1(twb, polyfitnormint,xqpnorm);
roundintnorm=round(intnorm,1);
```

```
intensityhalfnorm=min( polyfitnormint)+((max( polyfitnormint)-min( polyfitnormint))/2);
roundintensityhalfnorm=round(intensityhalfnorm,1);
[row, col] =find(roundintnorm==roundintensityhalfnorm);
dt=(lastimage-startimage+1)/length(intnorm);
thalfpnorm=col(1,1)*dt;
%% indices
%%%%%%%%%%%indices
IndeicesRaw=[AIwbrd*100,thalfrd,AUCrd,AAcrd,AMPrd];
IndeicesPolyfit=[AIwbp10*100,thalfp,AUCp10,AACp10,AMPp10];
IndeicesExp=[AIwbex*100,thalfex,AUCex,AACex,AMPex];
Indicest=[tfast, tslow];
%indices norm
IndeicesRawnorm=[AIwbrdnorm*100,thalfrdnorm,AUCrdnorm,AAcrdnorm,AMPrdnorm];
IndeicesPolyfitnorm=[AIwbp10norm*100,thalfpnorm,AUCp10norm,AACp10norm,AMPp10norm];
IndeicesExpnorm=[AIwbexnorm*100,thalfexnorm,AUCexnorm,AACexnorm,AMPexnorm];
%%indices mix
IRD=[AIwbrd*100 AIwbrdnorm*100 thalfrd thalfrdnorm AUCrd AUCrdnorm AAcrd AAcrdnorm AMPrd AMPrdnorm 0 0];
IEX=[AIwbex*100 AIwbexnorm*100 thalfex thalfexnorm AUCex AUCexnorm AACex AACexnorm AMPex AMPexnorm r_sqr_ex r_sqr_exnorm];
IP10=[AIwbp10*100 AIwbp10norm*100 thalfp thalfpnorm AUCp10 AUCp10norm AACp10 AACp10norm AMPp10 AMPp10norm r_sqr_p10 r_sqr_pnorm10];
IT=[0 0 0 0 0 0 0 0 0 0 tfast tslow];
%%indices all
IRD=[AIwbrd*100 AIwbrdnorm*100 thalfrd thalfrdnorm AUCrd AUCrdnorm AAcrd AAcrdnorm AMPrd AMPrdnorm 0 0];
IEX=[AIwbex*100 AIwbexnorm*100 thalfex thalfexnorm AUCex AUCexnorm AACex AACexnorm AMPex AMPexnorm 0 0];
IP10=[AIwbp10*100 AIwbp10norm*100 thalfp thalfpnorm AUCp10 AUCp10norm AACp10 AACp10norm AMPp10 AMPp10norm 0 0];
IT=[0 0 0 0 0 0 0 0 0 0 tfast tslow];
%%%indices need
IRDN=[AIwbrd*100 thalfrd AMPrdnorm/100 AUCrd tslow tfast]
IEXN=[AIwbex*100 thalfex AMPexnorm/100 AUCex tslow tfast]
IEXF1N=[AIwbexf1*100 thalfexf1norm AMPexf1/100 AUCexf1 tslow tfast]
IP10N=[AIwbp10*100 thalfp AMPp10norm/100 AUCp10 tslow tfast]
% Indicestnorm=[tfastnorm,tslownorm];
% IndeicesExpNewnorm=[AIwbexf1*100,thalfexf1norm,AUCexf1,AACexf1]
%indicesbar
c = categorical({'Raw Data','Polynomial','Expotential','Tfast and Tslow'});
y=[IRD;IP10;IEX;IT];
% y=[AIwbrd*100 AIwbrdnorm*100 thalfrd thalfrdnorm AUCrd AUCrdnorm AACrd AACrdnorm tfastnorm tslownorm;AIwbp10*100 AIwbp10norm*100 thalfp thalfpnorm Mp10 Mp10norm tfast tslow tfastnorm tslownorm; AIwbex*100 AIwbexnorm*100 thalfex thalfexnorm Mex Mexnorm tfast tslow tfastnorm tslownorm;];
% y=[IndeicesRawnorm;IndeicesPolyfitnorm;IndeicesPolyfitnorm]

%%%thalf indices raw raw norm exp2 exp2norm
thalf_H007_WB_0_nostent=[thalfrd thalfrdnorm thalfex thalfexnorm];
AMP_H007_WB_0_nostent=[AMPrd AMPrdnorm AMPex AMPexnorm];
AI_H007_WB_0_nostent=[AIwbrd AIwbrdnorm AIwbex AIwbexnorm];
figure
h=bar(c,y);
set(gca,'XTickLabel',{'Raw Data','Polynomial','Expotential','Tfast and Tslow'});
% set(gca,'legend')%,{'Raw Data','Polynomial','Expotential'});
l=cell(1,12);
l{1}='Aggregation Index'; l{2}='Aggregation index Normalized';
l{3}='Thalf'; l{4}='Thalf normalized'; l{5}='AUC'; l{6}='AUC Normalized';
l{7}='AAC';l{8}='AAC Normalized';l{9}='AMP';l{10}='AMPnorm';l{11}='Tfast';l{12}='Tslow';
%title('indices')

% subplot(5,2,2)
% h=bar(c,y)
% set(gca,'XTickLabel',{'Raw Data','Polynomial','Expotential','Tfast and Tslow'});
% % set(gca,'legend')%,{'Raw Data','Polynomial','Expotential'});
% l=cell(1,12);
% l{1}='Aggregation Index'; l{2}='Aggregation index Normalized';
l{3}='Thalf'; l{4}='Thalf normalized'; l{5}='AUC'; l{6}='AUC Normalized';
l{7}='AAC';l{8}='AAC Normalized';l{9}='AMP';l{10}='AMPnorm';l{11}='Tfast';l{12}='Tslow';
% l = legend(h,l);
% c2=categorical({'tfast' ,'tslow'});
% y2=[tfast tslow];
% hold on
% h2=bar(c2,y2)
%%%%%%%%%%%%%%%%%%%%%%%%%%%%%%%%%%%
%%%%%%%%%%%%%%%%%%%%%%%%%%%%%%%%%%%
%%%%%%%%%%%%%%%%
%%excel write
return
if r_sqr_exnewnorm > r_sqr_exnorm
A=[IRDN IP10N IEXF1N];
else
  A=[IRDN IP10N IEXN]
end
if frs==0 && frns==0
filename = 'testdata4.xlsx';
xlswrite(filename,A,1,'A1:R1')
 elseif frs==inf && frns==17.5
   filename = 'testdata4.xlsx';
 xlswrite(filename,A,1,'A2:R2');
 elseif frs==inf && frns==35
   filename = 'testdata4.xlsx';
 xlswrite(filename,A,1,'A3:R3');
  elseif frs==inf && frns==70
   filename = 'testdata4.xlsx';
 xlswrite(filename,A,1,'A4:R4');
  elseif frs==17.5 && frns==inf
   filename = 'testdata4.xlsx';
 xlswrite(filename,A,1,'A5:R5');
  elseif frs==35 && frns==inf
   filename = 'testdata4.xlsx';
 xlswrite(filename,A,1,'A6:R6');
  elseif frs==70 && frns==inf
   filename = 'testdata4.xlsx';
 xlswrite(filename,A,1,'A7:R7');
  elseif frs==703 && frns==inf
   filename = 'testdata4.xlsx';
 xlswrite(filename,A,1,'A8:R8');
end

%  cd ('F:\')
%  filename ='Book1.xlsx'
%  xlswrite(filename,A,1,'A2:R1')

 %%%%%double expotential fit new normalized
% % myfitc = fittype('a+b*exp(-1/c*x)+d*exp(-1/e*x)')
% myeqnorm='a+b*exp(-(1/c)*x)+d*exp(-(1/e)*x)'
% x=twb
% y=meanimagesgreym2dnorm
% %%%second order expotential fit new of  corrected intensity in cfit form
% f1norm = fit(x',y',myeqnorm);%,'Start', startPoints, 'Exclude', [1 10 25])
% coeff1norm=coeffvalues(f1norm);
% %%%%%%%%%tfast and tslow
% tfastnorm=coeff1norm(1,3);
% tslownorm=coeff1norm(1,5);
% %%%%%%%%%%%%plot second order expotential fit vs time froma raw data
% %subplot(5,2,10)
% figure
% plot(f1norm,twb,meanimagesgreym2dnorm)
% %title('double expotential fit new normalized')
% xlabel('time (s)')
% ylabel('I (-)')
```

```
% for i=startimage:lastimage
%     exf1norm(1,i)=f1norm(i);
% end
% exf1norm=exf1norm(1,startimage:lastimage);
% %r square of expotential normalized new  data of corrected intensity
% correlation_coeff_exf1norm = corr2(exf1norm,twb);
% r_sqr_exf1norm = power(correlation_coeff_exf1norm,2);
% %%%%%%%%%%%%%%%%%%%%%%%%% calculate them
% % % % amp=maxint-minint
% % % % sa=areea area under selectogram%auc
% %%%sa20area above curve%aac

% %% indices
% %%%%%%%%%%indices
% IndeicesRaw=[AIwbrd*100,thalfrd,AUCrd,AAcrd];
% IndeicesPolyfit=[AIwbp10*100,thalfp,AUCp10,AACp10];
% IndeicesExp=[AIwbex*100,thalfex,AUCex,AACex];
% Indicest=[tfast, tslow];
% %indices norm
%
IndeicesRawnorm=[AIwbrdnorm*100,thalfrdnorm,AUCrdnorm,AAcrdnor
m];
%
IndeicesPolyfitnorm=[AIwbp10norm*100,thalfpnorm,AUCp10norm,AAC
p10norm];
%
IndeicesExpnorm=[AIwbexnorm*100,thalfexnorm,AUCexnorm,AACexn
orm];
% %%indices mix
% IRD=[AIwbrd*100 AIwbrdnorm*100 thalfrd thalfrdnorm AUCrd
AUCrdnorm AAcrd AAcrdnorm 0 0];
% IEX=[AIwbex*100 AIwbexnorm*100 thalfex thalfexnorm AUCex
AUCexnorm AACex AACexnorm 0 0];
% IP10=[AIwbp10*100 AIwbp10norm*100 thalfp thalfpnorm AUCp10
AUCp10norm AACp10 AACp10norm 0 0];
% IT=[0 0 0 0 0 0 0 0 tfast tslow];
% % Indicestnorm=[tfastnorm,tslownorm];
% %
IndeicesExpNewnorm=[AIwbexf1*100,thalfexf1norm,AUCexf1,AACexf1
]
% %indicesbar
% c = categorical({'Raw Data','Polynomial','Expotential','Tfast and
Tslow'});
% y=[IRD;IP10;IEX;IT];
% % y=[AIwbrd*100 AIwbrdnorm*100 thalfrd thalfrdnorm AUCrd
AUCrdnorm AACrd AACrdnorm tfastnorm tslownorm;AIwbp10*100
AIwbp10norm*100 thalfp thalfpnorm Mp10 Mp10norm tfast tslow
tfastnorm tslownorm; AIwbex*100 AIwbexnorm*100 thalfex thalfexnorm
Mex Mexnorm tfast tslow tfastnorm tslownorm;];
% % y=[IndeicesRawnorm;IndeicesPolyfitnorm;IndeicesPolyfitnorm]
% subplot(5,2,2)
% h=bar(c,y)
% set(gca,'XTickLabel',{'Raw Data','Polynomial','Expotential','Tfast and
Tslow'});
% % set(gca,'legend')%,{'Raw Data','Polynomial','Expotential'});
% l=cell(1,10);
% l{1}='Aggregation Index'; l{2}='Aggregation index Normalized';
l{3}='Thalf'; l{4}='Thalf normalized'; l{5}='AUC'; l{6}='AUC Normalized';
l{7}='AAC';l{8}='AAC Normalized';l{9}='Tfast';l{10}='Tslow';
% l = legend(h,l);
% % c2=categorical({'tfast' ,'tslow'});
% % y2=[tfast tslow];
% % hold on
% % h2=bar(c2,y2)
% % %%%%%%double expotential fit new normalized
% % % myfitc = fittype('a+b*exp(-1/c*x)+d*exp(-1/e*x)')
% % myeqnorm='a+b*exp(-(1/c)*x)+d*exp(-(1/e)*x)'
% % x=twb
% % y=meanimagesgreym2dnorm
% % %%%second order expotential fit new of  corrected intensity in cfit
form
% % f1norm = fit(x',y',myeqnorm);%,'Start', startPoints, 'Exclude', [1 10
25])
% % coeff1norm=coeffvalues(f1norm);
% % %%%%%%%%%%tfast and tslow
% % tfastnorm=coeff1norm(1,3);
% % tslownorm=coeff1norm(1,5);
% % %%%%%%%%%%%%plot second order expotential fit vs time
froma raw data
% % %subplot(5,2,10)
% % figure
% % plot(f1norm,twb,meanimagesgreym2dnorm)
% % %title('double expotential fit new normalized')
% % xlabel('time (s)')
% % ylabel('I (-)')
% % for i=startimage:lastimage
% %     exf1norm(1,i)=f1norm(i);
% % end
% % exf1norm=exf1norm(1,startimage:lastimage);
% % %r square of expotential normalized new  data of corrected
intensity
% % correlation_coeff_exf1norm = corr2(exf1norm,twb);
% % r_sqr_exf1norm = power(correlation_coeff_exf1norm,2);
% % %%%%%%%%%%%%%%%%%%%%%%%%% calculate
them
% % % % % amp=maxint-minint
% % % % % sa=areea area under selectogram%auc
% % % %%%sa20area above curve%aac
%% graphs separately
% %% raw
% plot(twb,meanimagesgreym2d,'*')
% %title('whole blood intensity vs time','fontsize',14')
% xlabel('time (s)')
% ylabel('I (-)')
% %% raw corrected
% mean(meanimagesgreym2d)
% plot(twb,meanimagesgreym2d,'*')
% %title('whole blood intensity corrected vs time','fontsize',14')
% plot(twb,meanimagesgreym2d,'*')
% %title('whole blood intensity corrected vs time','fontsize',14')
% xlabel('time (s)')
% ylabel('I (-)')
% plot(twb,meanimagesgreym2dnorm,'-*');
% %title('whole blood intensity corrected normalized vs
time','fontsize',14')
% xlabel('time (s)')
% ylabel('Intensity Normalized with minimum(-)')
% plot(exfit,twb,meanimagesgreym2d)
% %title('double expotential fit')
% xlabel('time (s)')
% ylabel('I (-)')
% plot(exfitnorm,twb,meanimagesgreym2dnorm)
% %title('double expotential fit normalixed')
% xlabel('time (s)')
% ylabel('Intensity Normalized with minimum(-)')
 %%%thalf indices raw raw norm exp2 exp2norm
thalf_H007_WB_0_nostent=[thalfrd thalfrdnorm thalfex thalfexnorm];
AMP_H007_WB_0_nostent=[AMPrd AMPrdnorm AMPex AMPexnorm];
AI_H007_WB_0_nostent=[AIwbrd AIwbrdnorm AIwbex AIwbexnorm];

%%%thalf indices raw raw norm exp2 exp2norm new
thalf_H007_WB_0_nostent=[thalfrd thalfrdnorm thalfex thalfexf1norm];

AMP_H007_WB_0_nostent=[AMPrd AMPrdnorm AMPex AMPexf1];

AI_H007_WB_0_nostent=[AIwbrd AIwbrdnorm AIwbex AIwbexf1];
```